composites can therefore be ideally used as sensors having similar acoustic matching with the host structure material, concrete. The acoustic impedance of the composite can be calculated using Eq. 1 as follows;

$$I_c = \rho_c V_c \tag{1}$$

where I_c is the acoustic impedance of the composite, ρ_c is the density of the composite and V_c is the acoustic velocity of the composite. Therefore, research and development of the cement based piezoelectric composites play an important role in the development of structural health monitoring of concrete structure where they can be used as sensor making the structure so called smart or intelligent. Other connectivities other than 0–3 connectivity such as 1–3 and 2–2 of piezoelectric-cement composites has been reported to have better properties than 0–3 connectivity [18]. In this work, PZT ceramic-Portland cement composites of 2–2 connectivity were produced using a dice and fill method and their dielectric and piezoelectric properties were investigated.

2. Experimental Procedure

Lead zirconate titanate (PZT) powder of composition $Pb(Zr_{0.52}Ti_{0.48})O_3$ was produced from the two-stage mixed oxide method by calcining lead titanate and lead zirconate at 800°C. After calcining, PZT particles were sintered at 1,250°C for 3 hours to produce PZT ceramic disks of ≈12 mm diameter and ≈1.5 mm thickness. Poling of the PZT ceramics was then carried out under a poling field of 3 kV/mm for 20 mins in silicone oil at 130°C. After poling, PZT-cement composite of 2–2 connectivity was fabricated by cutting the PZT disk as the dispersed phase to make gaps in one horizontal direction using a diamond saw of ≈0.3 mm thick blade in order to obtain the volume content of 60, 70 and 80% (as shown in Fig. 1). The gaps were then filled with cement paste matrix using water to cement ratio of 0.5. Thereafter, the samples were cured at a temperature of 60°C and at 98% relatively humidity for five days.

The capacitance and the dissipation factor (dielectric loss or *tanδ*) of the composites were measured using an impedance meter (Hewlett Packard 4194A) at room temperature and at various frequencies (0.1 kHz–20 kHz) and the relative dielectric constant (ε_r) was then calculated from the following equation:

$$\varepsilon_r = \frac{Ct}{\varepsilon_0 A} \tag{2}$$

Figure 1. Schematic diagram of the 2–2 PZT-cement composite.

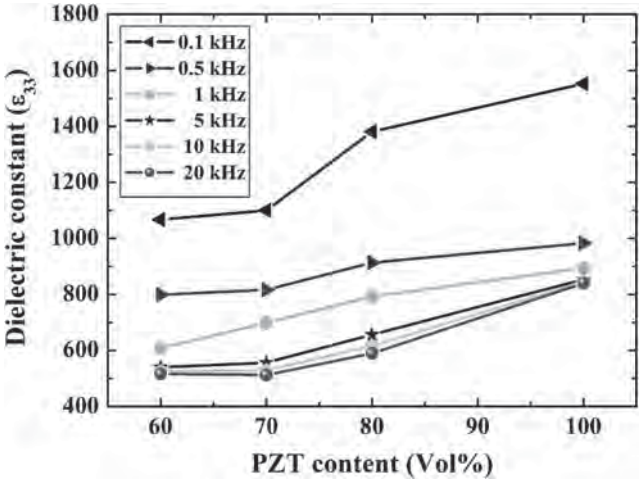

Figure 2. Dielectric constant results of 2–2 PZT-cement composites.

where C is the sample capacitance, t is the thickness, ε_0 is the permittivity of free space constant (8.854×10^{-12} Fm^{-1}), and A is the electrode area. The piezoelectric coefficient (d_{33}) was then measured using a d_{33} meter (piezometer System Model PM25).

3. Results and Discussion

The effect of PZT on the dielectric constant of 2–2 PZT-cement composites at various frequencies (0.1 kHz–20 kHz) can be seen in Fig. 2 where the dielectric constant is plotted against PZT content. The dielectric constant of the 2–2 composites can be seen to increase with PZT content since the dielectric constant of cement paste is much lower (≈79) than the pure PZT ceramic of ≈900–1,000 at 1 kHz [18] for all frequencies and that the dielectric constant at 0.1 kHz, 1 kHz and 20 kHz are 1,067, 608 and 516 for the composite with 60% PZT composite respectively. Where as for the composite with 70% composite at 1 kHz, the dielectric constant is 698. The values at 1 kHz are significantly higher than previously reported 0-3 PZT-cement composites [10, 21] where the dielectric value is in the region of 200–300 for 50–70% PZT by volume. Also, the value of 2–2 composite is comparatively much closer to the value of 100% PZT ceramic due to the better resemblance of the disk to the pure ceramic as a parallel model (Fig. 1).

The effect of PZT on the dielectric loss using the frequency from 0.1 kHz to 20 kHz can be seen in Fig. 3. In general, the dielectric loss of 2–2 PZT-cement composites was found to reduce when compared to the previous work reported on 0–3 composite at the same PZT volume content. The benefit of using a 2–2 connectivity can therefore be clearly observed where a significant reduction was found for example $tan\delta$ value of 60% PZT composite at 1 kHz is 0.44 when compared to that 0–3 composite of 0.75 [21] at the same frequency. However, both these values are higher than the pure PZT ceramic of 0.02 but much lower than that of cement paste of 2.41 [18].

Measured piezoelectric coefficient (d_{33}) results of PZT-PC composites showing the effect of PZT content can be seen in Fig. 4. The piezoelectric coefficient can be seen to increase with PZT content, as expected. The piezoelectric coefficient, d_{33}, value of the 2–2

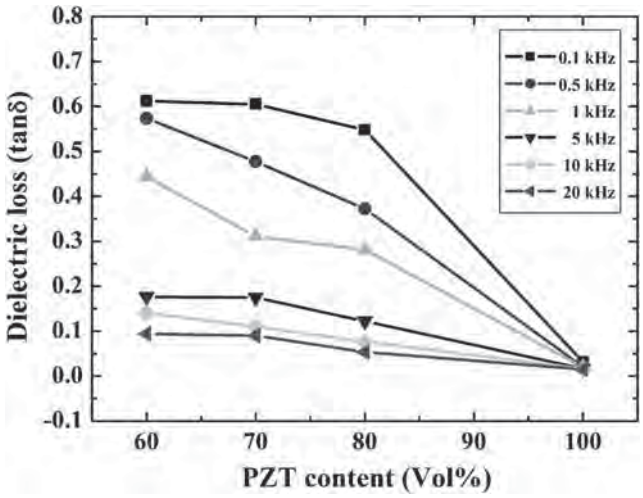

Figure 3. Dielectric loss results of 2–2 PZT-cement composites.

PZT-cement composite at PZT volume content of 60% is 99 pC/N which is significantly higher than that of previously tested 0–3 PZT-cement composites where d_{33} value is 42 [21]. For 2–2 composites with 70% and 80% PZT volume, d_{33} values are 113 pC/N and 146 pC/N respectively. This was found to be very close to the pure PZT ceramic where d_{33} value is ≈170 pC/N. Therefore, 2–2 composites, which represent a parallel model, are closer in resemblance to the pure PZT ceramic than those of 0-3 ceramics resulting in higher dielectric constant and piezoelectric coefficient.

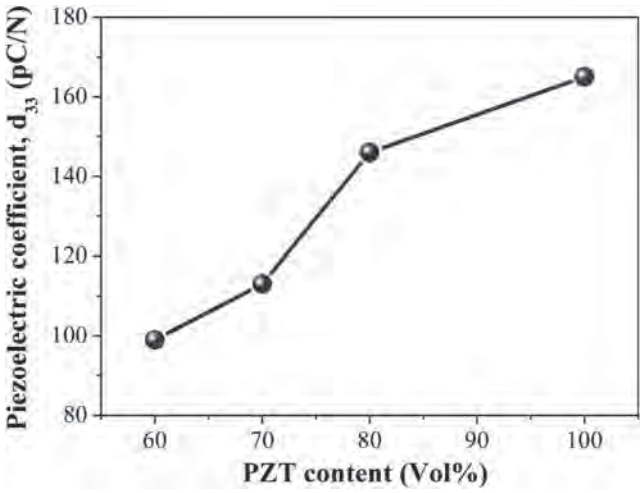

Figure 4. Piezoelectric coefficient results of 2–2 PZT-cement composites.

4. Conclusions

PZT ceramic-Portland cement composites of 2–2 connectivity were produced using dice and fill method. The dielectric constant of the 2–2 composites can be seen to increase with PZT content and that the dielectric constant at 1 kHz for 70% PZT is 698. The dielectric loss of 2–2 PZT-cement composites was found to be noticeably lower than previous work reported on 0–3 composite at the same PZT volume content. The piezoelectric coefficient, d_{33}, value of the 2–2 PZT-cement composite at PZT volume content of 60% is 99 pC/N, which is significantly higher than that of previously tested 0–3 PZT-cement composites. For 2–2 composites with 70% and 80% PZT volume, d_{33} values are 113 pC/N and 146 pC/N respectively. This was found to be very close to the pure PZT ceramic at the same condition. These results are very high when compared to previously published 0–3 PZT-cement composites at the same volume content. This is due to the 2–2 composites represent a parallel model and therefore, is closer to that of the PZT ceramic with improvement in dielectric and piezoelectric properties in comparison to that of 0–3 composites.

Acknowledgments

The authors would like to express their gratitude for research grant awarded to Assistant Prof. Dr. Arnon Chaipanich by the Thailand Research Fund (TRF). The authors are also grateful to the Thailand Research Fund (TRF) for the TRF Senior Research Scholar Contract No. RTA5480004 awarded to Professor Dr. Prinya Chindaprasirt.

References

1. R. Potong, R. Rianyoi, A. Ngamjarurojana, and A. Chaipanich, Dielectric and piezoelectric properties of 1–3 non-lead barium zirconate titanate-Portland cement composites. *Ceram. Int.* **39**, S53–S57 (2013).
2. R. Rianyoi, R. Potong, A. Ngamjarurojana, and A. Chaipanich, Influence of barium titanate content and particle size on electromechanical coupling coefficient of lead-free piezoelectric ceramic-Portland cement composites. *Ceram. Int.* **39**, S47–S51 (2013).
3. Z. Li, D. Zhang, and K. Wu, Cement based-0-3 piezoelectric composites. *J. Am. Ceram. Soc.* **85**, 305–313 (2002).
4. S. Huang, J. Chang, R. Xu, F. Liu, L. Lu, Z. Ye, and X. Cheng, Piezoelctric properties of 0–3 PZT/sulfoaluminate cement composites. *Smart Mater. Struct.* **13**, 270–274 (2004).
5. B. Dong and Z. Li, Cement-based piezoelectric ceramic smart composites. *Comp. Sci. Tech.* **65**, 1363–1371 (2005).
6. S. F. Huang, J. Chang, L. C. Lu, F. T. Liu, Z. M. Ye, and X. Cheng, Preparation and polarization of 0-3 cement based piezoelectric composites. *Mater. Res. Bull.* **41**, 291–297 (2006).
7. R. Potong, R. Rianyoi, A. Ngamjarurojana, and A. Chaipanich, Ferroelectric hysteresis properties of 0-3 lead-free barium zirconate titanate-Portland cement composites. *Ferr. Lett.* **39**(1–3), 15–19 (2012).
8. X. Cheng, S. F. Huang, J. Chang, and Z. Li, Piezoelectric, dielectric, and ferroelectric properties of 0–3 ceramic/cement composites. *J. Appl. Phys.* **101**, 094110 (2007).
9. A. Chaipanich and N. Jaitanong, Effect of PZT particle size on the electromechanical coupling coefficient of 0-3 PZT-cement composites. *Ferr. Lett.* **36**, 37–44 (2009).
10. K. Uchino, *Piezoelectrics and Ultrasonic Applications*. Kluwer: Deventer; 1998.
11. R. E. Newnham and A. Amin, Smart systems: Microphones, fish farming, and beyond. *Chemtech.* **29**, 38–46 (1999).

12. A. Chaipanich, R. Rianyoi, R. Potong, W. Suriya, N. Jaitanong, and P. Chindaprasirt, Dielectric properties of 2-2 PMN-PT/cement composites. *Ferr. Lett*. **39**(4–6), 76–80 (2012).
13. A. Chaipanich and N. Jaitanong, Effect of poling time on piezoelectric properties of 0-3 PZT-Portland cement composites. *Ferr. Lett*. **35**, 73–78 (2008).
14. N. Jaitanong and A. Chaipanich, Effect of poling temperature on piezoelectric properties of 0-3 PZT-Portland cement composites. *Ferr. Lett*. **35**, 17–23 (2008).
15. A. Chaipanich, N. Jaitanong, and T. Tunkasiri, Fabrication and properties of PZT-ordinary Portland cement composites. *Mater. Lett*. **61**, 5206–5208 (2007).
16. A. Chaipanich, G. Rujijanagul, and T. Tunkasiri, Properties of Sr and Sb doped PZT-Portland cement composites. *Appl. Phys. A*. **94**, 329–337 (2009).
17. A. Chaipanich, Effect of PZT particle size on dielectric and piezoelectric properties of PZT-cement composites. *Curr. Appl. Phys*. **7**, 574–577 (2007).
18. A. Chaipanich, Dielectric and piezoelectric properties of PZT-cement composites. *Curr. Appl. Phys*. **7**, 537–539 (2007).
19. A. Chaipanich, Dielectric and piezoelectric properties of PZT-silica fume cement Composites. *Curr. Appl. Phys*. **7**, 532–536 (2007).
20. Z. Li, B. Dong, and D. Zhang, Influence of polarization on properties of 0-3 cement-based PZT composites. *Cem. Concr. Compos*. **27**, 27–32 (2005).
21. A. Chaipanich and N. Jaitanong, Effect of polarization on the microstructure and piezoelectric properties of PZT-cement composites. *Adv. Mater. Res*. **55–57**, 381–384 (2008).
22. A. Chaipanich, N. Jaitanong, and R. Yimnirun, Effect of carbon addition on the ferroelectric hysteresis properties of lead zirconate-titanate ceramic-cement composites. *Ceram. Int*. **37**, 1181–1184 (2011).
23. N. Jaitanong, K. Wongjinda, P. Tammakun, G. Rujijanagul, and A. Chaipanich, Effect of carbon addition on dielectric properties of 0-3 PZT-Portland cement composite. *Adv. Mater. Res*. **55–57**, 377–380 (2008).

Materials and Design 53 (2014) 269–274

Contents lists available at SciVerse ScienceDirect

Materials and Design

journal homepage: www.elsevier.com/locate/matdes

Influence of curing conditions on properties of high calcium fly ash geopolymer containing Portland cement as additive

Saengsuree Pangdaeng, Tanakorn Phoo-ngernkham, Vanchai Sata, Prinya Chindaprasirt *

Sustainable Infrastructure Research and Development Center, Department of Civil Engineering, Faculty of Engineering, Khon Kaen University, Khon Kaen 40002, Thailand

ARTICLE INFO

Article history:
Received 17 May 2013
Accepted 4 July 2013
Available online 14 July 2013

Keywords:
Geopolymer
High calcium fly ash
Portland cement
Additive
Curing condition

ABSTRACT

This paper investigated the mechanical properties and microstructure of high calcium fly ash geopolymer containing ordinary Portland cement (OPC) as additive with different curing conditions. Fly ash (FA) was replaced with OPC at dosages of 0%, 5%, 10%, and 15% by weight of binders. Setting time and microstructure of geopolymer pastes, and flow, compressive strength, porosity and water absorption of geopolymer mortars were studied. Three curing methods viz., vapour-proof membrane curing, wet curing and temperature curing were used. The results showed that the use of OPC as additive improved the properties of high calcium fly ash geopolymer. The strength increased due to the formation of additional C–S–H and C–A–S–H gel. Curing methods also significantly affected the properties of geopolymers with OPC. Vapour-proof membrane curing and water curing resulted in additional OPC hydration and led to higher compressive strength. The temperature curing resulted in a high early compressive strength development.

1. Introduction

Clinker production process in the cement industry requires a lot of energy and emits a large amount of carbon dioxide (CO_2) to the atmosphere. The production of cement in 2005 accounted for around 7% of CO_2 world emission [1]. The negative environmental impact must be reduced by a reduction in the use of Portland cement. Fly ash, silica fumes and agro-waste ashes can be used as pozzolanic materials to reduce Portland cement usage and to curb emission of CO_2. Geopolymer is now receiving more attention as an alternative binder for use as building material. It is made from aluminosilicate source materials activated with high alkali solutions [2].

Fly ash is a by-product from coal burning to produce electricity. For Thailand, the major source of fly ash is from Mae Moh power station in the north. Approximately 3 million tons is produced annually and it is used extensively in the construction industry as supplementary cementitious materials to replace part of Portland cement. Many researchers have shown that it can be used for making good geopolymer [3–5].

At ambient temperature of around 25 °C, the fly ash geopolymer gains strength slowly [6]. To obtain reasonable strength fly ash geopolymers, temperature curing at 40–75 °C is normally required [7]. This is difficult for the construction practice in real construction. A number of researchers have, therefore, tried to improve the strength development of fly ash geopolymers. Some additives such as ground granulated blast furnace slag, flue gas desulfurization gypsum and Portland cement are used [6,8,9].

The use of OPC to improve strength of fly ash geopolymer is very attractive as OPC is a common commodity in construction industry. The reaction of OPC and water is an exothermal process at normal temperature and the developed heat should be beneficial to the enhancement of mechanical properties of geopolymer. In this research, the mechanical properties and microstructure of geopolymer with various levels of OPC replacement and curing condition were studied. The knowledge should be useful in the understanding and future utilization of the high calcium fly ash geopolymer containing OPC as additive.

2. Experimental details

2.1. Materials

Fly ash (FA) from Mae Moh power plant in Lampang province in northern Thailand, and ordinary Portland cement (OPC) were the materials used. The Blaine finenesses of FA and OPC were 2460 and 3600 cm^2/g. The alkaline solutions were 10 M sodium hydroxide (NaOH) and sodium silicate (Na_2SiO_3) with 15.32% Na_2O, 32.87% SiO_2, and 51.81% H_2O. Local river sand with specific gravity of 2.62 and fineness modulus of 2.90 was used for making geopolymer mortar.

The chemical compositions of materials are given in Table 1. The FA consisted of 36.0% SiO_2, 14.9% Al_2O_3 and 19.7% Fe_2O_3, and the CaO content was high at 19.4%. The sum of $SiO_2 + Al_2O_3 + Fe_2O_3$

* Corresponding author. Tel.: +66 4320 2355; fax: +66 4320 2355x12.
E-mail address: prinya@kku.ac.th (P. Chindaprasirt).

0261-3069/$ - see front matter © 2013 Elsevier Ltd. All rights reserved.
http://dx.doi.org/10.1016/j.matdes.2013.07.018

Table 1
Chemical composition of FA and OPC.

Materials	Chemical composition (%)								
	SiO_2	Al_2O_3	Fe_2O_3	CaO	MgO	Na_2O	K_2O	SO_3	LOI
FA	36.0	14.9	19.7	19.4	2.6	0.7	1.0	4.6	1.1
OPC	20.8	4.7	3.4	65.3	1.5	0.4	0.1	2.7	0.9

content of the FA were 70.6%. The high calcium content suggested that it was class C fly ash as specified by ASTM: C618.

2.2. Sample preparation

2.2.1. Mix proportion

Table 2 shows the mix proportion of the geopolymers. The mixes were named FA, 5PC, 10PC, and 15PC mixes with FA replaced by OPC at the dosages of 0%, 5%, 10%, and 15% by weight of binder, respectively. Constant liquid alkaline/binder ratio (L/B) of 0.40 and Na_2SiO_3/NaOH ratio of 0.67 were used for all mixes. The SiO_2/Al_2O_3 and CaO/SiO_2 ratios were computed and also presented in Table 2. For the geopolymer mortar mixes, sand/binder ratio of 2.75 was employed.

2.2.2. Mixing and curing method

For mixing of pastes, FA and OPC were thoroughly mixed until a uniform mixture was obtained which took approximately 2 min. For mortar mixes, sand was incorporated in the mixes with FA and OPC. Then NaOH was added and mixed for 5 min and Na_2SiO_3 was incorporated and mixed for another 5 min. The mixing was done in an air conditioned room with temperature around 25 °C.

After mixing, the fresh geopolymer pastes and mortars were placed into 50 × 50 × 50 mm cube moulds as described in ASTM: C109. The samples were covered with damp cloth and vinyl sheet and placed in 23 °C controlled room for a period of 24 h. They were then demoulded and put into different curing conditions as follows.

(1) Vapour-proof membrane curing (MC). The demoulded samples were wrapped with a vapour-proof membrane to prevent moisture loss and kept in a control 23 °C room.
(2) Temperature curing (TC). The samples were wrapped with a plastic membrane to prevent moisture loss and then oven-cured at 40 °C for 24 h. After that, the samples were demoulded and kept in a 23 °C room.
(3) Wet curing (WC). The demoulded samples were immersed in water in a 23 °C room until the testing age.

2.3. Setting time and flow

The setting time of geopolymer pastes were tested using Vicat apparatus in accordance with ASTM: C191. The flow of fresh geopolymer mortars were tested in accordance with ASTM: C1437. The reported results were the average of two tests.

Table 2
Mix proportions of geopolymer.

Mixes	FA:OPC	Na_2SiO_3/NaOH	SiO_2/Al_2O_3	CaO/SiO_2
FA	100:0	0.67	2.77	0.47
5PC	95:5	0.67	2.80	0.54
10PC	90:10	0.67	2.83	0.61
15PC	85:15	0.67	2.86	0.69

2.4. Compressive strength, porosity and water absorption

Compressive strengths of geopolymer mortars were tested at the ages of 3, 7, 28, and 90 days in accordance with ASTM: C109. The reported results were the average of three samples.

Porosity and water absorption of geopolymer mortars were tested at the age of 7 days in accordance with ASTM: C642. The measured values were calculated using Eqs. (1) and (2). The reported results were the average of two samples. The methods for measuring porosity and absorption were used successfully in a number of researches [10,11].

$$\text{Porosity}\ (\%) = \left(\frac{W_a - W_d}{W_a - W_w}\right) \times 100 \tag{1}$$

$$\text{Absorption}\ (\%) = \left(\frac{W_a - W_d}{W_d}\right) \times 100 \tag{2}$$

where Porosity is the vacuum saturation porosity of geopolymer mortar (%), Absorption is water absorption of geopolymer mortar (%), W_a is weight in air of saturated sample (g), W_d is weight of dried sample (g), and W_w is the weight in water of saturated sample (g).

2.5. SEM and XRD analysis

Scanning electron microscopy (SEM) and X-ray Diffraction (XRD) were used to study the microstructure of geopolymer pastes. The XRD scans were performed between 5 and 70° 2θ, with an increment of 0.02 deg/step and a scan speed of 0.5 s/step. The amorphous structure in geopolymer was determined by quantitative XRD using Bruker's TOPAS software.

3. Results and discussions

3.1. Setting time and flow

The results of setting time of geopolymer paste and flow of mortar are shown in Figs. 1 and 2. The addition of OPC resulted in the reduction of setting time of pastes and flow of fresh mortars. For the 0%, 5%, 10% and 15% OPC mixes, the initial setting times were 124, 66, 39 and 28 min. while the final setting times were 144, 82, 53 and 47 min. respectively, and the flow values reduced from 136% to 111%. As the OPC contained a reasonably high CaO content (65.3%), the incorporation of OPC, therefore, resulted in the

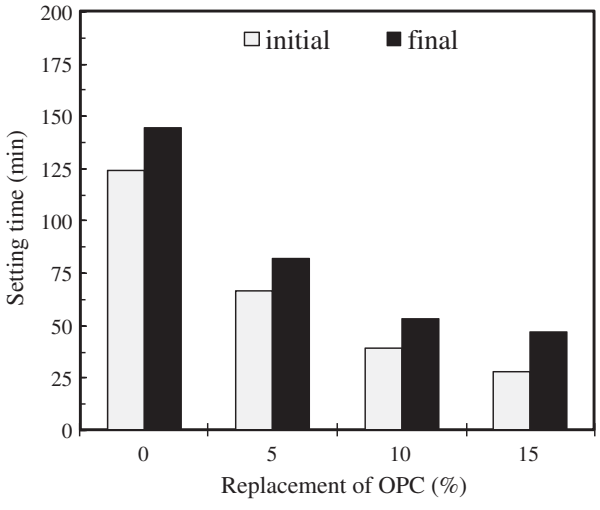

Fig. 1. Setting time of geopolymer paste.

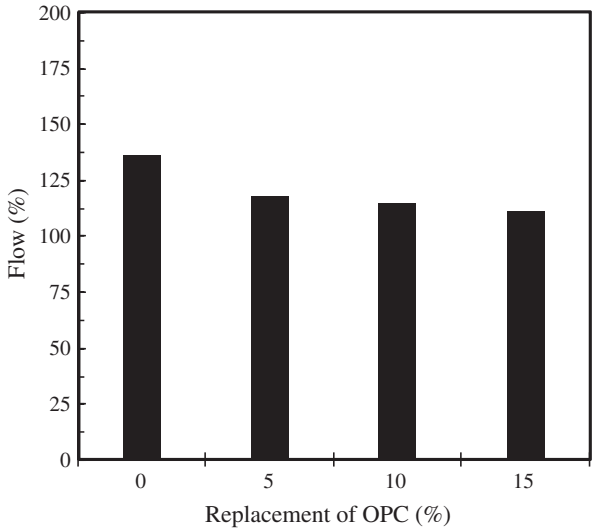

Fig. 2. Flow of geopolymer mortar.

Table 3
Compressive strengths of geopolymer mortars.

Mixes-cured	Compressive strength (MPa)			
	3 days	7 days	28 days	90 days
FA-MC	18.3	32.4	45.0	55.0
5PC-MC	30.4	37.7	52.1	59.0
10PC-MC	37.4	41.7	53.6	62.6
15PC-MC	39.3	41.4	57.8	67.9
FA-TC	40.8	50.7	57.3	59.0
5PC-TC	49.3	53.6	61.9	68.6
10PC-TC	53.5	55.6	65.4	73.5
15PC-TC	55.0	55.4	56.7	57.6
FA-WC	25.8	38.6	45.6	57.6
5PC-WC	37.9	48.8	55.7	68.4
10PC-WC	43.2	52.7	67.4	78.9
15PC-WC	46.4	53.4	67.8	75.3

increase in calcium content in the geopolymer system. The addition of calcium significantly accelerated the setting and hardening of pastes [12]. Additional calcium provided extra nucleation sites for precipitation of dissolved species which increased its solidification rate and cause rapid hardening [13].

3.2. Compressive strength

The results of compressive strengths of geopolymer mortars are shown in Table 3 and Fig. 3. The increase in OPC replacement level increased the compressive strength of geopolymer mortars. For example, the compressive strengths at 28 days of membrane cured FA, 5PC, 10PC and 15PC mortars were 18.3, 32.4, 45.0 and 55.0 MPa, respectively. The calcium elements reacted and formed additional C–S–H and C–A–S–H which coexisted with geopolymer products [14] and contributed to the strength development of mortar. The compressive strengths increased with curing age for all of MC, TC and WC series similar to that of OPC system. The increase in strength was more pronounced with the increase in OPC content and indicated additional reaction of calcium element. Moreover, the strength increases of WC series were larger than those of MC series suggesting the additional hydration of OPC due to wet curing. This led to the pore refinement similar to pozzolanic reaction in blended cements [15]. It was also suggested that the pozzolanic reaction in fly ash-alkaline liquid occurred much faster than the normal pozzolanic reaction in the Portland cement system [16].

The TC series exhibited higher early compressive strength than MC and WC series due to the strength development at an accelerated rate with characterize of quick geopolymerization process [17]. The TC series compressive strength was equivalent to those of MC and WC series at the later ages. It should be noted that the compressive strengths of geopolymer mortars with OPC as additive cured at ambient temperature were approximately the same as those of FA series temperature cured at 40 °C. For the high OPC content 15PC-TC mix, the compressive strength gain at early age was noticeable with the slowdown of strength gain at long term. The negative effects of temperature curing for the long term strength gain were related to modifications of the microstructure of the hydration products phase [18].

3.3. Porosity and water absorption

The results of porosities and water absorptions of mortars are shown in Table 4. The porosities and water absorption decreased with the increasing replacement of OPC compared with the control mortar as expected. For example, the porosities and water of water cured FA, 5PC, 10PC and 15PC mortars were 12.43%, 11.11%, 10.75% and 10.12%, respectively with the corresponding absorptions of 5.78%, 5.07%, 4.81% and 4.59%, respectively. The addition of OPC increased the hydration and amount of C–S–H and C–A–S–H. The products filled the pores and thus reduced both porosities and water absorptions with corresponding increase in compressive strengths. Thokchom et al. [11] reported a similar value of mortar

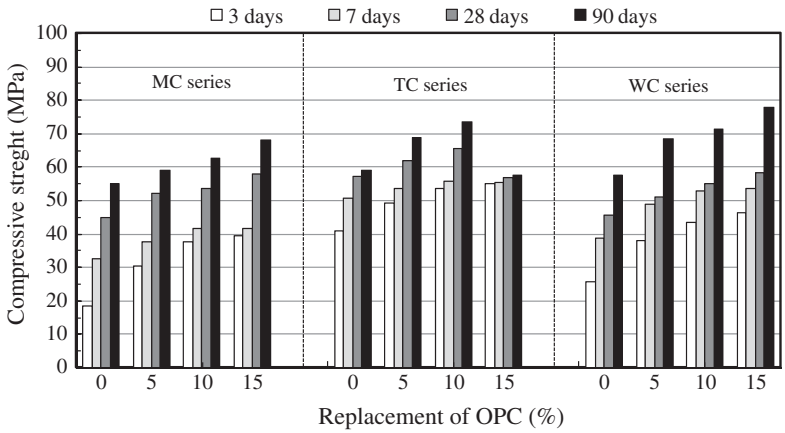

Fig. 3. Compressive strength of geopolymer mortar.

Table 4
Porosity and water absorption of geopolymer mortar at the age of 7 days.

Mixes	Porosity (%)			Water absorption (%)		
	MC	TC	WC	MC	TC	WC
FA	9.76	9.41	12.43	4.46	4.25	5.78
5PC	9.06	8.89	11.11	4.08	3.99	5.07
10PC	8.98	8.70	10.75	4.05	3.92	4.81
15PC	8.85	8.40	10.12	3.98	3.77	4.59

porosity of 12.54% for similar strengths between 32.4 and 53.4 MPa.

The porosities and water absorptions of WC series were, however, larger than those of MC and TC series. For example, the porosities at 7 days of FA-WC, FA-MC and FA-TC mortars were 12.43%, 9.76% and 9.41% and the water absorptions were 5.78%, 4.46% and 4.25% respectively. It was reported that the high calcium fly ash geopolymer mortars showed significant drying shrinkage in the dry atmosphere and swelling in the presence of water [19]. This contributed to the increase in porosities and water absorptions of WC mixes compared with those of MC and TC samples.

3.4. XRD analysis

The results of XRD of FA-TC, PC10-MC, PC10-TC and PC10-WC geopolymer pastes are shown in Fig. 4. The major phase of geopolymer was amorphous as indicated by the broad hump at the region of 25−37° 2θ. The FA-MC paste contained crystalline phases of vishnevite ($Na_8Al_6Si_6O_{24}(SO_4)_2{\cdot}H_2O$), quartz ($SiO_2$), magnesioferrite ($Fe_2MgO_4$) and calcite ($CaCO_3$). For addition of OPC, the 10PC-MC and 10PC-TC paste showed similar phases to those of FA-TC paste with some additional portlandite ($Ca(OH)_2$) and a small amount of chabazite ($Ca_{1.95}Al_{3.9}Si_{8.1}O_{24}$). The increase in porlandite phase was a direct result of OPC addition. For the WC paste, the 10PC-WC paste showed significant different crystalline phases to those of 10PC-MC and 10PC-TC paste. The vishnevite phase reduced, portlandite disappeared and calcite increased with water curing. With the presence of water, portlandite reacted with silica and alumina and formed C–S–H and C–A–S–H similar to the pozzolanic reaction in the blended cement paste [15]. The presence of geopolymer (or N–A–S–H gel) phases in the XRD patterns are usually associated with a broad peak around 28–35° 2θ and the C–S–H and C–A–S–H phases are indicated by the main peak at 30° 2θ [20–22]. The hydration products was shown to co-exist with the geopolymer products [14] and contributed to additional strength development.

3.5. SEM analysis

The SEM images of geopolymer pastes as shown in Fig. 5 showed the similar morphologies of control FA paste and 10PC paste. As mentioned, the additional C–S–H and C–A–S–H from the reaction of OPC and leached calcium from fly ash co-existed with the geopolymer products. Noticeable difference was observed between the differently cured samples. For the FA-MC paste, a large amount of non-reacted fly ash particles in the matrix was observed indicating a relatively low stage of geopolymerization. The FA-TC and FA-WC paste matrices appeared denser than the FA-MC paste and the 10PC-TC and 10PC-WC pastes also appeared denser than the 10PC-MC paste. Normally, the high calcium fly ash geopolymerization was slow at room temperature and needed temperature curing to accelerate the strength development [3]. The increases in the OPC content increased the calcium in the system and its reaction produced extra hydration products and liberated heat which also promoted the geopolymerization. The water curing resulted in the increasing hydration reaction of OPC in the geopolymer system compared with that of the MC series.

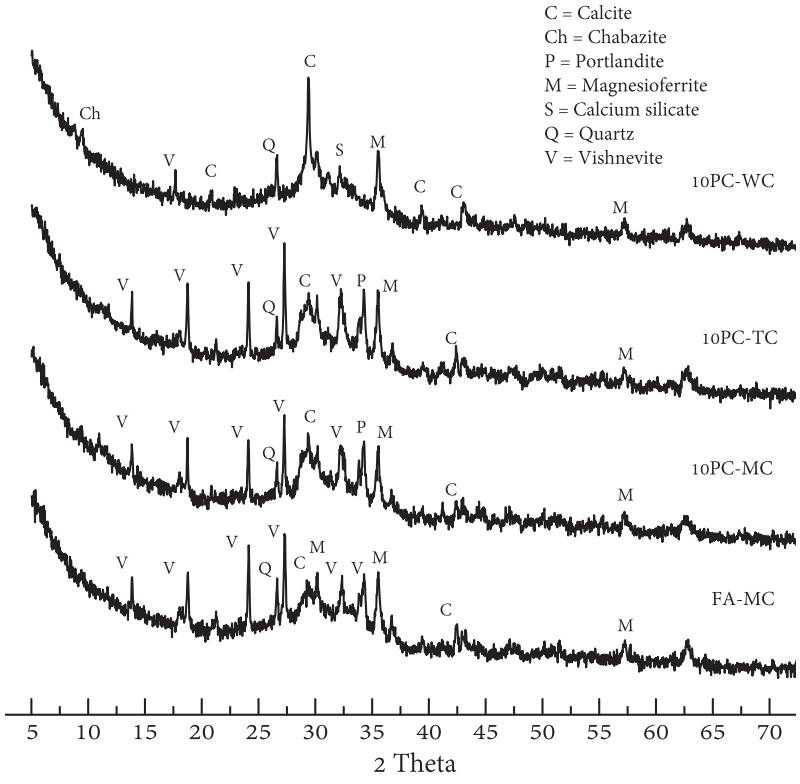

Fig. 4. XRD of geopolymer at the age of 7 days.

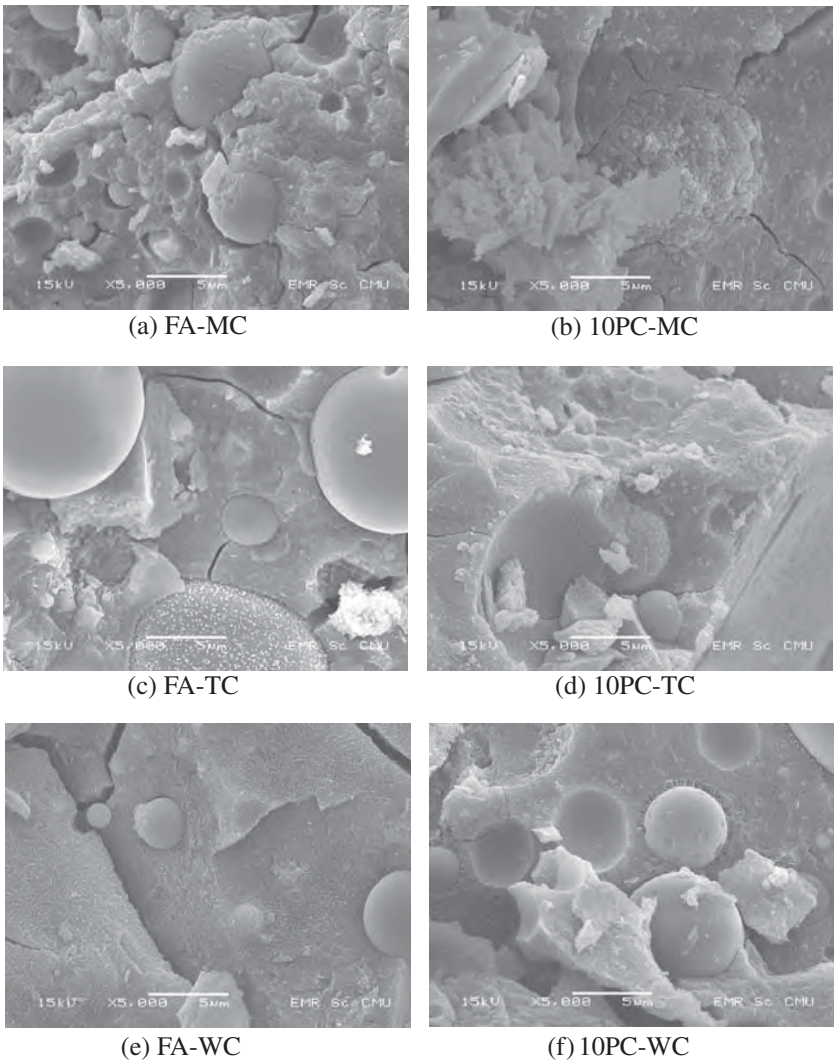

(a) FA-MC (b) 10PC-MC

(c) FA-TC (d) 10PC-TC

(e) FA-WC (f) 10PC-WC

Fig. 5. SEM of geopolymer at the age of 7 days.

4. Conclusions

The use of OPC as additive in high calcium FA geopolymer resulted in enhancement of mechanical properties viz., the reduction of porosities, and water absorption and an associated increase in the compressive strength as a result of additional formation of C–S–H and C–A–S–H gel which modified the microstructure and the pore, resulting in a dense and strong matrix. Curing methods also significantly affected the properties of geopolymers with OPC. The vapour-proof membrane curing and the water curing resulted in the addition OPC hydration and high compressive strength at a later age. The temperature curing resulted in a high early compressive strength.

Acknowledgements

This work was financially supported by the Higher Education Research Promotion and National Research University Project of Thailand, Office of the Higher Education Commission, through the Advanced Functional Materials Cluster of Khon Kaen University, and the Thailand Research Fund (TRF) under the TRF Senior Research Scholar, Grant No. RTA5480004 and TRF and Khon Kaen University under the TRF-Royal Golden Jubilee Ph.D. program (Grant No. PHD/0143/2554).

References

[1] Metz B, Davidson OR, Bosch PR, Dave R, Meyer LA. Climate change. Contribution of Working Group III to the Fourth Assessment Report of the Intergovernmental Panel on Climate Change. Cambridge, United Kingdom and New York (USA): Cambridge University Press; 2007. p. 447–96.
[2] Davidovits J. Geopolymers – inorganic polymeric new materials. J Therm Anal Calorim 1991;37:1633–56.
[3] Wongpa J, Kiattikomol K, Jaturapitakkul C, Chindaprasirt P. Compressive strength, modulus of elasticity, and water permeability of inorganic polymer concrete. Mater Des 2010;31:4748–54.
[4] Sata V, Sathonsaowaphak A, Chindaprasirt P. Resistance of lignite bottom ash geopolymer mortar to sulfate and sulfuric acid attack. Cement Concr Compos 2012;34:700–8.
[5] Chindaprasirt P, Chareerat T, Sirivivatnanon V. Workability and strength of coarse high calcium fly ash geopolymer. Cement Concr Compos 2007;29:224–9.
[6] Guo X, Shi H, Chen L, Dick WA. Alkali-activated complex binders from class C fly ash and Ca-containing admixtures. J Hazard Mater 2010;173:480–6.
[7] Bakharev T. Thermal behaviour of geopolymers prepared using class F fly ash and elevated temperature curing. Cem Concr Res 2006;36:1134–47.
[8] Allahverdi A, Kani EN, Yazdanipour M. Effects of blast-furnace slag on natural pozzolan-based geopolymer cement. Ceram-Silikaty 2011;55:68–78.
[9] Palomo A, Fernández-Jiménez A, Kovalchuk G, Ordoñez LM, Naranjo MC. OPC-fly ash cementitious systems: study of gel binders produced during alkaline hydration. J Mater Sci 2007;42:2958–66.
[10] Chindaprasirt P, Rukzon S. Strength, porosity and corrosion resistance of ternary blend Portland cement, rice husk ash and fly ash mortar. Constr Build Mater 2008;22:1601–6.
[11] Thokchom S, Ghosh P, Ghosh S. Effect of water absorption, porosity and sorptivity on durability of geopolymer mortars. ARPN J Eng Appl Sci 2009;4:28–32.

[12] Chindaprasirt P, Silva P, Sagoe-Crentsil K, Hanjitsuwan S. Effect of SiO_2 and Al_2O_3 on the setting and hardening of high calcium fly ash-based geopolymer systems. J Mater Sci 2012;47:4876–83.
[13] Lee WKW, van Deventer JSJ. The effects of inorganic salt contamination on the strength and durability of geopolymers. Colloids Surf, A 2002;211:115–26.
[14] Somna K, Jaturapitakkul C, Kajitvichyanukul P, Chindaprasirt P. NaOH-activated ground fly ash geopolymer cured at ambient temperature. Fuel 2011;90:2118–24.
[15] Kroehong W, Sinsiri T, Jaturapitakkul C, Chindaprasirt P. Effect of palm oil fuel ash fineness on the microstructure of blended cement paste. Constr Build Mater 2011;25:4095–104.
[16] Temuujin J, van Riessen A, Williams R. Influence of calcium compounds on the mechanical properties of fly ash geopolymer pastes. J Hazard Mater 2009;167:82–8.
[17] Davidovits J. Chemistry of geopolymeric systems, terminology. In: Second international conference on geopolymer. Saint-Quentin (France); 1999. p. 9–40.
[18] Maltais Y, Marchand J. Influence of curing temperature on cement hydration and mechanical strength development of fly ash mortars. Cem Concr Res 1997;27:1009–20.
[19] Ridtirud C, Chindaprasirt P, Pimraksa K. Factors affecting the shrinkage of fly ash geopolymers. Int J Min, Metall Mater 2011;18:100–4.
[20] Garcia-Lodeiro I, Palomo A, Fernández-Jiménez A, MacPhee DE. Compatibility studies between N–A–S–H and C–A–S–H gels. Study in the ternary diagram Na_2O–CaO–Al_2O_3–SiO_2–H_2O. Cem Concr Res 2011;41:923–31.
[21] Lecomte I, Henrist C, Liegeois M, Maseri F, Rulmont A, Cloots R. (Micro)-structural comparison between geopolymers, alkali-activated slag cement and Portland cement. J Eur Ceram Soc 2006;26:3789–97.
[22] Yip CK, Lukey GC, Van Deventer JSJ. The coexistence of geopolymeric gel and calcium silicate hydrate at the early stage of alkaline activation. Cem Concr Res 2005;35:1688–97.

Ferroelectrics, 457:53–61, 2013

ISSN: 0015-0193 print / 1563-5112 online
DOI: 10.1080/00150193.2013.847333

Compressive Strength and Microstructure of 0–3 Lead Zirconate Titanate Ceramic-Portland Cement Composites

ARNON CHAIPANICH,[1,*] RATTIYAKORN RIANYOI,[1] RUAMPORN POTONG,[1] NITTAYA JAITANONG,[1] AND PRINYA CHINDAPRASIRT[2]

[1]Department of Physics and Materials Science, Faculty of Science, Chiang Mai University, Chiang Mai 50200, Thailand
[2]Sustainable Infrastructure Research and Development Center, Department of Civil Engineering, Faculty of Engineering, Khon Kaen University, Khon Kaen 40002, Thailand

Lead zirconate titanate (PZT)-Portland cement (PC) composites have been reported to have good potential for use in smart structures. In this work, PZT-PC composites containing 40%, 50% and 60% of PZT by volume were produced and their mechanical and hydration properties were investigated. Compressive strengths of those typically used in normal concrete were found for all PZT-PC composites, with measured values of 41.5–45.0 MPa. Hydration products of Portland cement detected by thermal analysis were calcium silicate hydrates (the main cement hydration product), calcium hydroxide and ettringite. Furthermore, calcium silicate hydrates and ettringite can also be observed surrounding the PZT grains in the SEM micrograph.

Keywords PZT; cement; composites; compressive strength; microstructure

1. Introduction

Piezoelectric lead zirconate titanate – $Pb(Zr_{0.52}Ti_{0.48})O_3$ (PZT) – ceramic is well known for its high dielectric constant and high piezoelectric coupling coefficient. Uses of PZT are found in numerous applications such as sensors, transducers and actuators [1–3]. For smart civil engineering applications where a structure can sense and detect a movement, cement-based composites consisting of PZT have been developed [4–23] in order to provide matching with the host structure, concrete. Such piezoelectric–cement-based composites are known to exhibit better properties than other piezoelectric composites.

Li *et al*. [4] developed 0–3 PZT–white Portland cement composites using a spreading method where the composites were cast as pastes before setting. The composites were cured at 20°C before measurement. Difficulty in casting paste containing greater than 50% PZT by volume was reported due to reduction in paste workability caused by the increase of PZT particles. Using a pressing method before subjecting to curing at 20°C, Huang *et al*.

Received December 11, 2012; in final form March 13, 2013.
*Corresponding author. E-mail: arnonchaipanich@gmail.com

Table 1
Dielectric and piezoelectric results of the composite investigated [9]

MIX	PZT (% by volume)	ε_r	d_{33} (pC/N)
PZT40	40	139	22
PZT50	50	176	26
PZT60	60	290	42

[5] developed 0–3 PZT-sulfoaluminate cement composites where PZT of up to 85% by weight was investigated.

PZT compositions giving the closest match to concrete were reported to be between 40–60% by volume [4]. Chaipanich *et al*. [9] reported the fabrication and piezoelectric properties of 0-3 PZT-PC composites. Measured d_{33} values for composites with 50% and 60% PZT content were found to be 26 and 42 pC/N, respectively (Table 1). However, no reported works have been found on the mechanical properties in terms of compressive strength of such piezoelectric-cement composites. In this work, a normal Portland cement (also known as ordinary Portland cement) is used, since it is the most common cement type used in general concrete construction. PZT ceramic particles were mixed with Portland cement (PC) to form PZT-PC composites. In addition to compressive strength, the microstructure and hydration properties of the composites were also investigated.

2. Experimental

Lead zirconate titanate ceramic (PZT)–Portland cement (PC) composites were produced using PZT ceramics (median of 450 μm) and ordinary Portland cement. The dry solids were then pressed together to produce PZT-PC composites of 0–3 connectivity using different PZT volume contents of 40%, 50% and 60%. Composite samples were cast as cubes of 1 cm $\times$ 1 cm $\times$ 1 cm for compressive strength tests (S-series; Hounsfield Test Equipment, Surrey, UK) which were carried out after the samples were subjected to curing for 3 d. Thermal analysis of the composite at 50% PZT by volume (selected as representative) using the thermogravimetric analysis (TGA) technique was carried out after curing in order to determine the hydration products. The samples were heated from room temperature to 1,000°C with a scanning rate of 10°C/min under nitrogen atmosphere condition using a Mettler Toledo TGA/SDTA 851e.

A scanning electron microscope (SEM; JEOL JSM-840A,) was used to study the interfacial zone of the composites. Phase characterizations of the composites were also carried out by room temperature X-ray diffraction (XRD; Philips PW 1729 diffractometer) using Ni-filtered CuK radiation.

3. Results and Discussion

Densities of the PZT-PC composite samples were determined using the Archimedes principle; the results are plotted in Fig. 1. It can be seen that, as expected, the density increased with the addition of PZT due to PZT being a denser material (measured at 7.8 g/cm^3) when compared to the pure cement disk of 2.6 g/cm^3. The densities of these composites were found to be close to 4.5, 5.1 and 5.6 g/cm^3 for composites containing 40, 50 and

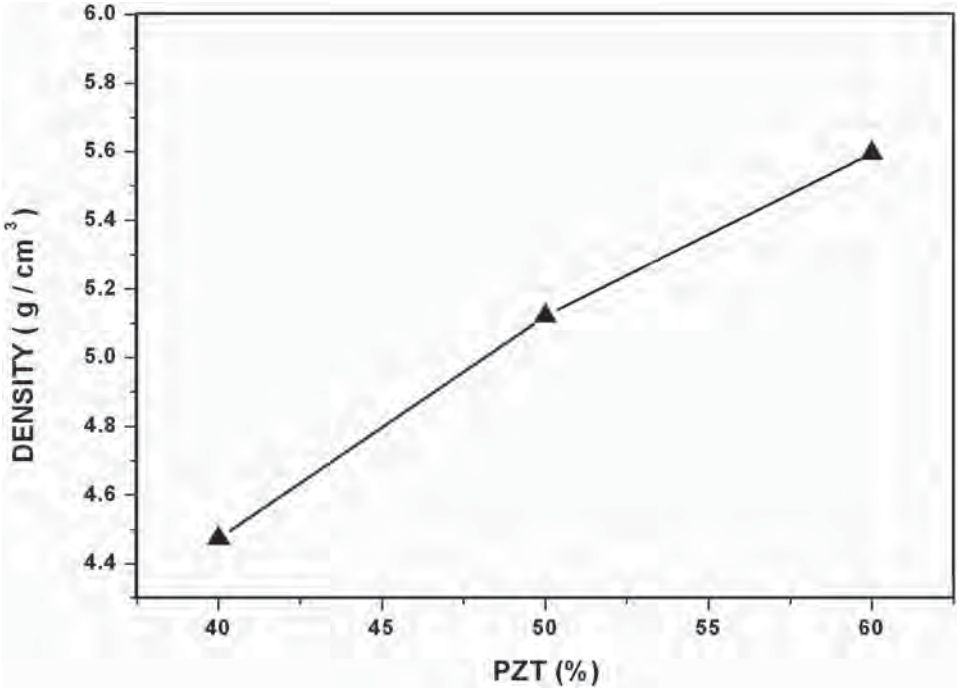

Figure 1. Density results of PZT-PC composites.

60% PZT by volume, respectively. Figure 2 shows the compressive strength test results of PZT-PC composites at 40–60% of PZT by volume. Compressive strength results were found in the region of 41.5–45.0 MPa for these PZT-PC composites, showing an increase of 3.5 MPa when PZT volume increases from 40% to 60%. This increase is similar to the results (≈4 MPa increase) for composite made of cement and aggregate when aggregate volume content increase from 40% to 60% [24]. Moreover, these mechanical strengths are similar to those used in normal concrete, and therefore would be able to resist the same mechanical loading as would the concrete host structure. Compressive strength of the PZT-PC composites can therefore be seen to increase when the PZT volume content increased from 40–60%. When further compared to the compressive strength of Portland cement (with no PZT) where the compressive strength is 56 MPa, these strength values are generally less than that of Portland cement with no PZT. However, when considering PZT as an aggregate in the cement-matrix composite, a comparison can be made to the report by Stock *et al.* [24] where the effect of construction aggregate type on compressive strength was studied. This finding was also mentioned by Neville [25], although the reason for this effect is not clear. Stock *et al.* [24] reported that when an aggregate of different volume is added, the compressive strength is found to decrease by up to 40% by volume; thereafter, there is an increase in strength when the aggregate volume is higher than 40%. Therefore, the compressive strength results of PZT-cement composites and the results reported previously for conventional construction aggregates were found to be in agreement.

XRD traces of Portland cement, PZT-PC composites (40%, 50% and 60% PZT) and PZT ceramic are shown in Fig. 3. In order to allow for a direct comparison, the XRD conditions used for both samples were the same. For Portland cement, crystalline peaks of calcium hydroxide ($Ca(OH)_2$), dicalcium silicates ($2CaO.SiO_2$ shown as Ca_2SiO_4) and

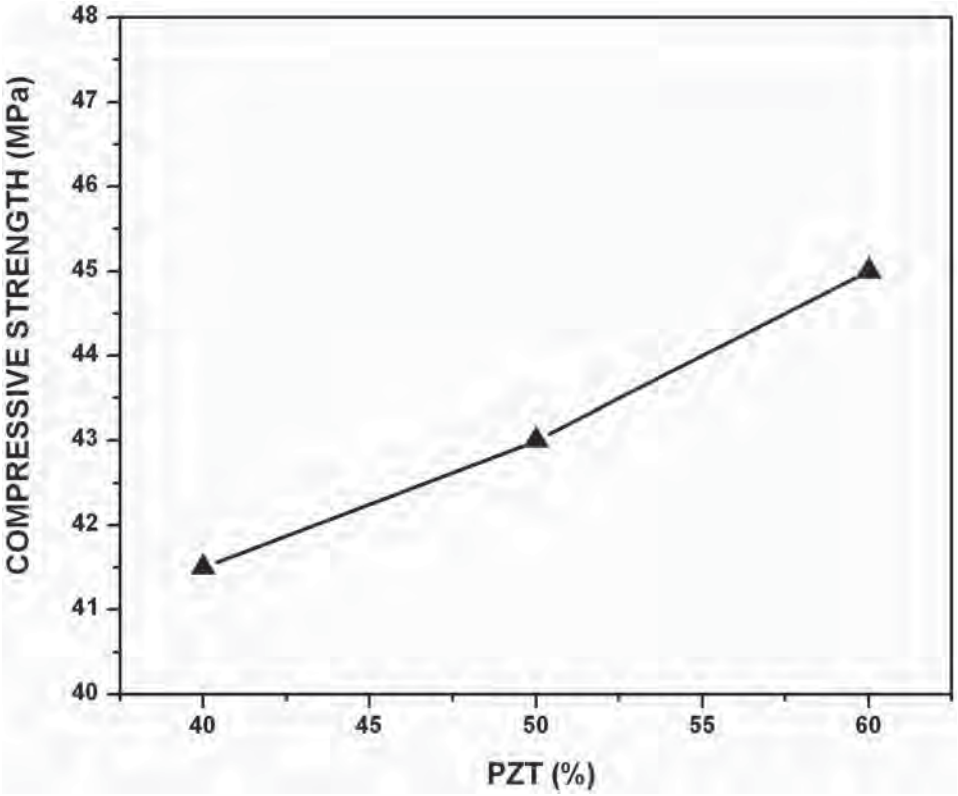

Figure 2. Compressive strength results of PZT-PC composites.

calcium carbonate ($CaCO_3$) can be seen. The most likely explanation for detected dicalcium silicates is that the samples were cured for 3 days using accelerated curing and that dicalcium silicates may remains since this particular compound require longer curing period [24–26]. Calcium hydroxide and calcium silicate hydrates (C−S−H) are the hydration products of tricalcium silicates ($3CaO.SiO_2$ or C_3S) in cement. Calcium hydroxide is therefore detected while the latter C−S−H on the other hand is poorly crystalline and is detected as an amorphous phase. Calcium carbonate is also seen detected as the result of a reaction between CO_2 and $Ca(OH)_2$ due to the sample exposure to air. For PZT-PC composites, the crystalline peaks attributed to PZT can be seen where these XRD peaks of the composites resemble those of a PZT ceramic matching JCPDS file no. 33–0784 [9]. The intensity of these peaks increases as PZT volume content increases. Nonetheless in the XRD trace of the composite, amorphous glassy phase was also detected due to the appearance of the main cement hydration product (calcium silicate hydrate or C−S−H). Furthermore, other crystalline peaks of hydrated phases from cement were not as dominant as those of PZT due to both the preferred orientation of PZT and the relatively greater quantity of PZT compared to the crystal hydrated products formed from cement hydration, such as ettringite or calcium hydroxide.

SEM micrographs of the PZT-PC composite at 50% PZT by volume are shown in Fig. 4(a,b). PZT ceramic particles with grain size of $\approx$2–3 μm can be seen quite clearly in the SEM micrographs. Cement hydration products such as calcium silicate hydrate (C−S−H)

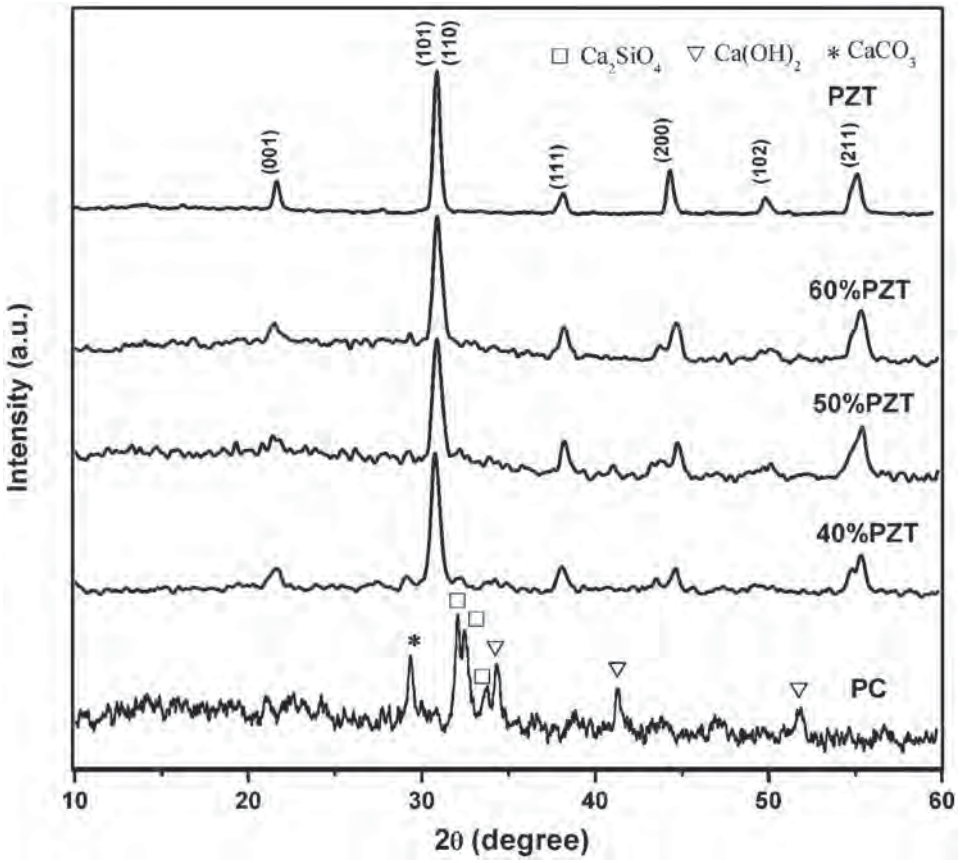

Figure 3. XRD patterns of PC, hydrated PZT-PC composites and PZT ceramic.

and $Ca(OH_2)$ can also be seen surrounding PZT ceramic particles in Fig. 4(a) [17]. These hydration products occurred as the result of hydration of calcium silicates (tricalcium silicate (C_3S) and dicalcium silicate (C_2S)). Another hydration product resulting from the hydration reaction of tricalcium aluminate (C_3A) was ettringite (ETT) – $6CaO.Al_2O_3.3SO_3.32H_2O$ – which can clearly be seen as needle shapes in the SEM micrograph (Fig. 4(b)). Furthermore, good binding between these cement hydration products and PZT ceramic particles is also apparent from the SEM micrographs. C—S—H occurred as hydration product from C_3S and is an important hydration product (as shown in SEM micrographs) that contributes significantly to the strength of the composite since C—S—H existed by more than half the volume of total hydration products resulted from the cement hydration [25–27].

While X-ray diffraction detected only crystalline peaks of PZT with amorphous glassy phase of CSH, other crystalline peaks would be diminished due to greater intensity of PZT in the composite. SEM micrographs, on the other hand, are pinpointed and are generally used to observe selected areas such as the interfacial zone, and may not detect all the phases occurring in the composite. In this case, thermogravimetric analysis (TGA) is used in combination with the above technique to give a more precise and overall analysis of the cement hydration products. Figure 5(a) shows the TGA result of the composite plotted as a weight percentage and as a derivative thermogravimetric (DTG) of the composite at

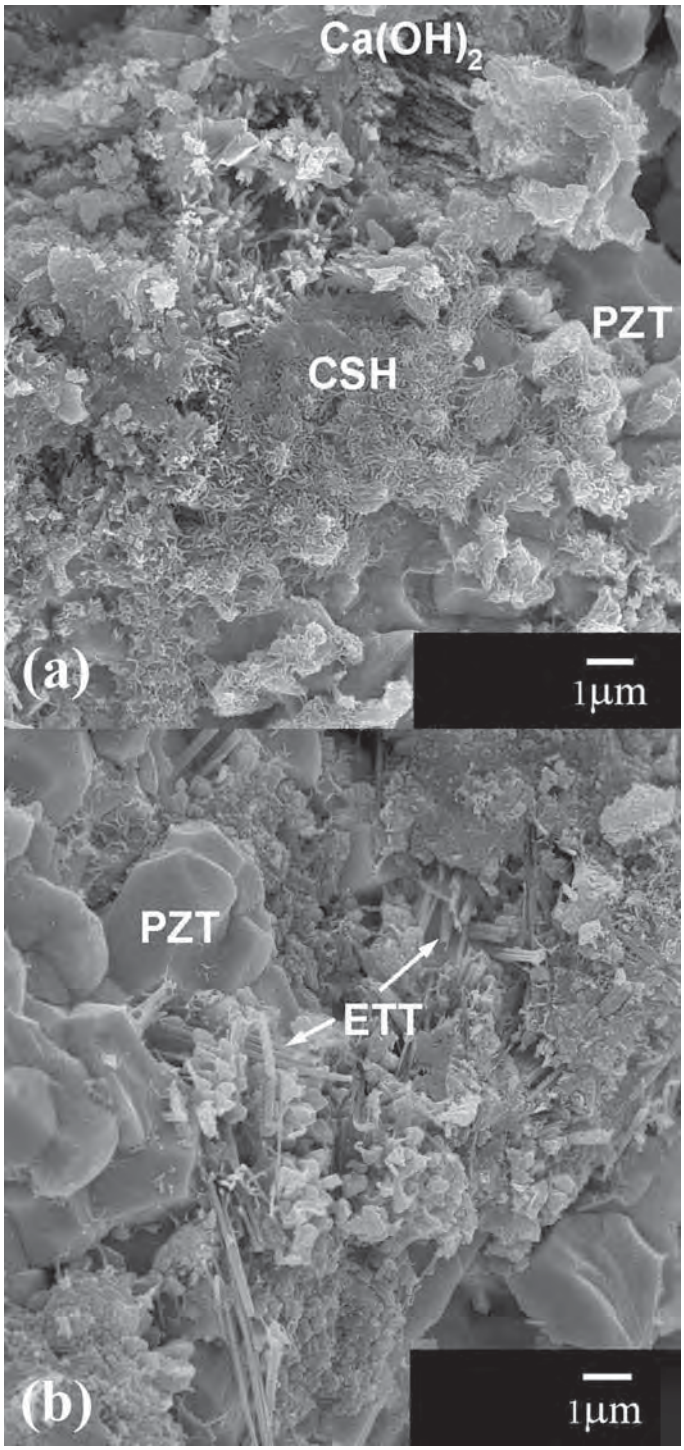

Figure 4. SEM micrographs of the interfacial zone of typical PZT-PC composite showing **(a)** PZT grains with CSH and $Ca(OH_2)$, and **(b)** PZT grains with ettringite (ETT).

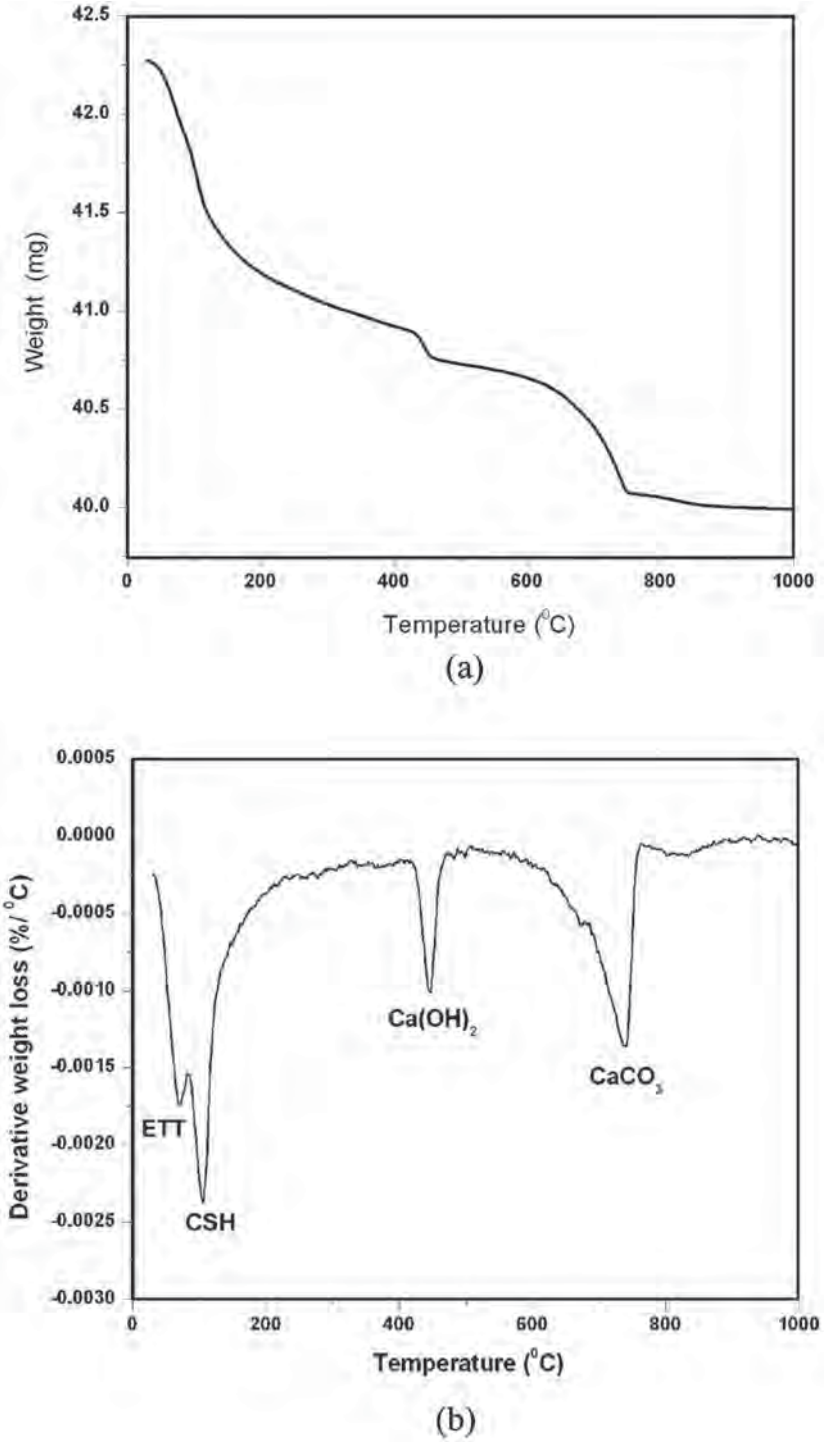

Figure 5. TGA results plotted as **(a)** weight loss, and **(b)** as DTG curve result of PZT-PC composites.

50% PZT by volume representing a typical hydration products occurring in PZT-Portland cement composites. The weight loss can be seen to occur mostly at ≈60°C, ≈120°C, 400–450°C and ≈600–750°C where peaks can be seen clearly using the derivative of the weight loss with temperature (DTG) as shown in Fig. 5b. DTG curve shows the weight loss due to dehydration of ettringite, CSH and $Ca(OH)_2$. All of which are hydration products of Portland cement, thus agreeing with the phases detected in the matrix of the composites as shown in the SEM micrographs.

Calcium carbonate was also detected as a result of the carbonation process, when part of the calcium hydroxide reacts with carbon dioxide to form calcium carbonate. Results concerning the dielectric constant and piezoelectric coefficient (d_{33}) of PZT-PC composites have been reported earlier [9], and are also given in Table 1. From this work, it can therefore be seen that good binding between PZT ceramic and cement hydration products is evident, and that typical cement hydration products were found to occur under an accelerated curing regime at 60°C.

4. Conclusions

Compressive strength results typical of those used in normal concrete were found at 41.5–45.0 MPa for all PZT-PC composites, and therefore would be able to resist the same mechanical loading as would the concrete host structure. The results showed a good binding between the cement matrix and PZT ceramic particles, where cement hydration products such as calcium silicate hydrates and ettringite were seen to surround PZT ceramic particles in the SEM micrograph. Using thermal analysis, calcium silicate hydrates, ettringite and calcium hydroxide, all of which are cement hydration products, were detected.

Acknowledgments

The authors are grateful to Professor Tawee Tunkasiri and staff members at the Chiang Mai University Electroceramics Research Laboratory for the research facilities which made this work possible. The authors would like to express their gratitude for the Research Grant awarded to Assistant Prof. Dr. Arnon Chaipanich by the Thailand Research Fund (TRF), the Commission on Higher Education (Thailand) and Chiang Mai University. The authors are also grateful to the Thailand Research Fund (TRF) for the TRF Senior Research Scholar Contract No. RTA5480004 awarded to Professor Dr. Prinya Chindaprasirt.

References

1. R. E. Newnham, and A. Amin, Smart systems: microphones, fish farming and beyond. *Chem. Tech*. **29**, 38–46 (1999).
2. K. Uchino, *Piezoelectric Actuators and Ultrasonic Motors*. Kluwer, Dordrecht, Netherlands, 1997.
3. A. Safari, A. Halliyal, R. E. Newnham, and I. M. Lachman, Transverse honeycomb composite transducers. *Mater. Res. Bull*. **17**, 301–308 (1982).
4. Z. Li, D. Zhang, and K. Wu, Cement-based 0–3 piezoelectric composites. *J. Am. Ceram. Soc*. **85**, 305–313 (2002).
5. S. Huang, J. Chang, R. Xu, F. Liu, L. Lu, Z. Ye, and X. Cheng, Piezoelectric properties of 0–3 PZT/sulfoaluminate cement composites. *Smart. Mater. Struct*. **13**, 270–274 (2004).
6. Z. Li, B. Dong, and D. Zhang, Influence of polarization on properties of 0–3 cement-based PZT composites. *Cem. Concr. Compos*. **27**, 27–32 (2005).

7. B. Dong, and Z. Li, Cement-based piezoelectric ceramic smart composites. *Comp. Sci. Tech.* **65**, 1363–1371 (2005).
8. A. Chaipanich, Effect of PZT particle size on dielectric and piezoelectric properties of PZT-cement composites. *Curr. Appl. Phys.* **7**, 574–577 (2007).
9. A. Chaipanich, N. Jaitanong, and T. Tunkasiri, Fabrication and properties of PZT–ordinary Portland cement composites. *Mater. Lett.* **61**, 5206–5208 (2007).
10. N. Jaitanong, and A. Chaipanich, Effect of poling temperature on piezoelectric properties of 0–3 PZT-Portland cement composites. *Ferr. Lett.* **35**, 17–23 (2008).
11. A. Chaipanich, Microstructure and properties of $Pb(Mg_{1/3}Nb_{2/3})O_3$–Portland cement composites. *Curr. Appl. Phys.* **7**, 285–288 (2007).
12. A. Chaipanich, and N. Jaitanong, Effect of poling time on piezoelectric properties of 0–3 PZT–Portland cement composites. *Ferr. Lett.* **35**, 73–78 (2008).
13. X. Cheng, S. Huang, J. Chang, R. Xu, F. Liu, and L. Lu, Piezoelectric and dielectric properties of piezoelectric ceramic–sulphoaluminate cement composites. *J. Eur. Ceram. Soc.* **25**, 3223–3228 (2005).
14. A. Chaipanich, Dielectric and piezoelectric properties of PZT-cement composites. *Curr. Appl. Phys.* **7**, 532–536 (2007).
15. A. Chaipanich, Dielectric and piezoelectric properties of PZT–silica fume cement composites. *Curr. Appl. Phys.* **7**, 537–539 (2007).
16. S. Huang, J. Chang, L. Lu, F. Liu, Z. Ye, and X. Cheng, Preparation and polarization of 0–3 cement-based piezoelectric composites. *Mater. Res. Bull.* **41**, 291–297 (2006).
17. N. Jaitanong, H. R. Zeng, G. R. Li, Q. R. Yin, W. C. Vittayakorn, R. Yimnirun, and A. Chaipanich, Interfacial morphology and domain configurations in 0–3 PZT–Portland cement composites. *Appl. Sur. Sci.* **256**, 3245–3248 (2010).
18. A. Chaipanich, N. Jaitanong, and R. Yimnirun, Effect of compressive stress on the ferroelectric hysteresis behavior in 0–3 PZT-cement composites. *Mater. Lett.* **64**, 562–564 (2010).
19. N. Jaitanong, and A. Chaipanich, Effect of poling temperature on piezoelectric properties of 0–3 PZT-Portland cement composites. *Ferr. Lett.* **35**, 17–23 (2008).
20. A. Chaipanich, N. Jaitanong, and R. Yimnirun, Ferroelectric hysteresis behavior in 0–3 PZT-cement composites: effects of frequency and electric field. *Ferr. Lett.* **36**, 59–66 (2009).
21. A. Chaipanich, and N. Jaitanong, Effect of PZT particle size on the electromechanical coupling coefficient of 0–3 PZT-cement composites. *Ferr. Lett.* **36**, 37–44 (2009).
22. A. Chaipanich, and N. Jaitanong, Effect of poling time on piezoelectric properties of 0–3 PZT–Portland cement composites. *Ferr. Lett.* **35**, 73–78 (2008).
23. A. Chaipanich, G. Rujijanagul, and T. Tunkasiri, Properties of Sr- and Sb-doped PZT–Portland cement composites. *Appl. Phys. A.* **94**, 329–337 (2009).
24. A. F. Stock, D. J. Hannant, and R. I. T. Williams, The effect of aggregate concentration upon the strength and modulus of elasticity of concrete. *Mag. Concr. Res.* **31**, 225–234 (1979).
25. A. M. Neville, *Properties of Concrete*. 4th ed. Longman, London, 1995.
26. S. Mindess, J. F. Young, and D. Darwin, *Concrete*. 2nd ed., Pearson Education, New Jersey, 2003.
27. American Concrete Institute, *ACI 22R99:Guide to the selection and Use of Hydraulic Cements*, ACI Manual of Concrete Practie, Part 1, Michigan, 2000.

Materials and Design 55 (2014) 58–65

Contents lists available at ScienceDirect

Materials and Design

journal homepage: www.elsevier.com/locate/matdes

The effect of adding nano-SiO_2 and nano-Al_2O_3 on properties of high calcium fly ash geopolymer cured at ambient temperature

Tanakorn Phoo-ngernkham [a], Prinya Chindaprasirt [a,*], Vanchai Sata [a], Sakonwan Hanjitsuwan [b], Shigemitsu Hatanaka [c]

[a] Sustainable Infrastructure Research and Development Center, Dept. of Civil Engineering, Faculty of Engineering, Khon Kaen University, Khon Kaen 40002, Thailand
[b] Program of Civil Technology, Faculty of Industrial Technology, Lampang Rajabhat University, Lampang 52100, Thailand
[c] Dept. of Architecture, Faculty of Engineering, Mie University, Mie 514-8504, Japan

ARTICLE INFO

Article history:
Received 10 August 2013
Accepted 21 September 2013
Available online 29 September 2013

Keywords:
Geopolymer
Nano-SiO_2
Nano-Al_2O_3
Compressive strength
Flexural strength
Shear bond strength

ABSTRACT

This article presents the effect of adding nano-SiO_2 and nano-Al_2O_3 on the properties of high calcium fly ash geopolymer pastes. Nano-particles were added to fly ash at the dosages of 0%, 1%, 2%, and 3% by weight. The sodium hydroxide concentration of 10 molars, sodium silicate to sodium hydroxide weight ratio of 2.0, the alkaline liquid/binder ratio of 0.60 and curing at ambient temperature of 23 °C were used in all mixtures. The results showed that the use of nano-SiO_2 as additive to fly ash results in the decrease of the setting time, while the addition of nano-Al_2O_3 results in only a slight reduction in setting time. Adding 1–2% nano-particles could improve compressive strength, flexural strength, and elastic modulus of pastes due to the formation of additional calcium silicate hydrate (CSH) or calcium aluminosilicate hydrate (CASH) and sodium aluminosilicate hydrate (NASH) or geopolymer gel in geopolymer matrix. In addition, the additions of both nano-SiO_2 and nano-Al_2O_3 enhances the shear bond strength between concrete substrate and geopolymer.

1. Introduction

At present, geopolymer is getting more attention as an alternative binder to normal cement binders for applications in concrete industry [1,2]. It is made from rich silica and alumina source materials such as fly ash, calcined kaolin, and blast furnace slag. In Thailand, the major source of fly ash is Mae Moh power station in the north. Approximately 3 million tons is produced annually and it is used mainly as supplementary cementitious materials to replace of Portland cement in construction industry. Many researchers have shown that it can also be used as starting material for making good geopolymer [3,4].

Geopolymeric reaction relies on the activation with alkali solutions and temperature curing at 40–75 °C [3,5]. The obtained geopolymer paste possesses similarly strength and appearance to normal Portland cement paste. However, when fly ash geopolymer material is cured at ambient temperature of around 25 °C, the strength development is rather slow and low strength is obtained [6]. Many researchers have tried to improve the strength development of fly ash geopolymers [7,8]. Khater et al. [9] and Riahi and Nazari [10] reported that the compressive strength of geopolymer depends on the type of starting material and its fineness. The fine particles induce higher leaching of silica and alumina in the alkali environment and leads to a higher strength geopolymer [3].

Recently, nanoparticle is receiving more attention as an alternative binder used for the improvement of nanostructure of building materials [9]. Nano-SiO_2 and nano-Al_2O_3 are most commonly used [11] to enhance compressive and tensile strengths of concrete by additional pozzolanic and filler effects [12]. The nano-SiO_2 particle belongs to highly pozzolanic materials because it consists essentially of SiO_2 in amorphous form with a high specific surface, therefore, exhibits great pozzolanic activity [13]. This research aims to study the properties and application of geopolymer paste made from high calcium fly ash containing nano-SiO_2 and nano-Al_2O_3. The obtained results should be very beneficial to the understanding and to the future applications of the materials.

2. Experimental details and testing analysis

2.1. Materials

The materials used in this study were high calcium fly ash (FA) from Mae Moh power plant in northern Thailand, nano-SiO_2 (S), and nano-Al_2O_3 (A). The liquid portions in the mixture were 10 M sodium hydroxide (NaOH) and sodium silicate (Na_2SiO_3) with 13.89% Na_2O, 32.15% SiO_2, and 46.04% H_2O.

The chemical composition and physical properties of FA are shown in Tables 1 and 2. The FA had specific gravity, Blaine

* Corresponding author. Tel.: +66 4320 2355; fax: +66 4320 2355x12.
E-mail address: prinya@kku.ac.th (P. Chindaprasirt).

0261-3069/$ - see front matter © 2013 Elsevier Ltd. All rights reserved.
http://dx.doi.org/10.1016/j.matdes.2013.09.049

fineness, and average particle sizes of 2.61, 4300 cm^2/g and 8.5 μm, respectively. The average particle sizes of S and A were 12 and 13 nm with specific surface areas (BET) of 200 ± 25 and 100 ± 15 m^2/g. The properties of S and A are shown in Table 3 and the mineral compositions are shown in Fig. 1.

2.2. Mix proportion and mix detail

The nano-particles (S and A) were added to high calcium FA at the dosages of 0%, 1%, 2%, and 3% by weight. Constant liquid to binder (L/B) ratio of 0.60 and Na_2SiO_3/NaOH ratio of 2.0 were used in all mixtures. The mix proportions of geopolymer pastes are shown in Table 4. For the mixing of pastes, NaOH and Na_2SiO_3 solutions were firstly mixed together and used as the liquid solution. The FA and S or A were dry mixed until the mixture was homogenous. Right after, the liquid solution was added and the mixing of pastes was done for 5 min.

2.3. Testing

2.3.1. X-ray diffraction (XRD)

At the age of 28 days, the geopolymer cube specimens were broken and ground to fine powder. The XRD scans were performed at 5 to 60 °2theta with an increment of 0.02 degree/step and a scan speed of 0.5 s/step. The amorphous phases of geopolymer pastes at the age of 28 days were determined by quantitative XRD analysis using Bruker's TOPAS software.

2.3.2. Scanning electron microscopy (SEM)

The geopolymer cube samples at the age of 28 days were broken and the middle portions were used for the SEM analyses. The specimen was placed on a brass stub sample holder with double stick carbon tape. The specimen was dried using infrared light for 5 min and then coated with a layer of gold approximately 20–25A thick using a blazer sputtering coater. The micrographs were recorded at 15 kV and 1000× magnification.

2.3.3. Setting time

The setting time of geopolymer pastes were tested in accordance with ASTM: C191.

2.3.4. Compressive strength and modulus of elasticity

The 50 × 50 × 50 mm cube specimens were used for compressive strength test in accordance with the ASTM: C109. The 25 mm diameter and 50 mm height cylindrical specimens were used for the determination of modulus of elasticity as described in ASTM: C469. The specimens were demolded at the age of 1 day and immediately wrapped with vinyl sheet to protect moisture loss and kept in the 23 °C controlled room. The compressive strength and modulus of elasticity were measured at the ages of 7, 28, and 90 days. The reported results were the average of three samples.

2.3.5. Flexural strength

The flexural strength of geopolymer pastes were obtained from modulus of rupture tests using 40 × 40 × 160 mm prisms in accordance with the ASTM: C293. The specimens were tested in deflection controlled with loading rate of 0.05 mm/min [14]. The flexural strength was measured at the ages of 7, 28, and 90 days. The reported results were the average of three samples.

2.3.6. Shear bond strength between concrete substrate and geopolymer pastes

The adhesion strength or shear bond strength was evaluated using the slant shear test as described in ASTM: C882 of geopolymer and concrete. The concrete specimens were cured in water for 28 days and then they were wrapped with vinyl sheet to protect moisture loss for 60 days. This long curing period was chosen to provide advanced concrete hydration as in the old concretes in field of construction [15]. The properties of concrete substrate are shown in Table 5. The slant shear 50 × 50 × 125 mm prisms with the interface line at 45° to the vertical as shown in Fig. 2 were used [2,16]. For casting of specimens, the paste was placed into a mold with concrete substrate in two equal layers. Each layer was tamped 25 times and then vibrated for 45 s to obtain good compaction. After the casting of samples, they were covered with vinyl sheet to protect moisture loss and kept in the 23 °C controlled room until the testing ages. The shear bond strength was the ratio of maximum load at failure and the bond area, and the specimens were tested in constant loading rate of 0.30 MPa/s. The shear bond strength was measured at the ages of 7, 28 and 90 days, and the reported results were the average of five samples.

Table 1
Chemical composition of FA (by weight).

Materials	Chemical composition (%)								
	SiO_2	Al_2O_3	Fe_2O_3	CaO	MgO	K_2O	Na_2O	SO_3	LOI
FA	29.32	12.96	15.64	25.79	2.94	2.93	2.83	7.29	0.30

3. Results and discussions

3.1. XRD analysis

The XRD patterns of fly ash and geopolymer pastes containing nano-SiO_2 are shown in Fig. 3. The as-received FA consisted of a glassy matrix as shown by the hump at 25–35 °2theta and crystalline phases of quartz (SiO_2), magnesioferrite ($MgFe_2O_4$) and calcium carbonate ($CaCO_3$). The XRD patterns of the geopolymer pastes containing nano-SiO_2 (Control, S1, S2, and S3) are similar with that of FA, with the presence of a larger amount of quartz and some magnesioferrite and the disappearance of calcium carbonate. The increase in the intensity of quartz is due to the presence of additional SiO_2 in the system. However, the amorphous phases were easily detected as broad hump around 25–38 °2theta due to transformation of the amorphous component in the geopolymer matrix [9], which was also reflected in a small shift of this hump compared with that of FA [17,18]. The presence of CSH phase could be confirmed by the presence of peaks at 29.5 and 32.05 °2theta [19]. The CSH co-existed with the geopolymer products and enhanced the strength of the geopolymer [20].

The XRD patterns of FA and geopolymer pastes containing nano-Al_2O_3 are shown in Fig. 4. The trends of XRD patterns of geopolymer pastes containing nano-Al_2O_3 were also similar to those of control and nano-SiO_2 pastes. The lower peak of quartz compared with that containing nano-SiO_2 was evident. The broad hump of amorphous gel was very significant indicating the advanced degree of reaction to form NASH gel.

3.2. SEM analysis

The SEM photos of geopolymer pastes are shown in Fig. 5. The control paste contained less dense matrix with a larger number of non-reacted and/or partially reacted fly ash particles embedded in a continuous matrix (Fig. 5a). For the 1–2% nano-SiO_2 (Fig. 5b and c) and nano-Al_2O_3 (Fig. 5e and f), less number of fly ash particles were observed, and the matrix appeared denser than that of the control paste. The high magnification (3000×) of 1% nano-SiO_2 (Fig. 5h) and nano-Al_2O_3 (Fig. 5i) showed the denser matrices compared with that of control paste. The uses of nano-SiO_2 and

Table 2
Physical properties of FA.

Materials	Specific gravity	Average particle size (μm)	Blaine fineness (cm^2/g)
FA	2.61	8.5	4300

Table 3
The properties of nano-SiO_2 and nano-Al_2O_3.

Materials	Average particle size (nm)	Specific surface area, BET (m^2/g)	Density (g/cm^3)	Purity (%)	Appearance
S	12	200 ± 25	<0.05	>99.98	White powder
A	13	100 ± 15	<0.12	>99.38	White powder

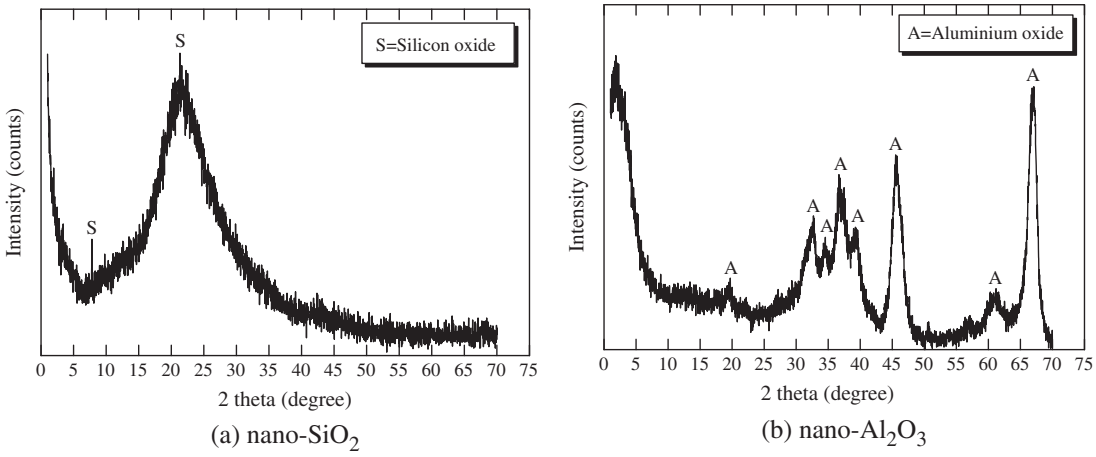

Fig. 1. XRD of nano-SiO_2 and nano-Al_2O_3.

Table 4
Mix proportions of geopolymer pastes.

Mix no.	Mix symbol	FA (g)	*S* (g)	*A* (g)	*L*/*B* ratio	NaOH (g)	Na_2SiO_3 (g)
1	Control	100	–	–	0.60	20	40
2	S1	100	1	–	0.60	20	40
3	S2	100	2	–	0.60	20	40
4	S3	100	3	–	0.60	20	40
5	A1	100	–	1	0.60	20	40
6	A2	100	–	2	0.60	20	40
7	A3	100	–	3	0.60	20	40

Table 5
Mix properties and main properties of concrete substrate.

Components	OPC (kg/m^3)	Aggregates (kg/m^3)		Water (kg/m^3)	Main properties of concrete substrate at 28 days (MPa)	
		Fine	Coarse		f_c	f_t
Proportions	495	1210	338	238	35.9	8.5

f_c = compressive strength at the age of 28 days, and average value of five specimens (100 mm in diameter and 200 mm in length).
f_t = flexural strength at the age of 28 days, and average value of five specimens (40 × 40 × 160 mm^3).

nano-Al_2O_3 in high calcium fly ash geopolymer results in the additional formation of CSH or CASH gels which co-existed with NASH gel [9] and thus led to the overall improvement in compressive strength of geopolymer. On the other hand, addition of 3% nano-SiO_2 (Fig. 5d) and nano-Al_2O_3 (Fig. 5e) resulted in a large amount of nano-SiO_2 and nano-Al_2O_3 observed and the matrix appeared less dense than the other mixtures indicating that the amount of nano-particles addition at this level of 3% was excessive.

3.3. Setting time

The setting time of geopolymer pastes at various addition levels of nano-SiO_2 and nano-Al_2O_3 are shown in Fig. 6. The initial setting time of control, S1, S2, and S3 pastes were 30, 27, 19, and 12 min, and the final setting time were 58, 53, 40, and 26 min, respectively. The initial setting time of A1, A2, and A3 pastes were 29, 29, and 28 min, and the final setting time of pastes were 57, 55, and 54 min, respectively. The setting time of pastes tended to obviously

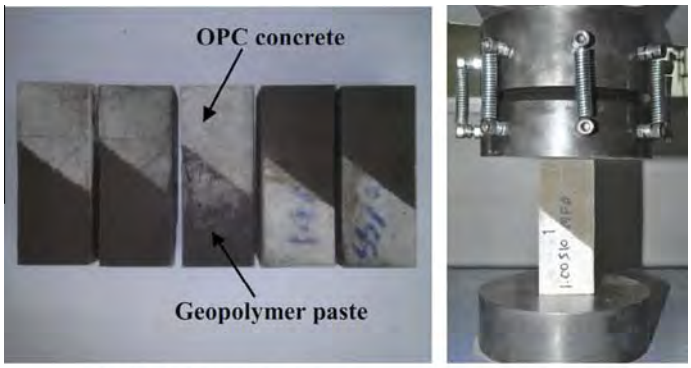

Fig. 2. Slant shear specimens and testing procedure.

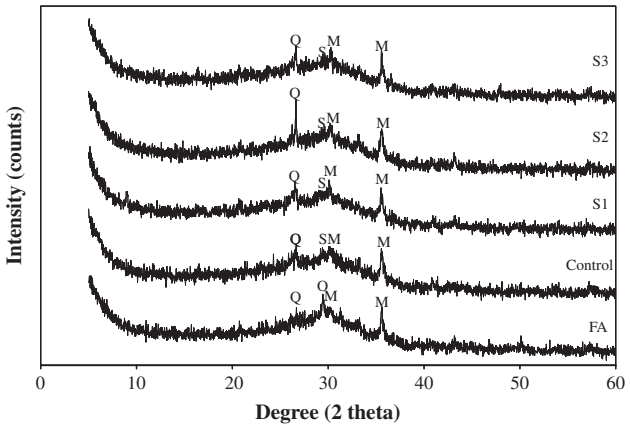

Fig. 3. XRD of geopolymer pastes at 28 days with various nano-SiO_2.

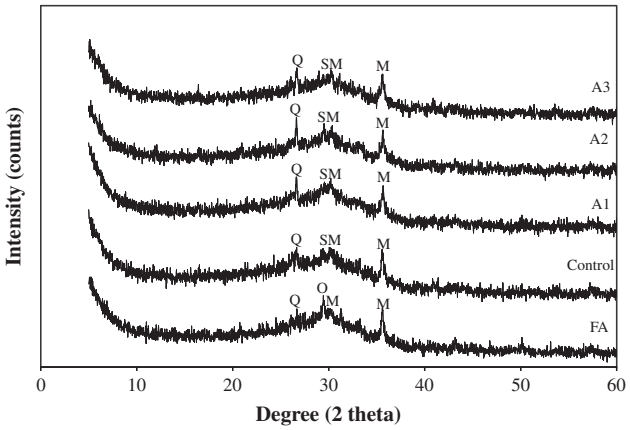

Fig. 4. XRD of geopolymer pastes at 28 days with various nano-Al_2O_3.

decreased with the addition of nano-SiO_2 due to the faster activation with readily available free calcium ions from high calcium FA and formed CSH [17]. The addition of nano-Al_2O_3 seemed to have a smaller effect on setting time compared with adding of nano-SiO_2. Chindaprasirt et al. [17] reported that the increase in nano-Al_2O_3 content more than 7% by weight of binder also resulted in a large reduction of setting time. The fast setting time of FA containing nano-SiO_2 at this level of addition could be used as repair binding materials.

3.4. Compressive strength and flexural strength

The compressive strengths and flexural strength of pastes are shown in Table 6. The compressive strength and flexural strengths of geopolymer pastes containing nano-SiO_2 and nano-Al_2O_3 were obviously higher than that of control paste. At 90 days, the compressive strengths of pastes containing 2% nano-SiO_2 and nano-Al_2O_3increased to 51.8 and 56.4 MPa, respectively compared with 39.4 MPa of the control paste. At 90 days, the flexural strengths of pastes containing 2% nano-SiO_2 and nano-Al_2O_3 were 5.98 and 5.92 MPa compared with 4.31 MPa of the control paste. The results followed the same trended as those of the compressive strength, and confirmed with other researches [11,21] that addition of nano-particles improved the strength of cement paste and concrete. The addition of 3% of nano-particles, however, started to adversely affect the strength of geopolymer. The compressive strengths at 90 days of 3% of nano-SiO_2 and nano-Al_2O_3 reduced to 48.1 and 46.1 MPa, respectively whereas the corresponding flexural strengths dropped to 5.23 and 5.26 MPa, respectively.

The compressive strength and flexural strength of the pastes were significantly improved due to the increase in the reaction products of the geopolymer matrix [22]. In the presence of high alkali environment and the presence of calcium from high calcium FA, the additional SiO_2 and Al_2O_3 could react and form CSH or CASH and NASH gels and led to a higher strength geopolymer [8,17]. The addition of SiO_2 and Al_2O_3 reduced the $Ca(OH)_2$ content of matrix, and the microstructure was refined similar to the pozzolanic reaction in the blended cement paste [23]. The results thus show that the properties of high calcium FA geopolymer could be enhanced with addition of 2% nano-SiO_2 and nano-Al_2O_3 by weight.

The relationship between compressive strength and flexural strength of geopolymer pastes is shown in Fig. 7. The flexural strength tended to increase linearly with the square root of ultimate compressive strength. The equation predicting this relationship can be written as;

$$f_t = 1.430\sqrt{f'_c} - 4.223 \quad (1)$$

where f_t is the flexural strength (MPa), and f'_c is the ultimate compressive strength (MPa).

The flexural strength of geopolymer pastes at age of 7 days expressed as a function of compressive strength was lower than those predicted by ACI 318 [24] as shown in Fig. 7. At an early age of 7 days, the flexural strengths were lower than the values given by ACI 318. However, at the ages of 28 and 90 days, they were higher than the values given by ACI 318. The results conformed with that of Sofi et al. [25] which indicated that the flexural strength of inorganic polymer concrete was generally higher than

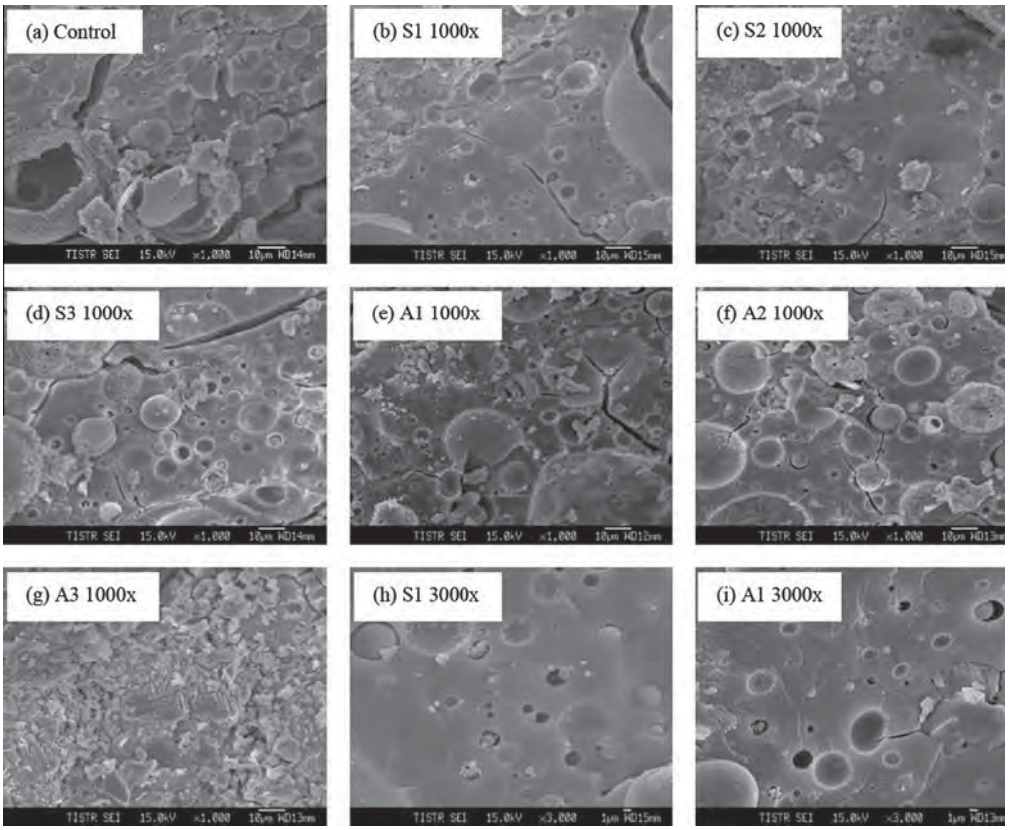

Fig. 5. SEM of geopolymer pastes at 28 days.

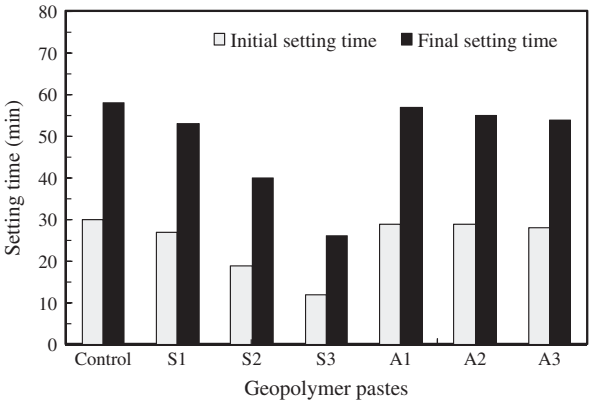

Fig. 6. Setting time of geopolymer pastes.

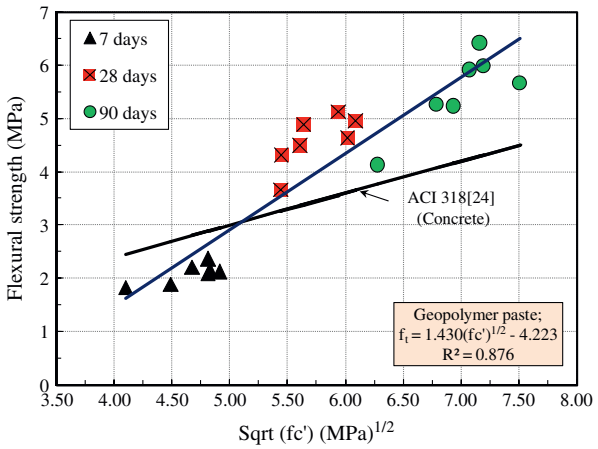

Fig. 7. Relationship between compressive strength and flexural strength of geopolymer pastes.

Table 6
Compressive strength and flexural strength of geopolymer pastes.

Mix	Compressive strength (MPa)			Flexural strength (MPa)		
	7 days	28 days	90 days	7 days	28 days	90 days
Control	16.8	29.6	39.4	1.83	3.66	4.13
S1	20.2	35.3	51.3	1.89	5.12	6.41
S2	24.1	31.8	51.8	2.13	4.89	5.98
S3	23.1	29.7	48.1	2.10	4.31	5.23
A1	21.8	36.2	56.4	2.22	4.63	5.67
A2	23.2	37.1	50.0	2.36	4.95	5.92
A3	23.3	31.4	46.1	2.14	4.49	5.26

that of the standard ordinary Portland cement concrete due to the dense and strong interfacial transition zone within geopolymer matrix. The increases in both compressive and flexural strengths from 28 days to 90 days were substantial and were the characteristics of samples with ambient temperature curing.

3.5. Modulus of elasticity

The elastic modulus of geopolymer pastes are shown in Table 7. The values of elastic modulus tended to increase with the addition of nano-particles. The pastes containing nano-particles were denser and stronger than that of control paste and this led to the increase of elasticity modulus (between 6.00 and 17.65 GPa). The elasticity modulus values of normal strength Portland cement pastes varied between 12.5 and 17.5 GPa [26,27] which were

Table 7
Elastic modulus of geopolymer pastes.

Mix	Modulus of elasticity (GPa)		
	7 days	28 days	90 days
Control	5.37	9.23	10.29
S1	6.30	11.67	16.00
S2	6.76	10.91	17.65
S3	6.15	9.60	14.12
A1	6.00	12.31	16.47
A2	6.92	11.32	14.48
A3	6.86	9.73	11.76

similar to those of pastes with1 to 2% nano-SiO_2 and nano-Al_2O_3. When adding nano-SiO_2 and nano-Al_2O_3, additional CSH, CASH and NASH formed within geopolymeric matrix and the rate of compressive strength and elastic modulus gain was significantly improved [28,29].

The relationship between elasticity modulus and compressive strength of geopolymer pastes is shown in Fig. 8. The elasticity modulus tended to increase linearly with the square root of compressive strength. The equation predicting this relationship can be written as;

$$E = 3.527\sqrt{f_c'} - 9.979 \quad (2)$$

where E is the modulus of elasticity (GPa), and f_c' is the ultimate compressive strength (MPa).

As shown in Fig. 8, the elasticity modulus of pastes containing nano-SiO_2 and nano-Al_2O_3 were slightly lower than that of Portland cement paste and geopolymer paste containing Portland cement [8,30]. The elastic modulus of geopolymer paste depended primarily on the strength of paste [6] which was related to the mix composition such as SiO_2/Al_2O_3 molar ratio [31] and curing temperature for the accelerated geopolymerization. In this study, the curing was at ambient temperature, therefore, the strength development was not really enhanced and this resulted in a more deformable characteristics [32]. Also, the strength and modulus of elasticity of pastes at the age of 90 days increased compared with those at the age of 28 days due to the increased reaction of SiO_2 and Al_2O_3 and Ca [8,17].

3.6. Shear bond strength between concrete substrate and geopolymer pastes

The 45° slant shear load carrying capacity of concrete substrate and geopolymer pastes are shown in Fig. 9. The shear bond strength could be calculated by performing stress transformation based on the peak strength of prism specimens. The shear bond strengths of geopolymer pastes containing nano-SiO_2 and nano-Al_2O_3 were obviously higher than that of control paste. At 28 days, the shear bond strength of pastes containing 1%, 2% and 3% nano-SiO_2 were 23.36, 20.64 and 17.49 MPa, respectively, whereas the pastes containing 1%, 2% and 3% nano-Al_2O_3 were 19.61, 20.61 and 20.32 MPa, respectively compared with 10.73 MPa of the control sample. The noticeable increase in shear bond strength due to the adding nano-SiO_2 and nano-Al_2O_3 could be attributed to the improvement of strength of geopolymers and the increased reaction products at the interface transition zone between concrete substrate and geopolymer pastes due to the reaction between the alkaline activator and surface product of old substrate, therefore, lead to denser interface zone and higher strength [1]. In addition, Pacheco-Torgal et al. [2] explained that a large amount of calcium hydroxide was found at the surfaces of concrete substrate, therefore the improved shear bond strength was due to SiO_2 and Al_2O_3 from raw materials reacted with $Ca(OH)_2$.

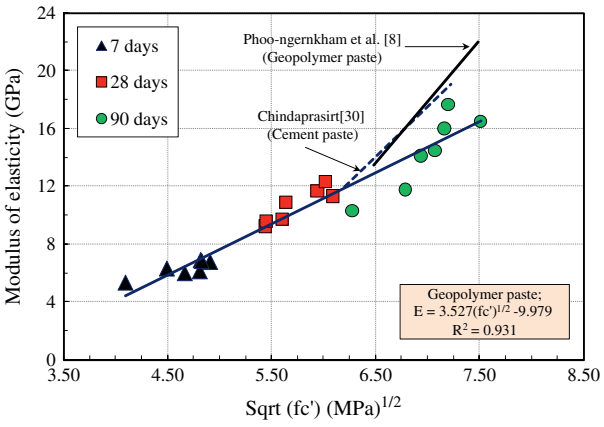

Fig. 8. Relationship between elasticity modulus and compressive strength of geopolymer pastes.

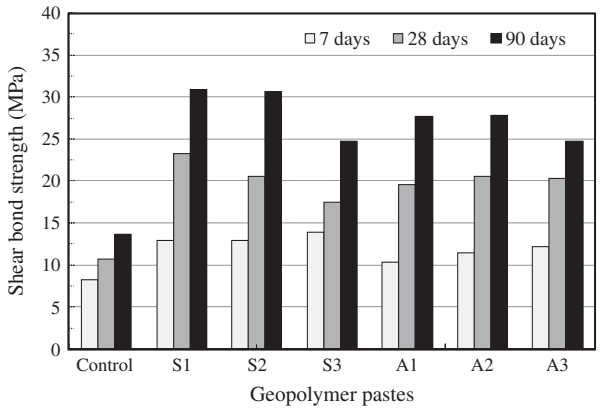

Fig. 9. Shear bond strength between concrete substrate and geopolymer pastes with interface line at 45° to the vertical.

The failure modes of the slant shear bond tests are shown in Fig. 10. The control sample with the normal geopolymer paste failed by cracking in the geopolymer paste (Fig. 10a) and the portion of geopolymer paste was severely damaged indicating the strength and stability of concrete substrate. For the geopolymers containing nano-SiO_2 and nano-Al_2O_3, the failures were all in the monolithic failure mode with concrete substrate and geopolymer containing nano-SiO_2 and nano-Al_2O_3 acted as a unit. The cracked samples showed that crackings in the vertical direction passed through the slant bond area and resulted in the monolithic failure mode. The slant of 45° in this experiment did not produce the shear failure mode, however, Pacheco-Torgal et al. [2] showed that the shear bond failure mode could be obtained with the reduction of slant to 30° to the vertical plane due to the high bond strength of geopolymer and concrete substrate. This test, however, indicated that the addition of 1–3% nano-SiO_2 and nano-Al_2O_3 improved the bonding of geopolymer and the concrete substrate.

4. Conclusions

Based on the results of this study, the follow conclusions could be drawn.

(1) The SEM and XRD results indicated that the microstructures of geopolymer pastes containing 1–2% nano-SiO_2 and nano-Al_2O_3 were enhanced with denser matrix and increased

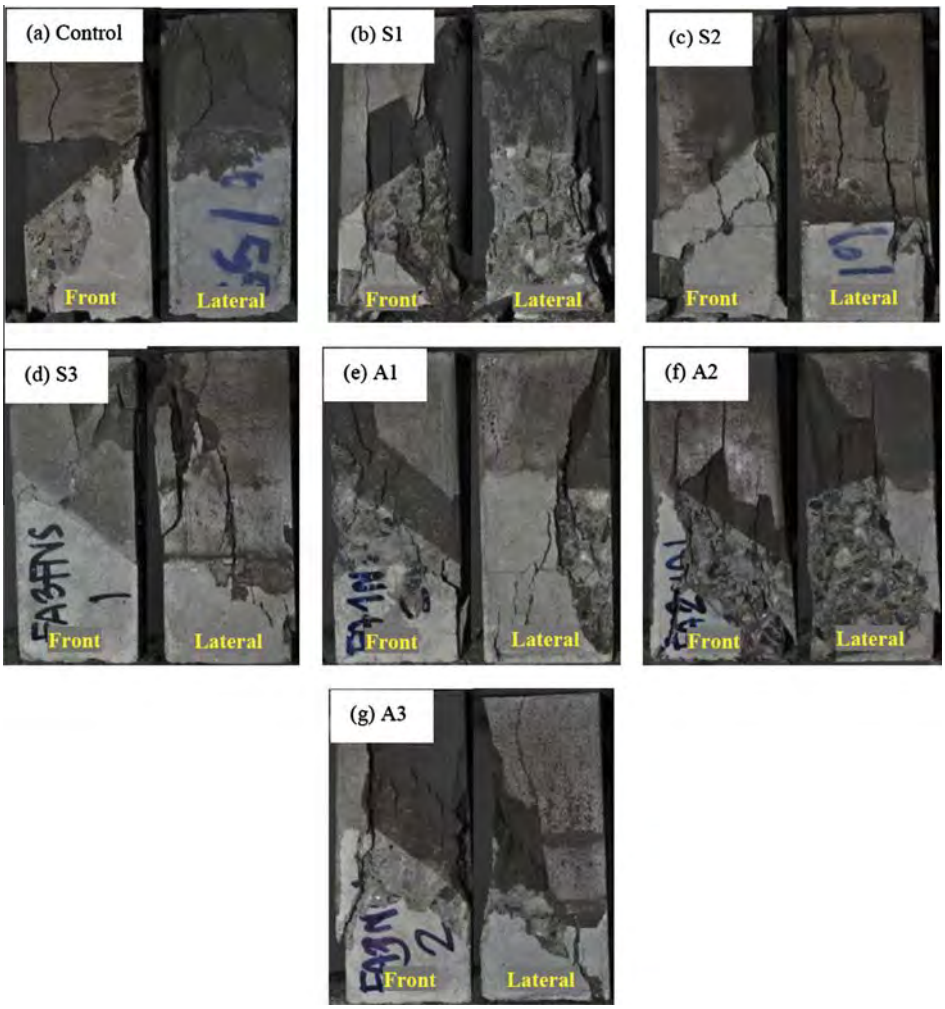

Fig. 10. Specimens failure mode at 28 days.

reaction product. However, the additional of 3% nano-SiO_2 and nano-Al_2O_3 resulted in an excessive amount of nano-particles and less dense structures were formed.

(2) The use of nano-SiO_2 as additive to high calcium fly ash geopolymer paste resulted in the decrease of setting time due to the formation of CSH which accelerated the setting and hardening of geopolymer pastes. While, the addition of same amount of nano-Al_2O_3 resulted in only a slight reduction in setting time. The fast setting time of high calcium FA geopolymer paste containing nano-SiO_2 could be beneficial for use as repair binding materials.

(3) The compressive strength, flexural strength, and elastic modulus of high calcium FA geopolymer paste containing nano-SiO_2 and nano-Al_2O_3 increased due to the formation of additional CSH or CASH and NASH gels in geopolymer matrix. These products are formed and filled the pore to make the dense and strong geopolymer. The relatively high compressive strengths of geopolymer pastes containing 2% nano-SiO_2 and 1% nano-Al_2O_3 cured for 90 days were 51.8 and 56.4 MPa, respectively.

(4) The addition of both nano-SiO_2 and nano-Al_2O_3 also improved the shear bond strength between concrete substrate and geopolymer. The high shear bond strength for 2% nano-SiO_2 and nano-Al_2O_3 cured for 28 days at 45° slant shear angle were 20.64 and 20.61 MPa, respectively comparing with 10.73 MPa of the control. The large increase was due to the improvement of strength of geopolymer pastes and the added reaction between the geopolymer paste and the concrete substrate at the contact zone.

Acknowledgements

This work was supported by the Higher Education Research Promotion and National Research University Project of Thailand, Office of the Higher Education Commission, through the Advanced Functional Materials Cluster of Khon Kaen University, and the Thailand Research Fund (TRF) under the TRF Senior Research Scholar, Grant No. RTA5480004; and TRF and Khon Kaen University under the TRF-Royal Golden Jubilee Ph.D. program Grant No. PHD/0340/2552.

References

[1] Hu S, Wang H, Zhang G, Ding Q. Bonding and abrasion resistance of geopolymeric repair material made with steel slag. Cem Concr Compos 2008;30:239–44.
[2] Pacheco-Torgal F, Castro-Gomes JP, Jalali S. Adhesion characterization of tungsten mine waste geopolymeric binder. Influence of OPC concrete substrate surface treatment. Constr Build Mater 2008;22:154–61.
[3] Chindaprasirt P, Chareerat T, Sirivivatnanon V. Workability and strength of coarse high calcium fly ash geopolymer. Cem Concr Compos 2007;29:224–9.

[4] Sinsiri T, Phoo-ngernkham T, Sata V, Chindaprasirt P. The effects of replacement fly ash with diatomite in geopolymer mortar. Computers Concr 2012;9:427–37.
[5] Pangdaeng S, Phoo-ngernkham T, Sata V, Chindaprasirt P. Influence of curing conditions on properties of high calcium fly ash geopolymer containing Portland cement as additive. Mater Des 2014;53:269–74.
[6] Guo X, Shi H, Chen L, Dick WA. Alkali-activated complex binders from class C fly ash and Ca-containing admixtures. J Hazard Mater 2010;173:480–6.
[7] Palomo A, Fernández-Jiménez A, Kovalchuk G, Ordoñez LM, Naranjo MC. OPC-fly ash cementitious systems: study of gel binders produced during alkaline hydration. J Mater Sci 2007;42:2958–66.
[8] Phoo-ngernkham T, Chindaprasirt P, Sata V, Pangdaeng S, Sinsiri T. Properties of high calcium fly ash geopolymer pastes containing Portaland cement as additive. Int J Miner Metall Mater 2013;20:214–20.
[9] Khater HM, El-Sabbagh BA, Fanny M, Ezzat M, Lottfy M. Effect of nano-silica on alkali activated water cooled slag geopolymer. ARPN J Eng Appl Sci 2012;2:170–6.
[10] Riahi S, Nazari A. The effects of nanoparticles on early age compressive strength of ash-based geopolymers. Ceram Int 2012;38:4467–76.
[11] Stefanidou M, Papayianni I. Influence of nano-SiO_2 on the Portland cement pastes. Composites Part B 2012;43:2706–10.
[12] Li G. Properties of high-volume fly ash concrete incorporating nano-SiO_2. Cem Concr Res 2004;34:1043–9.
[13] Qing Y, Zenan Z, Deyu K, Rongshen C. Influence of nano-SiO_2 addition on properties of hardened cement paste as compared with silica fume. Constr Build Mater 2007;21:539–45.
[14] Bharatkumar B, Raghuprasad B, Ramachandramurthy D, Narayanan R, Gopalakrishnan S. Effect of fly ash and slag on the fracture characteristics of high performance concrete. Mater Struct 2005;38:63–72.
[15] Hassan KE, Brooks JJ, Al-Alawi L. Compatibility of repair mortars with concrete in a hot-dry environment. Cem Concr Compos 2001;23:93–101.
[16] Austin S, Robins P, Pan Y. Shear bond testing of concrete repairs. Cem Concr Res 1999;29:1067–76.
[17] Chindaprasirt P, De Silva P, Sagoe-Crenstil K, Hanjitsuwan S. Effect of SiO_2 and Al_2O_3 on the setting and hardening of high calcium fly ash-based geopolymer systems. J Mater Sci 2012;47:4876–83.
[18] Rattanasak U, Chindaprasirt P. Influence of NaOH solution on the synthesis of fly ash geopolymer. Miner Eng 2009;22:1073–8.
[19] Lecomte I, Henrist C, Liegeois M, Maseri F, Rulmont A, Cloots R. (Micro)-structural comparison between geopolymers, alkali-activated slag cement and Portland cement. J Eur Ceram Soc 2006;26:3789–97.
[20] Somna K, Jaturapitakkul C, Kajitvichyanukul P, Chindaprasirt P. NaOH-activated ground fly ash geopolymer cured at ambient temperature. Fuel 2011;90:2118–24.
[21] Nazari A, Riahi S. Splitting tensile strength of concrete using ground granulated blast furnace slag and SiO_2 nanoparticles as binder. Energy Build 2011;43:864–72.
[22] Dombrowski K, Buchwald A, Weil M. The influence of calcium content on the structure and thermal performance of fly ash based geopolymers. J Mater Sci 2007;42:3033–43.
[23] Kroehong W, Sinsiri T, Jaturapitakkul C, Chindaprasirt P. Effect of palm oil fuel ash fineness on the microstructure of blended cement paste. Constr Build Mater 2011;25:4095–104.
[24] ACI 318. Building Code Requirement for Structure Concrete Practice (ACI 318-08) and Commentary. American Concrete Institute; 2008.
[25] Sofi M, van Deventer JSJ, Mendis PA, Lukey GC. Engineering properties of inorganic polymer concretes (IPCs). Cem Concr Res 2007;37:251–7.
[26] Cook DJ, Chindaprasirt P. A mathematical model for the prediction of damage in concrete. Cem Concr Res 1981;11:581–90.
[27] Feldman RF, Huang CY. Properties of Portland cement–silica fume pastes. Part 2: Mechanical properties. Cem Concr Res 1985;15:943–52.
[28] Yip CK, Lukey GC, Van Deventer JSJ. The coexistence of geopolymeric gel and calcium silicate hydrate at the early stage of alkaline activation. Cem Concr Res 2005;35:1688–97.
[29] Yip CK, Van Deventer JSJ. Microanalysis of calcium silicate hydrate gel formed within a geopolymeric binder. J Mater Sci 2003;38:3851–60.
[30] Chindaprasirt P. Influence of load history on the properties of concrete, PhD thesis, The University of New South Wales; 1980.
[31] Duxson P, Provis JL, Lukey GC, van Deventer JSJ. The role of inorganic polymer technology in the development of 'green concrete'. Cem Concr Res 2007;37:1590–7.
[32] Torres ML, García-Ruiz PA. Lightweight pozzolanic materials used in mortars: evaluation of their influence on density, mechanical strength and water absorption. Cem Concr Compos 2009;31:114–9.

Cement & Concrete Composites 45 (2014) 9–14

Contents lists available at ScienceDirect

Cement & Concrete Composites

journal homepage: www.elsevier.com/locate/cemconcomp

Effects of NaOH concentrations on physical and electrical properties of high calcium fly ash geopolymer paste

Sakonwan Hanjitsuwan [a], Sitchai Hunpratub [b], Prasit Thongbai [b], Santi Maensiri [c], Vanchai Sata [a], Prinya Chindaprasirt [a,*]

[a] Sustainable Infrastructure Research and Development Center, Department of Civil Engineering, Faculty of Engineering, Khon Kaen University, Khon Kaen 40002, Thailand
[b] Department of Physics, Faculty of Science, Khon Kaen University, Khon Kaen 40002, Thailand
[c] School of Physics, Institute of Science, Suranaree University of Technology, Nakhon Ratchasima 30000, Thailand

ARTICLE INFO

Article history:
Received 9 April 2012
Received in revised form 26 August 2013
Accepted 15 September 2013
Available online 21 September 2013

Keywords:
Fly ash
Geopolymer
Setting time
Dielectric
Electrical properties

ABSTRACT

The effects of sodium hydroxide (NaOH) concentration on setting time, compressive strength and electrical properties at the frequencies of 100 Hz–10 MHz of high calcium fly ash geopolymer pastes were investigated. Five NaOH concentrations (8, 10, 12, 15 and 18 molar) were studied. The liquid to ash ratio of 0.4, sodium silicate to sodium hydroxide ratio of 0.67 and low temperature curing at 40 °C were selected in making geopolymer pastes. The results showed that NaOH concentration had significant influence on the physical and electrical properties of geopolymer paste. The pastes with high NaOH concentrations showed increased setting time and compressive strength due to a high degree of geopolymerization as a result of the increased leaching of silica and alumina from fly ash. The dielectric constant and conductivity increased with NaOH concentration while $\tan\delta$ decreased due to an increase in geopolymerization. At the frequency of 10^3 Hz, the dielectric constants of all pastes were approximately 10^4 S/cm and decreased with increased frequency. The relaxation peaks of $\tan\delta$ reduced with an increase in NaOH concentration and ranged between 2.5 and 4.5. The AC conductivity behavior followed the universal power law and the values were in the range of 3.7×10^{-3}–1.5×10^{-2} at 10^5–10^6 Hz.

1. Introduction

Fly ash is an industrial by-product generated during the combustion of coal for energy production. Currently the annual production of coal ash worldwide is estimated around 600 million tons, with fly ash constituting about 500 million tons at 75–80% of the total ash produced [1]. In Thailand, the annual output of lignite fly ash from Mae Moh power station is around 3.0 million tons. Approximately 1.8 million tons are used as pozzolanic material in the cement and concrete industry. However, around 1.2 million tons are still left over and discarded at landfill site [2] which poses a serious environmental problem. This lignite fly ash contains a substantial amount of silica and alumina which can be used as a source material for making geopolymer [2–4]. The geopolymer materials have recently received considerable attention owing to their excellent fire resistance, excellent thermal properties, and environmentally friendly nature [5,6].

Aluminosilicate inorganic polymers, also called geopolymers, were firstly described by Davidovits as materials formed under high alkali condition from aluminosilicate solid and alkali silicate solutions [7]. The geopolymer is a type of cross-linked long chain inorganic polymer material between tetrahedral AlO_4 and SiO_4 units built in three dimensional structures. The linkages of AlO_4 and SiO_4 units require charge balancing from alkali ions such as Li^+, Na^+ and K^+. The mechanism of the existence of alkali ions in the molecular structure of geopolymer materials is not clearly understood at present. Usually the accustomed viewpoint is that the alkali metal ions play a charge balancing role or are actively bonded to the matrix. Therefore, the typical geopolymer composition is usually expressed as $n\boldsymbol{M}_2O{\cdot}Al_2O_3{\cdot}xSiO_2{\cdot}yH_2O$ where $\boldsymbol{M}$ is alkali metal element such as Li, Na or K [8]. Several materials containing silica and alumina can be used as starting source materials. These include the conventional starting materials viz., slag, metakaolin and class C fly ash [9,10]; other wastes or waste ashes such as rice husk ash, fluidized bed fly ash, glass cullet powder and waste concrete powder [11–14]; and Portland cement [15,16].

Recently it has been found that the chemosynthetic Al_2O_3–$2SiO_2$ geopolymer prepared by sol–gel method exhibits a high ionic electrical conductivity of about 1.5×10^{-6} S/cm in air at room temperature [8]. Such a high level of the ionic electrical conductivity observed in this geopolymer may be important properties as a promising fast-ionic conducting material for many applications such as solid-state batteries and other solid-state electrochemical

* Corresponding author. Tel.: +66 4320 2355; fax: +66 4320 2355x12.
E-mail address: prinya@kku.ac.th (P. Chindaprasirt).

0958-9465/$ - see front matter © 2013 Elsevier Ltd. All rights reserved.
http://dx.doi.org/10.1016/j.cemconcomp.2013.09.012

parts. It has also been found that the water content does not directly affect the electrical conductivity of hardened geopolymer materials [8]. However, the free Na ions, water molecules and hydroxide ions are the major components determining the dielectric loss. The $2.4H_3PO_4$–Al_2O_3–$2SiO_2$ geopolymer can reduce the ion transfer due to the lack of free alkali cations within the structure. In addition, the heat treatment can reduce dielectric loss from 10^{-2} to 10^{-3} due to the decrease in water from the structure [17].

In general, the ions that can conduct in ionic conductors are Li^+, Na^+, H^+, K^+, Ag^{2+}, O^{2-}, and F^- [18]. For geopolymer materials, free alkali metal ions are expected to play a role on the electrical properties. The concentrations of these free alkali metal ions are, therefore, closely related to the ionic electrical conductivity of fly ash geopolymer materials. Moreover, the electrical conductivity and dielectric constant of fly ash geopolymer pastes are dependent on the frequency range and liquid alkali to ash ratio [19].

In this study, the effects of NaOH concentrations on the physical and electrical properties, and the related dielectric response in fly ash geopolymer pastes (FAGP) were studied.

2. Materials and experimental procedures

2.1. Materials

Lignite high calcium fly ash from Mae Moh power plant in Thailand was used for this study. The median particle size was 23.5 μm and the percentage retained on sieve no. 325 was 40%. The chemical compositions were 35.21% SiO_2, 16.57% Al_2O_3, 25.52% CaO, 13.66% Fe_2O_3, 2.73% Na_2O and 6.31% other. The loss on ignition was low at 0.37. Sodium silicate with 32.39% SiO_2, 13.44% Na_2O and 54.17% H_2O by weight and NaOH solutions were used as alkali activators.

2.2. Geopolymer synthesis

The mixing procedure started with mixing fly ash (FA) and NaOH solution for 5 min. Sodium silicate solution was added and mixed for another 5 min. Liquid alkali solution to fly ash ratios (L/A) of 0.4 and sodium silicate to sodium hydroxide ratio of 0.67 were used. The concentrations of NaOH of 8, 10, 12, 15 and 18 molar were used. These values were selected based on the previous researches using the same lignite fly ash as source material [3,4,20]. The samples that contain the 8, 10, 12, 15 and 18 molar NaOH solutions are abbreviated as G8, G10, G12, G15, and G18 samples, respectively.

2.3. Sample preparation and testing

After being mixed, the fresh pastes were tested for setting times in a 25 °C room using standard Vicat needle apparatus in accordance with the ASTM C191 [21]. The reported results are the average of two tests.

The paste was then cast in a 3 cm diameter and 6 cm height plastic moulds for strength test. The cast samples were left standing in the 25 °C controlled room for 1 h. They were covered with clingfilm to avoid loss of water and put to cure in an electric oven at 40 °C for 24 h. After being cured, the specimens were left in the 25 °C controlled room until the age of 7 days. The compressive strength test was performed at the age of 7 days in accordance with the ASTM D1633 [22]. The reported results are the average of three specimens.

The microstructures of the pastes were investigated by X-ray diffraction (XRD) and scanning electron microscopy (SEM). The broken portion of the compressive strength specimens were used for these analyses.

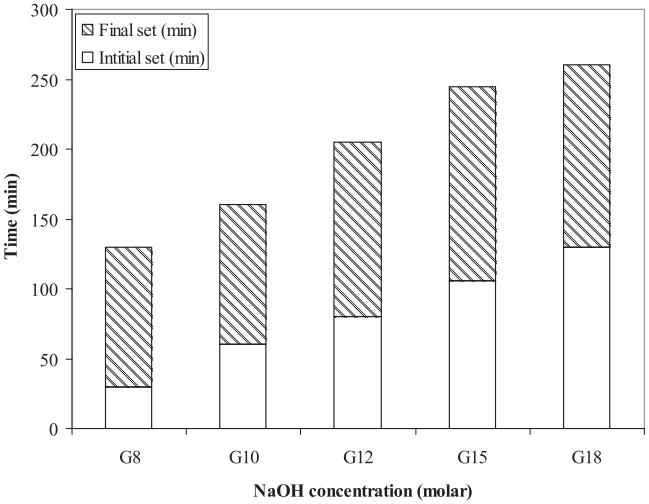

Fig. 1. Setting time of FAGP with various NaOH concentrations.

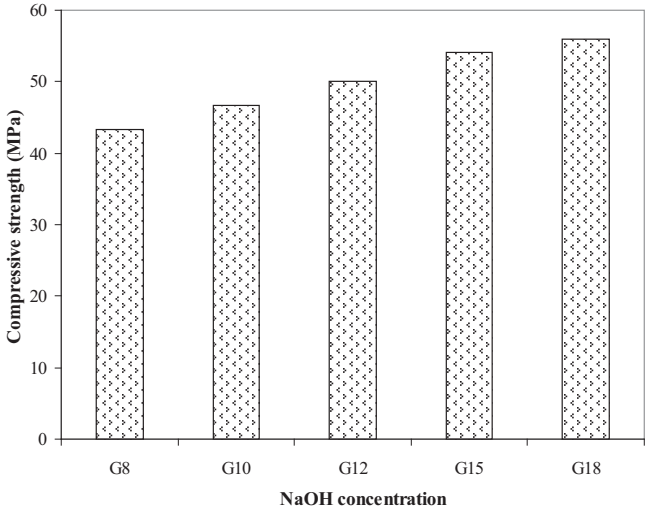

Fig. 2. Compressive strength of FAGP with various NaOH concentrations.

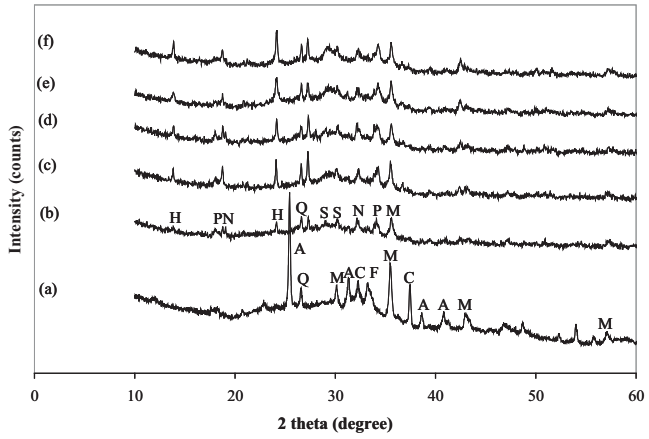

Fig. 3. XRD pattern of fly ash and FAGP with various NaOH concentrations (a) fly ash, (b) G8, (c) G10, (d) G12, (e) G15 and (f) G18.

For dielectric measurement, discs of 19 mm diameter and 2 mm thickness were cast and prepared in the same manner as the strength specimens. At the age of 7 days, the samples were

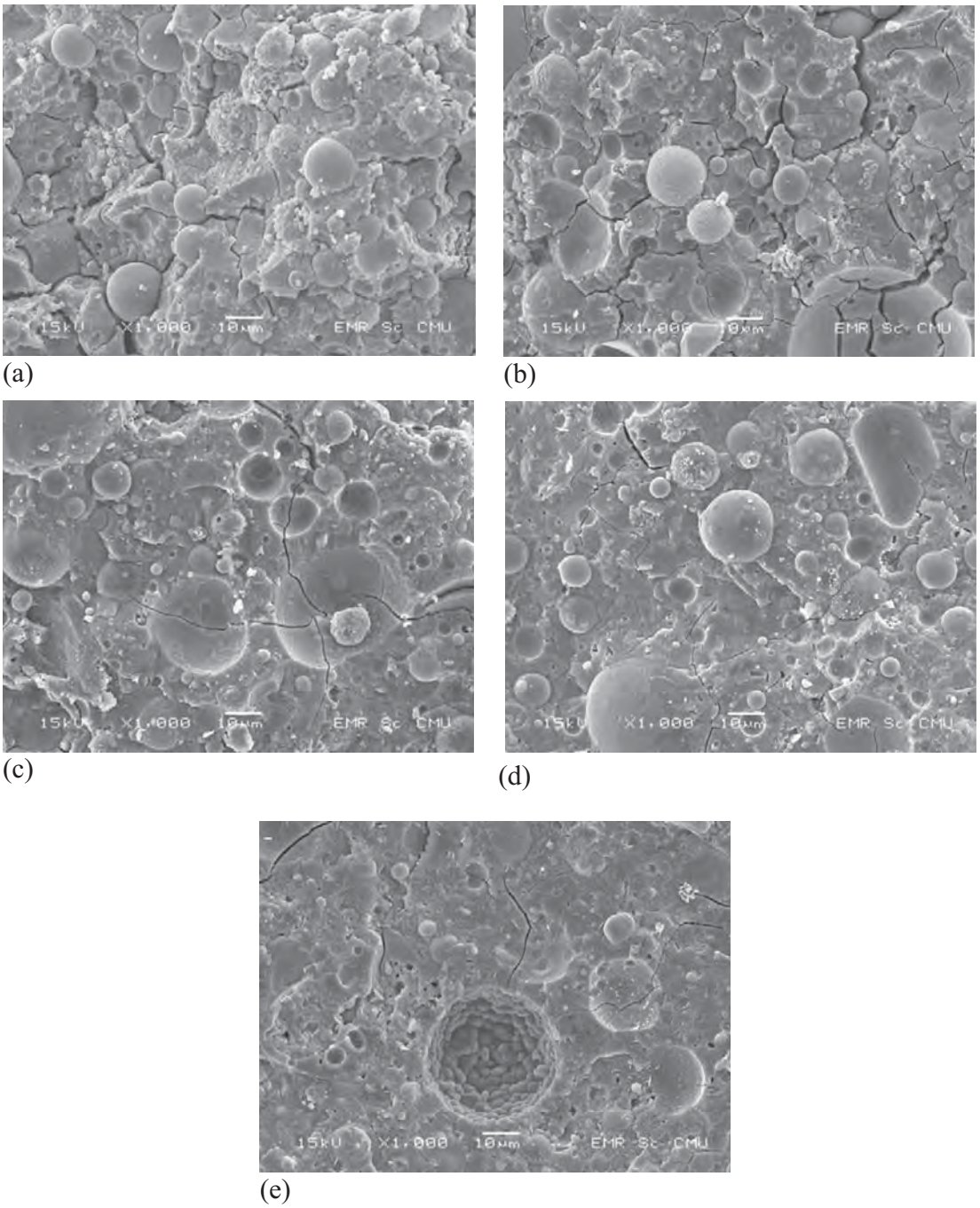

Fig. 4. SEM images of FAGP with various NaOH concentrations (a) G8, (b) G10, (c) G12, (d) G15 and (e) G18.

electroded by silver paint on both sides of the disk-shaped samples. The capacitance, dissipation factor, and electrical responses of the samples were measured with the use of a Hewlett Packard 4194A impedance gain phase analyzer over the frequency range of 102–106 Hz at room temperature and at oscillation voltage of 1.0 V. The relative permittivity or dielectric constant (εr) and dielectric loss (ε_r'') were calculated from Eqs. (1) and (2) [23,24]

$$\varepsilon_r = \frac{Ct}{\varepsilon_0 A} \tag{1}$$

where C is the capacitance of the sample, t is the thickness, ε_0 is the permittivity of free space constant (8.854×10^{-12}), and A is the electrode area;

$$\tan\delta = \frac{\varepsilon_r''}{\varepsilon_r} \tag{2}$$

where ε_r is the relative permittivity, ε_r'' is the dielectric loss, and $\tan\delta$ is the loss tangent.

3. Results and discussion

3.1. Setting time of geopolymer paste

The results of setting time are shown in Fig. 1. The initial and final setting times increased with an increase in NaOH concentration. The final setting times were 130, 160, 205, 245 and 260 min

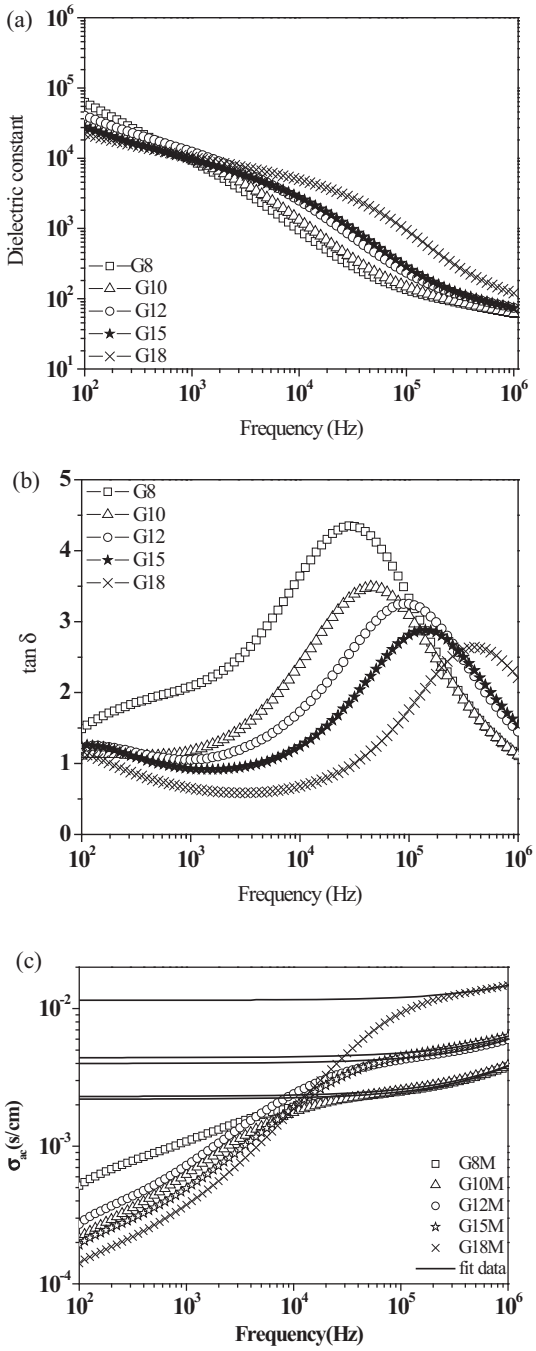

Fig. 5. Electrical properties of FAGP with various NaOH concentrations (a) dielectric constant, (b) tan δ, (c) AC conductivity (σ_{ac}).

Table 1
Parameters obtained from fitting universal power law curves of FAGP with various NaOH concentrations.

NaOH concentrations	σ_0 (S/cm)	A	n
8 M	0.0022	5.1×10^{-8}	0.75
10 M	0.0023	6.5×10^{-8}	0.73
12 M	0.0040	7.2×10^{-8}	0.74
15 M	0.0044	8.5×10^{-8}	0.72
18 M	0.0115	9.1×10^{-8}	0.76

for G8, G10, G12, G15, and G18 pastes, respectively. At low NaOH concentration, the leaching out of silica and alumina was low [20]. The leaching out of Ca^{2+} to the solution was not interrupted and the solution was thus filled with calcium. The amount of calcium was sufficient for the precipitation and reacted to form calcium silicate hydrate (CSH) and calcium aluminate hydrate (CAH). This resulted in the setting of paste and the setting time was thus short [25,26]. The setting time of geopolymer paste was thus related to the amount of the available calcium [27].

At high NaOH concentration, the leaching of silica and alumina was much better. The leaching out of calcium was hindered and the amount of calcium in the solution was limited. The setting of the paste was controlled by the normal geopolymerization process and the setting time was increased.

3.2. Compressive strength of geopolymer paste

The results of compressive strength are shown in Fig. 2. The compressive strength was increased with an increase in the NaOH concentration. They were 43.3, 46.7, 50.0, 54.1 and 56.0 MPa for the G8, G10, G12, G15, and G18 pastes, respectively. When the NaOH concentration was high, the dissolution of Si^{4+} and Al^{3+} ions from fly ash increased and the formation of sodium alumino-silicate was enhanced leading to an increase in strength [20,28,29].

The XRD patterns of fly ash and FAGP with various NaOH concentrations are shown in Fig. 3(a–f). The fly ash consists of an amorphous phase as indicated by the broad hump around 20–38° and crystalline phase as indicated by the sharp peaks of quartz (SiO_2), hematite (Fe_2O_3), anhydrite ($CaSO_4$), magnesioferrite ($MgFe_2O_4$) and calcium oxide (CaO). When the fly ash was activated with the alkali solutions, the glassy component was the first to dissolve and formed a new phase of alkaline aluminosilicate gel with apparent shift of broad hump around 25–38° [19,20,28,30]. Moreover, the peaks of quartz and magnesioferrite were still present from the remain of the unreacted or partially reacted fly ash with the disappearance of anhydrite. The new phases were portlandite ($Ca(OH)_2$), sodium sulfate (Na_2SO_4) and hydrosodalite ($Na_4Al_3Si_3O_{12}(OH)$). As discussed, the presence of $Ca(OH)_2$ affected the setting time of the paste. Moreover, the fly ash with high calcium oxide reacted with silicate compounds to form CSH similar to the hydration of Portland cement. The broad hump, therefore, included the geopolymeric gel and CSH gel [2,28]. A higher NaOH concentration had better ability to dissolve fly ash particles which resulted in better geopolymerization. The peaks of hydrosodalite and CSH increased with the increase in the NaOH concentration resulting in the increase in strength of paste.

Fig. 4(a–e) show the morphology of FAGP when activated by NaOH with various concentrations. The unreacted and/or partially reacted grains of fly ash and a continuous mass of alumino-silicate were easily detected. With increasing NaOH concentration, the unreacted fly ash particles were less abundant and the matrices looked rather dense. The findings were similar to the previously published results [31]. When the alumino-silicate source material came into contact with the alkali solution, the leaching of both silica and alumina started [32]. The increase in the NaOH concentration in the system resulted in the increase in leaching of silica and alumina from the fly ash particles to the solutions [20]. This resulted in a dense and strong geopolymer matrix which increased compressive strength of the paste.

Both the XRD and the SEM analyses reinforced the finding that the increase in compressive strength of high calcium fly ash ash geopolymer paste was due to the increase in NaOH concentration. The presence of calcium in substantial quantity in the system led to the formation of hydration products of CSH. At the same time, the high NaOH concentration of the system enhanced the leaching of silica and alumina and resulted in increased geopolymerization and formation of NASH gel. The CSH co-existed with NASH gel and increased the strength of paste [33].

3.3. Electrical properties of geopolymer pastes

Fig. 5 shows the electrical properties of FAGP with various NaOH concentrations. The results showed a decrease in dielectric constant (Fig. 5a) and increase in conductivity (Fig. 5b) with an increasing frequency which was indicative of a region of dispersion resulting from relaxation of a polarization process within the system [34]. For dielectric constant (Fig. 5a), the FAGP showed high dielectric constant values of 10^4–10^5at the low frequency range of 10^2–10^3 Hz which were the results of electrode/sample interfacial polarization and double-layer polarization on fly ash surface [33,34]. At the frequency of 10^3 Hz, the dielectric values of all samples were high at approximately 10^4. At the higher frequency, the dielectric values decreased and depended on the NaOH concentration. The dielectric values decreased less with the increase in NaOH concentration since the samples contained less unreacted fly ash and were denser than those of the low NaOH concentration mix.

For tan δ (Fig. 5b), the relaxation peaks of all samples were clearly observed and the trend of results was related to the dielectric constant values. The peak values of tan δ ranged between 2.5 and 4.5. When the NaOH concentration increased, the peak height decreased and the peak position shifted towards a higher frequency. This phenomenon was related to the denseness of structure. At high NaOH concentration, the leaching of alumina and silica was enhanced and the geopolymerization and formation of geopolymer gel increased [20] which led to a dense structure.

For the AC conductivity (Fig. 5c), the FAGP showed low conductivity in the range of 1.4×10^{-4}–5.2×10^{-4} at a low frequency as a result of electrode effect. At a high frequency, the conductivity increased with the increased frequency and NaOH concentration which was related to the increased geopolymerization. At 10^5–10^6 Hz, the AC conductivity values were 3.7×10^{-3}–1.5×10^{-2} S/cm. At a high frequency, the AC conductivity behavior follows the universal power law [35] as shown in Eq. (3).

$$\sigma(\omega) = \sigma_o + A\omega^n \tag{3}$$

where $\sigma(\omega)$ is the total conductivity, σ_0 is the DC conductivity, A is the pre-exponential factor, ω is the angular frequency, and n is the fractional exponent between 0 and 1.

The values of σ_0, A and n were obtained from Eq. (3) and shown in Table 1. The DC conductivity clearly increased with the increase in NaOH concentration which was due to the increase in geopolymerization.

4. Conclusions

Based on the results of the tests, the following conclusions can be made.

1. The NaOH concentration had significant influence on the physical and electrical properties of geopolymer paste. With an increase in NaOH concentration, the setting time and compressive strength increased resulting from a dense matrix with less unreacted fly ash in the microstructure.
2. The dielectric constant, loss and conductivity of geopolymer pastes were also affected by the NaOH concentration. At the low frequency range of 10^2–10^3 Hz, the geopolymer paste showed high dielectric constant values of 10^4–10^5. At the frequency of 10^3 Hz, all dielectric values of pastes were approximately the same at 10^4. At higher frequencies, the dielectric values decreased substantially and were related to the NaOH concentration. The decrease was less with the increases in NaOH concentration and strength of paste.
3. The relaxation peaks of tan δ of geopolymer paste ranged between 2.5 and 4.5, and were related to the dielectric constant values. When the NaOH concentration increased, the peak height decreased and the peak position shifted towards a higher frequency due to the increased denseness and strength of pastes.
4. For the AC conductivity, the geopolymer paste showed low conductivity of 1.4×10^{-4}–5.2×10^{-4}at a low frequency. At higher frequencies, the conductivity increased with the increased NaOH concentration. At 10^5–10^6 Hz, the AC conductivity values were 3.7×10^{-3}–1.5×10^{-2} S/cm. It was also found that the AC conductivity values of high calcium fly ash geopolymer pastes followed the universal power law.
5. It has been demonstrated that the physical and electrical properties of the high calcium fly ash geopolymer materials can be improved by using a suitable NaOH concentration.

Acknowledgements

The authors would like to acknowledge the financial supports from the Higher Education Research Promotion and National Research University Project of Thailand, Office of the Higher Education Commission, through the Advanced Functional Materials Cluster of Khon Kaen University; the Thailand Research Fund (TRF) under the TRF Senior Research Scholar Grant No. RTA5480004 and under the Royal Golden Jubilee Ph.D. Program (Grant No. PHD 0359/2550); and the TRF and Khon Kaen University under the Royal Golden Jubilee Ph.D. Program (Grant No. PHD 0352/2551)

References

[1] Ahmaruzzaman M. A review on the utilization of fly ash. Prog Energy Combust Sci 2010;36(3):327–63.
[2] Chindaprasirt P, Jaturapitakkul C, Chalee W, Rattanasak U. Comparative study on the characteristics of fly ash and bottom ash geopolymers. Waste Manage 2009;29(2):539–43.
[3] Chindaprasirt P, Chareerat T, Sirivivatnanon V. Workability and strength of coarse high calcium fly ash geopolymer. Cem Concr Compos 2007;29(3):224–9.
[4] Chindaprasirt P, Chareerat T, Hatanaka S, Cao T. High strength geopolymer using fine high calcium fly ash. J Mater Civ Eng 2011;23(3):264–70.
[5] He P, Jia D, Wang M, Zhou Y. Thermal evolution and crystallization kinetics of potassium-based geopolymer. Ceram Int 2011;37(1):59–63.
[6] Barbosa VFF, MacKenzie KJD. Thermal behaviour of inorganic geopolymers and composites derived from sodium polysialate. Mater Res Bull 2003;38(2):319–31.
[7] Khale D, Chaudhary R. Mechanism of geopolymerization and factors influencing its development: a review. J Mater Sci 2007;42(3):729–46.
[8] Cui XM, Zheng GJ, Han YC, Su F, Zhou J. A study on electrical conductivity of chemosynthetic Al_2O_3–$2SiO_2$ geoploymer materials. J Power Sources 2008;184(1):652–6.
[9] Duxson P, Fernández-Jiménez A, Provis JL, Lukey GC, Palomo A, Van Deventer JSJ. Geopolymer technology: the current state of the art. J Mater Sci 2007;42:2917–33.
[10] Pacheco-Torgal F, Castro-Gomes J, Jalali S. Alkali-activated binders: a review: Part 1. Historical background, terminology, reaction mechanisms and hydration products. Constr Build Mater 2008;22:1305–14.
[11] Detphan S, Chindaprasirt P. Preparation of fly ash and rice husk ash geopolymer. Int J Miner Metall Mater 2009;16(6):720–6.
[12] Chindaprasirt P, Rattanasak U. Utilization of blended fluidized bed combustion (FBC) ash and pulverized coal combustion (PCC) fly ash in geopolymer. Waste Manage 2010;30:667–72.
[13] Cyr M, Idir R, Poinot T. Properties of inorganic polymer (geopolymer) mortars made of glass cullet. J Mater Sci 2012;47:2782–97.
[14] Ahmari S, Ren X, Toufigh V, Zhang L. Production of geopolymeric binder from blended waste concrete powder and fly ash. Constr Build Mater 2012;35:718–29.
[15] Nazari A, Ghafouri Safarnejad M. Prediction early age compressive strength of OPC-based geopolymers with different alkali activators and seashell powder by gene expression programming. Ceram Int 2013;39(2):1433–42.
[16] Nazari A, Khanmohammadi H, Amini M, Hajiallahyari H, Rahimi A. Production geopolymers by Portland cement: designing the main parameters' effects on compressive strength by Taguchi method. Mater Des 2012;41:43–9.
[17] Cui XM, Liu LP, He Y, Chen JY, Zhou J. A novel aluminosilicate geopolymer materials with low dielectric loss. Mater Chem Phys 2011;130(1–2):1–4.

[18] Swain D, Row TNG. Structure, ionic conduction and dielectric relaxation in a novel fast ion conductor, Na2Cd(SO_4)$_2$. Chem Mater 2007;19(3):347–9.
[19] Hanjitsuwan S, Chindaprasirt P, Pimraksa K. Electrical conductivity and dielectric property of fly ash geopolymer pastes. Int J Miner Metall Mater 2011;18(1):94–9.
[20] Rattanasak U, Chindaprasirt P. Influence of NaOH solution on the synthesis of fly ash geopolymer. Miner Eng 2009;22(12):1073–8.
[21] American Society for Testing and Materials (ASTM) C191-08. Standard test method for time of setting of hydraulic cement by Vicat needle; 2008.
[22] American Society for Testing and Materials (ASTM) D1633-00. Standard test methods for compressive strength of molded soil–cement cylinders; 2007.
[23] Kasap SO. Principle of Electronic Materials and Devices. Boston: McGraw Hill; 2002.
[24] Van Beek A, Hilhorst MA. Dielectric measurements to characterize the microstructural changes of young concrete. Heron 1999;44(1):3–17.
[25] Alonso S, Palomo A. Calorimetric study of alkaline activation of calcium hydroxide-metakaolin solid mixtures. Cem Concr Res 2011;31(1):25–30.
[26] Chindaprasirt P, De Silva P, Sagoe-Crentsil K, Hanjitsuwan S. Effect of SiO_2 and Al_2O_3 on the setting and hardening of high calcium fly ash-based geopolymer systems. J Mater Sci 2012;47(12):4876–83.
[27] Rattanasak U, Pankhet K, Chindaprasirt P. Effect of chemical admixtures on properties of high-calcium fly ash. Int J Miner Metall Mater 2011;18(3):364–9.
[28] Guo X, Shi H, Dick WA. Compressive strength and microstructural characteristics of class C fly ash geopolymer. Cem Concr Compos 2010;32(2):142–7.
[29] De Vargas AS, Dal Molin DCC, Vilela ACF, De Silva FJ, Pavao B, Veit H. The effects of Na_2O/SiO_2 molar ratio, curing temperature and age on compressive strength, morphology and microstructure of alkali-activated fly ash-based geopolymers. Cem Concr Compos 2011;33(6):653–60.
[30] Guo X, Shi H, Dick WA. Alkali-activated complex binders from class C fly ash and Ca-containing admixtures. J Hazard Mater 2010;173(1–3):480–6.
[31] Albakri AMM, Kamarudin H, Bnhussain M, Nizar IK, Rafiza AR, Zarina Y. Microstructure of different NaOH molarity of fly ash based green polymeric cement. J Eng Tech Res 2011;3(2):44–9.
[32] Van Jaarsveld JGS, Van Deventer JSJ. Effect of the alkali metal activator on the properties of fly ash-based geopolymer. Ind Eng Chem Res 1999;38(10):3932–41.
[33] Somna K, Jaturapitakkul C, Kajitvichyanukul P, Chindaprasirt P. NaOH-activated ground fly ash geopolymer cured at ambient temperature. Fuel 2011;90(6):2118–24.
[34] McCarter WJ, Chrisp TM, Starrs G, Blewett J. Characterization and monitoring of cement-based systems using intrinsic electrical property measurement. Cem Concr Res 2003;33(2):197–206.
[35] McCarter WJ, Starrs G, Chrisp TM. The complex impedance response of fly-ash cement revisited. Cem Concr Res 2003;34(10):1837–43.

Available online at www.sciencedirect.com

ScienceDirect

Ceramics International 40 (2014) 1209–1213

CERAMICS INTERNATIONAL

www.elsevier.com/locate/ceramint

Short communication

Effect of particle size on the dielectric and piezoelectric properties of 0–3BCTZO/cement composites

Sitchai Hunpratub[a], Teeraporn Yamwong[b], Sutham Srilomsak[c], Santi Maensiri[d], Prinya Chindaprasirt[e,*]

[a]Materials Science and Nanotechnology Programs, Faculty of Science, Khon Kaen University, Khon Kaen 40002, Thailand
[b]Thailand National Metal and Materials Technology Center (MTEC), Thailand Science Park, Pathumthani 12120, Thailand
[c]School of Ceramic Engineering, Institute of Engineering, Suranaree University of Technology, Nakhon Ratchasima 30000, Thailand
[d]School of Physics, Institute of Science, Suranaree University of Technology, Nakhon Ratchasima 30000 Thailand
[e]Sustainable Infrastructure Research and Development Center, Department of Civil Engineering, Faculty of Engineer, Khon Kaen University, Khon Kaen 40002, Thailand

Received 13 May 2013; accepted 30 May 2013
Available online 5 June 2013

Abstract

0–3 $Ba_{0.85}Ca_{0.15}Ti_{0.9}Zr_{0.1}O_3$ (BCTZO)–cement composites were prepared by normal mixing and pressing of Ordinary Portland cement and BCTZO particles with average sizes of 569.8 and 8.9 μm. Three different composites were prepared with BCTZO to cement ratios of 30%, 50%, and 70% by volume. The effect of BCTZO particle size on the dielectric and piezoelectric properties of cement based 0–3 piezoelectric composites was investigated. The dielectric constant increases with both increasing BCTZO particle content and increasing BCTZO particle size. The piezoelectric properties were found to increase with the increasing BCTZO particle content and decreasing BCTZO particle size. It was found that a 70% BCTZO composite with an average particle size of 8.9 μm produced good dielectric constant, tan δ and piezoelectric properties of 107, 0.09 and 52 pC/N, respectively.

Keywords: C. Dielectric properties; C. Piezoelectric properties; Cement composites; Particle size

1. Introduction

Recently, cement based-piezoelectric composites (0–3, 1–3, 2–2 etc.) have been of interest because of their promising applications in civil engineering structures such as sensors and actuators [1–5]. In particular, cement composites of 0–3 connectivity, cement–piezoelectric material composites, were first reported by Li et al. [1]. They fabricated the lead zirconate titanate (PZT)–cement composites using normal mixing and spreading methods and have shown that the composites have compatibility with cement and have potential to be used for sensor applications. Xin et al. [2] investigated 0–3 lead magnesium niobate (PMN)– sulphoaluminate cement composites using a ball milling and pressing method and found good performances of both piezoelectricity and electromechanical coupling. Chaipanich's group et al.[3–5] investigated the piezoelectric and dielectric properties of PZT–cement-based composites prepared by normal mixing and compressing. However, these piezoelectric–cement composites are made using PZT or PMN and are toxic on the environment. As an alternative, $BaTiO_3$ (BTO)–cement composites of 0–3 connectivity were fabricated using a normal mixing and compassing method by Rianyoi et al. [6]. However, the piezoelectric properties of these composites are lower than those of the PZT–cement composites. Therefore, they tried to form the piezoelectric–cement composites in 1–3 types [7], which have good piezoelectric properties than those of 0–3 type cement composites.

Today, $BaTi_{0.8}Zr_{0.2}O_3$–$Ba_{0.7}Ca_{0.3}TiO_3$ (BZT–BCT) piezoelectric ceramics, with a composition close to the morphotropic phase boundary (MPB), exhibit large piezoelectric response, large dielectric constant and high spontaneous polarization [8–11], and are replacing PZT in sensor applications. Therefore, it is expected that this piezoelectric will play a more active role than those of 0–3 lead free piezoelectric–cement composites.

*Corresponding author. Tel.: +66 81871 9588; fax: +66 4320 2355x12.
E-mail address: prinya@kku.ac.th (P. Chindaprasirt).

0272-8842/$ - see front matter © 2013 Elsevier Ltd and Techna Group S.r.l. All rights reserved.
http://dx.doi.org/10.1016/j.ceramint.2013.05.118

In this study, we report the $Ba_{0.85}Ca_{0.15}Ti_{0.9}Zr_{0.1}O_3$ (BCTZO)–cement composites with high piezoelectric coefficient, produced by the normal mixing and compressing of white cement and BCTZO ceramic particles. The dielectric and piezoelectric properties of these composites were investigated.

2. Experimental

$Ba_{0.85}Ca_{0.15}Ti_{0.9}Zr_{0.1}O_3$ (BCTZO) ceramic particles were prepared by a solid state reaction method. $BaCO_3$ (99%), $CaCO_3$ (96%), TiO_2 (99%) and ZrO_2 (99%) were used as the

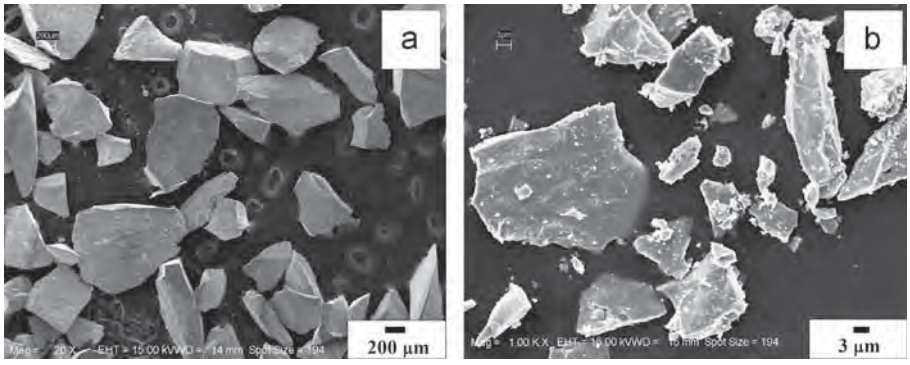

Fig. 1. The SEM images of BCTZO particles with the average particle size (a) 569.8 μm and 8.9 μm.

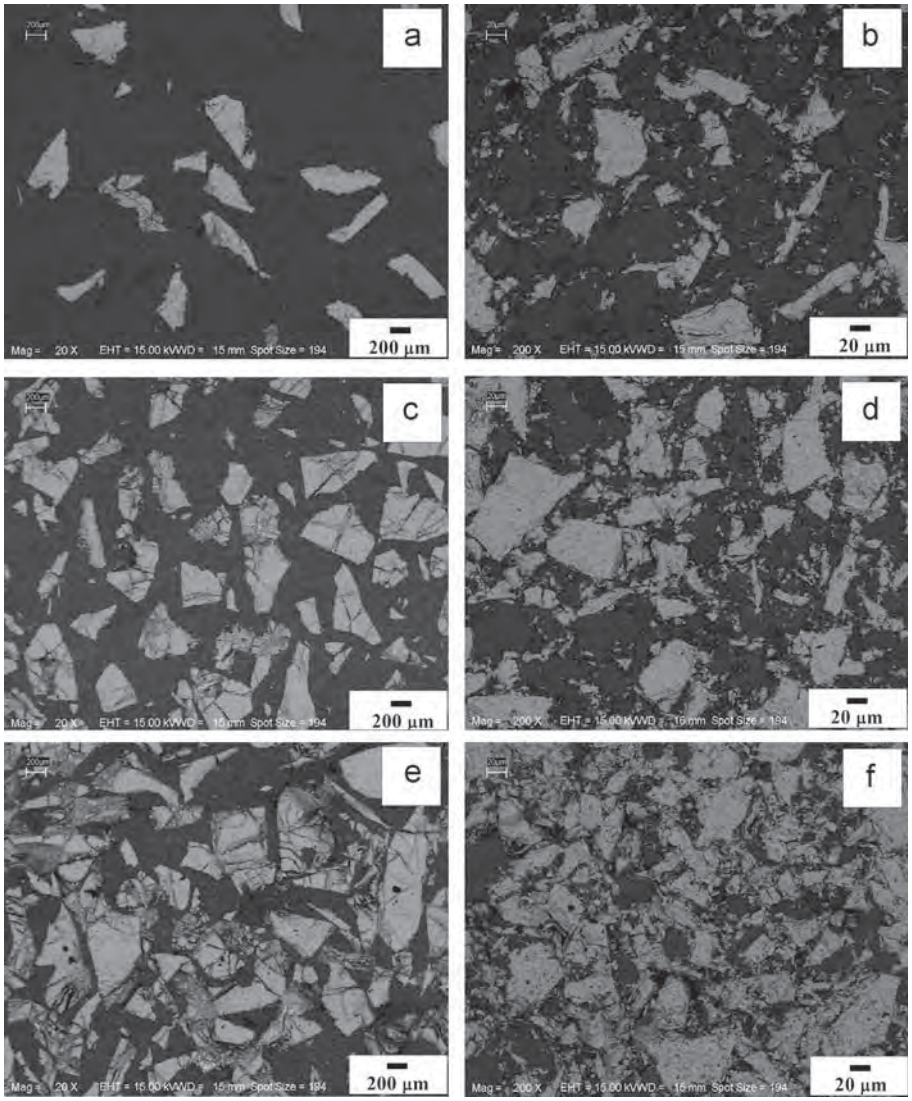

Fig. 2. The backscattered electrons SEM images of BCTZO–cement composites (a) 30%BCTZO, (b) 50%BCTZO and (c) 70%BCTZO for the average particle size as 569.8 μm, and (d) 30%BCTZO, (e) 50%BCTZO and (f) 70%BCTZO for the average particle size as 8.9 μm.

starting materials. Initially, all of these materials were mixed with 2-propanol and were ball milled for 24 h. After drying, the mixture precursor powders were calcined at 1300 °C for 3 h. The calcined BCTZO powders were compacted into disk-shaped pellets with a diameter of 13 mm and thickness of 1.5 mm with 221 MPa pressure. The green pellets were sintered at 1450 °C for 3 h. The sintered BCTZO ceramics were ground and sieved to select the size of BCTZO particles. To prepare the BCTZO–cement composites, the sintered BCTZO particles and Ordinary Portland cement were mixed and then pressed under a pressure of 146 MPa to form discs with a diameter of 16 mm and a thickness of about 2.5 mm. The disc specimens were cured in water vapor at 60 °C for 3 days and then dried.

The morphology of these samples was characterized by scanning electron microscopy (SEM, LEO VP1450, UK). Silver paint was used as the electrode and the dielectric properties of the composite discs were measured at room temperature by using an Agilent 4294A Precision impedance analyzer. The dielectric constant (ε_r) was calculated from the following equation:

$$\varepsilon_r = \frac{C_p t}{\varepsilon_0 A}$$

where C_p is the sample capacitance, t is the thickness, ε_0 is the permittivity of free space constant (8.854×10^{-12} F/m) and A is the electrode area.

The piezoelectric properties of composite discs were polarized at room temperature in silicon oil for 45 min under an electric field of 1 kV/mm. After being held for 24 h at room temperature, the piezoelectric strain factor (d_{33}) of the composite discs was measured by using a d_{33} meter (Model 90-2030, APD International, Ltd.).

3. Results and discussion

The morphology of the BCTZO particles was studied by SEM as shown in Fig. 1(a and b). The ground BCTZO particles have plate-like sharpness with sizes ranging from 294.8 to 1113.8 μm (Fig. 1(a)) or with sizes ranging from 1.6 to 36.9 μm (Fig. 1(b)). The average particle sizes of the ground BCTZO particles were evaluated to be 569.8 and 8.9 μm. SEM images of the composites, with 30%, 50% and 70% by volume of BCTZO particles, are shown in Fig. 2(a)–(f). In the backscattered electron SEM images, the black phase is cement and the white phase is BCTZO particles. It can be seen that using low content BCTZO particle results in their being isolated in the cement matrix, whereas using high content BCTZO particle results in their contact. However, with high content of BCTZO particles many cracks are observed, which are due to high compression during the formation of composite bulk.

The dielectric constants and tan δ, for the BCTZO–cement 0–3 composites of 30%, 50 %and 70% by volume and average particle size of 569.8 μm, are shown, respectively in Fig. 3(a)–(b). The dielectric properties were measured at 1 kHz and it was found that the dielectric constant increases with increasing BCTZO particle content. The values of dielectric constant were found to be 46.1, 80.7 and 154.0 and tan δ was found to be 0.12, 0.1 and 0.11 correspondingly. It was found that the dielectric constant of composites with the average particle size of 8.9 μm also increases with the increasing BCTZO particle content. The values of dielectric constant were found to be 38.7, 64.1 and 107.0 and tan δ was found to be 0.11, 0.12 and 0.09 correspondingly (Fig. 4). The dielectric constants and tan δ of the BCTZO–cement 0–3 composites, for the average particle size of 569.8 and 8.9 μm, are summarized in Table 1. From these results, it can be seen that all of the samples behave similarly to those in previous studies which show increasing dielectric constant with increasing piezoelectric particle content [1–6]. The dielectric constant increases with the increasing BCTZO particle size because of the influence of the dielectric constant of BCTZO bulks (4270 at 1 kHz), which is higher than that of cement bulk (19.7 at 1 kHz) and is explained by the composites model [1,6,12]. It was also found that the dielectric constant decreases with decreasing BCTZO particle size because of the low polarizations in small particles resulting in a lower dielectric constant in the samples.

The piezoelectric strain factor (d_{33}) values of the BCTZO–cement 0–3 composites of 30%, 50% and 70% by volume for the average particle sizes of 569.8 and 8.9 μm are also summarized in Table 1. It was found that the piezoelectric

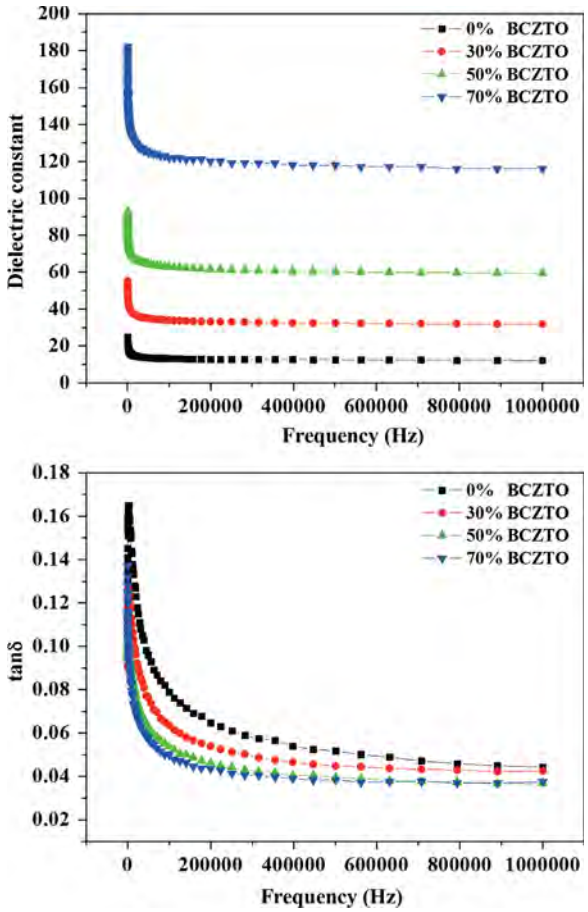

Fig. 3. Dielectric constant and tan δ of various BCTZO–cement composites with the average particle size as 569.8 μm measured at room temperature.

strain factor increases with increasing BCTZO particle content. In the composites with average particle size as 569.8 μm, the values of piezoelectric strain factor were found to be 4, 18 and 44 pC/N correspondingly. For composites with an average particle size of 8.9 μm, it was found that piezoelectric strain factor also increases with increasing BCTZO particle content. The values of piezoelectric strain factor were found to be 10, 32 and 52 pC/N. It is well known that cement is not piezoelectric and the incorporated BCTZO particles play an important role in the piezoelectricity of the composite. And then it can be seen that the piezoelectric strain factor of composites increases with decreasing BCTZO particle size [13,14]. Shifeng et al. [13] reported that piezoelectric properties decreased with decreasing ceramic particle size because the small ceramic particles (1.45–68.5 μm) have a high surface area and the volume ratio of lead lithium niobate to lead zirconate to lead titanate (PLN) leads to low piezoelectric properties or non-piezoelectric properties on the surface layer. On the other hand, because the chances for large ceramic particles (107.08–294.07 μm) to contact each other increase, the connectivity patterns change. In addition, Li et al. found that high piezoelectric properties can be obtained by using high crystalline nano-PZT particle (200 nm) cement composites [14] with a high d_{33} value of 52 pC/N. However, this study shows that smaller BCTZO particles have higher surface areas leading to lower interface space, resulting in better contact between the individual BCTZO particles. This is quite clear from the SEM results. The authors obtained quite good performances compared to those obtained by others at Composites with 70 vol% of piezoelectric particles, the BCTZO–cement composites, with average sizes of 569.8 and 8.9 μm have d_{33} values of 44 and 52 pC/N, respectively, which are higher than that of the BTO–cement composite (16 pC/N) [6] and the PZT–cement composite (43 pC/N) [3]. Therefore, the authors expect that 1–3 will play a more active role than 0–3 lead free piezoelectric–cement composites for sensors and actuators applications in civil engineering structures.

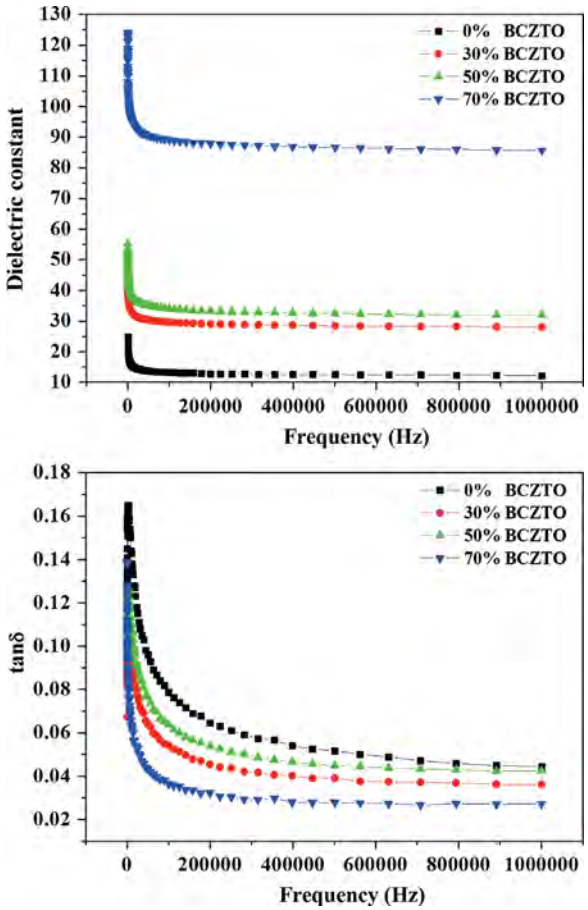

Fig. 4. Dielectric constant and tan δ of various BCTZO–cement composites with average particle size as 8.9 μm measured at room temperature.

4. Conclusion

In this study, $Ba_{0.85}Ca_{0.15}Ti_{0.9}Zr_{0.1}O_3$ particles were prepared by the solid state reaction method. The cement based 0–3 piezoelectric composites were fabricated by normal mixing and pressing of Ordinary Portland cement and BCTZO particles and curing in water vapor at 60 °C for 3 days. It was found that the dielectric constant and piezoelectric strain factor increase with increasing volume percentage of BCTZO particles. Good values for dielectric constant, dielectric loss and piezoelectric strain factor were obtained (107, 0.19 and 52 pC/N, respectively) for 70 vol% BCTZO particles with an average particle size of 8.9 μm. The piezoelectricity of the composites containing small BCTZO particles was high due to the high surface area and low interface space between the individual BCTZO particles, leading to good connection between those particles.

Table 1
Dielectric constant, tan δ and piezoelectric strain factor of various BCTZO–cement composites with the average particle size 569.8 and 8.9 μm measured at room temperature.

BCTZO particle content (vol%)	Dielectric constant ε_r measured at 1 kHz		tan δ, measured at 1 kHz		Piezoelectric charge constant, d_{33} (pC/N)	
	569.8 μm	8.9 μm	569.8 μm	8.9 μm	569.8 μm	8.9 μm
30	46.1	38.7	0.12	0.11	4	10
50	80.7	64.1	0.10	0.12	18	32
70	154.0	107.0	0.11	0.09	44	52

Acknowledgments

This work was supported by the Higher Education Research Promotion and National Research University Project of Thailand, Office of the Higher Education Commission, through the Advanced Functional Materials Cluster of Khon Kaen University, the Thailand Research Fund (TRF) under the TRF Senior Research Scholar, Grant no. RTA5480004, and the Royal Golden Jubilee PHD program, Grant no. PHD/0352/2551.

References

[1] Z.J. Li, D. Zhang, K. Wu, Cement-based 0–3 piezoelectric composites, Journal of the American Ceramic Society Advanced Materials 85 (2) (2002) 305–313.

[2] C. Xin, H. Shifeng, C. Jun, X Ronghua, L. Futian, L. Lingchao, Piezoelectric and dielectric properties of piezoelectric ceramic–sulphoaluminate cement composites, Journal of the European Ceramic Society 25 (2005) 3223–3228.

[3] A. Chaipanich, Dielectric and piezoelectric properties of PZT–cement composites, Current Applied Physics 7 (2007) 537–539.

[4] N. Jaitanong, A. Chaipanich, T. Tunkasiri, Properties of 0–3 PZT–Portland cement composites, Ceramics International 34 (2008) 793–794.

[5] A. Chaipanich, G. Rujiganagul, T. Tunkasiri, Properties of Sr- and Sb-doped PZT–Portland cement composites, Applied Physics A 94 (2009) 329–337.

[6] R. Rianyoi, R. Potong, N. Jaitanong, R. Yimnirun, Dielectric, ferroelectric and piezoelectric properties of 0–3 barium titanate–Portland cement composites, Applied Physics A 104 (2011) 661–666.

[7] R. Potong, R. Rianyoi, A. Ngamjarurojana, A. Chaipanich, Dielectric and piezoelectric properties of 1–3 non-lead barium zirconate titanate–Portland cement composites, Ceramics International 39 (2013) S53–S57.

[8] W.F. Liu, X.B. Ren, Large piezoelectric effect in Pb-free ceramics, Physical Review Letters 103 (2009) 257602.

[9] P. Wang, Y.X. Li, Y.Q. Lu, Enhanced piezoelectric properties of $(Ba_{0.85}Ca_{0.15})(Ti_{0.9}Zr_{0.1})O_3$ lead-free ceramics by optimizing calcination and sintering temperature, Journal of the European Ceramic. Society 31 (2011) 2005–2012.

[10] J.G. Wu, D.Q. Xiao, W.J. Wu, J.G. Zhu, J. Wang, Effect of dwell time during sintering on piezoelectric properties of $(Ba_{0.85}Ca_{0.15})(Ti_{0.90}Zr_{0.10})O_3$ lead-free ceramics, Journal of Alloys and Compounds 509 (2011) L359–L361.

[11] D.Z. Xue, Y.M. Zhou, H.X. Bao, C. Zhou, J.H. Gao, X.B. Ren, Elastic, piezoelectric, and dielectric properties of $Ba(Zr_{0.2}Ti_{0.8})O_3$–$50(Ba_{0.7}Ca_{0.3})TiO_3$ Pb-free ceramic at the morphotropic phase boundary, Journal of Applied Physics 109 (2011) 054110.

[12] R. Potong, R. Rianyoi, A. Chaipanich, Dielectric properties of lead-free composites from 0–3 barium zirconate titanate–Portland cement composites,, Ferroelectrics. Letters 38 (2011) 18–23.

[13] H. Shifeng, L. Lingchao, C. Jun, X. Dongyu, F. Futian, C. Xin, Influence of ceramic particle size on piezoelectric properties of cement-based piezoelectric composites, Ferroelectrics. Letters 332 (2006) 187–194.

[14] Z.J. Li, H.Y. Yu, Y.J. Zhang, Fabrication and piezoelectricity of 0–3 cement based composite with nano-PZT powder, Current Applied Physics 33 (2009) 588–591.

Construction and Building Materials 66 (2014) 72–78

Contents lists available at ScienceDirect

Construction and Building Materials

journal homepage: www.elsevier.com/locate/conbuildmat

Characterizations of FBC/PCC fly ash geopolymeric composites

Prinya Chindaprasirt [a], Supichart Jenjirapanya [b], Ubolluk Rattanasak [c,*]

[a] Sustainable Infrastructure Research and Development Center, Department of Civil Engineering, Faculty of Engineering, Khon Kaen University, Khon Kaen 40002, Thailand
[b] Department of Applied Science, Faculty of Sciences, Chandrakasem Rajabhat University, Bangkok 10900, Thailand
[c] Department of Chemistry and Center of Excellence for Innovation in Chemistry, Faculty of Science, Burapha University, Chonburi 20131, Thailand

HIGHLIGHTS

- FBC fly ash was used as a source material of geopolymeric composite.
- Grinding was applied to improve the physical property of FBC fly ash.
- PCC fly ash was blended with ground FBC fly ash to increase the glassy phase of source material.
- Results showed the changes in chemical compositions in the composite and physical performance.

GRAPHICAL ABSTRACT

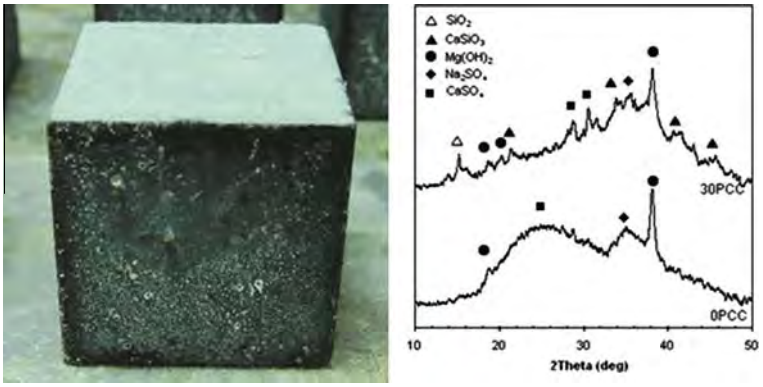

ARTICLE INFO

Article history:
Received 28 January 2014
Received in revised form 19 April 2014
Accepted 16 May 2014

Keywords:
Characterizations
Geopolymeric composite
Fluidized bed combustion
Coal fly ash

ABSTRACT

Fluidized bed combustion (FBC) is a well-established coal burning process for small factories owing to energy efficiency and low environmental impact. Due to the low burning temperatures at 800–900 °C, FBC fly ash is not suitable for use as pozzolan in concrete mixture and requires proper improvement before utilization. This research proposed the use of FBC fly ash as a source material for geopolymeric composite. Grinding was applied to improve the physical property of FBC fly ash. In addition, the ground FBC fly ash was blended with pulverized coal combustion (PCC) high calcium fly ash to increase its glassy phase. The geopolymeric composites were then prepared using the blended powder mixed with alkali solutions, and thermally-cured to promote the reaction. The hardened specimens were subjected to chemical and physical tests. Resistance to acid and salt attacks of PCC/FBC fly ash composites was also investigated. Results showed the changes in chemical compositions and physical performances of geopolymeric materials. PCC fly ash helped enhance the properties of FBC fly ash based composite and the dense and homogeneous matrix was achieved. Additional C—S—H was formed resulting in the increase in strength of composites as a function of time. However, the durability was affected with the use of the high calcium PCC fly ash due to the presence of calcium and the associated hydration products.

1. Introduction

Fluidized bed combustion (FBC) is an environmentally-friendly coal combustion process and is growing particularly in the small factories due to the low release of SO_2 and NO_x gasses in the flue gas. Combustion temperature of FBC unit is around 800–900 °C at which NO_2 cannot be generated and thus low-grade fuel can be efficiently burnt in the bed. SO_2 gas is effectively absorbed with ground limestone feeding resulting in no need of hi-tech flue gas desulfurization equipment [1]. Low combustion temperature

* Corresponding author. Tel.: +66 38 103066; fax: +66 38 393494.
E-mail address: ubolluk@buu.ac.th (U. Rattanasak).

http://dx.doi.org/10.1016/j.conbuildmat.2014.05.067
0950-0618/

results in a low glassy phase in FBC fly ash and hence it is not recommended to use as a cement replacement in concrete [2].

Alkali-activated composites have been widely studied owing to high strength gain in a short period of curing. Pulverized coal combustion (PCC) fly ash is a suitable alumino-silicate source and is effectively used as a source material for making an alkali-activated composite due to its pozzolanic property and availability. Aluminum and silicon ions are leached by alkali solutions (e.g. sodium hydroxide and sodium silicate solutions) from fly ash particles resulting in Al—O—Si geopolymerization chain [3–5]. The curing temperatures vary from ambient temperature to 90 °C. The resulting product is assigned as "geopolymer" [3]. PCC fly ash geopolymers possess excellent cementing, durability and thermal properties [4–8]. PCC fly ash consists of fine spherical particles of approximately 1–200 μm with high amorphous (glassy) phase content and high reactivity. It is widely use as pozzolanic material for partial replacement of Portland cement [9–11].

Numerous alumino-silicate source materials such as metakaolin [12,13], blast-furnace slag [14], rice husk ash [15], Al-rich waste [16] and red mud [17] have been used as source materials for the synthesis of geopolymer. Another alternative source material is FBC fly ash [18–20] as it contains silica and alumina and a large amount is produced annually. However, the use of FBC fly ash results in low strength geopolymer. Therefore, grinding and blending with PCC fly ash were applied to improve the mechanical properties of composites [19,20]. Proper grinding of FBC fly ash removed pores and cavities and increased the surface area [19].

The utilization of FBC fly ash is limited for making the geopolymer, non-cement binding, as it is a material with low reactivity. This research attempted to improve FBC fly ash as a starting material for geopolymer preparation. As the strength of FBC fly ash geopolymer was low, grinding was employed to increase its surface area and reactivity. In addition, the reactive PCC fly ash was used to blend with FBC fly ash to improve the properties of starting material. This was achieved without using Portland cement. Chemical and physical properties of FBC/PCC fly ash geopolymeric composites were characterized by XRD, SEM, FTIR, TGA techniques. Compressive strength tests of the cube specimens under normal curing condition and after immersion in 3% H_2SO_4 and 5% $MgSO_4$ solutions were performed in order to investigate the durability of composites.

2. Materials and methods

2.1. Materials

FBC and PCC fly ashes were obtained from two power plants in Thailand and used as alumino-silicate source materials. Bituminous coal was a feedstock of FBC unit, while lignite coal was a feedstock of PCC unit. Combustion temperatures of FBC and PCC units were 850 °C and 1200 °C, respectively. Particle shapes of fly ashes are shown in Fig. 1. FBC fly ash was irregular in shape owing to the low combustion temperature. High combustion temperature of PCC unit led to sintering of ash particle and thus resulted in a spherical shape fly ash. The median particle sizes (D_{50}) of FBC and PCC fly ashes as measured by the particle size analyzer (Malvern Mastersizer S) were 24 μm and 19 μm, respectively. Chemical oxides of PCC and FBC fly ashes were determined by X-ray fluorescence (XRF) spectrometer and shown in Table 1.

FBC fly ash had surprisingly low CaO and SO_3 contents of 8.2% and 2.3% owing to the high efficiency of bituminous FBC boiler. The use of bituminous coal reduced the retention time of fuel in combustion bed for any heat load and resulted in a relatively diluted calcium sulfate and residual lime content [21]. However, high calcium sulfate was detected in FBC fly ash when low grade lignite coal was used [19,20]. The FBC fly ash's loss on ignition (LOI) of 5.7% was substantially higher than 0.8% of PCC fly ash. The remaining residue decomposed at LOI heating temperature of 1000 °C. PCC fly ash had high CaO and Fe_2O_3 contents of 16.4% and 12.0% due to low grade lignite coal feedstock. XRD patterns of fly ashes are shown in Fig. 2. FBC fly ash had high crystalline phase with sharp peaks implying a low reactivity. Broad peak was present in PCC fly ash at 22–38° indicating a higher amount of amorphous phase than that of FBC fly ash. To enhance the reactivity with structural changes and increased surface area of FBC fly ash, grinding was performed on FBC fly ash with a laboratory ball mill for 2 h. A longer grinding time approached the grinding limit and did not significantly increase the fineness [22]. Ground FBC fly ash had a median particle size (D_{50}) of 6 μm.

In addition, sodium hydroxide solution (NaOH) and sodium silicate solution (Na_2SiO_3) with 9% Na_2O and 30% SiO_2 by weight were used as liquid activators. To increase Al and Si ions leachability from FBC fly ash particle and to control the ettringite formation, 15 M NaOH was used [23]. Graded-river sand with specific gravity of 2.65 and fineness modulus of 2.7 was used to prepare the mortar mixes. The 5-cm mortar cubes were used for compressive strength test in accordance with ASTM C109.

2.2. Mix preparation and experimental program

Ground FBC fly ash was replaced with as-received PCC fly ash at the dosages of 0%, 5%, 10%, 20% and 30% by weight. They were thoroughly mixed until uniform blend was obtained. Liquid mixture of 15 M NaOH and Na_2SiO_3 was then poured into the fly ash blend. NaOH helped the leaching of Al^{3+} and Si^{4+} ions from fly ash surface and the subsequent geopolymerization [24]. In addition, Na_2SiO_3 solution was used as the external source of dissolved SiO_2. A high proportion of Na_2SiO_3 in the mixture resulted in stiff paste, rapid setting and excess solid Na_2SiO_3 formation in the hardened-composite. Therefore, the Na_2SiO_3-to-NaOH ratio of 2.0 by weight was used [19,20] and the solid fraction was kept at 0.55 as high liquid content resulted in low strength mixes.

Pan mixer was used to prepare the geopolymeric paste. Mixing was performed for 5 min before paste was cast into 25 mm diameter × 25 mm height plastic cylinder molds. Specimens were vibrated for 10 s and subsequently cured in oven at 65 °C for 48 h. After that, the specimens were demolded and continuously cured at 25 °C in 80% RH chamber until the testing age. Mix proportion of geopolymeric pastes is tabulated in Table 2.

For strength test, 50 cm cube geopolymeric mortars were prepared. Powder and alkali solutions were mixed as described in the mixing of paste. The graded-river sand was then added to the mixture at final step with the sand-to-fly ash blend ratio of 2 (by weight), which 450 g of sand was added in the mixture in case of mortar preparation. Mixing was continued for another minute before casting into 5-cm cubic molds with the aid of vibration. The curing condition was the same as for the paste specimens.

The studies of morphology, microstructure, FTIR functional spectrometry and thermal properties were performed on the geopolymeric pastes at the age of 30 days. The compressive strengths of geopolymeric mortars under normal curing and after immersion in 3% H_2SO_4 and 5% $MgSO_4$ solutions were determined in order to investigate the durability of composites. The compressive strength tests were performed at the ages of 7, 30, 90 and 180 days and the reported results were the averages of three samples.

3. Results and discussion

3.1. Characterization of geopolymeric composites

The results of X-ray diffraction (XRD) pattern of geopolymeric composites are shown in Fig. 3. The XRD of composites showed the increase in broad peak and higher peak area starting from

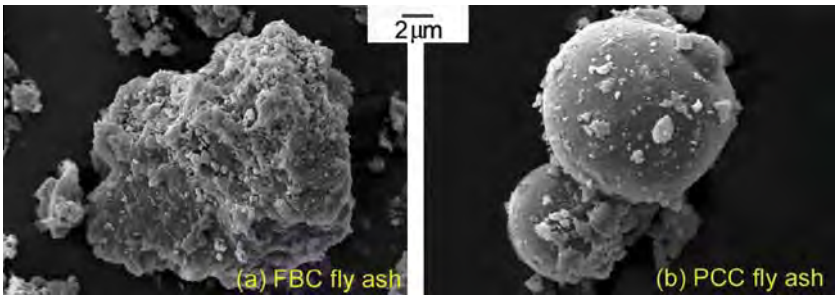

Fig. 1. Particle shape of the as-received fly ashes.

Table 1
Chemical composition and LOI of fly ashes.

Chemical compositions	FBC fly ash (wt%)	PCC fly ash (wt%)
SiO_2	47.1	36.1
Al_2O_3	22.6	25.0
CaO	8.2	16.4
Fe_2O_3	8.9	12.0
SO_3	2.3	3.3
MgO	2.7	2.2
K_2O	1.5	2.6
Na_2O	1.0	1.6
Loss on ignition (LOI)	5.7	0.8

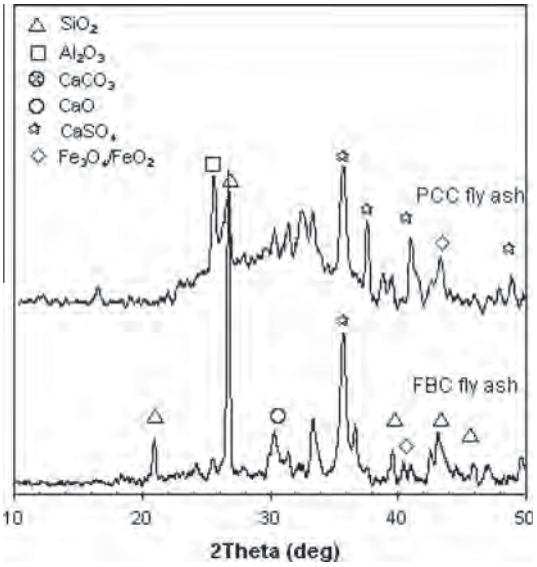

Fig. 2. XRD patterns of fly ashes.

20° to 38° compared with that of FBC fly ash. Broad peak of XRD pattern represented the amorphous phase of composite, and sharp peak was the crystalline phase. Composites consequently appeared as semi-crystalline with the highly disorder silicate glass phase [24]. Heat curing enhanced the geopolymeric reaction resulting in phase conversion with formation of glassy and crystalline phase products. Products consisting of aluminosilicate and calcium silicate hydrate (C—S—H) were also detected. The aluminosilicate compound was from the reaction between the alumina and silica in fly ashes and alkali solutions (i.e. NaOH and sodium silicate solution). In addition, C—S—H was obtained from the reaction between calcium and silicate compounds similar to the hydration reaction of Portland cement. However, unreacted oxide compounds of source material were also detected.

Blending FBC fly ash with PCC fly ash seemed to decrease the sharp peaks at 20° (SiO_2), 30.5° (CaO) and 37° (SiO_2). Increase in PCC fly ash content resulted in more reactive compound in reaction

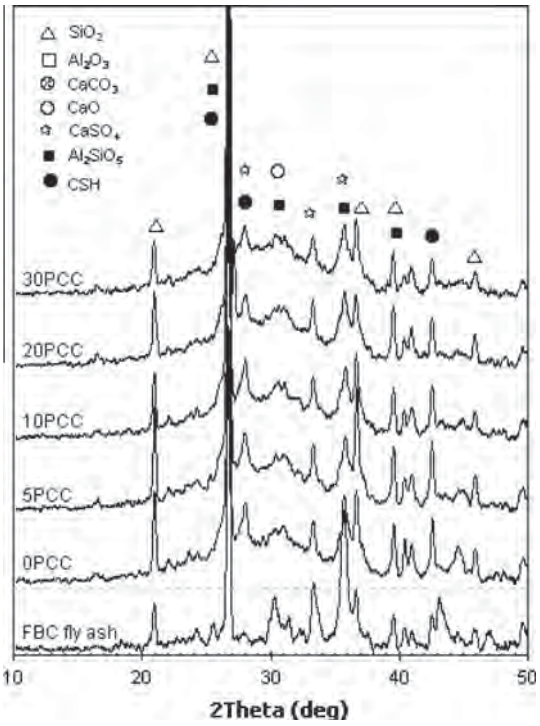

Fig. 3. XRD patterns of composites.

and low peak height of these compounds. As a result, the amorphous phase was increased with the increase in the amount of PCC fly ash.

Microstructural study of composites was conducted by SEM and the results are presented in Fig. 4. Ground FBC fly ash geopolymeric composite (sample 0PCC) showed the matrix with partially reacted-ash particles. Cracks and voids were easily observed throughout the matrix leading to the low physical properties of composite. Addition of PCC fly ash led to a dense and continuous matrix owing to the high glassy phase of fly ash. The high content of PCC fly ash resulted in the dense matrix compared with solitary FBC fly ash composite (0PCC). PCC fly ash was used to increase the reactivity and to develop the properties of geopolymeric matrix. Generally, fly ash consisted of glassy phase at the surface of the particles and crystalline phase in the interior [25]. This glassy phase played an important role in geopolymeric reaction and was easily leached out by alkali solutions to form the silica and alumina chain [24]. In the presence of alkali, alumina and silica in the source materials were leached out and resulted in aluminate ($Al(OH)_4^-$) and silicate (SiO_3^{2-}) species and consequent aluminosilicate formation. With high calcium in the source material, additional C—S—H was formed. Cracks were also seen due to the use of heat curing to accelerate the geopolymeric reaction and the evaporation of bound water in the alkali solution.

Table 2
Mix proportion of geopolymeric pastes.

Samples	Blended powder (g)		15 M NaOH (ml)	Na_2SiO_3 (ml)	Solid fraction
	FBC fly ash	PCC fly ash			
0PCC	225	0	61	123	0.55
5PCC	214	11	61	123	0.55
10PCC	202	23	61	123	0.55
20PCC	180	45	61	123	0.55
30PCC	157	68	61	123	0.55

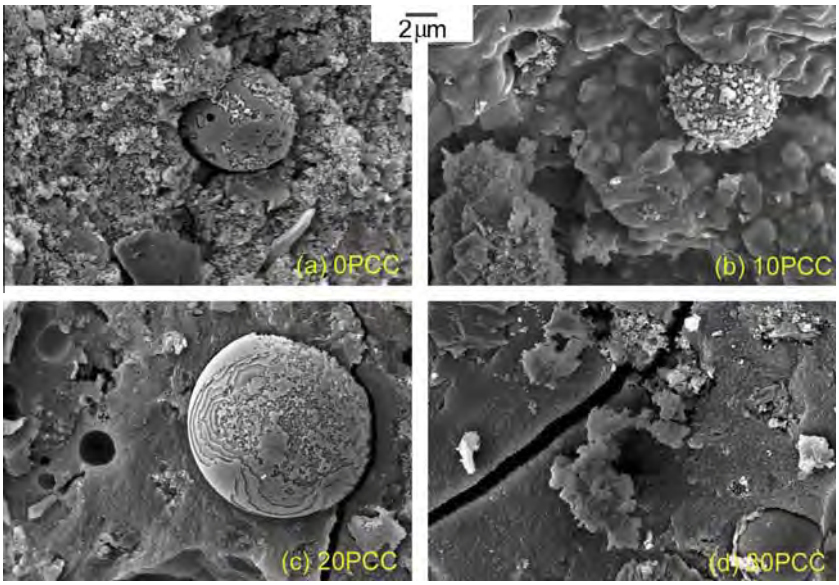

Fig. 4. Microstructure of composites.

Characterization of functional groups in geopolymeric composites was performed by Fourier Transform Infrared Spectroscopy (FTIR) at wavenumber between 3000 and 400 cm^{-1}. The results of spectrum bands are shown in Fig. 5. The vibration at a specific configuration of chemical bonding was related to the absorption band. Si—O and Al—O bonds were prominent in aluminosilicate geopolymer system. Spectrum of fly ashes and composites consisted of broad bands at 3450 cm^{-1} and 1600 cm^{-1} assigning to O—H stretching and O—H bending, respectively and C=O band (in CO_3^{2-} compound) at ~1460 cm^{-1} [26,27]. C=O band occurred in all fly ashes and composites due to the carbonation between alkaline solution (or moisture, in case of fly ash) and CO_2 in the environment. Si—O bending mode was observed near 460 cm^{-1}. The weak band at 575 cm^{-1} indicated Al—O stretching vibration. Si—O—Al and Si—O—Si stretching modes were recognized at the wavenumber range of 1100–1000 cm^{-1} assigning to the anti-symmetric stretching vibrations of the Si—O—Si in amorphous silica and Si—O—Al networks. Si—O—Al stretching mode was more noticeable than Si—O—Si bending mode. Si—O—Al stretching mode was therefore logically assigned to indicate the degree of geopolymerization [24,26,28].

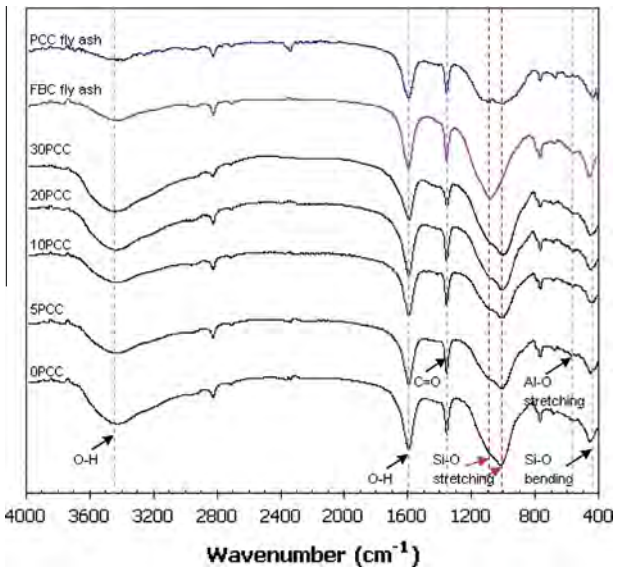

Fig. 5. FT-IR spectra of fly ashes and composites.

Addition of PCC fly ash in the composites resulted in a broader peak of Si—O stretching vibration at 1100–1000 cm^{-1} than that of the solitary FBC fly ash composite. This band was also found at 1100 cm^{-1} in FBC fly ash and shifted towards lower wavenumber of 1000 cm^{-1} as a result of a decrease in the average Si—O bond angle and increase in number of tetrahedral aluminum atoms [28]. This doublet peak probably resulted from asymmetry in the tetrahedral sites due to Al substitution [29] and indicated the —OH deformation for Al—OH leading to the possible assignment of a new type of Al—O bonds in the composite [30]. Shift of wavenumber also highlighted the structural disorder of the composite, breaking of interatomic bonds and formation of complex molecular units with strong bonding in composite. This implied that Si—O bond of SiO_2 in fly ashes was converted to new Si—O bond in composites.

Thermogravimetric analysis (TGA) and differential thermogravimetry (DTG) were used to characterize the thermal property of composites by measuring the weight change of a sample as a function of temperature in a precisely controlled atmosphere. DTG presented the decomposition temperature of specific volatile components in composites. TGA/DTG curves of samples are shown in Fig. 6. FBC fly ash showed the weight change at 100, 400, 650 and 700 °C due to the moisture evaporation, and decompositions of $Ca(OH)_2$, CaO and $CaCO_3$, respectively. Weight loss of FBC fly ash was approximately 7% corresponding to its loss on ignition (LOI). The DTG curves of the composites displayed the same decomposition temperatures of compounds and therefore only one overlapped DTG curve (sample 0PCC) was presented. The weight losses of composites were higher than that of FBC fly ash since the composites consisted of alkali solutions and the free water remained in the geopolymer pore system. Weight changes of composites were detected at 100 and 600 °C implying the evaporation of bound water used in alkali solutions and decomposition of CaO. The peak of $Ca(OH)_2$ at 400 °C disappeared in the geopolymeric composites due to the conversion of $Ca(OH)_2$ to C—S—H or more stable calcium compounds. Addition of up to 10% PCC fly ash into composites resulted in low weight loss and the reaction was enhanced due to the high glassy phase of source material. This resulted in strong composites with good heat resistance and ther-

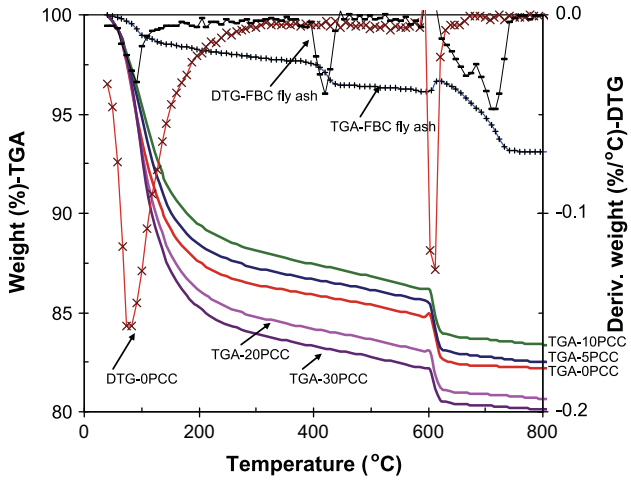

Fig. 6. TGA/DTG curves of fly ashes and composites.

mal stability at high temperature. However, the use of more than 10% PCC fly ash content resulted in the adverse effect on the weight loss of composites. The PCC fly ash contained high calcium content which decomposed during the TGA test. The remaining weights were 83% for the solitary FBC fly ash mix and 80% for the 30%PPCC mix. However, these remaining weights were significantly higher than OPC pastes with W/C ratios of 0.30–0.33 which was about 65% [31,32]. The result implied that geopolymeric composite had good heat resistance and thermal stability.

3.2. Chemical resistance

Chemical resistance of composites was presented as compressive strength of composite normally cured at 25 °C comparing with those immersed in 3% H_2SO_4 solution and in 5% $MgSO_4$ solution. Fig. 7 shows the compressive strength of composites cured at 25 °C. The control or FBC fly ash composite (0PCC) gave low strength of 10.0 MPa at the age of 180 days. FBC fly ash with high crystalline phase content was not reactive and thus the leaching out of Si and Al ions by alkali solutions was more difficult. Crystalline phases required high energy or temperature to break the strong bonding and orderly structure. Addition of PCC fly ash in the composites gave higher strengths of 11.0, 12.0, 12.5 and 18.0 MPa for composites with PCC fly ash contents of 5%, 10%, 20% and 30%, respectively. The glassy phases in PCC fly ash were conducive to the leaching of Si and Al ions to geopolymeric system and resulted in continuous aluminosilicate matrix as shown in the SEM images. This affected the strength of composites. The strength increased with age especially with PCC fly ash contained-composites since PCC fly ash had high calcium content. These calcium compounds reacted with alkali solutions resulted in $Ca(OH)_2$ compound. $Ca(OH)_2$ continued to react with silicon ions and formed C—S—H which contributed the strength of composites as curing continued. The reaction was similar to the hydration reaction of Portland cement. Compressive strength at 180 days of 24.0 MPa was achieved for 30PCC mix.

The results of strengths of composites after immersion in 3% H_2SO_4 and 5% $MgSO_4$ solutions are shown in Fig. 8. 3% H_2SO_4 was the acid solution and 5% $MgSO_4$ was salt solution representing the sewage water and saline soil environment. At 90 days, the immersion of composites in acid resulted in slightly higher compressive strengths than those of normal curing. However, 20–30% reductions in strengths after 180 immersion days for PCC fly ash content up to 20% compared with those of normal curing were obtained. With 30% content of PCC fly ash provided higher strength loss than all samples owing to the high content of calcium in composite. Calcium was easily dissolved in strong acid remaining the pores and cracks as shown in Eq. (1) [33].

$$Ca(OH)_2\ (s) + H_2SO_4\ (aq) \rightarrow CaSO_4 \cdot 2H_2O\ (s) \quad (1)$$

In addition, C—S—H also reacted with H_2SO_4 forming amorphous silica gel and calcium sulfate (Eq. (2)) which adversely affected the strength of composites [34].

$$3CaO \cdot SiO_2\ (s) + 3H_2SO_4\ (aq) + 3H_2O\ (l) \rightarrow 3CaSO_4 \cdot 2H_2O\ (s) + SiO_2\ (s) \quad (2)$$

Moreover, hydrogen ions (H^+) from H_2SO_4 ionization penalized the alumino-silicate network in composites at aluminum sites (—Al—O—Si—O—). The breaking of oxy-aluminum bridge (—Al—O—Si—O) weakened the composite in acid condition [35].

In case of 5 wt% $MgSO_4$ condition, the compressive strength of composites decreased more than those in acid solution. Low strength was observed for longer immersion time. With 30% content of PCC fly ash, the strength was not adversely affected. The deposit of white substance on the surface of composites was observed as shown in Fig. 9. XRD pattern indicated the occurrence of magnesium hydroxide ($Mg(OH)_2$), calcium sulfate ($CaSO_4$) and sodium sulfate (Na_2SO_4) for FBC fly ash composite (0PCC). The composite with 30% PCC fly ash (30PCC) gave many sharp peaks including the peaks of silica (SiO_2) and calcium silicate ($CaSiO_3$). The white powders were $Mg(OH)_2$ and $CaSO_4$ deposits obtained

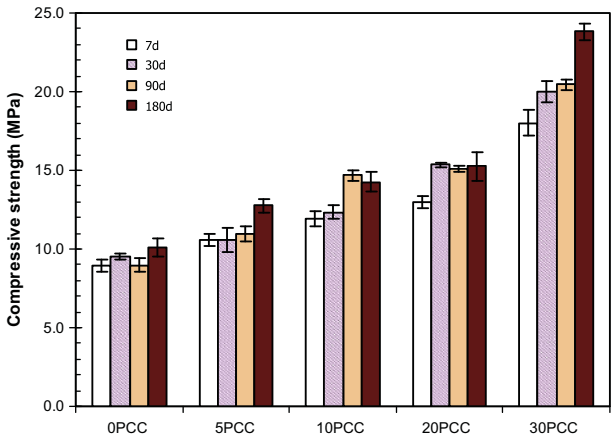

Fig. 7. Compressive strength of composites cured at 25 °C.

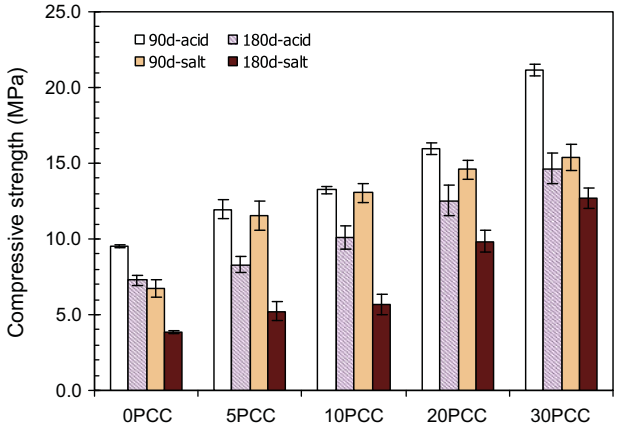

Fig. 8. Compressive strength of composites after immersion in 3% H_2SO_4 and 5% $MgSO_4$ solutions.

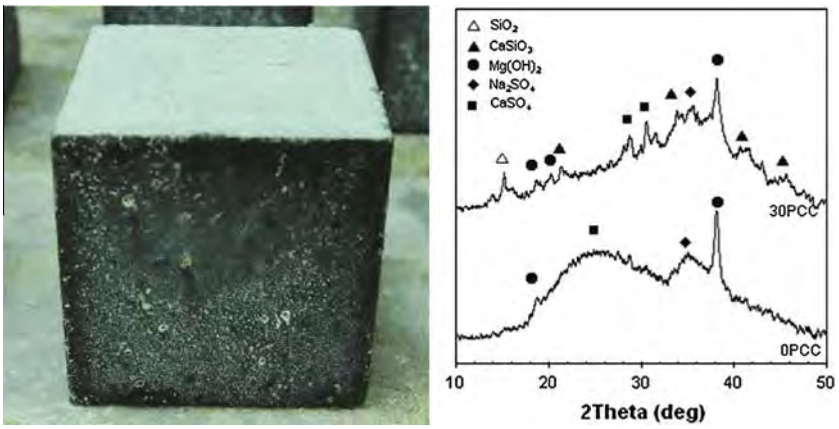

Fig. 9. White substance on composite surface and XRD pattern.

from the reaction between Mg^{2+}, SO_4^{2-} ion and hydroxyl ion (OH^-) from $Ca(OH)_2$ as shown in Eq. (3) [34].

$$Mg^{2+}\ (aq) + SO_4^{2-}\ (aq) + Ca(OH)_2\ (s) + H_2O\ (l) \rightarrow Mg(OH)_2\ (s) + CaSO_4 \cdot 2H_2O \quad (3)$$

C—S—H phase in FBC/PCC fly ash composites was attacked quite rapidly by $MgSO_4$ leading to the strength loss and forming of silica gel as detected in sample 30PCC. The equation is described as follows [34]:

$$3Mg^{2+}\ (aq) + 3SO_4^{2-}\ (aq) + 3CaO \cdot SiO_2\ (s) + 9H_2O\ (l) \rightarrow 3Mg(OH)_2\ (s) + 3[CaSO_4 \cdot 2H_2O]\ (s) + SiO_2\ (s) \quad (4)$$

The deterioration of composite in $MgSO_4$ solution seemed to be more severe than in H_2SO_4 solution. SO_4^{2-} ion was strongly absorbed on the alminosilicate composite due to the strong interaction between the ion and aluminol site (Al—OH) on the composite surface. This interaction led to high void ratio in the composite and resulted in low compressive strength [36].

4. Conclusions

The properties of FBC fly ash based-geopolymeric composite were enhanced by grinding of FBC fly ash and addition of high calcium PCC fly ash. The PCC fly ash had high glassy phase content and Si and Al ions were easily leached out by alkali solutions forming the linking network in geopolymeric composites. This resulted in dense and strong matrix. With high calcium PCC fly ash, additional C—S—H was formed and the strength of composites continued to develop with time. In addition, IR result showed that the Si—O bond shifted from 1100 cm^{-1} towards lower wavenumber of 1000 cm^{-1} implying the structural disorder, breaking of interatomic bonds and formation of molecular units with strong bonding of composite. This was supported by the DTG curve which showed the disappearance of $Ca(OH)_2$ peak at 400 °C in composites indicating the conversion of $Ca(OH)_2$ to C—S—H or more stable calcium compounds. The incorporation of PCC fly ash also improved the resistance of PCC/FBC fly ash composites to acid and salt attacks. However, the resistant properties were affected with the high calcium content and long period of immersion. FBC/PCC fly ash geopolymer can be used as alternative binding material with acceptable strength, durability and thermal properties.

Acknowledgements

This work was supported by Office of the Higher Education Commission and the Thailand Research Fund (TRF) under TRF Senior Research Scholar contract no. RTA5480004. Appreciation is also extended to Chandrakasem Rajabhat University and the Center of Excellence for Innovation in Chemistry (PERCH-CIC), Office of the Higher Education Commission, Ministry of Education, Thailand.

References

[1] Basu P. Combustion of coal in circulating fluidized-bed boilers: a review. Chem Eng Sci 1999;54:5547.
[2] Glinicki MA, Zieliński M. The influence of CFBC-fly ash addition on the phase composition of air-entrained concrete. Bull Polish Acad Sci 2008;56:45.
[3] Davidovit J. Geopolymer: inorganic polymeric new materials. J Therm Anal 1991;37:1633.
[4] van Jaarsveld GGS, van Deventer JSJ. Effect of the alkali metal activator on the properties of fly ash-based geopolymer. Ind Eng Chem Res 1999;88:3932.
[5] Barbosa V, MacKenzie K, Thaumaturgo C. Synthesis and characterisation of materials based on inorganic polymers of alumina and silica: sodium polysialate polymer. Int J Inorg Mater 2000;2:309.
[6] Fernández-Jiménez A, Palomo A, Sobrados I, Sanz J. The role played by the reactive alumina content in the alkaline activation of fly ashes. Micropor Mesopor Mater 2006;91:111.
[7] Sata V, Wongsa A, Chindaprasirt P. Properties of pervious geopolymer concrete using recycled aggregates. Constr Build Mater 2013;42:33.
[8] Turner LK, Collins FG. Carbon dioxide equivalent (CO_2-e) emissions: a comparison between geopolymer and OPC cement concrete. Constr Build Mater 2013;43:80.
[9] Mehta PK. Role of pozzolanic and cementitious by-products in sustainable development of the concrete industry. In: Proc. Sixth CANMET/ACI/JCI conference: fly ash, silica fume, slag and natural pozzolans in concrete, Bangkok, Thailand; 1998.
[10] Maholtra VM. Introduction: sustainable development and concrete technology. ACI Concr Int 2002;24:22.
[11] Chindaprasirt P, Jaturapitakkul C, Sinsiri T. Effect of fly ash fineness on microstructure of blended cement paste. Constr Build Mater 2007;21:1534.
[12] Palomo A, Glasser FP. Chemically-bonded cementitious materials based on metakaolin. Br Ceram Trans 1992;91:107.
[13] Gao K, Lin KL, Wang DY, Hwang CL, Shiu HS, Chang YM, et al. Effects SiO_2/Na_2O molar ratio on mechanical properties and the microstructure of nano-SiO_2 metakaolin-based geopolymers. Constr Build Mater 2014;53:503.
[14] Cheng TW, Chiu JP. Fire-resistant geopolymer produced by granulated blast furnace slag. Miner Eng 2003;16:205.
[15] Rattanasak U, Chindaprasirt P, Suwanvitaya P. Development of high volume rice husk ash alumino-silicate composite. Int J Miner Metall Mater 2010;17:654.
[16] Chindaprasirt P, Rattanasak U, Vongvoradit P, Jenjirapanya S. Thermal treatment and utilization of Al-rich waste in high calcium fly ash geopolymeric materials. Int J Miner Metall Mater 2012;19:872.
[17] He J, Jie Y, Zhang J, Yu Y, Zhang G. Synthesis and characterization of red mud and rice husk ash-based geopolymer composites. Cem Concr Compos 2013;37:108.
[18] Xu H, Li H, Shen L, Zhang M, Zhai J. Low-reactive circulating fluidized bed combustion (CFBC) fly ashes as source material for geopolymer synthesis. Waste Manage (Oxford) 2010;30:57.
[19] Chindaprasirt P, Rattanasak U. Utilization of blended fluidized bed combustion (FBC) ash and pulverized coal combustion (PCC) fly ash in geopolymer. Waste Manage (Oxford) 2010;30:667.
[20] Chindaprasirt P, Rattanasak U, Jaturapitakkul C. Utilization of fly ash blends from pulverized coal and fluidized bed combustions in geopolymeric materials. Cem Concr Compos 2011;33:55.

[21] Robl T, Oberlink A, Brien J, Pagnotti J. The utilization potential of anthracite CFBC spent bed fly ash as a concrete additive. In: Proc. 2011 World of coal ash (WOCA) conference, Denver, CO, United States; 2011.
[22] Kotake N, Kuboki M, Kiya S, Kanda Y. Influence of dry and wet grinding conditions on fineness and shape of particle size distribution of product in a ball mill. Adv Powder Technol 2011;22:86.
[23] Chindaprasirt P, Thaiwitcharoen S, Kaewpirom K, Rattanasak U. Controlling ettringite formation in FBC fly ash geopolymer concrete. Cem Concr Compos 2013;41:24.
[24] Rattanasak U, Chindaprasirt P. Influence of NaOH solution on the synthesis of fly ash geopolymer. Miner Eng 2009;22:1073.
[25] Chindaprasirt P, Rattanasak U, Taebuanhuad S. Role of microwave radiation in curing the fly ash geopolymer. Adv Power Technol 2013;24:703.
[26] Chindaprasirt P, Jaturapitakkul C, Chalee W, Rattanasak U. Comparative study on the characteristics of fly ash and bottom ash geopolymers. Waste Manage (Oxford) 2009;29:539.
[27] Günzler H, Gremlich H. IR spectroscopy: an introduction. Germany: Wiley-VCH Verlag GmbH; 2002.
[28] Lee WKW, van Deventer JSJ. Structural reorganization of class F fly ash in alkaline silicate solutions. Colloids Surf A 2002;211:49.
[29] Bishop JL, Murad E. Characterization of minerals and biogeochemical markers on Mars: a Raman and IR spectroscopic study of montmorillonite. J Raman Spectrosc 2004;35:480.
[30] Theo KJ, Ray FL, Leisel H. FT-Raman and FT-IR spectroscopic study of the local structure of synthetic Mg/Zn/Al-hydrotalcites. J Raman Spectrosc 2004;35:967.
[31] Villain G, Thiery M, Platret G. Measurement methods of carbonation profiles in concrete: Thermogravimetry, chemical analysis and gammadensimetry. Cem Concr Res 2007;37:1182.
[32] Alarcon-Ruiz L, Platret G, Massieu E, Ehrlacher A. The use of thermal analysis in assessing the effect of temperature on a cement paste. Cem Concr Res 2005;35:609.
[33] Chindaprasirt P, Rattanasak U, Taebuanhuad S. Resistance to acid and sulfate solutions of microwave-assisted high calcium fly ash geopolymer. Mater Struct 2013;46:375.
[34] Skalny J, Marchand J, Odler I. Sulfate attack on concrete. London: Spon Press; 2002.
[35] Wilson AD, Nicholson JW. Acid–base cements: their biomedical and industrial applications (chemistry of solid state materials). New York: Cambridge University Press; 1993.
[36] Sridharan A, Rao SM, Gajarajan VS. Effect of sulfate contamination on the volume change behaviour of bentonite. In: Physico-chemical aspects of soils and related materials ASTM STP 1095; 1990. p. 60–68.

journal

J. Am. Ceram. Soc., 1–6 (2014)
DOI: 10.1111/jace.12812

Improved Dielectric and Nonlinear Electrical Properties of Fine-Grained $CaCu_3Ti_4O_{12}$ Ceramics Prepared by a Glycine-Nitrate Process

Prasit Thongbai,[‡,§,†] Teerapon Yamwong,[¶] Santi Maensiri,[‖] Vittaya Amornkitbamrung,[‡,§] and Prinya Chindaprasirt[††]

[‡]Department of Physics, Faculty of Science, Khon Kaen University, Khon Kaen 40002, Thailand

[§]Integrated Nanotechnology Research Center (INRC), Khon Kaen University, Khon Kaen 40002, Thailand

[¶]National Metal and Materials Technology Center (MTEC), Thailand Science Park, Pathumthani 12120, Thailand

[‖]School of Physics, Institute of Science, Suranaree University, Nakhon Ratchasima 30000, Thailand

[††]Sustainable Infrastructure Research and Development Center, Department of Civil Engineering, Faculty of Engineering, Khon Kaen University, Khon Kaen 40002, Thailand

Pure $CaCu_3Ti_4O_{12}$ was successfully prepared by a glycine-nitrate process using a relatively low calcination temperature and short reaction time of 760°C for 4 h. Fine-grained $CaCu_3Ti_4O_{12}$ ceramics with dense microstructure and small grain size were obtained after sintering for 1 h. The nonlinear coefficient of a fine-grained $CaCu_3Ti_4O_{12}$ ceramic calculated in the range 1–10 mA/cm^2 was found to be very high of ~16.39 with high breakdown electric field strength of 1.46×10^4 V/cm. This fine-grained $CaCu_3Ti_4O_{12}$ ceramic also exhibited a very low loss tangent of 0.017 at 20°C with temperature stability over the range −55°C to 85°C. The grain growth rate of the $CaCu_3Ti_4O_{12}$ ceramics was found to be very fast after increasing the sintering time from 1.5 to 3 h, leading to formation of a coarse-grained $CaCu_3Ti_4O_{12}$ ceramic with grain size of about 100–200 μm. The dielectric permittivity of this coarse-grained ceramic was found to be as high as 1.03×10^5 with a low loss tangent of 0.054.

I. Introduction

Since the extremely high dielectric response (sometimes called the colossal dielectric response) of $CaCu_3Ti_4O_{12}$ (CCTO) was first discovered by Subramanian *et al.*,[1] CCTO polycrystalline ceramics have attracted considerable attention for two reasons. The first is due to the progressive development of small-sized multilayer ceramic capacitors. These devices require a dielectric material that can exhibit a very high dielectric permittivity (ε′) and temperature stability of ε′ as well as a low loss tangent (tanδ).[2] This type of capacitor can be miniaturized using a material with the so-called "giant" or "colossal" dielectric material, replacing materials used in recent years. It was also found that the current density-electric field strength (*J-E*) characteristic is nonlinear,[3] resulting from the formation of Schottky barriers at the grain boundaries (GBs) sandwiched between semiconducting grains. Such electrical behavior can potentially be used to develop CCTO polycrystalline ceramics in varistor applications if the nonlinear coefficient (α) and electric field breakdown strength (E_b) can be tuned to acceptable values.[4] The second reason is scientific elucidation. The origin of the giant dielectric response in CCTO ceramics is not yet clear. Many investigations have been performed to describe the exact giant dielectric response in CCTO ceramics. These were accompanied by the development of many models.[5–10] The internal barrier layer capacitor (IBLC) model of Schottky barriers at GBs is one of the most important models describing the giant dielectric response in CCTO polycrystalline ceramics. The IBLC model is based on the different electrical responses of grains and GBs investigated by using impedance spectroscopy and scanning Kelvin microprobe analysis.[3,5] It clearly shows that the microstructure of CCTO ceramics consists of an insulating component at the GBs and semiconducting component inside grains. The model predicts that dielectric and related electrical properties of CCTO ceramics can be modified by tuning their microstructure.

To study CCTO ceramics for use application in electronic devices, selection of the preparation method is one of the most important decisions, which largely determines the final bulk properties of CCTO ceramics. $CaCO_3$, CuO, and TiO_2 are usually selected as the starting raw materials to synthesize CCTO powder used to form a green body before sintering. This process is called the solid-state reaction (SSR) method. There are many disadvantages of the SSR fabrication method. The SSR method requires high temperatures and long reaction times to produce a pure CCTO phase. To best of our knowledge, to form a pure CCTO phase, CCTO powder prepared by the SSR method must be calcined at temperatures higher than 850°C using reaction times of more than 6 h.[11] Practically, sintered CCTO ceramics with fine-grained microstructure and with no pores are difficult to produce. Sintered CCTO ceramics prepared by the SSR method usually have microstructure with abnormal grain growth due to their high sintering temperatures and long sintering times.[12,13] Alternatively, CCTO ceramics with small grain size (<5 μm) may be obtained if the sintering temperature and sintering time are reduced. However, a large number of pores are usually formed in the resulting microstructure,[14] which is undesirable for all electronic device applications.

Syntheses of ceramic powder from chemical solutions offer the possibility of closer stoichiometric control compared to the SSR method. Low-temperature chemical reactions with short reaction times are usually sufficient used to produce a pure phase.[15,16] Recently, there have been many studies investigating preparation of CCTO ceramics by chemical methods.[15–27] Unfortunately, impurities such as CuO, $CaTiO_3$, and TiO_2 are usually residual in the resulting CCTO powders.[18–20,23,24,26,27] Although the impurities disappeared

D. Damjanovic—contributing editor

Manuscript No. 33916. Received October 10, 2013; approved December 23, 2013.
[†]Author to whom correspondence should be addressed. e-mail: pthongbai@kku.ac.th

in final products due to high sintering temperatures, the residual impurities leave microstructural imperfections. These appear as pores and abnormal grain growth. Only some chemical methods can effectively produce a pure CCTO phase powder by calcination at temperature lowers than 800°C with short reaction times. These methods are pyrolysis of organic solutions,[15] combustion method using ammonia as a fuel,[16] ethylenediaminetetraacetic acid (EDTA) precursor,[25] and oxalate coprecipitation methods.[22] A pure CCTO phase was obtained by these methods and calcined at 700°C for 2 h, 800°C for 0.5 h, 800°C for 3 h, and 700°C for 1 h, respectively. Although there have been reports of successful chemical preparation of CCTO at relatively low temperatures and short reaction times, it is useful to develop new methods to increase the number of design options and to support a variety of applications in the future. Therefore, a new wet chemical solution route to prepare CCTO is worthy of study.

Among of these four primary methods as mentioned above, the combustion method using ammonia as a fuel[16] and EDTA route[25] are classified as the combustion process. Organic compounds like glycine, urea, citric acid, and EDTA have been widely used as fuels for gel combustion.[28] The glycine-nitrate process (GNP) is one of the most attractive methods. The GNP method was firstly reported by Chick *et al.*,[29] which can be used effectively to prepare homogeneous nanoparticles of ceramic powders by a self-ignited combustion process using glycine and metal nitrates. In this process, the amine ($-NH_2$) and carboxyl (–COO) groups can make complexes with metal ions, thus preventing the metal nitrates from segregating before the combustion reaction occurs.[29,30] The GNP process has the advantages of relatively low-cost, high-energy efficiency, fast heating rates, short reaction times, and high composition homogeneity.[31,32]

In this work, GNP was used to prepare CCTO ceramics. Pure phase of CCTO powder was successfully prepared using a relatively low calcination temperature and short reaction time. A fine-grained CCTO ceramic microstructure with good dielectric and nonlinear electrical properties was obtained.

II. Experimental Procedure

In this work, $Ca(NO_3)_2{\cdot}4H_2O$ (99%, Sigma-Aldrich, St. Louis, MO), $Cu(NO_3)_2{\cdot}4H_2O$ (99.5%, Carlo Erba, Strada Rivoltana, Italy), $C_{16}H_{28}O_6Ti$ (75 wt% in isopropanol, Sigma-Aldrich), deionized water, citric acid, and glycine were used as the starting raw materials. First, 1.2312 g of $Ca(NO_3)_2{\cdot}4H_2O$ and 3.7789 g of $Cu(NO_3)_2{\cdot}4H_2O$ were dissolved in 80 mL of aqueous solution of citric acid (2.5 wt%) with constant stirring at room temperature. Then, 10 mL of $C_{16}H_{28}O_6Ti$ solution was added into the metal ion solution above under constant stirring until a clear and transparent solution was obtained. Next, 1.0 g of glycine powder was added into the mixed solution with stirring at 150°C until a viscous gel was obtained. Finally, the gel was dried at 350°C for 30 min. Combustion was observed when the temperature was 200°C. The resulting dried porous precursors were ground and calcined at 700°C–760°C for 4 h. It was found that the CCTO powder calcined at 760°C for 4 h exhibited a CCTO phase with no impurities. A very small amount of CuO secondary phase was observed in the CCTO powders calcined at 720°C and 740°C for 4 h. The pure CCTO powder (calcined at 760°C) was selected for further investigation. The powder was pressed into pellets having dimensions of 9.5 mm in diameter and ~1–2 mm in thickness by uniaxial compression at 200 MPa. Finally, these pellets were sintered in air under various conditions. CCTO ceramics sintered at 1050°C for 0.5, 1.0, 1.5, and 3.0 h are referenced as the CCTO50-0.5h, CCTO50-1h, CCTO50-1.5h, and CCTO50-3h samples, respectively. CCTO ceramics sintered at 1035°C, 1050°C, 1065°C, and 1080°C for 1 h are referred to as the CCTO35-1h, CCTO50-1h, CCTO65-1h, and CCTO80-1h samples, respectively.

XRD (PW3040 Philips; Eindhoven, the Netherlands) and scanning electron microscopy LEO 1450VP; Cambridge, UK) techniques were used to characterize the phase compositions and surface morphologies of the sintered CCTO ceramics, respectively. Particle size and shape of the CCTO powders prepared by using various temperatures were revealed using transmission electron microscopy (TEM; FEI Tecnai G^2, Eindhoven, the Netherlands). Each pellet face was polished and sputtered with Au at a current of 25 mA for 8 min using a Polaron SC500 sputter coating unit. The dielectric measurement was performed by using an Agilent (Hayward, CA) 4294A Precision Impedance Analyzer over the frequency range from 10^2 to 10^7 Hz using an oscillation voltage of 500 mV. The dielectric properties were measured over the temperature range from −70°C to 220°C with step increases of 10°C. Each temperature step was held with an accuracy of ±1°C. Current-voltage measurements were done at room temperature using a high-voltage measurement unit (Keithley Model 247, Estado St Pasadena, CA). The breakdown electric field (E_b) was obtained at the current density of 1 mA/cm^2. The nonlinear coefficient (α) was calculated over the range 1–10 mA/cm^2 as the following:

$$\alpha = \frac{\log(J_2/J_1)}{\log(E_2/E_1)} \quad (1)$$

where E_1 and E_2 are the electric fields corresponding to J_1 = 1 and J_2 = 10 mA/cm^2, respectively.

III. Results and Discussion

Figure 1(a) shows the XRD patterns of CCTO powders calcined at different temperatures for 4 h. The main XRD peaks corresponding to CCTO crystal structure were observed in the samples that were calcined at 720°C, 740°C, and 760°C. It is likely that pure CCTO phase with no impurities can be achieved by calcination at a very low temperature and short reaction time, that is, 720°C for 4 h. However, as shown in Fig. 1(b), careful inspection revealed that a very small amount of CuO secondary phase was present as shown in the XRD patterns of the CCTO powders calcined at 720°C and 740°C. Pure phase of CCTO powder was obtained at 760°C for 4 h. It is worth noting that a GNP effectively produced a pure CCTO phase powder using a low temperature and short reaction time. Figure 2 shows the TEM images of CCTO powders calcined at different temperatures for 4 h. Particle sizes of CCTO powders prepared by a GNP were in the range 100–200 nm. The particles size tended to increase as the calcining temperature was increased.

Figures 3 and 4 show the XRD patterns of CCTO ceramics sintered under different conditions. The XRD results revealed that all of the sintered CCTO ceramic samples were pure phase just as their powder. Sintering time and temperature

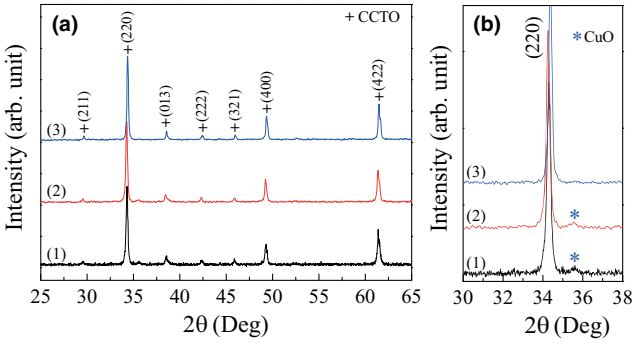

Fig. 1. XRD patterns of CCTO powders calcined at (1) 720, (2) 740, and (3) 760°C for 4 h. (a) and (b) represent the XRD patterns in a wide range scale of 2θ (25°–65°) and narrow range scale 2θ (30°–38°), respectively, revealing the existence a second CuO phase.

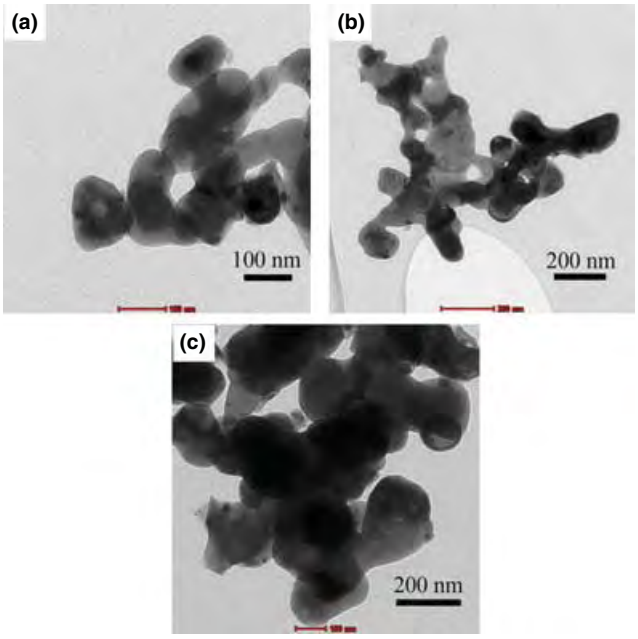

Fig. 2. Transmission electron microscopy images of CCTO powders calcined at (a) 720, (b) 740, and (c) 760°C for 4 h.

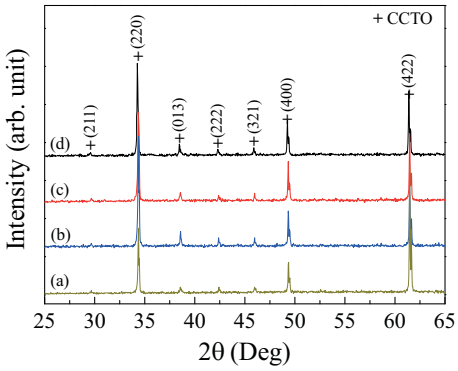

Fig. 3. XRD patterns of CCTO ceramics sintered at (a) 1035°C, (b) 1050°C, (c) 1065°C, and (d) 1080°C for 1 h.

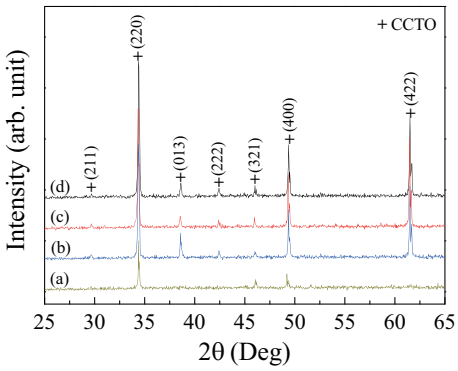

Fig. 4. XRD patterns of CCTO ceramics sintered at 1050°C for (a) 3.0 h, (b) 1.5 h, (c) 1.0 h, and (d) 0.5 h.

had no an effect on the phase formation of the CCTO ceramics in this study. This is due to the fact that CuO start to decompose at the sintering temperature of about 1100°C.[33]

Figure 5 shows the surface morphologies of the CCTO ceramics sintered in air for 1 h at various temperatures from 1035°C to 1080°C. All the samples had a fine-grained ceramic microstructure with grain sizes of about 2–4 μm. However, porosity in the form of large pores in the microstructure was still observed in the CCTO35-1h sample. Usually, a fine-grained CCTO microstructure with no pores is difficult to fabricate even when sintering at a low temperatures and/or using short reaction times. CCTO ceramic products with small grain sizes sintered at low temperatures and/or using short reaction times usually have residual pores in their microstructure.[14] In contrast, using high temperatures and/or long reaction times results in abnormal grain growth due to a liquid phase sintering mechanism that normally occurs in CCTO ceramics.[13] This is undesirable for many applications. Generally, residual impurities in ceramic powders used to prepare bulk sintered ceramics are a negative factor. They promote formation of large pores or results in a region of uncontrolled grain growth even when the ceramic was prepared from fine ceramic nanoparticles.[32] To overcome this problem, the use of high purity CCTO powder and proper powder compaction when forming the green body are good solutions. These can lead to fine-grained CCTO microstructure with no large pores in their microstructure. Therefore, high purity CCTO and fine nanoparticles used to form a green body may be important factors that contributed to the observed fine-grained ceramic microstructure of the CCTO50-1h, CCTO65-1h, and CCTO80-1h samples.

Figure 6 demonstrates the influence of sintering time on the microstructure of CCTO ceramics. It was found that grain growth rate in CCTO was very low when the ceramics were sintered at 1050°C for 0.5–1.0 h. The overall microstructures of the CCTO50-0.5h and CCTO50-1h samples are very similar. When sintering time was increased to 1.5 h, abnormal grain growth was observed. Some grains grew rapidly to very large sizes of about 100 μm within a fine-grained matrix having grain sizes of about 2–4 μm. The rapid grain growth observed in the CCTO ceramic sintered for 3 h is shown in Fig. 6(d). Grain sizes of the CCTO50-3h are about 100–200 μm, which is higher than those of the other three samples by a factor of 50. Pores are still observed in the grains of CCTO50-3h sample, which is indicative of abnormal grain growth.[32] The large grain size of the CCTO50-3h sample can be comparable to those of CCTO ceramics prepared by SSR methods sintered at relatively high temperatures and/or very long sintering times.[3,5,7,12,13] Comparing the grain growth rate of CCTO ceramics, it can be seen that grains of the CCTO50-3h sample grew faster than those of the samples prepared by an SSR method.

The fine-grained microstructure of CCTO ceramics shown in Figs. 5 and 6 was expected to have improved dielectric and nonlinear electrical properties. This is because CCTO polycrystalline ceramics are electrically heterogeneous, consisting of semiconducting grains enclosed by an insulating GB layer.[3,5] Thus, both the geometric and intrinsic properties of the GBs of CCTO ceramics are key factors determining their overall properties. Using the geometric approach, dielectric properties (especially tanδ) and the nonlinear electrical properties of CCTO prepared by a GNP should be significantly improved. The increase in the GB density due to the reduction in grain size can cause an increase in E_b and enhancement of the total resistance of GBs, leading to the reduction in tanδ in CCTO ceramics. The effect of the GB density (or the mean grain size) on the nonlinear electrical properties was also observed in commercial ZnO varistors.[4] Figure 7 shows the nonlinear electrical characteristics of all the ceramic samples. The E_b and α values of all the samples are summarized in Table I. The effect of geometric properties of the microstructure on the nonlinear properties of CCTO ceramics is clearly seen in Fig. 7(a). The CCTO50-0.5h and CCTO50-1h ceramic samples have closed grain size; therefore, these two ceramics have closed E_b. Comparing the microstructure of CCTO50-0.5h (or CCTO50-1h) sample to that of the CCTO50-3h sample, E_b strongly decreased by a factor of about 75 as the grain size increased from 2–5 μm to

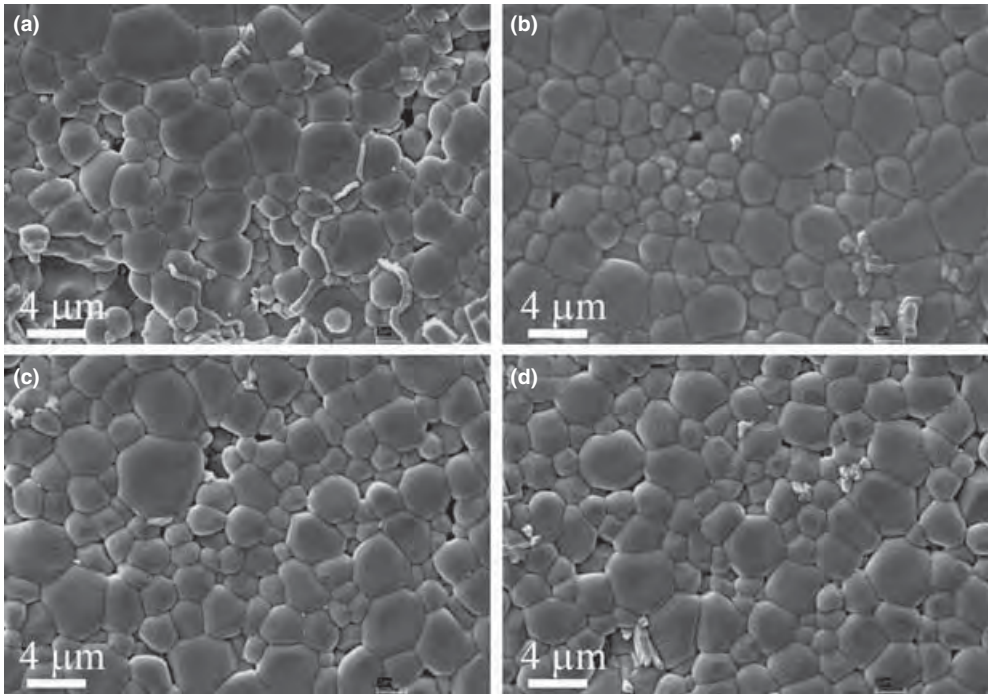

Fig. 5. Scanning electron microscopy images of polished surface morphologies of CCTO ceramics sintered at 1035°C, (b) 1050°C, (c) 1065°C, and (d) 1080°C for 1 h.

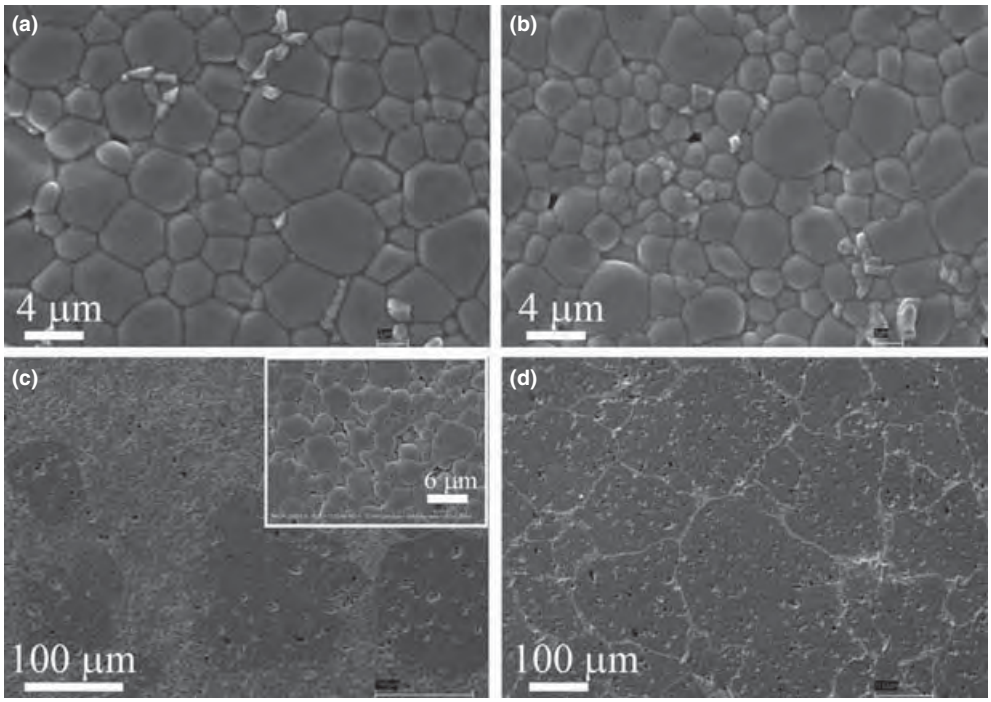

Fig. 6. Scanning electron microscopy images of polished surface morphologies of CCTO ceramics sintered at 1050°C for (a) 0.5 h, (b) 1.0 h, (c) 1.5 h, and (d) 3.0 h; the inset of (c) shows a high magnification image, revealing a fine-grained region.

100–200 μm. These results are consistent with the geometric approach if some GBs are considered to be electrically inactive boundaries. Furthermore, a strong decrease in E_b of the CCTO50-1.5h sample compared with that of the CCTO50-0.5h and CCTO50-1h samples was also observed. This result is attributed to detour of electric charge current within the ceramic arising as the current avoids the fine-grained regions. This is due to the impedance related to the high density of GBs in such regions.[34] More electric charge current can pass through the large-grain regions leading to a large drop in E_b. Furthermore, with fewer large grains in its microstructure, α of CCTO50-1.5h decreased by a factor of $\approx$2. This is attributed from the detour of the current, which can cause a drop in the voltage across an insulating interface (GBs) between fine grains. The CCTO50-1h ceramic sample exhibited the best nonlinear properties among all the samples with $\alpha = 16.39$ and $E_b = 14.6$ kV/cm. To our best knowledge, this α value is the highest value for undoped CCTO ceramics yet reported in the literature. This value is comparable to the value of $\alpha \approx 17$ (calculated over the range of 1–10 mA/cm^2) for the Sn-doped CCTO ($CaCu_3Ti_{3.8}Sn_{0.2}O_{12}$) ceramic.[35] However, α of the CCTO50-1h sample is lower than that of the Tb-doped CCTO ($Ca_{0.775}Tb_{0.15}Cu_3Ti_4O_{12}$) ceramic for which $\alpha = 29.67$.[36]

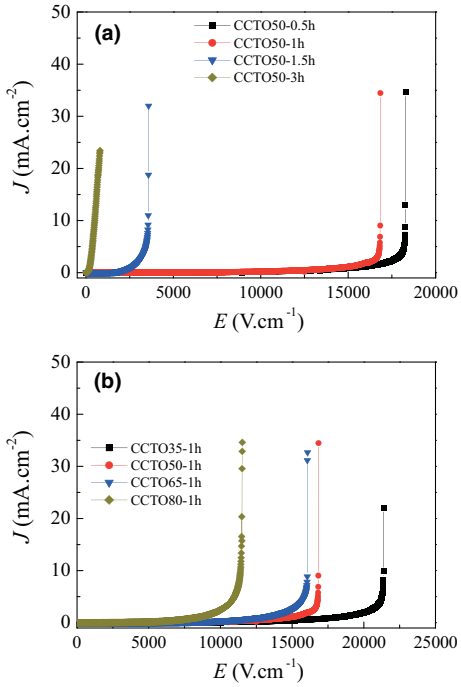

Fig. 7. *J-E* characteristics of (a) CCTO ceramics sintered at 1050°C for different times and (b) CCTO ceramics sintered at various temperatures for 1.0 h.

Table I. Dielectric Properties (ε′ and tanδ) at 1 kHz and 20°C and Nonlinear Electrical Properties (α and E_b) Measured at Room Temperature

CCTO sample	ε′	tanδ	α	E_b (V/cm^2)
CCTO35-1h	2932	0.019	13.24	17 991
CCTO50-1h	3045	0.017	16.39	14 640
CCTO65-1h	2645	0.024	9.71	12 685
CCTO80-1h	4108	0.017	7.45	8384
CCTO50-0.5h	2893	0.017	13.68	15 452
CCTO50-1.5h	4835	0.021	6.77	2539
CCTO50-3h	103 873	0.054	2.54	206

According to the results shown in Fig. 7(a), the geometric properties of the microstructure clearly show a strong effect on the nonlinear electrical properties of CCTO ceramics. Another factor that has an influence on the nonlinear properties of CCTO ceramics is the intrinsic properties of the GBs. Figure 7(b) shows *J-E* curves of CCTO ceramics sintered for 1 h at different temperatures as means control the fine-grain microstructure. E_b of the CCTO ceramics decreased significantly as the sintering temperature was increased even through their microstructures had very similar morphologies. This means that the intrinsic properties of GBs have an effect on the nonlinear properties of CCTO ceramics. In the traditional metal oxide non-Ohmic-based systems,[37] nonlinear electrical properties are related to oxygen enrichment at the GBs. Therefore, the decrease in E_b among these samples may have resulted from enhancement of oxygen vacancy concentration as the sintering temperature was increased. It was reported that E_b could be enhanced by annealing CCTO ceramics in O_2 atmosphere[38] or sintering in an O_2 atmosphere.[39] α values of the CCTO35-1h, CCTO50-1h, CCTO65-1h, and CCTO80-1h samples are of about 13.24, 16.39, 9.71, and 7.45, respectively.

Figures 8 and 9 demonstrate the frequency dependence of ε′ at 20°C of CCTO ceramics prepared by a GNP using different sintering conditions. Their insets show tanδ as a function of frequency at 20°C. The values of ε′ and tanδ at 20°C

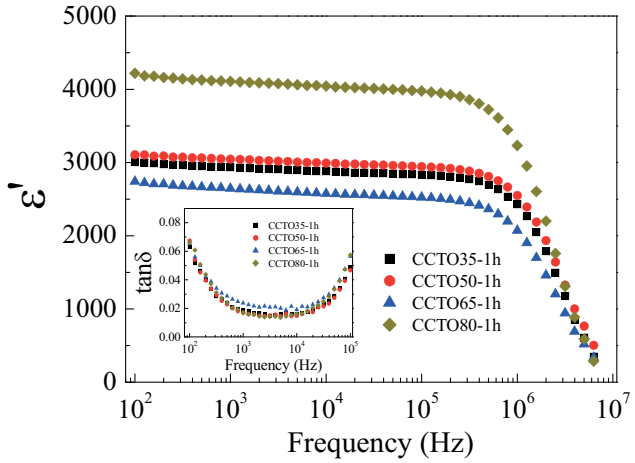

Fig. 8. ε′ as a function of frequency measured at 20°C of CCTO ceramics sintered at different temperatures for 1.0 h. The inset shows the frequency dependence of tanδ at 20°C.

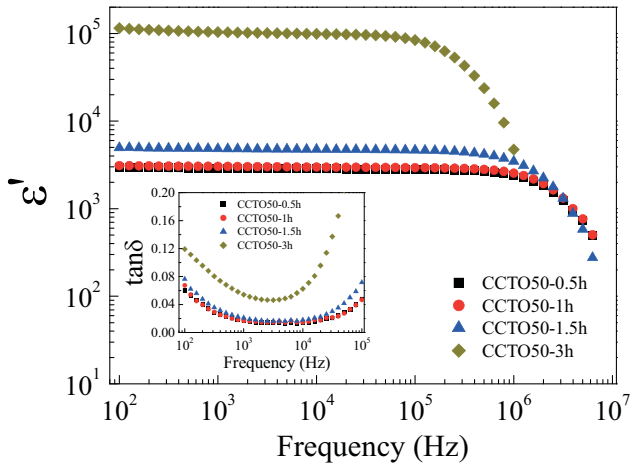

Fig. 9. ε′ as a function of frequency measured at 20°C of CCTO ceramics sintered at 1050°C for 0.5 h, 1.0 h, 1.5 h, and 3.0 h. The inset shows the frequency dependence of tanδ at 20°C.

and 1 kHz of all samples are summarized in Table I. ε′ values of the fine-grained ceramic microstructure were in the range 2893–4108. For these samples, tanδ values were very low, less than 0.024 at 1 kHz. These are acceptable values for ceramic capacitor applications. These values of ε′ and tanδ can be comparable to those observed in a CCTO/CTO composite system.[40] The CCTO50-3h sample with coarse-grained ceramic microstructure exhibited a very high ε′ of about 103,873; whereas, tanδ is still too low, 0.054 at 20°C and 1 kHz. As seen in Figs. 8 and 9, ε′ values for all the fine-grained CCTO ceramics are nearly independent of frequency over the range of 10^2–10^6 Hz. Furthermore, tanδ values of all fine-grained CCTO ceramics are lower than 0.08 over a wide frequency range from 10^2 to 10^5 Hz, as clearly seen in the insets of Figs. 8 and 9. The experimental results also revealed that the temperature coefficient of ε′ is less than ±15% (compared to the ε′ value at 20°C) over the temperature range −55°C to 85°C. Notably, CCTO ceramics prepared using a GNP have good dielectric properties and may be suitable for capacitor applications. Furthermore, their nonlinear electrical properties were improved, especially for the CCTO50-1h sample.

IV. Conclusion

Pure phase CCTO powder was successfully prepared at a relatively low temperature of 760°C and short reaction time for

4 h using a GNP. Fine-grained CCTO ceramics with few pores and small grain sizes were obtained by sintering the green body of compacted fine CCTO powders in air at temperatures of 1050°C–1080°C for 1 h. α of the fine-grained CCTO ceramic sintered at 1050°C for 1 h was extremely high of about 16.39. Furthermore, E_b was 1.46×10^4 V/cm, which is also high. For capacitor applications, all of the fine-grained $CaCu_3Ti_4O_{12}$ ceramics exhibited good dielectric properties. ε′ was higher than 2600 and tanδ ≈0.017 at 20°C and 1 kHz. Temperature stability of ε′ over the range −55°C to 85°C was <±15%. Very high ε′ (≈1.03×10^5) and low tanδ (≈0.054) were observed in the coarse-grained CCTO ceramics sintered at 1050°C for 3 h. This observation of a largely coarse-grained microstructure indicated a high grain growth rate over a narrow sintering time range.

Acknowledgments

This work was financially supported by the Higher Education Research Promotion and National Research University Project of Thailand, Office of the Higher Education Commission, through the Advanced Functional Materials Cluster of Khon Kaen University and the Thailand Research Fund (TRF) under the TRF Senior Research Scholar contract no. RTA5480004.

References

[1]M. A. Subramanian, D. Li, N. Duan, B. A. Reisner, and A. W. Sleight, "High Dielectric Constant in $ACu_3Ti_4O_{12}$ and $ACu_3Ti_3FeO_{12}$ Phases," *J. Solid State Chem.*, **151** [2] 323–5 (2000).

[2]A. J. Moulson and J. M. Herbert, *Electroceramics: Materials, Properties, Applications*, 2nd edition. Wiley, Chichester, 2003.

[3]S.-Y. Chung, I.-D. Kim, and S.-J. L. Kang, "Strong Nonlinear Current-Voltage Behaviour in Perovskite-Derivative Calcium Copper Titanate," *Nat. Mater.*, **3** [11] 774–8 (2004).

[4]D. R. Clarke, "Varistor Ceramics," *J. Am. Ceram. Soc.*, **82** [3] 485–502 (1999).

[5]T. B. Adams, D. C. Sinclair, and A. R. West, "Giant Barrier Layer Capacitance Effects in $CaCu_3Ti_4O_{12}$ Ceramics," *Adv. Mater.*, **14** [18] 1321–3 (2002).

[6]C. C. Homes, T. Vogt, S. M. Shapiro, S. Wakimoto, and A. P. Ramirez, "Optical Response of High-Dielectric-Constant Perovskite-Related Oxide," *Science*, **293** 673–6 (2001).

[7]L. Ni and X. M. Chen, "Enhancement of Giant Dielectric Response in $CaCu_3Ti_4O_{12}$ Ceramics by Zn Substitution," *J. Am. Ceram. Soc.*, **93** [1] 184–9 (2010).

[8]Y. Zhu, J. Zheng, L. Wu, A. Frenkel, J. Hanson, P. Northrup, and W. Ku, "Nanoscale Disorder in $CaCu_3Ti_4O_{12}$: A New Route to the Enhanced Dielectric Response," *Phys. Rev. Lett.*, **99** [3] 037602 (2007).

[9]W. C. Ribeiro, E. Joanni, R. Savu, and P. R. Bueno, "Nanoscale Effects and Polaronic Relaxation in Compounds," *Solid State Commun.*, **151** [2] 173–6 (2011).

[10]X. Sun, C. Wang, G. Wang, C. Lei, T. Li, L. Liu, and A. Feteira, "Low-Temperature Dielectric Relaxations Associated with Mixed-Valent Structure in $Na_{0.5}Bi_{0.5}Cu_3Ti_4O_{12}$," *J. Am. Ceram. Soc.*, **96** [5] 1497–503 (2013).

[11]M. A. de la Rubia, P. Leret, J. de Frutos, J. F. Fernández, and D. Damjanovic, "Effect of the Synthesis Route on the Microstructure and the Dielectric Behavior of $CaCu_3Ti_4O_{12}$ Ceramics," *J. Am. Ceram. Soc.*, **95** [6] 1866–70 (2012).

[12]L. Ni, X. M. Chen, X. Q. Liu, and R. Z. Hou, "Microstructure-Dependent Giant Dielectric Response in $CaCu_3Ti_4O_{12}$ Ceramics," *Solid State Commun.*, **139** [2] 45–50 (2006).

[13]T. B. Adams, D. C. Sinclair, and A. R. West, "Influence of Processing Conditions on the Electrical Properties of $CaCu_3Ti_4O_{12}$ Ceramics," *J. Am. Ceram. Soc.*, **89** [10] 3129–35 (2006).

[14]P. Thongbai, K. Meeporn, T. Yamwong, and S. Maensiri, "Extreme Effects of Na Doping on Microstructure, Giant Dielectric Response and Dielectric Relaxation Behavior in $CaCu_3Ti_4O_{12}$ Ceramics," *Mater. Lett.*, **106**, 129–32 (2013).

[15]J. Liu, Y. Sui, C.-G. Duan, W.-N. Mei, R. W. Smith, and J. R. Hardy, "$CaCu_3Ti_4O_{12}$: Low-Temperature Synthesis by Pyrolysis of an Organic Solution," *Chem. Mater.*, **18** [16] 3878–82 (2006).

[16]J. Liu, R. W. Smith, and W.-N. Mei, "Synthesis of the Giant Dielectric Constant Material $CaCu_3Ti_4O_{12}$ by Wet-Chemistry Methods," *Chem. Mater.*, **19** [24] 6020–4 (2007).

[17]P. Jha, P. Arora, and A. K. Ganguli, "Polymeric Citrate Precursor Route to the Synthesis of the High Dielectric Constant Oxide, $CaCu_3Ti_4O_{12}$," *Mater. Lett.*, **57** [16-17] 2443–6 (2003).

[18]S. Jin, H. Xia, Y. Zhang, J. Guo, and J. Xu, "Synthesis of $CaCu_3Ti_4O_{12}$ Ceramic via a Sol-Gel Method," *Mater. Lett.*, **61** [6] 1404–7 (2007).

[19]L. Liu, H. Fan, P. Fang, and L. Jin, "Electrical Heterogeneity in $CaCu_3Ti_4O_{12}$ Ceramics Fabricated by Sol-Gel Method," *Solid State Commun.*, **142** [10] 573–6 (2007).

[20]L. Liu, H. Fan, P. Fang, and X. Chen, "Sol-Gel Derived $CaCu_3Ti_4O_{12}$ Ceramics: Synthesis, Characterization and Electrical Properties," *Mater. Res. Bull.*, **43** [7] 1800–7 (2008).

[21]D.-L. Sun, A.-Y. Wu, and S.-T. Yin, "Structure, Properties, and Impedance Spectroscopy of $CaCu_3Ti_4O_{12}$ Ceramics Prepared by Sol-Gel Process," *J. Am. Ceram. Soc.*, **91** [1] 169–73 (2008).

[22]B. Zhu, Z. Wang, Y. Zhang, Z. Yu, J. Shi, and R. Xiong, "Low Temperature Fabrication of the Giant Dielectric Material $CaCu_3Ti_4O_{12}$ by Oxalate Co-precipitation Method," *Mater. Chem. Phys.*, **113** [2-3] 746–8 (2009).

[23]Z. Li and H. Fan, "Structure and Electric Properties of Sol-Gel Derived $CaCu_3Ti_4O_{12}$ Ceramics as a Pyroelectric Sensor," *Solid State Ionics*, **192** [1] 682–7 (2011).

[24]J. Zhao, J. Liu, and G. Ma, "Preparation, Characterization and Dielectric Properties of $CaCu_3Ti_4O_{12}$ Ceramics," *Ceram. Int.*, **38** [2] 1221–5 (2012).

[25]Y. He, T. Liu, Y. Xu, J. Zhao, and Z. Du, "Synthesis of the Giant Dielectric Constant Oxide $CaCu_3Ti_4O_{12}$ via Ethylenediaminetetraacetic Acid Precursor," *Mater. Res. Bull.*, **47** [5] 1181–4 (2012).

[26]D. Xu, C. Zhang, Y. Lin, L. Jiao, H. Yuan, G. Zhao, and X. Cheng, "Influence of Zinc on Electrical and Microstructural Properties of $CaCu_3Ti_4O_{12}$ Ceramics Prepared by Sol-Gel Process," *J. Alloys Compd*, **522**, 157–61 (2012).

[27]Y. Zhao, R. Gao, G. Su, H. Lin, C. Wang, and C. Cheng, "Effect of Dispersant on $CaCu_3Ti_4O_{12}$ Powders Synthesized by Oxalate Co-Precipitation Method," *Mater. Lett.*, **91**, 187–90 (2013).

[28]S. Mukherjee, M. R. Gonal, M. K. Patel, M. Roy, A. Patra, A. K. Tyagi, and M. Menon, "Microstructure Characterization and Electrical Conductivity Measurement of $La_{1-x}Ca_xCrO_3$ (x = 0.25, 0.4, 0.5) Prepared by Aspartic Acid-Assisted Solution Combustion," *J. Am. Ceram. Soc.*, **95** [1] 290–5 (2012).

[29]L. A. Chick, L. R. Pederson, G. D. Maupin, J. L. Bates, L. E. Thomas, and G. J. Exarhos, "Glycine-Nitrate Combustion Synthesis of Oxide Ceramic Powders," *Mater. Lett.*, **10** [1-2] 6–12 (1990).

[30]E. Thomas, D. H. Lee, M. Y. Yoon, S. H. Ehrman, and H. J. Hwang, "Synthesis and Sintering Behavior of $La_{0.8}Sr_{0.2}CrO_3$ by a Glycine Nitrate Process," *Ceram. Int.*, **37** [7] 2269–74 (2011).

[31]B. Liu and Y. Zhang, "$Ba_{0.5}Sr_{0.5}Co_{0.8}Fe_{0.2}O_3$ Nanopowders Prepared by Glycine-Nitrate Process for Solid Oxide Fuel Cell Cathode," *J. Alloys Compd.*, **453** [1-2] 418–22 (2008).

[32]M. N. Rahaman, *Ceramic Processing and Sintering*, 2nd edition. M. Dekker, New York, 2003.

[33]W. Yuan, "Investigation on the Decomposable Process and the Secondary Liquid Phase Effect on the Dielectric Properties of $CaCu_3Ti_4O_{12}$ Ceramics," *J. Phys. D: Appl. Phys.*, **42** [17] 175401 (2009).

[34]T. Adams, D. Sinclair, and A. West, "Characterization of Grain Boundary Impedances in Fine- and Coarse-Grained $CaCu_3Ti_4O_{12}$ Ceramics," *Phys. Rev. B*, **73** [9] 094124 (2006).

[35]W. C. Ribeiro, R. G. C. Araújo, and P. R. Bueno, "The Dielectric Suppress and the Control of Semiconductor Non-Ohmic Feature of $CaCu_3Ti_4O_{12}$ by Means of Tin Doping," *Appl. Phys. Lett.*, **98** [13] 132906 (2011).

[36]P. Thongbai, J. Boonlakhorn, B. Putasaeng, T. Yamwong, and S. Maensiri, "Extremely Enhanced Nonlinear Current-Voltage Properties of Tb-Doped $CaCu_3Ti_4O_{12}$Ceramics," *J. Am. Ceram. Soc.*, **96** [2] 379–81 (2013).

[37]P. R. Bueno, E. R. Leite, M. M. Oliveira, M. O. Orlandi, and E. Longo, "Role of Oxygen at the Grain Boundary of Metal Oxide Varistors: A Potential Barrier Formation Mechanism," *Appl. Phys. Lett.*, **79** [1] 48 (2001).

[38]V. P. B. Marques, P. R. Bueno, A. Z. Simões, M. Cilense, J. A. Varela, E. Longo, and E. R. Leite, "Nature of Potential Barrier in $(Ca_{1/4},Cu_{3/4})TiO_3$ Polycrystalline Perovskite," *Solid State Commun.*, **138** [1] 1–4 (2006).

[39]R. Yu, H. Xue, Z. Cao, L. Chen, and Z. Xiong, "Effect of Oxygen Sintering Atmosphere on the Electrical Behavior of CCTO Ceramics," *J. Eur. Ceram. Soc.*, **32** [6] 1245–9 (2012).

[40]P. Thongbai, B. Putasaeng, T. Yamwong, and S. Maensiri, "Improved Dielectric and Non-Ohmic Properties of $Ca_2Cu_2Ti_4O_{12}$ Ceramics Prepared by a Polymer Pyrolysis Method," *J. Alloys Compd*, **509** [27] 7416–20 (2011). □

Advanced Powder Technology 25 (2014) 1087–1093

Contents lists available at ScienceDirect

Advanced Powder Technology

journal homepage: www.elsevier.com/locate/apt

Original Research Paper

Strength and resistance to sulfate and sulfuric acid of ground fluidized bed combustion fly ash–silica fume alkali-activated composite

Prinya Chindaprasirt [a], Pattanapong Paisitsrisawat [b], Ubolluk Rattanasak [b,*]

[a] Sustainable Infrastructure Research and Development Center, Department of Civil Engineering, Faculty of Engineering, Khon Kaen University, Khon Kaen 40002, Thailand
[b] Department of Chemistry and Center of Excellence for Innovation in Chemistry, Faculty of Science, Burapha University, Chonburi 20131, Thailand

ARTICLE INFO

Article history:
Received 13 November 2013
Received in revised form 20 January 2014
Accepted 11 February 2014
Available online 22 February 2014

Keywords:
Alkali-activated composite
Geopolymer
Fluidized bed coal combustion
Silica fume

ABSTRACT

Fluidized bed combustion (FBC) is an environmentally friendly process for burning of coal and is used in many small factories located in urban area. The FBC fly ash is an environmental problem and needs good disposal or utilization. This research studied the strength and resistance to sulfate and acid of alkali-activated FBC fly ash–silica fume composite. The FBC fly ash was interground with silica fume (at the dosage levels of 1.5%, 3.75% and 5.0%) to make the source material homogenous with increased reactivity. Addition of silica fume enabled the adjustment of SiO_2/Al_2O_3 ratios (6.55-7.54) of composite and improved the strength and resistance to sulfate and acid of composite. The composite with 3.75% silica fume showed the optimum strength with 28-day compressive strength of 17.0 MPa. The compressive strengths of composite with 3.75% silica fume immersed in 5% magnesium sulfate solution and 3% sulfuric acid solutions were substantially higher than the control. The strength loss was from the high calcium content of FBC fly ash and incorporation of silica fume thus increased the durability of the composite.

1. Introduction

Fluidized bed combustion (FBC) is a promising environmentally-friendly coal combustion process with operating temperature of 800–900 °C comparing with pulverized coal combustion. The low temperature prohibits the nitrogen oxides (NOx) emission [1]. The amount of FBC fly ash has, therefore, increased significantly over the past few years owing to the rapid growth of FBC technology [1]. The fly ash has low glassy phase material and possesses very low pozzolanic property. Improvement on its reactivity can be obtained from an intense grinding to reduce the particle size [2]. In addition, it contains high amount of calcium compounds (CaO and $CaSO_4$) from the use of lime powder to capture SO_2. The use of FBC fly ash as a pozzolan to partially replace Portland cement is therefore not recommended [3].

Researches have focused on the utilization of fly ash as a source material in alkali-activated composite or "geopolymer" [4,5]. This composite is alumino-silicate compound and can be produced from the alumino-silicate source materials (e.g. fly ash or metakaolin) in alkaline solutions e.g. sodium hydroxide and sodium silicate solutions [6–8]. Heat curing (60–90 °C) is usually applied to accelerate the reaction. The aluminosilicate product with high early strength and stability up to temperature of 1400 °C could be obtained [9].

In addition, fly ash geopolymer is resistant to acid and sulfate solutions compared with OPC materials. Immersion of geopolymer in these solutions has small impact on the strength of material because of the nature of aluminosilicate gel in geopolymer [7,8]. The stability of materials depends on the type of activator and type of cation in the sulfate media [8]. For magnesium sulfate immersion, gypsum, $Mg(OH)_2$, SiO_2, and magnesium silicate hydrate can be formed. This caused the deterioration of materials and reflected in compressive strength loss [7].

Researchers have investigated the use of FBC fly ash as an alternative source material for preparation of alkali-activated composite [2,10,11]. However, as-received FBC fly ash provided both low strength and acid resistance owing to high calcium content in composite [2,10].

Due to high content of calcium compounds in FBC fly ash, additional pozzolanic reaction is possible in geopolymer which will lead to the formation of calcium silicate hydrate (C–S–H). Silica fume is a micro sphere of non-crystalline silica with very high surface area. It contains more than 78% SiO_2 in glassy form and is suitable for use as cement additive [12] with a large filler effect in concrete. In concrete application, the use of silica fume improves the strength and other physical properties of concrete [13,14]. It

* Corresponding author. Tel.: +66 38 103066; fax: +66 38 393494.
E-mail address: ubolluk@buu.ac.th (U. Rattanasak).

http://dx.doi.org/10.1016/j.apt.2014.02.007

has also been shown that silica fume can also be used to prepare sodium silicate for geopolymer synthesis using sol–gel condensation reaction [15].

The use of silica fume as a silica source to enhance the properties of alkali-activated FBC fly ash composite is, therefore, promising. High calcium fly ash reacts and forms C–S–H and other calcium compounds e.g. $Ca(OH)_2$ in the presence of alkali solution [2,9]. This research has proposed that active silica fume should react with these calcium compounds (from FBC fly ash and products) forming the C–S–H in composite and contributing to the strength gain and good physical properties of alkali-activated composite. Owing to low reactivity and high pore volume of FBC fly ash, grinding of FBC fly ash was recommended to remove the void, refine the pore structure and increase surface area before using as source material for geopolymer preparation [2]. Therefore, grinding of the source materials was performed in this research.

2. Experimental procedure

2.1. Materials

The FBC-fly ash and silica fume were used as source materials for the synthesis of alkali-activated composite. This FBC fly ash mainly consisted of silica (SiO_2), alumina (Al_2O_3), lime (CaO) and sulfur trioxide (SO_3) determined by X-ray fluorescence (XRF) as tabulated in Table 1. High CaO content of 38.7 wt% was found in FBC fly ash owing to the addition of lime for sulfur absorption. SEM image of FBC fly ash showed that the particle shapes were irregular (Fig. 1) with the median particle size (D_{50}) of 24 μm. FBC fly ash contains low glassy material due to the low burning temperature. Three dosages of silica fume addition of 1.5%, 3.75% and 5% by weight were selected to intergrind with FBC fly ash. Intergrinding of materials helped to obtain the homogeneous blended powder. The blend was ground in a laboratory ball mill for 2 h as a longer milling time only marginally increased the fineness of the blend. The homogeneous blends with a median particle size (D_{50}) of 5–7 μm measured by particle size analyzer (Malvern Mastersizer S), which retention on sieve No. 325 (45 μm opening) of 3.5–4.0 wt% were obtained. XRD patterns of raw materials are presented in Fig. 2. Quantitative XRD analysis of source materials was performed to obtain the amorphous content by using α-Al_2O_3 (corundum) as an internal standard. It was found that the amorphous contents of FBC fly ash and silica fume were 37% and 97% respectively. Therefore, incorporation of silica fume into FBC fly ash resulted in more glassy phases of the blend as the broad peak was detected in the XRD curve.

In addition to the source materials, 15 M sodium hydroxide (15 M NaOH) and commercial grade sodium silicate solution (Na_2SiO_3) with 9 wt% Na_2O and 30 wt% SiO_2 were used as an alkaline activator. For mortar preparation, the river sand with specific gravity of 2.65 and fineness modulus of 2.8 was employed. The compressive strength of mortars was tested in accordance with ASTM C109 at the ages of 7, 28 and 90 days. The results were reported as the average of five samples.

Table 1
Chemical composition and FBC fly ash and silica fume.

Chemical composition	FBC fly ash (wt%)	Silica fume (wt%)
SiO_2	21.2	98.2
Al_2O_3	10.7	–
CaO	38.7	–
Fe_2O_3	7.0	–
SO_3	14.9	–
Na_2O	2.5	0.5
K_2O	0.9	0.6
TiO_2	1.1	–
MgO	1.9	0.7
P_2O_5	0.1	–
Loss on ignition (LOI)	1.0	–

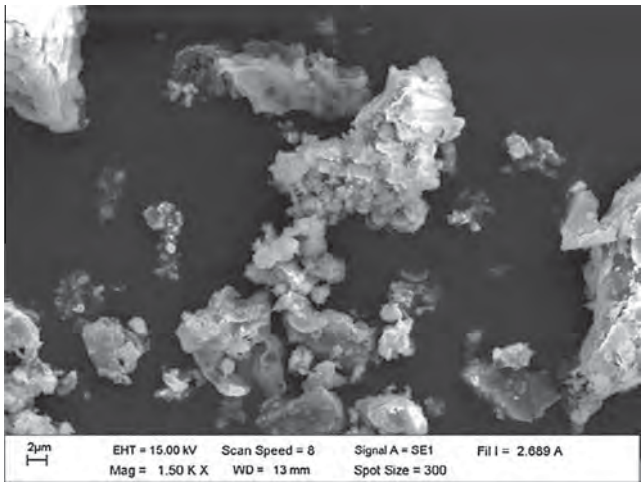

Fig. 1. Microstructure of FBC fly ash.

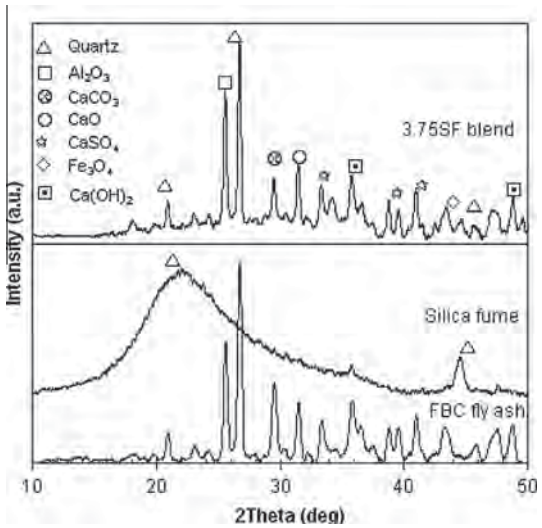

Fig. 2. XRD patterns of source materials.

2.2. Composite preparation

From a preliminary study, there was no ettringite formation in FBC geopolymer with NaOH concentration higher than 15 M [16]. The high NaOH concentration converted gypsum in the FBC fly ash system to calcium hydroxide ($Ca(OH)_2$) and aqueous sodium salt as shown in Eq. (1) and hindered the ettringite formation [17]. $Ca(OH)_2$, then, reacted with SiO_2 and resulted in C–S–H in the composite matrix.

$$CaSO_4 \cdot 2H_2O\ (s) + NaOH\ (aq) \rightarrow 4Ca(OH)_2\ (s) + Na_2SO_4\ (aq) \quad (1)$$

The Na_2SiO_3-to-NaOH mass ratio of 2 was used for the study as the higher ratio resulted in low strength composite as a result of excess silica gel and zeolite formation [18]. The blended powder-to-liquid mass ratio of 1.0 was employed. 15 M NaOH was thoroughly mixed with blended source material and Na_2SiO_3 was subsequently added to the mixture. The mix proportion is

tabulated in Table 2. The paste mixture was continuously mixed in a pan mixer for 2 min and was cast in the 5-cm cubic acrylic moulds. The casting was done in two layers with tamping in accordance with ASTM C109 with final compaction using a vibrating table for 10 s to remove the air bubbles. The specimens were then covered with clingfilm and cured at 65 °C for 24 h. After heat curing, the specimens were continuously cured in a 25 °C chamber (80% relative humidity) until the age of testing.

For the composite mortar, sand-to-blended powder mass ratio of 2 was employed. After mixing the paste, sand was added to the mixture and mixing was continued for another 2 min. The casting and curing conditions were the same as those of the paste preparation.

2.3. Sulfate and acid resistances

Composite mortars were tested for the durability in term of the strength loss after 3-month immersion in the 5 wt% $MgSO_4$ and 3 vol% H_2SO_4 compared with the room temperature (25 °C) cured mortars. One layer of specimens with 1-cm space were used for the storage of specimens in a plastic basket and immersed in closed 10-liter container which was filled with solution. Immersion was performed until the test date. The solutions were replaced every week for the first month and monthly thereafter.

2.4. Composite testing

Composite pastes were ground and used for the X-ray diffraction (XRD), and thermogravimetry (TGA) analyses. The amount of $Ca(OH)_2$ was calculated directly from TGA curves at its decomposition temperature of 400–450 °C using Eq. (2) [19].

$$\%Ca(OH)_2 = \%\text{weight loss}_{Ca(OH)_2} \cdot \frac{MW_{Ca(OH)_2}}{MW_{water}} \quad (2)$$

where $MW_{Ca(OH)_2}$ and MW_{water} are molecular weight of $Ca(OH)_2$ and water, respectively. For the scanning electron microscopy (SEM) analysis and pore size distribution/surface area determination with BET method, small pieces of pastes were employed. The condition for pore size distribution/surface area determination was as following; nitrogen gas was used as adsorbate with the out gas temperature of 120 °C. The samples were subjected to 99-point adsorption–desorption (BJH Theory) isotherms.

3. Results and discussion

3.1. Morphology of composites

The results of the XRD patterns of composites are shown in Fig. 3. Numerous sharp peaks of crystalline phases were presented in the control and blended FBC fly ash and silica fume composite. However, the heights of sharp peaks decreased in the blend composites compared with those of the control owing to the addition of a highly reactive silica fume. The broad hump around 30° 2θ for the composite pastes indicated the converted amorphous phases of the composite and the geopolymerization reaction

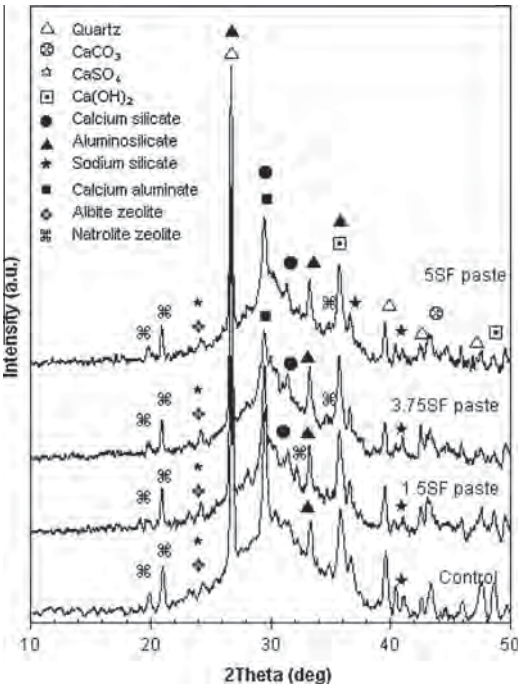

Fig. 3. XRD pattern of control and blend composite.

[20–22]. This led to the highly disorder material in the form of amorphous phases and some crystalline products. The main products consisted of the aluminosilicate and calcium silicate compounds. Due to the use of high concentration sodium hydroxide (15 M NaOH), sodium silicate, calcium aluminate and zeolites (i.e. albite and natrolite) were also formed.

Addition of silica fume (SiO_2) in composite mixture led to the formation of the calcium silicate ($3CaO{\cdot}2SiO_2{\cdot}3H_2O$, C–S–H) as shown in Eqs. (3) and (4) [23].

$$CaO\ (s) + H_2O\ (l) \rightarrow Ca(OH)_2\ (aq) \quad (3)$$

$$3Ca(OH)_2\ (aq) + 2SiO_2\ (s) \rightarrow 3CaO \cdot 2SiO_2 \cdot 3H_2O\ (s) \quad (4)$$

Aluminosilicate and calcium silicate were important products in the composite and contributed to the good physical properties of the composite matrix. However, the increase in silica fume content in the mixture could lead to a high SiO_2/Al_2O_3 ratio and resulted in the composite with lower strength [24].

3.2. Compressive strengths of composites

The results of compressive strengths of blend composite mortars are shown in Fig. 4. The compressive strength of control mortar was comparatively low at all ages. The compressive strengths at the ages of 7, 28 and 90 days were 10.5, 10.8 and 12.0 MPa, respectively. The increase in strength with curing age was low due to the low reactive of FBC fly ash. On the one hand,

Table 2
Mix proportion of composite.

Samples	Blend (g)		15 M NaOH (g)	Na_2SiO_3 (g)	Molar ratio	
	FBC fly ash	Silica fume			SiO_2/Na_2O	SiO_2/Al_2O_3
Control	100	0	33	67	0.39	6.55
1.5SF	98.5	1.5	33	67	0.38	6.83
3.75SF	96.25	3.75	33	67	0.36	7.28
5.0SF	95.0	5.0	33	67	0.35	7.54

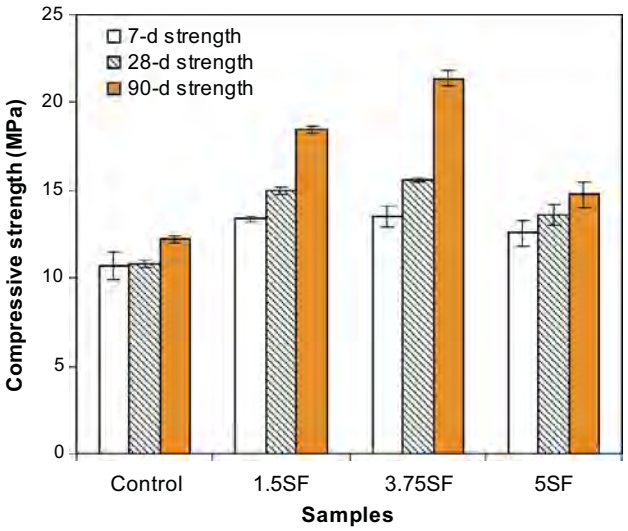

Fig. 4. Compressive strengths of composite mortars at 7, 28 and 90 days.

the increase in strength with curing age could be noticed with the blend composite mortars. The strengths at the age of 7, 28 and 90 days of 3.75SF mortar were 13.0, 15.5 and 22.0 MPa, respectively. The strength at 90 days of 3.75SF mortar was almost double that of the control. In addition to aluminosilicate compound, silica fume in FBC geopolymer matrix reacted with calcium hydroxide and formed calcium silicate hydrate (C–S–H) as confirmed by the XRD results. For the system with substantial amount of calcium, C–S–H was formed and co-existed with the geopolymer products and the strength of composite developed with curing age [25,26]. The strength at 90 days of 1.5SF mortar was also significantly improved to 18.0 MPa.

For the use of 5% silica fume (5SF sample), the compressive strength also developed with curing age due to the pozzolanic reaction. However, gradual improvement in strength was obtained in this case. This was the result of sodium silicate and zeolites (i.e. albite and natrolite) formation which was detected on the XRD pattern. The presence of crystallized zeolite resulted in the composite with lower strength [18]. The excess silica fume acted as the filler in composite matrix. The increase in the silica resulted in a high SiO_2/Al_2O_3 ratio of composite mix with low strength [24].

3.3. Microstructural study

Fig. 5 showed the microstructure of the control and 3.75SF mortar specimens. In addition to the composite matrix and other compounds, the unreacted fly ash particles were found. Reaction occurred at the surfaces of fly ash and silica fume and resulted in the binding property of the geopolymer. The control paste contained a relatively loose matrix and several microcracks since FBC fly ash had low reactivity and high content of calcium compounds. This caused the low strength of geopolymer mortar. Owing to the high reactivity of silica fume and intergrinding of FBC fly ash, dense matrix was formed in the 3.75SF geopolymer paste. High NaOH concentration of 15 M helped the leaching of Si^{4+} and Al^{3+} ions from fly ash surface and the subsequent geopolymerization [27]. The dissolution of calcium sulfate was also enhanced and this led to calcium hydroxide formation as previously presented in Eq. (1). Subsequently, the pozzolanic reaction between calcium hydroxide and silica fume formed more C–S–H in the matrix as shown in Eq. (4) and this enhanced the strength development of the geopolymers.

3.4. Thermal property of composites

Physical changes in materials were presented by thermogravimetric analysis (TGA) and differential thermogravimetry (DTG) as shown in Fig. 6. TGA/DTG was use to determine a thermal stability of geopolymer and its fraction of volatile components by monitoring the weight change during heating of specimen. FBC fly ash showed the weight loss at approximately 100, 400 and 700 °C due to the evaporation of water (from sodium hydroxide and sodium silicate solution), and decompositions of portlandite ($Ca(OH)_2$) and calcium carbonate ($CaCO_3$) into CaO and CO_2, respectively [28] (Fig. 6a). At 600 °C, increase in weight was found on the TGA curve due to the carbon oxidation (carbonation). This led to an upward swing of the TGA curve prior to the bulk of the weight loss, which made the definition of onset temperature (T_{onset}) even more difficult and ambiguous [29].

The DTG curves of the composite pastes were similar and they are shown as one overlapped curve in Fig. 6b. The control FBC composite showed the highest weight loss among the composite pastes. The loss was greatest between 50 and 150 °C indicating the loss of water. The blended composite pastes gave lower weight loss compared with that of the control FBC composite at the same temperature. With low range heating temperature of 200–500 °C, weight of blend geopolymer paste was approximately 5% higher than the control. The addition of silica fume resulted in the additional C–S–H. The water molecules were consumed and the calcium silicate became the integral part of the C–S–H gel [23]. Thermal resistant product was obtained as indicated by low weight loss compared with that of the control. This was due to more binding materials (i.e. aluminosilicate and calcium silicate compounds) and calcium silicate hydrate formed in matrix. Weight loss of the blend samples slightly reduced with the increase in the silica fume content. The remained weight of the control and 1.5SF pastes were 66.5% and 68.0% respectively and were similar to those of OPC pastes with W/C ratio of 0.30–0.33 conformed with other findings

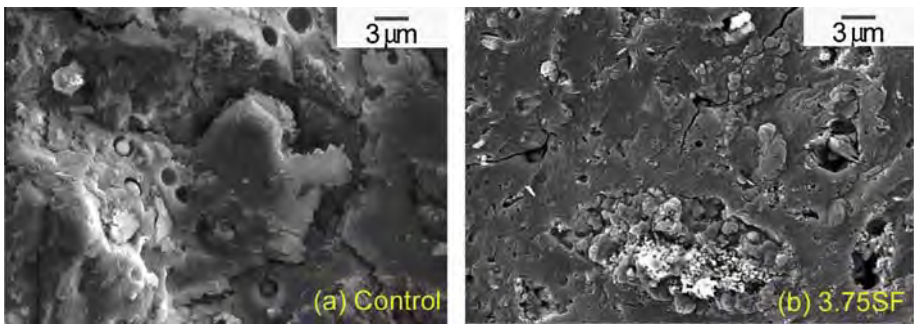

Fig. 5. SEM micrographs of composite pastes at the age of 28 days.

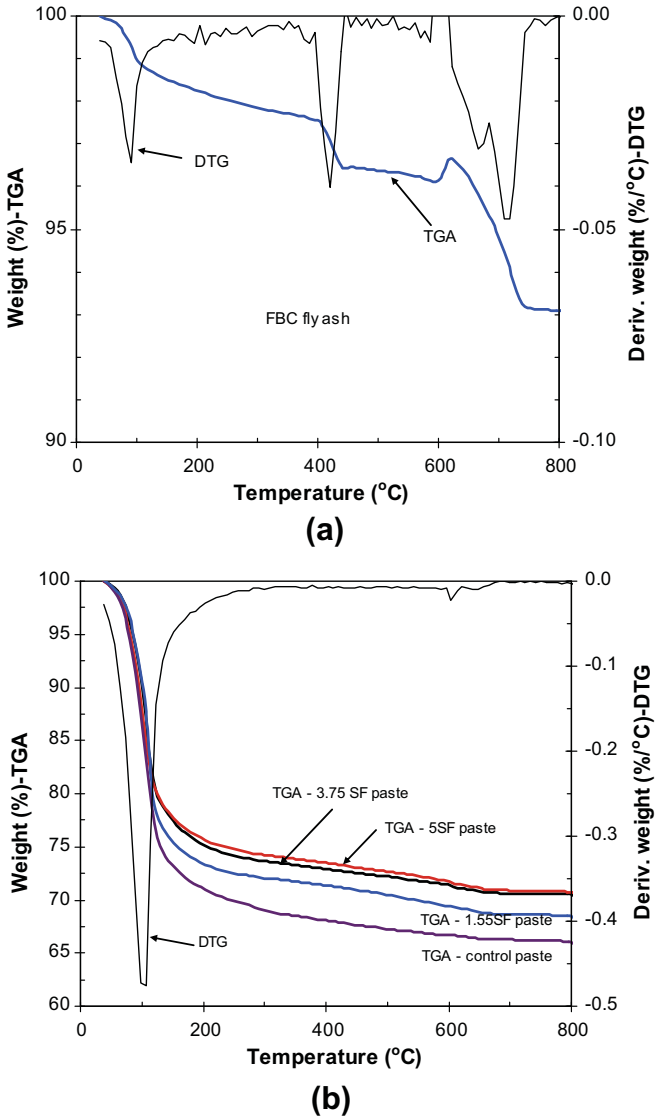

Fig. 6. TGA/DTG curves of FBC fly ash and composite pastes.

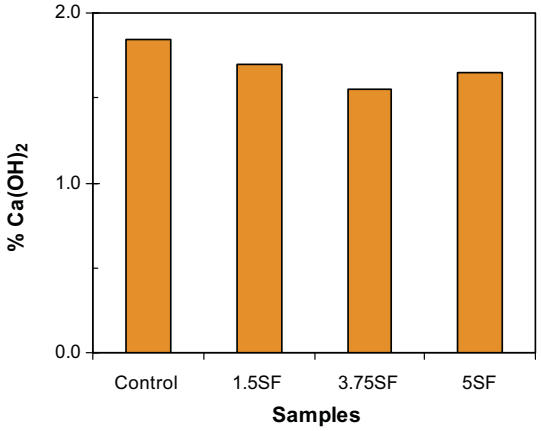

Fig. 7. $Ca(OH)_2$ content of composite pastes.

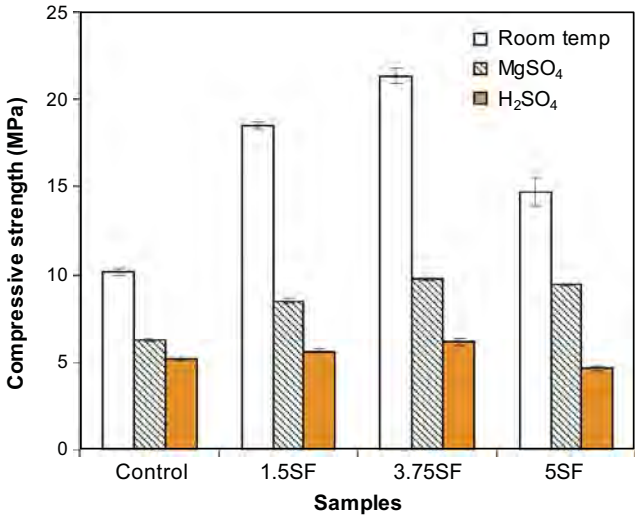

Fig. 8. Compressive strengths of composite under $MgSO_4$ and H_2SO_4 attack.

[30,31]. The increases in silica fume to 3.75% and 5% by weight of FBC fly ash achieved the lower weight loss.

For the derivative thermogram (DTG) profile of geopolymers, a peak corresponding to maximum weight loss at around 100 °C was observed resulting from evaporation of bound water. A small peak was also found at 400 °C indicating the decomposition of $Ca(OH)_2$ formed as a result of reaction between an alkaline solution and calcium from FBC fly ash. Amounts of $Ca(OH)_2$ are presented in Fig. 7. It was found that the $Ca(OH)_2$ contents reduced with the addition of silica fume indicating its conversion to calcium silicate hydrate.

In addition, low decompositions at 400 and 700 °C were found which was due to the conversion of calcium compounds in high calcium FBC fly ash to the thermal stable products in presence of alkali solutions. The reduced $Ca(OH)_2$ and the associated formation of additional C–S–H supported the results of the compressive strength.

3.5. Durability of composites

The results of the durability test of composite mortars in term of the strength loss after 3-month immersion in 5 wt% $MgSO_4$ and 3 vol% H_2SO_4 are shown in Fig. 8. The strength of composite significantly decreased after immersion in both 5 wt% $MgSO_4$ and 3 vol% H_2SO_4 solutions. The high calcium content of FBC fly ash was possibly the cause of this strength loss. For immersion in 5 wt% $MgSO_4$, the strength of control and blend composite mortars reduced to 6 MPa and 10 MPa, respectively. The sample surfaces were deposited with white substance of magnesium hydroxide ($Mg(OH)_2$), silica (SiO_2), magnesium silicate and calcium magnesium silicate compounds [7,32]. Mg^{2+} ion reacted with hydroxyl ion (OH^-) from $Ca(OH)_2$ and NaOH in geopolymer matrix yielded the insoluble $Mg(OH)_2$ leading to the deposition on material surface. In addition, C–S–H phase was attacked and decomposed in the present of $MgSO_4$ resulting in low stability C–S–H and strength loss [32,33]. It was also reported that the hydrated magnesium silicate had no binding capacity which adversely affected the physical property of composite [33].

For immersion in H_2SO_4, higher strength losses were detected compared with the immersion in $MgSO_4$ solution due to the attack of calcium compound with strong acid solution. High calcium fly ash is very susceptible under acid condition. This adversely affected the leaching of calcium and resulted in physical and chemical damages.

The remaining strengths of blend geopolymer mortars were not still significantly higher than that of the control. The strength of 3.75SF blended was only slightly higher than the others. For instant, the compressive strengths of mortars with 0, 1.5%, 3.75%

Table 3
BET results of composite pastes.

Samples	Specific pore area (m^2/g)	Pore volume (cm^3/g)
Control	39.2	0.118
1.5SF	40.1	0.130
3.75SF	52.9	0.167
5SF	72.2	0.217

and 5% SF after 90 days immersion in magnesium sulfate were 6.5, 8.5, 9.5 and 9.0 MPa respectively, whereas those immersed in sulfuric acid were 5.5, 6.0, 6.5 and 4.5 MPa, respectively. In the acid environment, in addition to calcium compound dissolution, C–S–H reacted with H_2SO_4 and formed $CaSO_4$ and amorphous silica gel [33,34]. It was also reported that H^+ (from H_2SO_4 ionization) could destroy the alumino-silicate network in geopolymer and yielded silicic acid ($Si(OH)_4$) and aluminum ions (Al^{3+}) [32,34]. The breaking of oxy-aluminum bridge caused the deterioration of geopolymer in acid condition. With high silica fume content of 5%, the remaining strength of immersed mortar was lower than that of the control. The high strength loss was due to the low initial strength of mortar and the favorable dissolution of excess silica in acid solution.

3.6. BET pore areas and pore volumes of composites

The BET pore areas and pore volumes of composite pastes at the age of 30 days were measured by N_2 adsorption and are given in Table 3. Both pore area and volume increased with the increase in the silica fume content. The pore distributions of composite pastes are presented in Fig. 9. The pores mainly distributed between 200 and 30 nm which corresponded to the gel pores. The addition of silica fume increased the average pore of the samples due mainly to the increase in the C–S–H gel. The main peak of the pore of the control was around 7 nm and those of the pastes containing silica fume were approximately 9 nm. The increase in the C–S–H was mainly responsible for the strength improvement of the sample with addition of up to 3.75% silica fume. Addition of silica fume could refine the pore size resulting in higher amount of small pore than that of the control. This also contributed to the higher cumulative pore volume.

At high silica fume content of 5%, the strength dropped as the silica content was too high and the composite gel consisted of high free SiO_2 resulting in a paste with low strength and also high pore area and volume. The presence of silica fume in composites divided the large pores into smaller pores [23]. It also acted as filler due to its fineness and filled into spaces between fly ash grains. This improvement in pore structure was reflected in the higher strength. Pore diameter in the range of 10–50 nm mainly affected the strength of the material while the smaller pore diameter affected the shrinkage [35]. The refinement of pore structure led to a reduction in the diffusion of harmful ions, a reduction in calcium hydroxide content and a conversion of lime in high calcium fly ah through pozzolanic reaction. This behavior resulted in a high resistance to sulfate attack which also indicated by the durability results. However, magnesium sulfates had a more damaging effect than sodium sulfates [36].

4. Conclusions

The interground FBC fly ash and silica fume can be used as a source material for making alkali-activated composites. The

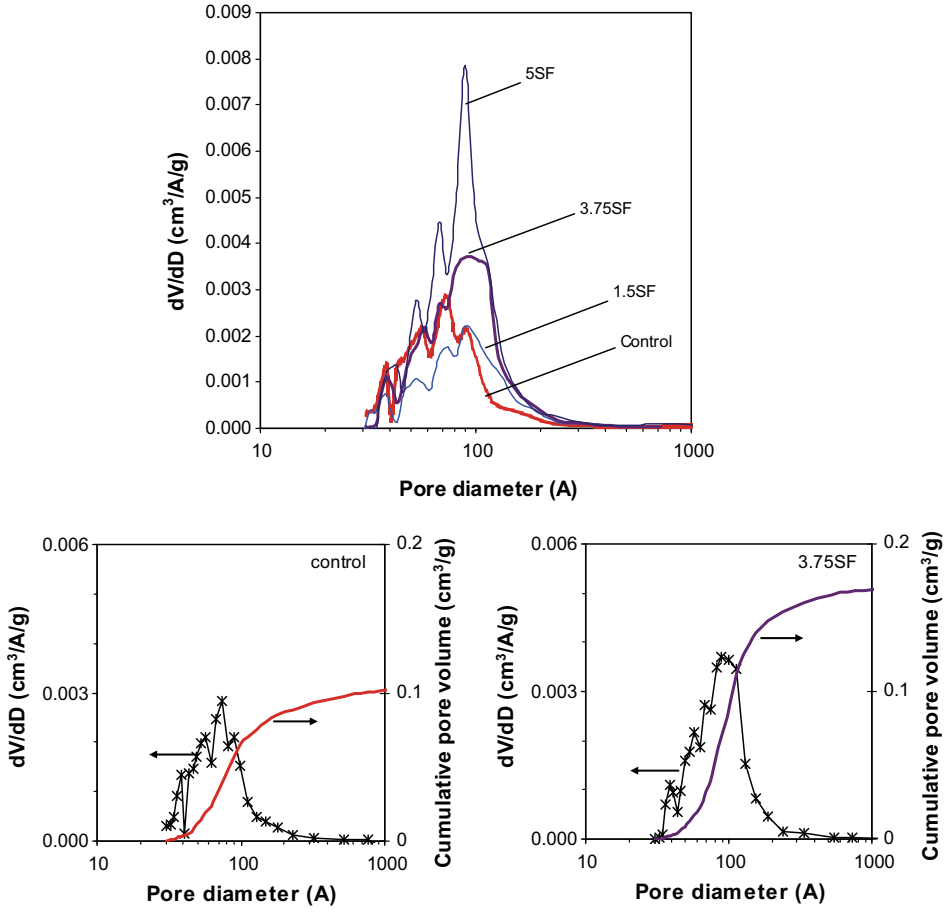

Fig. 9. Pore size distribution of composite pastes.

grinding improved the reactivity of FBC fly ash and the presence of reactive silica fume also helped to increase the reactivity of the system. Silica fume reacted to form aluminosilicate and additional calcium silicate compounds in the composite matrix. These compounds enhanced the physical properties of composite. However, high content of silica fume in geopolymer mixture increased the SiO_2/Al_2O_3 ratio beyond the optimum and adversely affected the strength of composite. The optimum silica fume content was 3.75% for both strength and durability of the composites. Incorporation of silica fume also increased the resistance to magnesium sulfate and sulfuric acid attack of the composite. This is due to the increase in the C–S–H which resulted in the increased strength and reduction of calcium as a result of C–S–H formation. Higher SiO_2/Al_2O_3 ratio resulted in a low strength composite as a result of excess silica gel and zeolite formation. Addition of silica fume resulted in thermal resistant product with low weight loss as calcium hydroxide was converted to calcium silicate compound which was more stable at high temperature up to 800 °C.

Acknowledgements

This work was supported by the Higher Education Research Promotion and National Research University Project of Thailand, Office of the Higher Education Commission, through the Advanced Functional Materials Cluster of Khon Kaen University and the Thailand Research Fund (TRF) under TRF Senior Research Scholar contract no. RTA5480004. Appreciation is also extended to the Center of Excellence for Innovation in Chemistry (PERCH-CIC), Office of the Higher Education Commission, Ministry of Education.

References

[1] F. Botha, Overview of the fluidized bed combustion process and material, in: Proceedings of State Regulation of Coal Combustion By-Product Placement at Mine Sites: A Technical Interactive Forum, Pennsylvania, 2004, pp. 1–4.
[2] P. Chindaprasirt, U. Rattanasak, C. Jaturapitakkul, Utilization of fly ash blends from pulverized coal and fluidized bed combustions in geopolymeric materials, Cement Concr. Compos. 33 (2011) 55–60.
[3] T. Robl, A. Oberlink, J. Brien, J. Pagnotti, The utilization potential of anthracite CFBC spent bed fly ash as a concrete additive, in: Proc. 2011 World of Coal Ash (WOCA) Conference, Denver, CO, United States, 2011.
[4] J. Davidovit, Geopolymer: inorganic polymeric new materials, J. Therm. Anal. 37 (1991) 1633–1656.
[5] H. Xu, J.S.L. van Deventer, The geopolymerisation of alumino-silicate minerals, Int. J. Miner. Process. 59 (2000) 247–266.
[6] J.L. Provis, P. Duxson, J.S.J. van Deventer, The role of particle technology in developing sustainable construction material, Adv. Power Technol. 21 (2010) 2–7.
[7] P. Chindaprasirt, U. Rattanasak, S. Taebuanhuad, Resistance to acid and sulfate solutions of microwave-assisted high calcium fly ash geopolymer, Mater. Struct. 46 (2013) 375–381.
[8] T. Bakharev, Durability of geopolymer materials in sodium and magnesium sulfate solutions, Cem. Concr. Res. 35 (2005) 1233–1246.
[9] M. Hussain, R.J. Varley, Y.B. Cheng, Z. Mathys, G.P. Simon, Synthesis and thermal behavior of inorganic-organic hybrid geopolymer composites, J. Appl. Polym. Sci. 96 (2005) 112–121.
[10] P. Chindaprasirt, U. Rattanasak, Utilization of blended fluidized bed combustion (FBC) ash and pulverized coal combustion (PCC) fly ash in geopolymer, Waste Manage. (Oxford) 30 (2010) 667–672.
[11] H. Xu, H. Li, L. Shen, M. Zhang, J. Zhai, Low-reactive circulating fluidized bed combustion (CFBC) fly ashes as source material for geopolymer synthesis, Waste Manage. (Oxford) 30 (2010) 57–62.
[12] V.M. Malhotra, P.K. Metha PK, Pozzolanic and cementitious materials, in: Advances in Concrete Technology (volume 1). Gordon and Breach Science Publisher SA, Amsterdam, 1996.
[13] V.T. Giner, S. Ivorra, F.J. Baeza, E. Zornoza, B. Ferrer, Silica fume admixture effect on the dynamic properties of concrete, Constr. Build. Mater. 25 (2011) 3272–3277.
[14] C. Jaturapitakkul, K. Kiattikomol, V. Sata, T. Leekeeratikul, Use of ground coarse fly ash as a replacement of condensed silica fume in producing high-strength concrete, Cem. Concr. Res. 34 (2004) 549–555.
[15] D.R.M. Brew, K.J.D. MacKenzie, Geopolymer synthesis using silica fume and sodium aluminate, J. Mater. Sci. 42 (2007) 3990–3993.
[16] P. Chindaprasirt, S. Thaiwitcharoen, S. Kaewpirom, U. Rattanasak, Controlling ettringite formation in FBC fly ash geopolymer concrete, Cement Concr. Compos. 41 (2013) 24–28.
[17] B.A. Clark, P.W. Brown, Formation of ettringite from monosubstituted calcium sulfoaluminate hydrate and gypsum, J. Am. Ceram. Soc. 82 (1999) 2900–2905.
[18] U. Rattanasak, P. Chindaprasirt, P. Suwanvitaya, Development of high volume rice husk ash alumino silicate composites, Int. J. Miner. Metall. Mater. 17 (2010) (2010) 654–659.
[19] A. Peschard, A. Govin, P. Grosseau, B. Guilhot, R. Guyonnet, Effect of polysaccharides on the hydration of cement paste at early ages, Cem. Concr. Res. 34 (2004) 2153–2158.
[20] P. Chindaprasirt, U. Rattanasak, S. Taebuanhuad, Role of microwave radiation in curing the fly ash geopolymer, Adv. Power Technol. 24 (2013) 703–707.
[21] T. Bakharev, Thermal behaviour of geopolymers prepared using class F fly ash and elevated temperature curing, Cem. Concr. Res. 36 (2006) 1134–1147.
[22] R.R. Lloyd, J.L. Provis, J.S.J. van Deventer, Microscopy and microanalysis of inorganic polymer cements. 1: Remnant fly ash particles, J. Mater. Sci. 44 (2009) 608–619.
[23] P.C. Hewlett, Lea's Chemistry of Cement and Concrete, fourth ed., Butterworth-Heinemann, Oxford, 1998.
[24] S. Songpiriyakij, T. Kubprasit, C. Jaturapitakkul, P. Chindaprasirt, Compressive strength and degree of reaction of biomass- and fly ash-based geopolymer, Constr. Build. Mater. 24 (2010) 236–240.
[25] K. Somna, C. Jaturapitakkul, P. Kajitvichyanukul, P. Chindaprasirt, NaOH-activated ground fly ash geopolymer cured at ambient temperature, Fuel 90 (2011) 2118–2124.
[26] G. Xiaolu, S. Huisheng, A.D. Warren, Compressive strength and microstructural characteristics of class C fly ash geopolymer, Cement Concr. Compos. 32 (2010) 142–147.
[27] U. Rattanasak, P. Chindaprasirt, Influence of NaOH solution on the synthesis of fly ash geopolymer, Miner. Eng. 22 (2009) 1073–1078.
[28] R.K. Tiwari, Special report/Instrumentation: Thermal techniques for material characterization, Ceramic Industry Magazine, May 2008 (online version).
[29] S. Freiman, S. Hooker, K. Migler, S. Arepalli, Measurement issues in single wall carbon nanotubes, Special publication 960-19, National Institute of Standards and Technology, Washington DC, 2008.
[30] G. Villain, M. Thiery, G. Platret, Measurement methods of carbonation profiles in concrete: thermogravimetry, chemical analysis and gammadensimetry, Cem. Concr. Res. 37 (2007) 1182–1192.
[31] L. Alarcon-Ruiz, G. Platret, E. Massieu, A. Ehrlacher, The use of thermal analysis in assessing the effect of temperature on a cement paste, Cem. Concr. Res. 35 (2005) 609–613.
[32] I. Ismail, S.A. Bernal, J.L. Provis, S. Hamdan, J.S.J. van Deventer, Microstructural changes in alkali activated fly ash/slag geopolymers with sulfate exposure, Mater. Struct. 46 (2013) 361–373.
[33] J. Skalny, J. Marchand, I. Odler, Sulfate Attack on Concrete, Spon Press, London, 2002.
[34] A.D. Wilson, J.W. Nicholson, Acid-base cements: their biomedical and industrial applications (Chemistry of solid state materials), Cambridge University Press, New York, 1993.
[35] S. Mindess, J.F. Young, D. Darwin, Concrete, second ed., Prentice Hall, New Jersey, 2002.
[36] R. Siddique, M. Iqbal Khan, Supplementary Cementing Materials, Springer, Heidelberg, 2011.

Construction and Building Materials 63 (2014) 303–310

Contents lists available at ScienceDirect

Construction and Building Materials

journal homepage: www.elsevier.com/locate/conbuildmat

Effect of sodium hydroxide concentration on chloride penetration and steel corrosion of fly ash-based geopolymer concrete under marine site

P. Chindaprasirt [a], W. Chalee [b,*]

[a] Sustainable Infrastructure Research and Development Center, Department of Civil Engineering, Faculty of Engineering, Khon Kaen University, Khon Kaen 40002, Thailand
[b] Department of Civil Engineering, Faculty of Engineering, Burapha University, Chonburi 20131, Thailand

HIGHLIGHTS

- The long term durability of geopolymer concrete under marine site was investigated.
- The findings provide valuable data for a practice guide line of geopolymer concrete.
- The findings could help select for fly ash geopolymer concrete used in marine site.

ARTICLE INFO

Article history:
Received 6 August 2013
Received in revised form 27 February 2014
Accepted 1 April 2014

Keywords:
Marine environment
Fly ash-based geopolymer concretes
Chloride penetration
Steel corrosion
Sodium hydroxide concentration

ABSTRACT

In this research, the effect of sodium hydroxide (Na(OH)) concentrations on chloride penetration, steel corrosion and compressive strength of fly ash-based geopolymer concretes under marine environment were studied. The geopolymer concrete were prepared from class C fly ash with sodium silicate (Na_2SiO_3) and sodium hydroxide (Na(OH)) solutions. The concentrations of Na(OH) of 8, 10, 12, 14, 16 and 18 molar, and the constant molar ratio of SiO_2/Al_2O_3 were used. The $200 \times 200 \times 200\ mm^3$ concrete cube specimens with steel bar embedded at coverings of 20, 50 and 75 mm were investigated. The specimens were air-cured in laboratory for 28 days and then were exposed to tidal zone of marine environment in the Gulf of Thailand. After 3-year exposure, the specimens were tested for compressive strength, chloride penetration and corrosion of embedded steel bar. The results showed that the chloride penetration and corrosion of embedded steel decreased with the increasing of Na(OH) concentration. The steel corrosion was related to the compressive strength of geopolymer concrete. The corrosion is high with the concrete of low compressive strength. In addition, increasing the Na(OH) concentration in geopolymer concrete resulted in a decrease in the chloride binding capacity.

1. Introduction

The high performances materials (low cost, high durability and high strength) needed to be achieved in the new construction. The new materials from industrial wastes are an interesting possibility for sustainability and economically use of resource. An industrial waste is generally used as pozzolanic materials to partially replace Portland cement for a high performance concrete (good mechanical and durability properties) [1–3]. However, they cannot totally replace Portland cement since silica (SiO_2) and alumina (Al_2O_3) in pozzolanic materials still need $Ca(OH)_2$ from hydration process for its pozzolanic reaction to produce calcium silicate hydrate (CSH) and calcium aluminate hydrate (CAH) which is primarily responsible for the concrete strength [4]. Recently, it was found that pozzolanic materials containing SiO_2 and Al_2O_3 could be activated with alkaline solution at room temperature to produce a cementitious material called geopolymer [5]. Previous research had studied the effect of various factors such as alkalinity concentrations, curing condition and types of source materials on the microstructure and mechanical properties of geopolymer paste or mortar [6–10]. However, there are only a few reports concerning the durability properties of geopolymer concrete in real exposure which is significant for practical used, especially, the deterioration of geopolymer concrete caused by severe environment.

Current researches on geopolymer concrete are mainly focused on geopolymer properties such as mechanical properties, paste properties [6–10] and durability properties in laboratory [11–13]. However, no specific publications are available concerning the durability of geopolymer concrete in the actual marine site which is mainly due to sulfate attack and the corrosion of steel under chloride attack [14,15]. However, all of these mechanisms are the

* Corresponding author. Tel.: +66 8 97915171.
E-mail address: wichian@buu.ac.th (W. Chalee).

http://dx.doi.org/10.1016/j.conbuildmat.2014.04.010
0950-0618/

combination of many influences, such as moisture, temperature, impact force and abrasion by sand in sea water. The combined destruction of chemical and physical aggressive of actual environment are complicated. Consequently, the long term durability study in marine site was needed for the development of good practice guide line on selection and design for fly ash geopolymer concrete in marine environment. Thus, the goal of the study was to study the fly ash-based geopolymer concrete under the marine environment in order to achieve the good mechanical and durability properties for marine structure. The effect of sodium hydroxide (NaOH) concentrations on compressive strength, chloride penetration profile, chloride binding capacity and steel corrosion of fly ash-based geopolymer concretes under 3-year exposure in tidal zone of marine environment were carried out.

2. Experimental program

2.1. Materials and specimens

The geopolymer concrete mixtures were prepared from Mae Moh class C fly ash with a 30-μm median particle size (by sieve analysis), sodium silicate (Na_2SiO_3, NS) solution with 9% Na_2O and 30% SiO_2 by weight, NaOH solution, graded sand, and crushed limestone with a maximum size of 19 mm. The chemical compositions of fly ash are shown in Table 1. The NaOH concentrations were varied at 8, 10, 12, 14, 16 and 18 molar and the molar ratio of SiO_2/Al_2O_3 was kept constant. The liquid to binder ratio (L/B) was kept constant of 0.60. Mixture proportions of fly ash-based geopolymer concrete are shown in Table 2. For the mixture procedure, the fly ash and aggregates were dry-mixed with a power mixer, the alkaline liquids (NaOH and sodium silicate solutions) were sequentially added and the wet-mixing was continued for 1 min. These were similar to the mixing of normal concrete. Concrete cylinder having 100-mm in diameter and 200-mm in height were prepared for compressive strength test. For chloride penetration and steel corrosion tests, the $200 \times 200 \times 200\ mm^3$ geopolymer concrete cube specimens were cast and the steel bars (12-mm in diameter and 50-mm in length) were embedded at the corners of concrete specimens with the covering depths of 20, 50, and 75 mm. The embedded steel bars which is commonly used for reinforced concrete construction were cut from 12-mm diameter round bar graded SR24 (yield strength of 240 MPa). Geopolymer concrete specimens preparations are shown in Fig. 1(a). The geopolymer concrete specimens were removed from the molds at the age of 1 day and then were air cured until the age of 28 days. Consequently, the geopolymer concrete specimens were transferred to the tidal zone of the marine site in the Gulf of Thailand as shown in Fig. 1(b). The ranges of annual temperature at this site are between 26 and 35 °C, and based on chemical analysis of the seawater, chloride and sulfate compositions range from 16,000 to 18,000 and 2200 to 2600 mg/l, respectively. The geopolymer concrete specimens were exposed to two wet–dry cycles of seawater daily.

2.2. Tested program

2.2.1. Compressive strength

The compressive strengths of geopolymer concretes at 28 days and at 3 years exposure in marine environment were investigated in accordance with ASTM C39/39M [16]. The compressive strength was collected based on the average of values obtained from three samples.

2.2.2. Chloride penetration

After being exposed to seawater for 3 years, the top surface of concrete cube specimens were cored to obtain 75-mm diameter cylinders. The core specimens were dry-cut from the surface to obtain a series of 10-mm thick slices, and then were ground into small powdery particles. The powder sample from each slice was selected for chloride tests by acid-soluble and water-soluble to determine the total and free chloride contents in geopolymer concrete, respectively. The acid-soluble and water-soluble chloride tests were conformed to ASTM C 1152 [17] and ASTM C1218 [18], respectively. The specimens preparation for chloride penetration test are shown in Fig. 2(a).

Table 1
Chemical composition of fly ash.

Chemical composition (%)	
Silicon dioxide, SiO_2	32.10
Aluminum oxide, Al_2O_3	19.90
Iron oxide, Fe_2O_3	16.91
Calcium oxide, CaO	18.75
Magnesium oxide, MgO	3.47
Sodium oxide, Na_2O_3	0.69
Potassium oxide, K_2O	2.38
Sulfur trioxide, SO_3	2.24
Loss on ignition, LOI	0.07

Table 2
Mixture proportions of fly ash-based geopolymer concrete.

Mix	Mixture proportion (kg/m^3)				
	Fly ash	Fine aggregate	Coarse aggregate	NaOH	NS
8-M	390	585	1092	67	167
10-M	390	585	1092	67	167
12-M	390	585	1092	67	167
14-M	390	585	1092	67	167
16-M	390	585	1092	67	167
18-M	390	585	1092	67	167

2.2.3. Steel corrosion and chloride content at the position of embedded steel

The embedded steel corrosions were measured in terms both of the percentage of rusted area (RA) and percentage of weight loss (WL). After 3-year exposure in marine site, the geopolymer concrete specimens were broken, and then the embedded steel bars were removed. An image of each visible surface of rusted steel was recorded. For the percentage of rusted area, transparent paper with a grid composed of 1 mm-squares was then wrapped around each embedded steel bar. The visible surface of the rusted steel was marked on the paper and evaluated (Fig. 2(b)). The corrosion of the embedded steel bars was measured in terms of the percentage of rusted area by comparing the surface rusted area to the total surface area of the embedded steel. Also, the percentage of weight loss of embedded steel bar were determined by comparing the amount of steel weight loss due to corrosion (the decrease in embedded steel weight during the exposed time period) to the initial steel weight (the steel weight before embedding in geopolymer concrete). In addition, mortar debris was collected from the position of the embedded steel–concrete matrix interface and ground to powder. Its water-soluble chloride content was determined and represented the free chloride content at the position of the embedded steel.

3. Results and discussions

3.1. Compressive strength

Table 3 shows the compressive strength results for fly ash-based geopolymer concretes after 28-day curing in air and 3 years exposure in the tidal zone of marine site. Also shown is the strength at 3 years as a proportion of the 28-day strength in order to present the degree of strength loss or strength gain. The 28-day compressive strength of geopolymer concretes increases with the increase in NaOH concentration. All geopolymer concretes recorded no strength loss between 28 days and 3 years, especially in geopolymer concrete with high strength grade. The increasing compressive strength of geopolymer concrete between 28 days and 3 years tended to be high with the increase of Na(OH) concentration and the highest increase was in geopolymer concrete with sodium hydroxide concentration of 18 molar. For instance, geopolymer concrete with Na(OH) concentration of 8, 10, 12, 14, 16 and 18 molar had percentage compressive strength at 3 years as compared to 28 days of 107.3%, 112.8%, 117.7%, 125.2%, 125.2% and 126.1%, respectively. During exposure period, the compressive strength gain of geopolymer concrete with higher strength grade (higher NaOH concentration) was larger than the lower strength grade (lower NaOH concentration). The high concentration of NaOH resulted in the leaching of a larger amount of Si and Al from fly ash [8] and thus produced a better degree of polycondensation and resulted in a high development of long-term compressive strength of geopolymer concrete [19–21]. However, some previous research [9] found that the leaching of Si and Al from fly ash tend to decrease at a high concentration of Na(OH). This may be caused by an increase in the viscosity and density of NaOH solution result in a high viscosity and low flow ability. Consequently, lower pore surface-solution interaction is expected. This trend was consistent

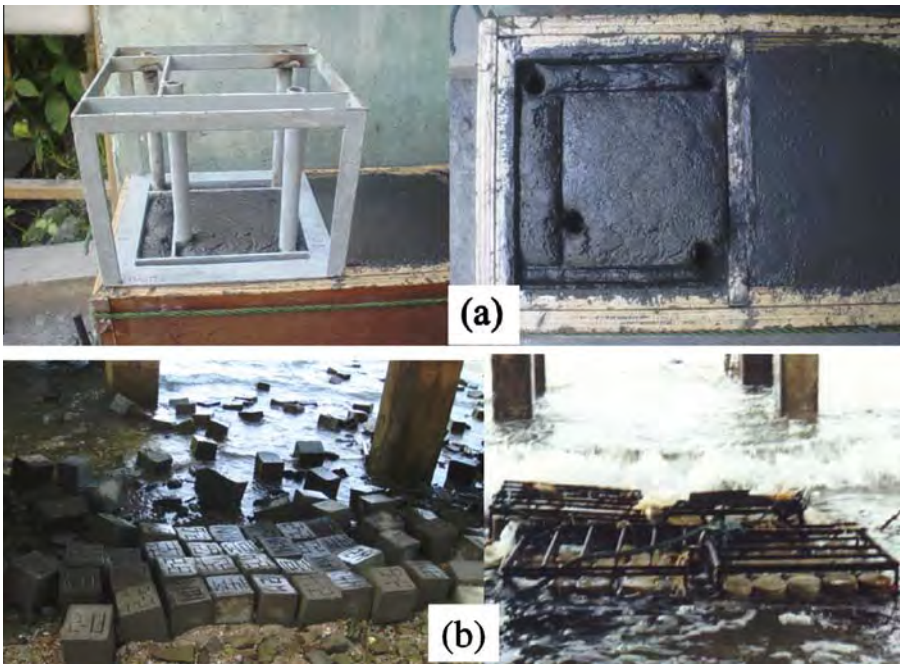

Fig. 1. (a) Geopolymer concrete specimens preparation and (b) geopolymer concrete specimens at a tidal zone of marine site.

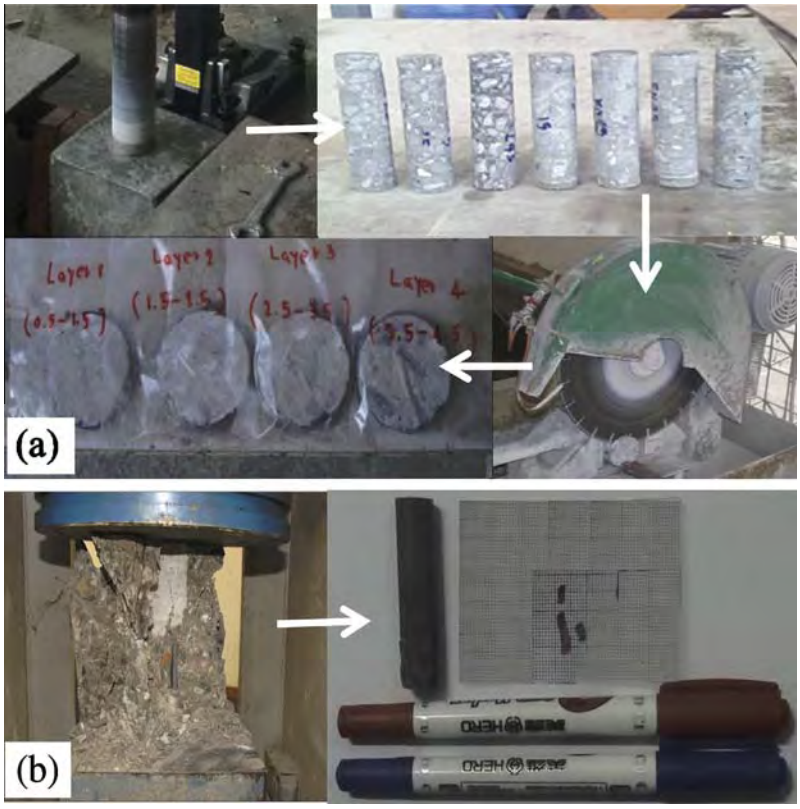

Fig. 2. Specimens preparation for (a) chloride penetration test and (b) corrosion of embedded steel bar.

with the results from this study that the compressive strength of geopolymer concrete (at 28 days and 3 years exposure) increase with NaOH concentration but they were found to slightly decrease when the NaOH concentration was high (up to 18 molar). Besides, previous research showed that the strength loss of cement based concrete due to seawater was caused from a complex combination of physical (such as abrasion, temperature, moisture) and chemical processes (sulfate attack) [14,22]. The sulfate ions in seawater (about 0.22–0.27% by weight of seawater, for marine site in this study) caused deterioration from expansive reactions which also produced non-cohesive products and resulted in strength loss of concrete. Similar to normal Portland cement concrete, the

Table 3
Compressive strength of fly ash-based geopolymer concrete after 28 days and 3 years of exposure in a marine environment.

Mix	Compressive strength (MPa)		
	28-Day curing	3-Year exposure	3-Year/28-day (%)
8-M	23.4	25.1	107.3
10-M	25.0	28.2	112.8
12-M	28.2	33.2	117.7
14-M	31.8	39.8	125.2
16-M	32.2	40.3	125.2
18-M	30.3	38.2	126.1

geopolymer concrete exposed to an external source of sulfate deteriorated by expansive reactions with products such as magnesium hydroxide ($Mg(OH)_2$) and calcium sulfate ($CaSO_4$) [11,12] which resulted in the loss of cohesion of paste matrix. The high early strength of high NaOH concentration geopolymer concrete in this study resulted in a low porosity paste leading to reduce amount of sulfate ions ingress into concrete and thus showed a low strength loss (high strength gain) when compared with a low NaOH concentration geopolymer concrete. Also, the increase of NaOH concentration (increased compressive strength) helped to resist the physical attack which strongly affected the surface layers of geopolymer concrete [23].

3.2. Chloride penetration

The total and free chloride penetration profiles of fly ash-based geopolymer concrete at 3-year exposure in a tidal zone of marine environment are shown in Fig. 3(a) and (b). The chloride penetration in geopolymer concretes decreased with the increasing of NaOH concentration. For instance, geopolymer concrete with NaOH concentration of 8, 10, 12, 14, 16 and 18 molar had total chloride (Fig. 3(a)) and free chloride (Fig. 3(b)) concentrations at 35-mm cover depth of 0.30%, 0.16%, 0.15%, 0.12%, 0.11%, 0.09% and 0.22%, 0.12%, 0.11%, 0.08%, 0.07%, 0.04% by weight of concrete, respectively. The reduction in chloride penetration found in concrete with high concentration NaOH could be attributed to the refinement of the pore structures as a result of polycondensation reaction and filler effect. The relatively high concentration of NaOH enabled the leaching of more Si and Al from fly ash, produced a better degree of polycondensation and resulted in a decrease of geopolymer concrete porosity.

This result is consistent with several other researches [24,25] which indicated that the polycondensation reaction of ash-based geopolymer concrete with a higher concentration of NaOH produced lower permeability and higher strength, thus leads to lower chloride ingress than those with lower NaOH concentration. In addition, $Ca(OH)_2$ (the product from a reaction between calcium from fly ash and alkaline activated in geopolymer) reacted with Si and resulted in calcium silicate hydrate (CSH) which is primarily responsible for the strength in cement based materials [4,25,26].

3.3. Chloride diffusion coefficients (D_c)

In this study, D_c was evaluated based on Fick's second law of diffusion as given by Eq. (1) [27].

$$\frac{\partial C}{\partial t} = D_c \frac{\partial^2 c}{\partial x^2} \quad (1)$$

If D_c in this equation is a constant at a specific exposure time, a general solution of Eq. (1) is given in Eq. (2)

$$C_{x,t} = C_o\left[1 - erf\left(\frac{x}{2\sqrt{D_c t}}\right)\right] \quad (2)$$

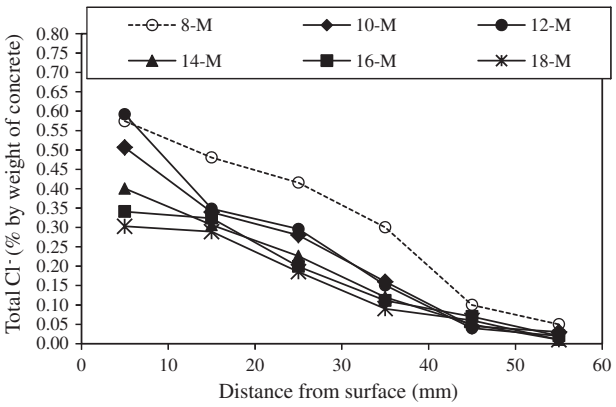

(a) total chloride penetration

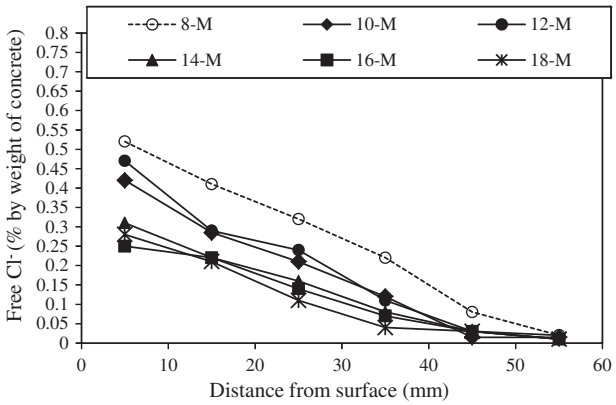

(b) free chloride penetration

Fig. 3. Chloride penetration profiles of fly ash-based geopolymer concrete at 3-year exposure in a tidal zone of marine environment.

where $C_{x,t}$ = chloride concentration (% by weight of concrete) at the position x and exposure time t, x = distance from concrete surface (mm), t = exposure time (s), C_o = chloride concentration at concrete surface (% by weight of concrete) at exposure time t, D_c = diffusion coefficient (mm^2/s) at exposure time t, erf = error function.

The general solution in Eq. (2) provides the chloride concentration at any depth and at any exposure time under the constant of D_c and C_o. Consequently, the value of D_c by this equation can be obtained when the value of D_c is a constant at a specific exposure time. Also, the value of C_o can be determined by extrapolation of the chloride penetration profile to depth $x = 0$. The determination of D_c in geopolymer concrete can be evaluated by fitting the Fick's second law on chloride penetration profile from experiment. Fig. 4 shows the fitting curve of general solution of Fick's second law on total chloride penetration profile in fly ash-based geopolymer concrete with difference NaOH concentration at 3-year exposure in a tidal zone of marine environment.

The effect of NaOH concentrations on chloride diffusion coefficient of fly ash-based geopolymer concrete are shown in Fig. 5. The results showed that the increase of NaOH concentrations in geopolymer concrete clearly reduced the rate of chloride ingress into geopolymer concrete. For instance, geopolymer concretes with NaOH concentration of 8, 10, 12, 14, 16 and 18 molar had the D_c at 3-year exposure in marine environment of 6.2×10^{-6} mm^2/s, 4.1×10^{-6} mm^2/s, 3.9×10^{-6} mm^2/s, 3.7×10^{-6} mm^2/s, 3.5×10^{-6} mm^2/s and 2.9×10^{-6} mm^2/s, respectively. This is due to the high NaOH concentrations resulted in geopolymer concretes with high compressive strength as mentioned in Section 3.1. This is similar to cement based concrete that the higher

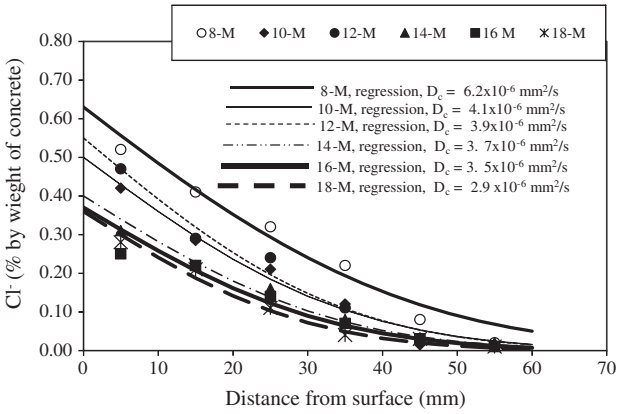

Fig. 4. The fitting curve of general solution of Fick's second law on chloride penetration profile in fly ash-based geopolymer concrete at 3-year exposure in a tidal zone of marine environment.

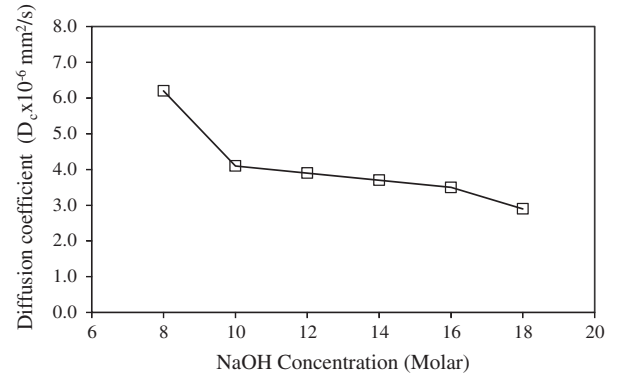

Fig. 5. The effect of sodium hydroxide (Na(OH)) concentrations on chloride diffusion coefficient of fly ash-based geopolymer concrete.

compressive strength lead to lower water permeability and lower chloride ingress [28,29]. In addition, a high concentration of NaOH enhances the leaching of Si and Al from fly ash to produce the higher degree of geopolymerization than that of concrete with low NaOH concentration. This leads to dense matrix and increased ability to resist chloride ions penetration in geopolymer concrete [24]. The SEM were also used to characterize the geopolymer concrete with NaOH concentration of 8 and 18 molar (after exposed to marine site for 3 years) as shown in Fig. 6(a) and (b), respectively. It was found that the geopolymer concrete with high concentration of NaOH solution was denser than that of geopolymer concrete with low NaOH concentration. This result is also consistent with that of chloride diffusion coefficient in geopolymer concrete.

Previous researches [2,30] studied chloride diffusion coefficient of Portland cement type I concretes with W/B ratios of 0.45, 0.55, and 0.65 after 3-year exposure in the gulf of Thailand, the same location where fly ash-based geopolymer concrete specimens in this study were placed. Relationships between compressive strength at 28 days and chloride diffusion coefficients of fly ash-based geopolymer concretes obtained from this study were generated and compared to those of Portland cement type I concretes obtained from previous researches as shown in Fig. 7. According to the figure, chloride diffusion coefficients of fly ash-based geopolymer concretes were lower than those of Portland cement type I concretes even though their compressive strength at 28 days were lower than those of Portland cement type I concrete. As a result, if the compressive strength of fly ash-based geopolymer concrete were improved to be as high as that of Portland cement type I concrete, fly ash-based geopolymer concrete tended to provide a higher resistance to chloride diffusion than Portland cement type I concrete does.

3.4. Chloride binding capacity

The chloride binding capacity in cement based concrete can be calculated by subtracting the free chloride content from total chloride content. For the geopolymer concrete in this study, the chloride binding capacity was evaluated similarly to cement based concrete in terms of percentage chloride binding capacity compared to the total chloride content (P_{cb}). The findings are similar to previous research [31]. Fig. 8 illustrates the relationship between free chloride (C_f) and total chloride content (C_t) in geopolymer concretes at 3-year exposure in marine site. Consequently, the linear regression is used to determine their relation and to produce the equation for C_f in terms of C_t as shown in Fig. 8. According to the relationship between C_f and C_t, the percentage chloride binding capacity (P_{cb}) as compared to the total chloride content can be determined from Eq. (3):

$$P_{cb} = \frac{[(C_t - C_f) \times 100]}{C_t} \quad (3)$$

By substituting C_f in terms of C_t in Eq. (3), the percentage chloride binding capacity (P_{cb}) of fly ash-based geopolymer concrete with NaOH concentration of 8, 10, 12, 14, 16 and 18 molar are 14.3%, 19.0%, 19.8%, 25.8%, 30.2% and 30.8%, respectively.

Fig. 9 presents the effect of NaOH concentration on chloride binding capacity (P_{cb}). The results show that the chloride binding capacity in terms of P_{cb} clearly increased as the NaOH concentration increased. Generally, chloride binding capacity of cement based concrete depends on the physical binding and chemical

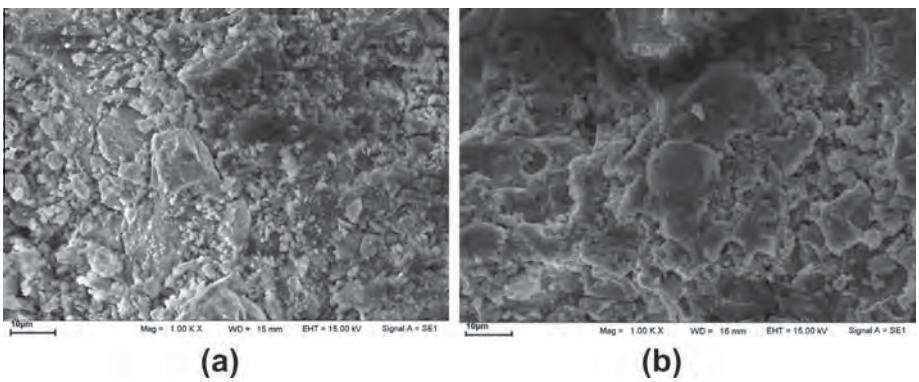

Fig. 6. SEM analysis of fly ash geopolymer concrete with NaOH concentration of (a) 8 molar and (b) 18 molar after exposed to marine site for 3 years.

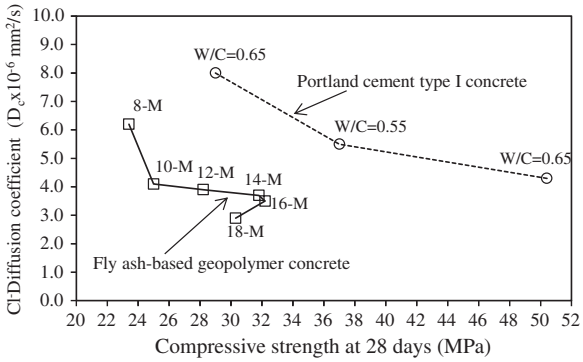

Fig. 7. Relationship between compressive strength at 28 days and chloride diffusion coefficient of Portland cement type I and fly ash-based geopolymer concretes at 3-year exposure.

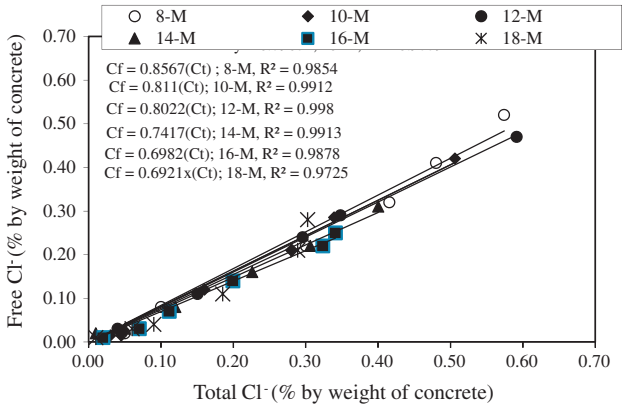

Fig. 8. Relationship between the free and total chloride contents of fly ash-based geopolymer concrete at 3-year exposure in a tidal zone of marine environment.

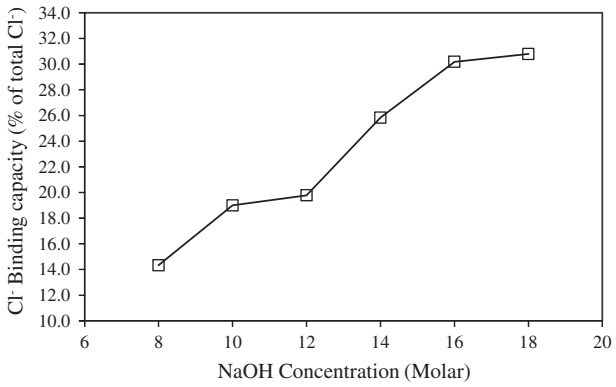

Fig. 9. The effect of sodium hydroxide (Na(OH)) concentrations on chloride binding capacity of fly ash-based geopolymer concrete.

binding [32,33]. The chemical chloride binding can take place only as a result of hydrated calcium aluminate derived from C_3A, produces calcium chloroaluminate hydrate (Friedel's salt). Thus, more chloride ions should be bound when cement contains higher C_3A. Besides, the physical binding, chloride can be physically adsorbed on the surface of hardened gel from the hydration process, such as calcium silicate hydrate (the main product of the hydration reaction which possess cementitious properties) and calcium aluminate hydrate. Previous research had reported that more chloride ions are bound in cement based concrete with higher strengths than those with lower strengths [34]. This confirmed the fact mentioned above. In this study, more chloride ions was bound in geopolymer concrete with higher NaOH concentration than that with lower NaOH concentration due to the physical binding of chloride ions in geopolymer concrete. Since, the use of high NaOH concentration in geopolymer concrete resulted in increased compressive strength, this implied that the hardened gel products from polycondensation reaction was increased. Besides, the fly ash with high calcium oxide can be reacted with silicate compounds to form calcium silicate hydrate, which was the cement gel similar to the hydration reaction of Portland cement concrete [20]. As a result, chloride ions were more physically adsorbed on the surface of hardened gel when compared with the low strength geopolymer concrete. Moreover, the decrease of both total (C_t) and bound chlorides ($C_t - C_f$) in a high NaOH concentration geopolymer resulted in the decrease of P_{cb}, due to a large reduction of C_t as compared with bound chloride. For instance, geopolymer concrete with Na(OH) concentration of 8, 10, 12, 14, 16 and 18 molar had P_{cb} of 14.3%, 19.0%, 19.8%, 25.8%, 30.2%, and 30.8%, respectively.

3.5. Steel corrosion

In this study, the steel corrosion of geopolymer concrete with different concentrations of NaOH was investigated in terms of percentage weight loss (WL) and percentage rusted area (RA). The embedded steel bars at covering depth of 20, 50 and 75 mm at 3-year exposure in a tidal zone of marine environment are shown in Fig. 10(a)–(c). The result indicated that the steel corrosion of geopolymer concretes tended to decrease with the increasing of NaOH concentration. It is consistent with the proposed results in this study that the higher NaOH concentration produces a lower chloride diffusion coefficient and a higher compressive strength. For instance, geopolymer concretes with NaOH concentration of 8, 10, 12, 14, 16 and 18 molar, the percentage of rusted area and weight loss of embedded steel bar at the covering depth of 20 mm were 76.7%, 62.0%, 56.1%, 46.9%, 27.8%, 23.8% and 2.07%, 0.23%, 0.21%, 0.13%, 0.12%, 0.11%, respectively. Also, the same trend of steel corrosion in geopolymer concrete were found at the deeper covering depths of 50 mm and 75 mm. The use of high NaOH concentrations of 16 and 18 molar in geopolymer concretes clearly reduced the embedded steel corrosion at all covering depth when compared with other lower NaOH concentrations. Although, geopolymer concretes were exposed to marine site up to 3 years, it presented low steel corrosion at any depth of concrete and did not show the corrosion of embedded steel bar at 75-mm covering depth.

Generally, the corrosion of steel in cement based concrete in seawater has deteriorated due to the incompatibility of the mix constituents. Both physical characteristics (i.e. pore distribution, pore size, connectivity of pores, shrinkage and movement cracks) [35,36] and chemical characteristics (i.e. chloride binding capacity, alkalinity) [37,38] of cement paste significantly affect the corrosion rates of steel in concrete. In this study, the reduction in steel corrosion was greater in geopolymer concretes with higher NaOH concentrations than that with lower NaOH concentrations. It was due to a lower permeability of a high NaOH concentration geopolymer concrete improved the physical characteristics of paste and led to a lower chloride ingress and steel corrosion in geopolymer concrete. Besides, the improved chemical characteristics of geopolymer paste for protecting the steel corrosion was produced by the increase in the chloride binding capacity of concretes. Thus, the use of a high NaOH concentration solution in geopolymer concrete in this study resulted in increased chloride binding capacity (as mentioned in Section 3.4) and led to a lower free chloride content in pore solution and lower steel corrosion.

By considering the free chloride content at the position of embedded steel bar (Fig. 11), the result also indicated the

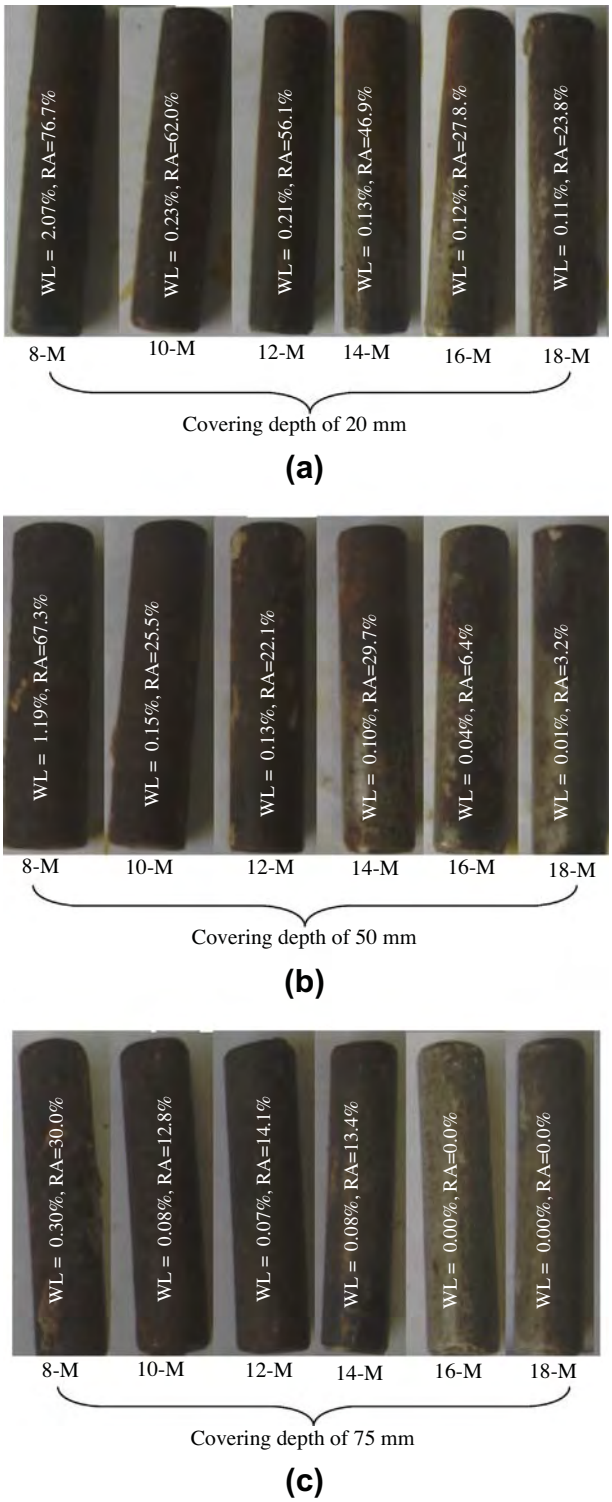

Fig. 10. Corrosion of embedded steel bars at covering depth of (a) 20 mm (b) 50 mm and (c) 75 mm in fly ash-based geopolymer concrete at 3-year exposure in a tidal zone of marine environment.

consistent trend of steel corrosion that the higher chloride content in geopolymer concrete resulted in the higher corrosion of embedded steel bar. The use of 16–18 molar NaOH concentration solutions in geopolymer concrete significantly reduced the free chloride content and increases its durability. For instance, geopolymer concretes having NaOH concentrations of 8, 10, 12, 14, 16 and 18 molar were found to have free chloride contents at 50 mm

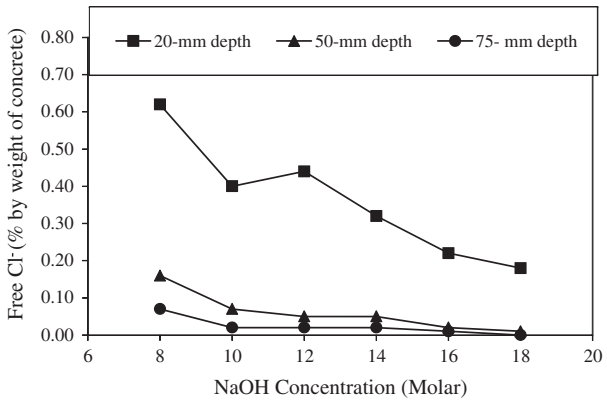

Fig. 11. The effect of sodium hydroxide (Na(OH)) concentrations on chloride contents at the position of embedded steel bars of fly ash-based geopolymer concrete.

depth of 0.16%, 0.07%, 0.05%, 0.05%, 0.02% and 0.01% by weight of concrete, respectively.

4. Conclusions

Based on the results and discussions for the high calcium fly ash-based geopolymer concrete, the following conclusions are made.

(1) During 3-year exposure in seawater, fly ash-based geopolymer concrete with a high NaOH concentration continuously gain strength faster than that with a low NaOH concentration.
(2) Evidently, higher NaOH concentration in fly ash-based geopolymer concrete resulted in lowering of both of free and total chloride ingresses in geopolymer concrete.
(3) The increase in NaOH concentration in geopolymer concrete resulted in the decrease of chloride diffusion coefficient (D_c) and steel corrosion in geopolymer concrete.
(4) Increasing the NaOH concentration in geopolymer concrete resulted in a decreasing the percentage of chloride binding capacity (P_{cb}) as compared to the total chloride content.

Acknowledgements

The authors gratefully acknowledge financial supports from the Research and Development Funds, Faculty of Engineering, Burapha University, Thailand Grant No. 20/2555 and the Thailand Research Fund (TRF) under the TRF Senior Research Scholar Contract No. RTA5480004.

References

[1] Chalee W, Sasakul T, Suwanmaneechot P, Jaturapitakkul C. Utilization of rice husk-bark ash to improve the corrosion resistance of concrete under 5-year exposure in a marine environment. Cem Concr Compos 2013;37:47–53.
[2] Chalee W, Ausapanit P, Jaturapitakkul C. Utilization of fly ash concrete in marine environment for long term design life analysis. Mater Des 2010;3:1242–9.
[3] Krammart P, Tangtermsirikul S. Properties of cement made by partially replacing cement law materials with municipal solid waste ashes and calcium carbide waste. Constr Build Mater 2004;18:579–83.
[4] Neville AM. Properties of concrete. 4th ed. England: Addison Wesley; 1996.
[5] Davidovits J. Geopolymer inorganic polymeric new materials. J Therm Anal 1991;37:1633–59.
[6] Zhu Huajun, Zhang Zuhua, Deng Fenggan, Cao Yalong. The effects of phase changes on the bonding property of geopolymer to hydrated cement. Constr Build Mater 2013;48:124–30.

[7] Ryu Gum Sung, Lee Young Bok, Koh Kyung Taek, Chung Young Soo. The mechanical properties of fly ash-based geopolymer concrete with alkaline activators. Constr Build Mater 2013;47:409–18.
[8] Rattanasak U, Chindaprasirt P. Influence of Na(OH) solution on the synthesis of fly ash geopolymer. Miner Eng 2009;22:1073–8.
[9] Chindaprasirt P, Chalee W, Jaturapitakkul C, Rattanasak U. Comparative study on the characteristics of fly ash and bottom ash geopolymers. Waste Manage 2009;29:539–43.
[10] Anurag M, Deepika C, Namrata J, Manish K, Nidhi S, Durga D. Effect of concentration of alkali liquid and curing time on strength and water absorption of geopolymer concrete. Eng Appl Sci 2008;3:14–8.
[11] Chindaprasirt P, Rattanasak U, Taebuanhuad S. Resistance to acid and sulfate solutions of microwave-assisted high calcium fly ash geopolymer. Mater Struct 2013;46:375–81.
[12] Sata V, Sathonsaowaphak A, Chindaprasirt P. Resistance of lignite bottom ash geopolymer mortar to sulfate and sulfuric acid attack. Cem Concr Compos 2012;34:700–8.
[13] Ariffin MAM, Bhutta MAR, Hussin MW, Mohd Tahir M, Aziah Nor. Sulfuric acid resistance of blended ash geopolymer concrete. Constr Build Mater 2013;43:80–6.
[14] Thomas MDA, Matthews JD. Performance of pfa concrete in a marine environment-10-year results. Cem Concr Res 2004;26:5–20.
[15] Lopez-Calvo HZ, Montes-Garcia P, Bremner TW, Thomas MDA, Jiménez-Quero VG. Compressive strength of HPC containing CNI and fly ash after long-term exposure to a marine environment. Cem Concr Compos 2012;34:110–8.
[16] ASTM C39/C 39M-05. Standard test method for compressive strength of cylindrical Concrete specimens V. 04.02, 2006.
[17] ASTM C1152. Standard test method for acid-soluble chloride in mortar and concrete. Annual Book of ASTM Standards, V. 04.02, 2008.
[18] ASTM C1218. Standard test method for water-soluble chloride in mortar and concrete. Annual Book of ASTM Standards, V. 04.01, 1997.
[19] Bakharev T. Geopolymeric materials prepared using Class F fly ash and elevated temperature curing. Cem Concr Res 2005;35:1224–32.
[20] Hanjitsuwan S, Hunpratub S, Thongbai P, Maensiri S, Sata V, Chindaprasirt P. Effects of NaOH concentrations on physical and electrical properties of high calcium fly ash geopolymer paste. Cem Concr Compos 2014;45:9–14.
[21] Palomo A, Grutzek MW, Blanco MT. Alkali-activated fly ashes, a cement for the future. Cem Concr Res 1999;29:1323–9.
[22] Chalee W, Teekavanit M, Kiattikomol K, Siripanichgorn A, Jaturapitakkul C. Effect of W/C ratio on covering depth of fly ash concrete in marine environment. Constr Build Mater 2007;21:965–71.
[23] Capozucca R. Damage to reinforced concrete due to reinforcement corrosion. Constr Build Mater 1995;9:295–303.
[24] Ryu Gum Sung, Lee Young Bok, Koh Kyung Taek, Chung Young Soo. The mechanical properties of fly ash-based geopolymer concrete with alkaline activators. Constr Build Mater 2007;47:409–18.
[25] Chindaprasirt P, Chareerat T, Sirivivatnanon V. Workability and strength of coarse high calcium fly ash geopolymer. Cem Concr Compos 2007;29:224–9.
[26] Caoa Cheng, Sun Wei, Qin Honggen. The analysis on strength and fly ash effect of roller-compacted concrete with high volume fly ash. Cem Concr Res 2000;30:71–5.
[27] Crank J. The mathematics of diffusion. 2nd ed. London: Oxford Press; 1975.
[28] Shi Xianming, Xie Ning, Fortune Keith, Gong Jing. Durability of steel reinforced concrete in chloride environments: an overview. Constr Build Mater 2012;30:125–38.
[29] Meira GR, Andrade C, Alonso C, Borba JC, Padilha M. Durability of concrete structures in marine atmosphere zones – the use of chloride deposition rate on the wet candle as an environmental indicator. Cem Concr Compos 2010;32:427–35.
[30] Chalee W, Jaturapitakkul C. Effect of W/B ratios and fly ash finenesses on chloride diffusion coefficient of concrete in marine environment. Mater Struct 2009;42:505–15.
[31] Cheewaket T, Jaturapitakkul C, Chalee W. Long term performance of chloride binding capacity in fly ash concrete in a marine environment. Constr Build Mater 2010;24:1352–7.
[32] Luo Rui, Cai Yuebo, Wang Changyi, Huang Xiaoming. Study of chloride binding and diffusion in GGBS concrete. Cem Concr Res 2003;33:1–7.
[33] Hiroshi Hirao, Yamada Kazuo, Takahashi Haruka, Zibara Hassan. Chloride binding of cement estimated by binding isotherms of hydrates. J Adv Concr Tech 2005;3:77–84.
[34] Arya C, Buenfeld NR, Newman JB. Factors influencing chloride binding in concrete. Cem Concr Res 1990;20:291–300.
[35] Sanjuan MA, Mufioz-Martialay R. Oven-drying as a preconditioning method for air permeability test. Mater Lett 1996;27:263–8.
[36] Tangpagasit J, Cheerarot R, Jaturapitakkul C, Kiattikomol K. Packing effect and pozzolanic reaction of fly ash in mortar. Constr Build Mater 2005;35:1145–51.
[37] Jensen HU, Pratt PL. The binding of chloride ions by pozzolanic product in fly ash cement blends. Adv Cem Res 1989;7:121–9.
[38] Broomfield JP. Corrosion of steel in concrete. England Taylor & Francis Ltd.; 1996. p. 1–10.

Applied Clay Science 95 (2014) 357–364

Contents lists available at ScienceDirect

Applied Clay Science

journal homepage: www.elsevier.com/locate/clay

Research paper

Lime-calcined clay materials with alkaline activation: Phase development and reaction transition zone

S. Boonjaeng [a], P. Chindaprasirt [b], K. Pimraksa [c,*]

[a] Department of Physics and Materials Science, Faculty of Science, Chiang Mai University, Chiang Mai 50200, Thailand
[b] Sustainable Infrastructure Research and Development Center, Faculty of Engineering, KhonKaen University, KhonKaen 40002, Thailand
[c] Department of Industrial Chemistry, Faculty of Science, Chiang Mai University, Chiang Mai 50200, Thailand

ARTICLE INFO

Article history:
Received 8 October 2013
Received in revised form 27 April 2014
Accepted 3 May 2014
Available online 24 May 2014

Keywords:
Kaolinite
Metakaolin
Pozzolanic reaction
Alkali activated lime pozzolan

ABSTRACT

The research aim was to investigate phase development and reaction transition zone of alkaline activated lime-calcined clay materials. Locally available china clay mainly supplied metakaolin (MK) after calcination. MK and calcium hydroxide (CH) were used to supply SiO_2 and CaO, respectively. The CH to MK ratio of 0.4 with CaO/SiO_2 of 1.18 was selected to coincide with the theoretical CaO/SiO_2 of calcium silicate hydrate in tobermorite group ($Ca_5Si_6O_{16}(OH)_2$). Phase development was investigated using X-ray diffraction and Fourier transform infrared spectroscopy. Compressive strength and density were also investigated to confirm binding properties of the pozzolanic reaction products. The reaction of mixture was dependent on the NaOH concentration. At low concentration of NaOH (<1 M), the pozzolanic reaction was dominant while the zeolitic reaction and geopolymerization became dominant at medium NaOH concentration (>1 M) and at high NaOH concentration, respectively. The activations of CH:MK mixtures with 0.01 and 0.1 M NaOH promoted semicrystalline calcium silicate hydrate (CSH (I)) and crystalline calcium aluminosilicate hydrate (CASH) formations. The mixture with 0.01 M NaOH gave the highest compressive strength of 19.0 MPa. With 3 and 5 M NaOH activations, sodium aluminosilicate hydrate (NASH) and sodium calcium silicate hydrate (NCSH) compounds were formed instead of CSH (I) gel and crystalline CASH phase. At 10 M NaOH, NCSH disappeared and only NASH was formed and resulted in a relatively low compressive strength of 6.7 MPa.

1. Introduction

Pozzolans have been receiving high attention as their use as supplementary cementing material to react with calcium hydroxide (CH), so called "pozzolanic reaction" to form compounds possessing binding properties resulting in concrete strength enhancement (ASTM C125, 2011). Uses of pozzolans as supplementary cementing material from various sources such as volcanic ash, clay minerals, and coal ashes aim to reduce cost and overall environmental impact according to CO_2 emission. Calcium silicate hydrate (CSH) gel is a pozzolanic reaction product for strength improvement together with porosity reduction (Chindaprasirt and Pimraksa, 2008; Frías et al., 2000; García et al., 2009 and García et al., 2009; Kakali et al., 2001; García et al., 2009; Siddique and Klaus, 2009; Sabir et al., 2001). The CSH gel formed at ambient temperature exists in both amorphous and semicrystalline phases at which a distorted semicrystalline phase referred as CSH (I) is normally found as hydration product. Its composition varies considerably depending on parameters such as the component materials (CaO/SiO_2 ratio) and the pH of the surrounding medium (Chen et al., 2004; García et al., 2008; Yip et al., 2005). CSH gel has been found to be compatible to other hydrated products such as sodium aluminosilicate hydrate gel (NASH) which is a new family of aluminosilicate polymers (geopolymers) (García et al., 2008, 2010; Yip et al., 2005). However, CSH and/or calcium aluminosilicate hydrate (CASH) compounds could also precipitate as well-crystalline solids. Geopolymers are usually precipitated by reacting active aluminosilicate materials such as metakaolin (MK) and fly ash, with an appropriate proportion of alkali metals (Na, K, Ca) under very high alkalinity conditions in which the water content is limited (Davidovits, 1989, 1991; Khale and Chaudhary, 2007; Steveson and Sagoe-Crentsil, 2005; Verdolotti et al., 2008).

The mechanism of alkaline activated CH and MK materials are quite close to geopolymer cement (Khale and Chaudhary, 2007; Yip et al., 2005). Geopolymer cement is formed by 2 main steps; dissolution of reactive starting materials and polycondensation of reaction products. For alkaline activated CH and MK materials, the second step includes the precipitation of the pozzoalnic reaction products in addition to the polycondensation. Therefore, chemical structures of alkaline activated CH and MK materials compose of several forms of products ranging from highly alkaline products such as geopolymer, zeolite material

* Corresponding author.
E-mail address: kedsarin.p@cmu.ac.th (K. Pimraksa).

http://dx.doi.org/10.1016/j.clay.2014.05.002
0169-1317/

and hydration gel products of CSH and CASH. Not many works explored the relation between CSH and CASH/MASH gels (M = alkali metals) by alkaline activation, to their mechanical properties (Alonso and Palomo, 2001a,b; Yip et al., 2005). However, the coexistence of geopolymeric and CSH gels obtained from using ground granulated blast furnace slag and MK as starting material is responsible for the strength enhancement as geopolymeric binder works as micro-aggregate, thus resulting in the homogeneous and dense structures (Yip et al., 2005). In synthesizing CSH gel including pozzolanic reaction and sol–gel procedures, the CSH gel was produced cooperating with alkaline aluminosilicate product at high alkalinity (Alonso and Palomo, 2001a,b; Bondar et al., 2011; Granizo et al., 2002; García et al., 2008, 2010). Sol–gel procedure was used to synthesize both CSH and NASH gels. pH level was found to play a determinant role as pH >11 and >12 resulted in CSH and NASH gels, respectively (García et al., 2008).

This study, therefore, proposed an investigation of alkaline activated CH and MK materials in terms of their phase development and reaction transition zone. The attention to explore pozzolanic reaction of MK was due to the advantages of abundantly local availability and its highly reactive nature. Locally available clay is used as starting material to obtain MK in this study. Not only does such clay contain kaolinite (Kaol), but also muscovite and quartz. With calcination during 500–800 °C, Kaol is transformed to MK by dehydroxylation at which bound hydroxyl groups located at octahedral sites of Kaol are dispelled resulting to a disruption of Kaol structure (Sabir et al., 2001; Siddique and Klaus, 2009; Vizcayno et al., 2010). However, some clay minerals are much less reactive although they undergo dehydroxylation due to their crystallinity are not all disrupted, for example, illite or muscovite and montmorillonite (Fernandez et al, 2011). Quartz is also inert to pozzolanic reaction (Carroll and Starkey, 1971; Deschner et al., 2012; Fennis et al., 2009; Mechti et al., 2012; Yock, 2009). Many researchers reported some inert minerals also influenced on mechanical properties of material structure due to filling effect (Deschner et al., 2012; Fennis et al., 2009; Jaturapitakkul et al., 2011; Mechti et al., 2012). With alkaline activation, such inert minerals have been found to be dissolved. For example, the findings from dissolution of aluminosilicate minerals in alkaline solutions at low and high concentrations, found that minerals composed of crystalline phases (cristobalite, feldspar, K-alunite, quartz, Kaol, illite, zeolite) could be dissolved to be aluminate and silicate ions in high concentration of alkaline activation (Panagiotopoulou et al., 2007). The pozzolanic reaction of MK under alkaline activation was, therefore, studied in term of mineralogical development in order to figure out the reaction transition zone of the formation between calcium based hydrate products and sodium based hydrate products using X-ray diffraction (XRD) and Fourier transform infrared spectroscopy (FTIR) spectroscopy and the related mechanical properties. The reaction of secondary minerals such muscovite and quartz was also investigated. This finding would no doubt lay a solid ground work to explain the uses of locally available clay instead of pure MK.

2. Materials and experimental methods

2.1. Raw materials

Kaolin in this study was obtained from Ranong Province in southern Thailand supplied by Sibelco Mineral (Thailand) Co., Ltd. Its chemical composition characterized by X-ray Fluorescence (XRF) using a Horiba Mesa-500W with principle of energy dispersive XRF Analyzer and XEROPHY high-purity silicon used as detector, the results are shown in Table 1. Mineralogical composition was identified by XRD using a Rigaku Miniflex with CuKα radiation and Kb-filter (λ = 1.540 Å), the current and voltage intensity applied to the generating X-ray tubes were 15 mA and 30 kW, the analysis was performed over the diffraction angle range $5° \le 2\theta \le 70°$ with a 12 degree min^{-1} and step width of 0.015°, as shown in Fig. 1 and in Table 1. The calcination temperature of kaolin was investigated by thermal differential analysis and thermal gravimetric analysis (DTA/TGA) using a Seiko SSC-5000 analyzer with temperature range of room temperature to 1000 °C and heating rate of 10 °C/mim. The DTA/TGA curves are shown in Fig. 2. From the DTA/TGA result, kaolin was calcined at 750 °C for transforming Kaol into MK phase (dehydroxylation). XRD was used to confirm phase formation of MK. The mineralogical compositions of Kaol were quantitatively calculated by Rietveld method refinement using X'pert high score plus software to report the degree of Kaol structure disorder.

Table 1
Chemical and mineralogical compositions of kaolin.

Characteristics	
Chemical composition (mass %):	
SiO_2	53.08
Al_2O_3	30.69
Fe_2O_3	1.51
CaO	0.08
K_2O	2.46
MnO	0.11
Y_2O_3	0.07
LOI	12.00
Mineralogical composition (mass %)	
Kaolinite	53.70
Muscovite	14.70
Quartz	31.60
Volume mean diameter, D[4,3] (μm)	20.01
Specific surface area (m^2/g)	21.07
Specific gravity	2.62
SiO_2/Al_2O_3 molar ratio	2.93

Particle sizes and specific surface areas of clays were measured by Laser diffraction and by Brunauer–Emmett–Teller method (BET), respectively. The results are shown in Table 1. A commercial grade CH and analytical grade sodium hydroxide (NaOH) were used in this study.

2.2. Solubility of kaolin and MK in alkaline solutions

The solubility of amorphous phase contained MK due to phase transformation from Kaol to MK was studied using 0.500 g of kaolin and MK mixed with 20 mL of NaOH solutions at various concentrations (0.01, 0.1, 1, 3, 5 and 10 M). The solutions were filtrated by Whatman filter paper (no. 5) and 5 mL of solutions were diluted into 250 mL and adjusted to pH < 1 by hydrochloric acid. Atomic absorption spectrometer (AAS, SHIMADZU AA-6200) was used to analyze the dissolved Si and Al ion concentrations (Panagiotopoulou et al., 2007).

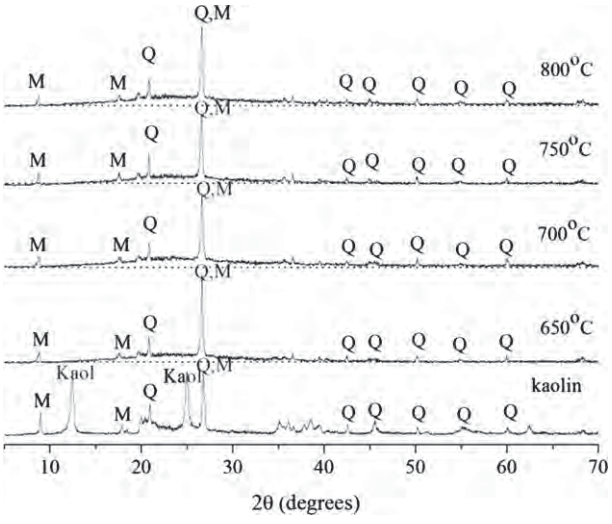

M = muscovite, Kaol = kaolinite, Q = quartz

Fig. 1. XRD patterns of kaolin and calcined kaolin at 650–800 °C.

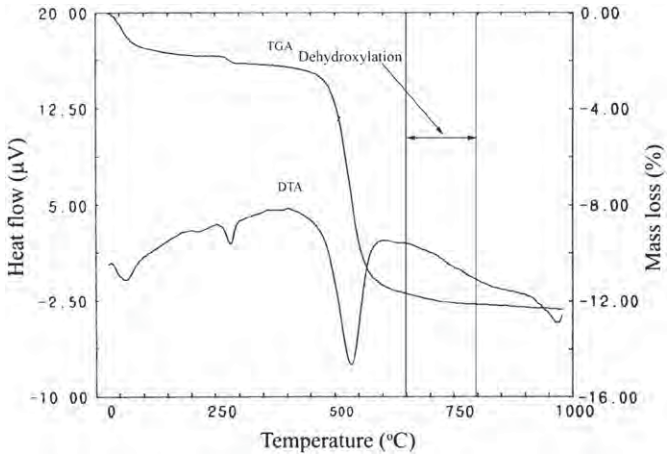

Fig. 2. DTA and TGA graphs of kaolin.

2.3. Pozzolanic reactivity of MK under various NaOH concentrations

The samples were prepared by using 750 °C MK and CH at CH:MK ratios of 0.2, 0.4, 0.6, 0.8 and 1 by mass with corresponding CaO/SiO_2 molar ratios of 0.59, 1.18, 1.76, 2.35 and 2.94, respectively. The same consistency of paste as measured by Vicat apparatus was used by controlling the liquid to solid ratio (L/S) as shown in Table 2.

The mixture was cast into cylinder molds with 20 mm in diameter and 40 mm in height. The samples were placed in the 98% RH and 25 °C chamber. The strength was performed at the age of 28 days using 3 samples. The broken samples were used for the investigation of mineralogical composition by XRD, molecular structure by FTIR, Nicolet 6700 FT-IR Spectrometer, Thermo Fisher Scientific, with attenuated total reflection mode (ATR) and microstructure by scanning electron microscopy (SEM) and energy dispersive X-ray spectroscopy (EDS). Prior to the characterizations, the hydration reaction of the samples was stopped by soaking in acetone for 48 h and dried before the tests (Poon et al., 2001).

The CH:MK of 0.4 with CaO/SiO_2 of 1.18 was selected to study the effect of alkaline activation. The mixtures were blended with 0.01, 0.1, 1, 3, 5 and 10 M NaOH solutions at the same liquid (NaOH solution) to solid ratio as shown in Table 2.

3. Results and discussions

3.1. Characteristics of kaolin and MK

Chemical compositions and mineralogical compositions of kaolin are shown in Table 1 and Fig. 1. The major chemical compositions were approximately 53.08% of SiO_2 and 30.67% of Al_2O_3. The calculated Kaol was about 53.70%. Some quartz and muscovite were also found in the kaolin sample. Dehydroxylation temperature was about 450–650 °C from DTA-pattern while TGA showed the major mass loss at the same temperature as shown in Fig. 2. The degree of dehydroxylation (D_{TG}) of Kaol was around 650–800 °C as indicated by high D_{TG} value (Bich et al., 2009; Shvarzman et al., 2003) at which $DT_G = 1 - (M/M_{max})$, where M and M_{max} were residual and maximum mass loss, respectively. Therefore, the calcination temperature of 650–800 °C was selected which was slightly higher than the evidence obtained from DTA. The XRD of MK showed the transformation of Kaol to MK and crystalline phases such quartz and muscovite did not change. The broad diffuse halo reflection was found in the range of major diffraction reflection in the crystalline state of Kaol with 650–800 °C of calcinations as shown in Fig. 1. At 650 °C, there was no Kaol contained in kaolin sample.

Table 2
Compositions of mixtures.

CH:MK ratios	Composition of mixtures				
	CH (mass)	MK (mass)	Ca/Si	NaOH (M)	L/S
0.2	0.2	1	0.59	No	0.63
0.4	0.4	1	1.18	No	0.62
0.6	0.6	1	1.76	No	0.61
0.8	0.8	1	2.35	No	0.61
1	1	1	2.94	No	0.60
0.4, 0.01 M	0.4	1	1.18	0.01	0.60
0.4, 0.1 M	0.4	1	1.18	0.1	0.60
0.4, 1 M	0.4	1	1.18	1	0.60
0.4, 3 M	0.4	1	1.18	3	0.60
0.4, 5 M	0.4	1	1.18	5	0.60
0.4, 10 M	0.4	1	1.18	10	0.60

Ca is the mole of CaO calculated from the CH content. Si is the mole of reactive SiO_2 calculated from the kaolinite content

3.2. Solubility of kaolin and MK

The concentration of dissolved Si and Al ions of kaolin and MK in 0.01, 0.1, 1, 3, 5 and 10 M are shown in Table 3. The results showed that high alkaline concentration resulted in high solubility of Si and Al from kaolin sample. In addition to alkalinity, the calcination temperature played a role on the solubility of Si and Al ions. MK was more reactive than kaolin as indicated by higher solubility in alkaline solution to produce Si and Al ions. The calcinations temperatures for providing high concentration of Si and Al ion were at 700–800 °C due to complete transformation of Kaol to MK (amorphous). At 750 °C, the highest amount of Si ions was obtained with the use of 10 M NaOH. The maximum content of Al ions was obtained at 700 °C calcined temperature. 750 °C MK was chosen for next experiments and MK was stand for the 750 °C calcined kaolin.

3.3. Characteristics and properties of CH–MK samples

3.3.1. Mineralogical compositions from XRD patterns

XRD patterns of the pozzolanic reaction products made of CH and MK are shown in Fig. 3. The alteration of spectra clearly observed at 26.75° and 34.25° 2θ were assigned as quartz (Q) (SiO_2, 88-2302) and Portlandite (P) ($Ca(OH)_2$, 87-0673), respectively. The available CH left behind after the pozzolanic reaction at 28 days curing was maximum

Table 3
Silicon and aluminum ion concentrations in sodium hydroxide solution after leaching tests.

NaOH solution	Si ion (ppm)				
	non-calcine	650 °C	700 °C	750 °C	800 °C
0.01 M	2.52	5.46	6.80	6.13	6.00
0.1 M	5.86	7.87	7.60	8.94	11.61
1 M	10.68	29.00	28.20	28.73	29.00
3 M	20.47	116.70	149.99	151.14	149.32
5 M	29.94	188.16	191.03	244.11	230.44
10 M	52.61	193.89	232.54	247.37	241.15
NaOH solution	Al ion (ppm)				
	non-calcine	650 °C	700 °C	750 °C	800 °C
0.01 M	n.a.	n.a.	n.a.	n.a.	n.a.
0.1 M	n.a.	0.05	0.05	0.29	0.06
1 M	1.40	11.21	11.32	10.65	10.99
3 M	8.89	90.66	82.59	80.97	82.95
5 M	31.95	109.83	166.86	162.71	156.45
10 M	42.99	103.38	160.83	153.91	158.16

n.a. is not available.

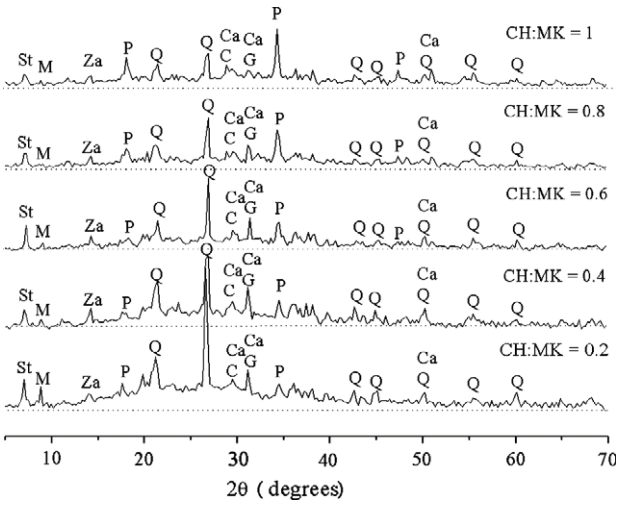

C = calcite, Ca = CSH (I), G = gehlenite, M = muscovite, P = portlandite, Q = quartz, St = stratlingite, Za = zeolite A

Fig. 3. XRD patterns of pozzolanic reaction products with different CH:MK ratios.

at CH:MK of 1.0 and minimum at 0.2. It was shown that CH was required in the reaction at the certain amount. Muscovite and quartz were higher reactive with an increase in CH content resulting in the reduction of their reflection intensity. Calcium silicate hydrate in a form of CSH (I) gel was found. The previous research reported the formation of poorly crystalline CSH (I) in lime--pozzolan system with hydrothermal activation and suitable curing time corresponding to around 7.82°, 29.35°, 32.05° and 50.08° of 2θ (Hong and Glasser, 2004). In addition, the occurrence of tobermorite like C-S-H (I) with CaO/SiO_2 of ~0.67–1.5 was reported in several works (Richardson, 2004, García et al., 2009; Zhang et al., 2009). In this study, semicrystalline CSH (I) was found in every varied ratio. Calcium aluminosilicate hydrate (CASH) compounds composed of stratlingite ($Ca_2Al_2SiO_78H_2O$; C_2ASH_8, 29-0285), gehlenite ($Ca_2Al_2SiO_78H_2O$; C_2ASH_8, 19-0210) and zeolite A ($((Si_4Al_8Ca_2)_{24}(H_2O)_{12}$,86-2218). As shown in Fig. 3, the high contents of zeolite and gehlenite were at CH:MK of 0.4. Therefore, the amount of CaO and SiO_2 significantly affected on the phase formation of both CSH (I) gel and CASH compounds.

3.3.2. Microstructure from FTIR

The FTIR spectra of CH:MK = 0.2–1.0 pastes are shown in Fig. 4. The spectra exhibited the presence of typical O–H stretching vibrations (ν).

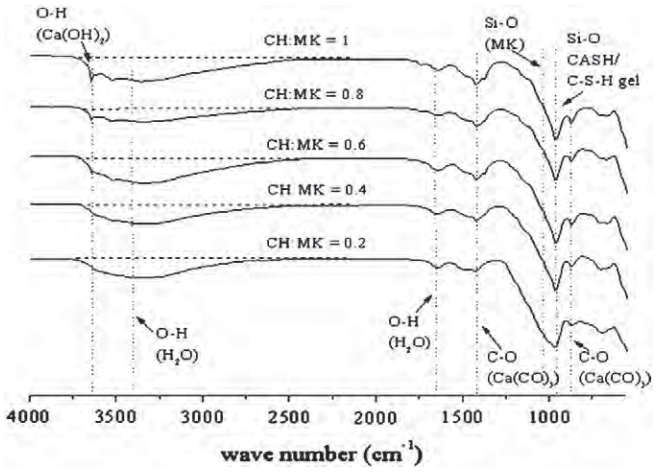

Fig. 4. FTIR spectra of pozzolanic reaction products with different CH:MK ratios.

A broad transmission around 3400 cm^{-1} corresponded to CSH (I) gel. A sharp band at 3630 cm^{-1} corresponding to O–H in calcium hydroxide (Panagiotopoulou et al., 2007) was clearly seen in the mixtures with CH:MK of 0.6–1.0. This indicated the high content of CH remained after pozzolanic reaction and was consistent with the XRD results. The spectra were deconvoluted at the range of 1800–550 cm^{-1} to identify the overlapping peaks at the same frequency with computer software that fits the theoretical curve to the original spectrum (García et al., 2008) as shown in Fig. 5. At CH:MK of 0.2, broad peaks of 1030 cm^{-1} (g) corresponded to the stretching vibration (García et al., 2008) of Si–O in the residue MK after the pozzolanic reaction. Peak at 975 cm^{-1} (h) corresponding to Si–O in CSH gel phase (García et al., 2008, 2010) was detected with the highest content at CH:MK of 0.6. High CH:MK of 0.4–1.0 increased the peak areas around 630 cm^{-1} (l) of Si–O (Si–O–Si, Si–O–Al) bending vibration (δ). In addition, calcite ($CaCO_3$) with C–O stretching vibration around 850–700 cm^{-1} (i, j) and around 1500–1420 cm^{-1} (c, d) (García et al., 2008, 2010) was found in every mixture. Peaks around 1640 cm^{-1} (b) corresponded to O–H bending vibration of H_2O. The results showed that CH:MK of 0.4 contained small residue of CH with the higher CH:MK ratios and was consistence with the XRD result.

3.3.3. Mechanical properties and density

The results of compressive strength and bulk density are shown in Table 4. The highest compressive strength of 17.0 MPa were obtained from samples with CH:MK 0.4 and 0.6. While, the lowest strength (11.0 MPa) was obtained from CH:MK of 1.0 due to the excess hydrated lime. The CH:MK of 0.2 also gave low strength of 12.0 MPa due to

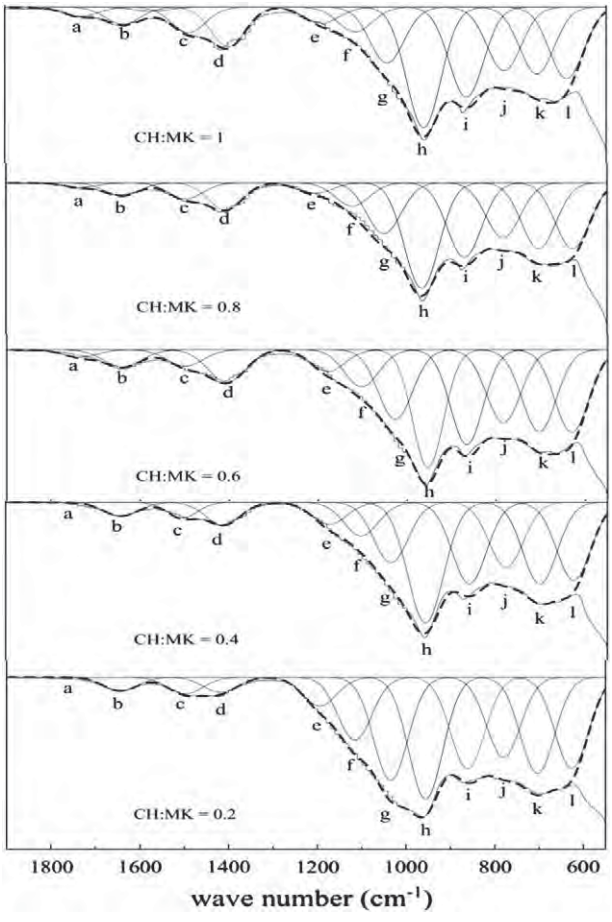

Fig. 5. Deconvolution of FTIR spectra of pozzolanic reaction products with different CH:MK ratios.

Table 4
Compressive strength and density of CH–MK products with different CH:MK ratios.

Samples CH:MK	Properties of products	
	Compressive strength (MPa)/Std.	Density (g/cm^3)
0.2	12.0/0.52	1.05
0.4	17.0/0.21	1.06
0.6	17.0/0.76	1.12
0.8	15.0/0.12	1.11
1.0	11.0/0.62	1.10

Std. = standard deviation.

insufficient CH content for the pozzolanic reaction. The highest density of 1.12 g/cm^3 was obtained with the CH:MK of 0.6 and was in good agreement with the highest compressive strength and CSH gel contents confirmed by XRD and FTIR results. However, the density of sample made of CH:MK of 0.4 (1.06 g/cm^3) was slightly lower than that sample made of CH:MK of 0.6 (1.12 g/cm^3), while their strengths were similar. The difference in the density could be from the difference in the secondary phase resulting in different packing behaviors of samples.

3.4. Characteristics and properties of CH and MK mixed product in NaOH solution with different concentration

3.4.1. Mineralogical compositions from XRD patterns

Fig. 6 shows XRD-patterns of the pozzolanic reaction products using CH:MK of 0.4 (CaO/SiO$_2$ of 1.18) with various alkalinities of 0.01, 0.1, 1, 3, 5, 10 M NaOH solutions. Portlandite was found in samples activated with low NaOH concentration representing incomplete chemical reaction between CaO and SiO$_2$ and/or Al$_2$O$_3$. CaCO$_3$ was also found in samples both with and without alkaline activation. However, muscovite and quartz were still left behind under alkaline activation. At low NaOH concentrations (0.01 and 0.1 M), poorly crystalline CSH (I) and crystalline CASH compounds of stratlingite, gehlenite and zeolite could be observed. At higher NaOH concentration (1 M), stratlingite, zeolite and poorly crystalline CSH (I) disappeared. At 3 M NaOH, sodium aluminosilicate hydrate (NASH) compounds were formed corresponding to chabazite ($Na_{3.16}Al_{3.72}Si_{8.28}O_{24}(H_2O)_{9.68}$, 88-1261) together with the formations of gmelinite ($Na_2Si_4Al_2O_{12}(H_2O)_5$, 75-1682) and zeolite ZK-14 (84-0695). Moreover, some part of Na^+ ions was found in a form of Na_2CO_3. The NASH compound was found around 7.15° 2θ corresponding to gmelinite ($Na_2Si_4Al_2O_{12}(H_2O)_5$, 75-1682) with the presence of lawsonite, ($CaAl_2$ (Si_2O_7)$(OH)_2(H_2O)$, 76-1808). At 5 M NaOH, the phase formation was similar to that of 3 M NaOH. In addition, the combination of sodium and calcium ions could be found in a form of sodium calcium silicate hydrate ($Na_2CaSi_2O_6(H_2O)_2$, NCSH) due to a substitution of Na^+ ion in Ca^{+2} site of CSH compounds (Hong and Glasser, 2004). At 10 M NaOH, NASH, NCSH and katoite (calcium aluminium silicate hydroxide, $Ca_3Al_2(SiO_4)(OH)_8$), 38-0368) occurred with the disappearance of Portlandite. Poorly crystalline CSH (I) and CASH compounds disappeared at the high alkaline activation and NASH was developed in significant quantity. Calcium ions, therefore, precipitated favorably as CaCO$_3$ in a great quantity. At high alkalinity (>1 M) sodium ions from NaOH solution played an important role both in dissolution and precipitation stages.

For alkaline activated CH–MK with CaO/SiO$_2$ of 1.18, the boundary of phase transformation from no sodium bearing compounds to sodium bearing compounds was at 1 M NaOH. From the above results, pozzolanic reaction products (poorly crystalline CSH (I) and CASH compounds) were found at 0.01 M NaOH, but at 1 M NaOH, pozzolanic reaction products disappeared and NASH was formed and played a role on the obstruction of pozzolanic reaction product formation. The alkaline aluminosilicates viz., NASH in the forms of zeolitic and geopolymeric products were formed rapidly within 24 h (Khale and Chaudhary, 2007) rather than pozzolanic reaction product formation in form of CSH gel and crystalline CASH phases (more than 24 h) (Cabrera and Rojas, 2001; Sabir et al., 2001; Siddique and Klaus, 2009). At the same time of building up geopolymer structure via polymerization, crystalline zeolite could also be formed (Chindaprasirt et al., 2009). Moreover, the [OH$^-$] species impeded Ca(OH)$_2$ dissolution and resulting in insufficient Ca^{2+} ions existed to achieve saturation and no CSH gel was formed (Alonso and Palomo, 2001b). At 3–5 M NaOH, a large amount of zeolitic products was found as compared with that of 1 M NaOH. For 10 M NaOH

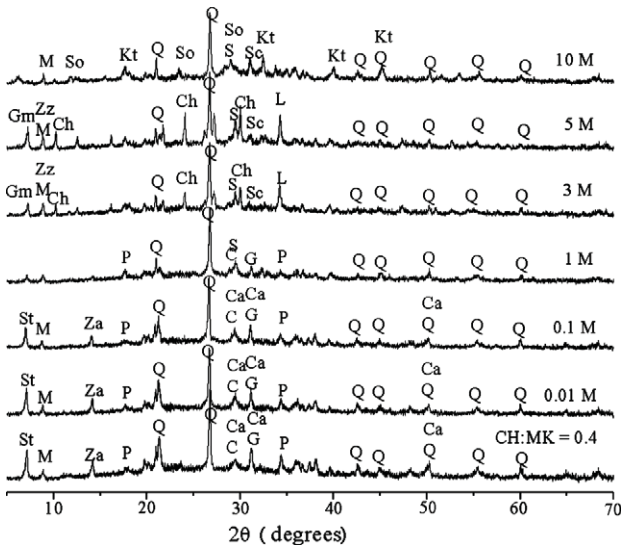

C = calcite, Ca = CSH (I), Ch = chabazite, G = gehlenite, Gm = gmelinite, Kt = katoite, L = lawsonite, M = muscovite,P = portlandite, Q = quartz, S = sodium carbonate, Sc = sodium calcium silicate hydrate, So = sodium alumino silicate hydrate, St = stratlingite, Za = Zeolite A, Zz = zeolite ZK-14

Fig. 6. XRD patterns of alkaline activated CH–MK with 0.4 of CH:MK ratio at various alkaline concentration activations (0.01, 0.1, 1, 3, 5 and 10 M NaOH).

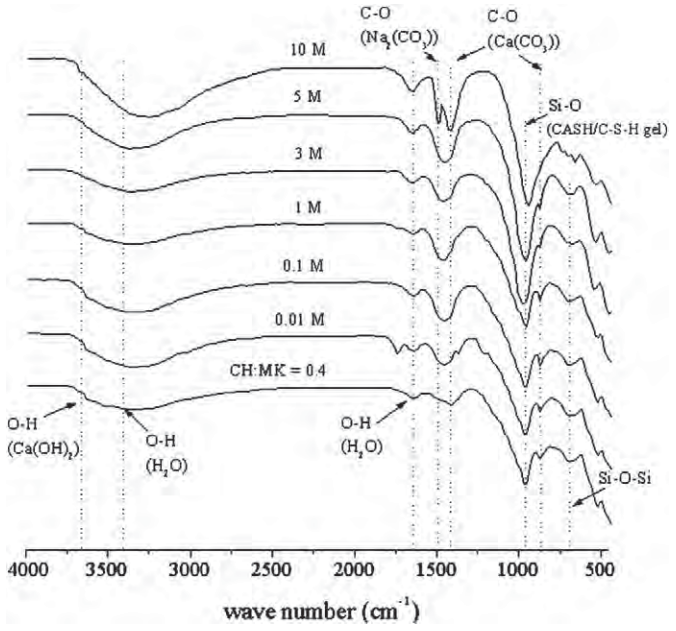

Fig. 7. FTIR spectra of alkaline activated CH–MK with CH:MK of 0.4 at various NaOH concentrations.

activation, both pozzolanic reaction products and zeolitic products disappeared due to the presence of very large amount of [OH^-] species which affected the formation of CSH gel, and the structural rearrangement to form crystalline zeolite was also obstructed. However, geopolymer gel could be formed (Davidovits, 1989, 1991) but was very difficult to be identified by XRD.

3.4.2. Microstructure from FTIR

The FTIR spectra of the mixture at 0.4 CH:MK with 0.01–10 M NaOH are shown in the Fig. 7. Peak around 3630 cm^{-1} corresponded to O–H in calcium hydroxide at 0.01 M, 0.1 and 1 M NaOH activations, but disappeared at 3 M, 5 M and 10 M NaOH activations. The wave number around 550–1800 cm^{-1} represented phase transformation. The spectra in this range were deconvoluted to identify the overlapped peaks as shown in Fig. 8. Si–O stretching vibration peaks around 960–950 cm^{-1} (García et al., 2008, 2010) of CSH gel, and crystalline CASH, NASH and NCSH compounds were found. Peaks around 1030–1073 cm^{-1} of Si–O of quartz (García et al., 2008, 2010) were also found in every NaOH concentration. In addition, the other phase observed in the sample activated by 0.01–5 M NaOH was around 1500–1400 cm^{-1} and 870 cm^{-1} corresponding to C–O vibration of CO_3^{-2} in $CaCO_3$. At 10 M NaOH, the spectrum showed different character from the other NaOH concentrations with two sharp spectrums at around 1500–1400 cm^{-1} and disappeared at 870 cm^{-1}. This suggested that $CaCO_3$ was transformed to the other phase. Moreover, the spectrum around 1070–950 cm^{-1} corresponded to Si–O indicated three categorizes of structures at low 0.01–1 M, medium 3–5 M and high at 10 M NaOH. At 0.01–1 M, sharp peaks around 960–955 cm^{-1} corresponding to Si–O stretching vibration of CSH gel (tobermorite-like structure) (García et al., 2008, 2010) could be observed. At 3–5 M NaOH, peaks around 960–955 cm^{-1} corresponding to Si–O stretching vibration of zeolitic products could be detected. Peaks around 1070–1000 cm^{-1} corresponding to Si–O stretching vibration of quartz and Si–O of geopolymer gel were found. At 10 M NaOH, the height of peaks of around 1000–950 cm^{-1} decreased due to the reduction of zeolitic products. This indicated that the alkalinity affected on phase transformation of samples made of CH:MK ratio of 0.4.

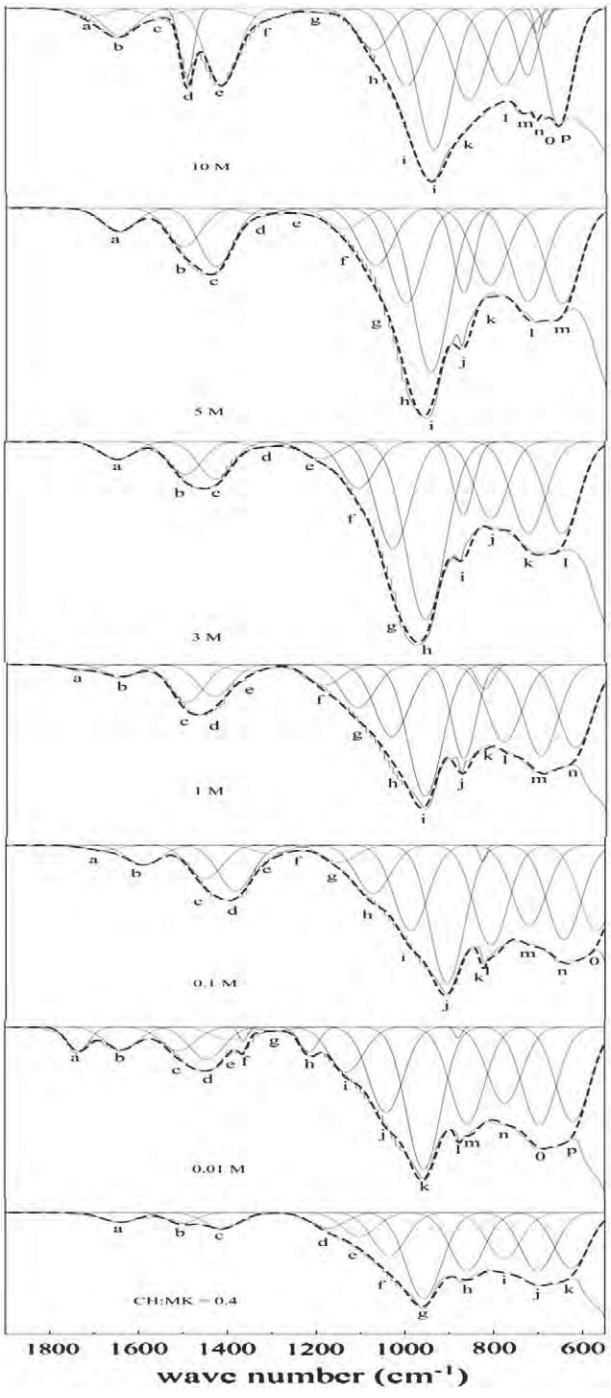

Fig. 8. Deconvolution of FTIR spectra of alkaline activated CH–MK with CH:MK of 0.4 at various NaOH concentrations.

At low concentration of NaOH (<1 M), the pozzolanic reaction was dominant. While the zeolitic reaction and geopolymerization became dominant at medium NaOH concentration (1 M < NaOH < 5 M) and at high NaOH concentration (>5 M), respectively as shown in the following equation.

$$\underset{}{MK + CH + H_2O} \overset{NaOH<1M}{=>} \text{Pozzolanic reaction} \overset{1M<NaOH<5\ M}{=>} \text{Zeolitic reaction} \overset{NaOH>5\ M}{=>} \text{Geopolymerization}$$

3.4.3. Microstructure from SEM

SEM-photomicrographs and EDS spectrum of CH:MK mixture under NaOH activation are shown in Fig. 9. The structure of CH:MK activated with 0.01 and 0.1 M as shown in Fig. 9(b, c) did not change comparing to non-activation system. At 1 M activation as shown in Fig. 9(d), the structure was deformed to have very small particles and fragment. At 3 and 5 M activation as shown in Fig. 9(e, f), the small content of CSH gel (A) and of NASH gel (B) were found as confirmed by EDS. In addition, very small crystalline NASH (C) was found. At the medium range of concentration, microstructures of samples showed highly interconnected phases of CSH and NASH gels. At 10 M as shown in Fig. 9(g), NASH phase was found in form of particulates with particle size around 1 μm. At high NaOH concentration, the development of NASH particles resulted in the disruption of interconnecting phase and the porosity of matrix was thus high.

3.4.4. Mechanical properties and density

The result of compressive strength and density of samples made of 0.4 CH:MK ratio with various NaOH concentrations are shown in Table 5. The highest strength of 19.0 MPa was obtained with 0.01 M NaOH activation due to the formations of both CSH (I) gel and CASH compounds. The strength of 0.1 M NaOH sample slightly decreased to 18.0 MPa. From the microstructure of low alkaline activated products, the CSH gel network was found which affected on the high strength. The strength decreased significantly to 12.0 MPa with an increase in NaOH concentration to 1 M due to the disappearance of CSH (I) gel phase as the pozzolanic reaction was obstructed by [OH^-] species. At 3 M and 5 M NaOH, the compressive strength increased to 13.0 and 17.0 MPa, respectively because zeolitic products viz., chabazite and gmelinite and new CASH compound were formed as the cause of

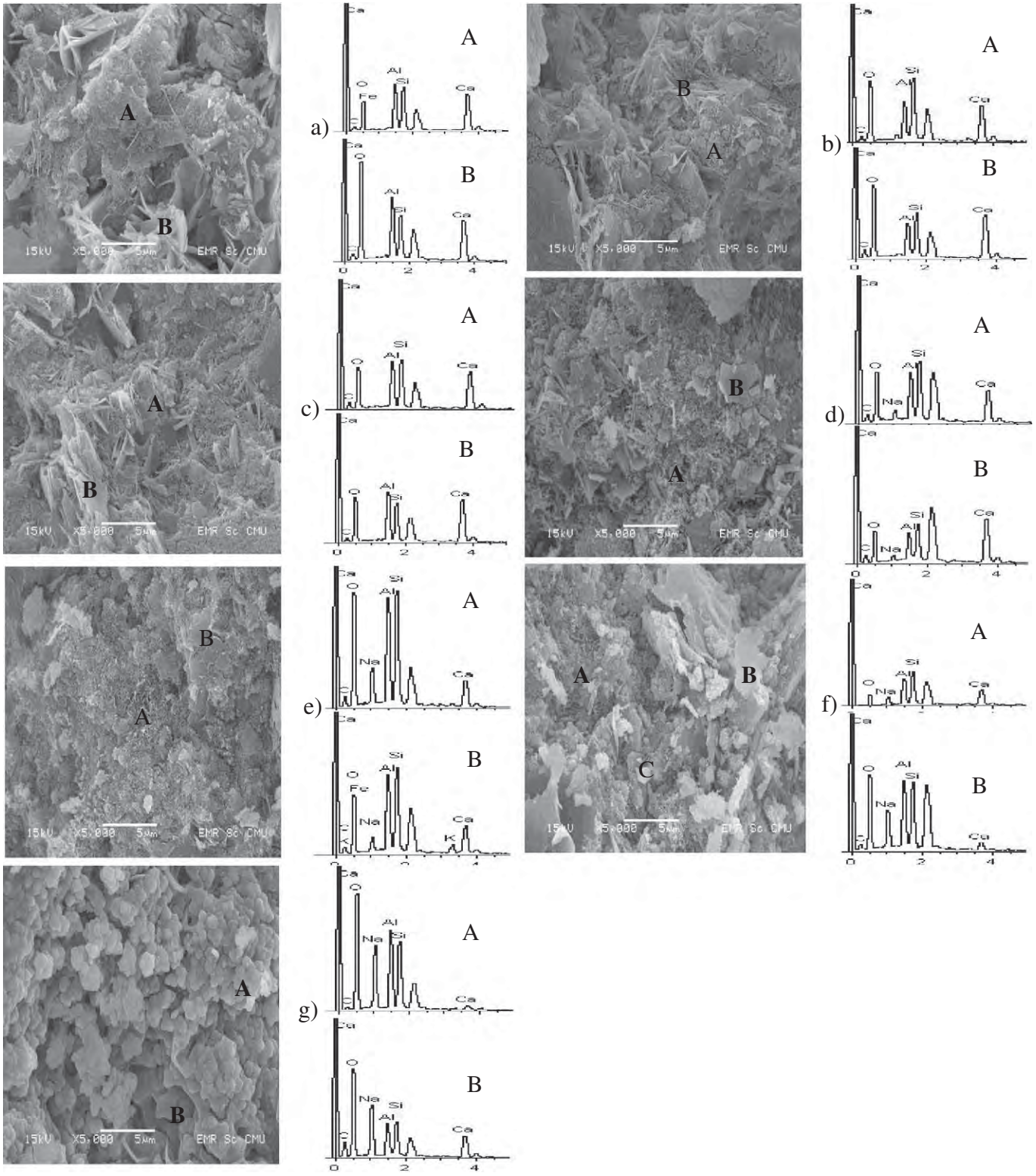

Fig. 9. SEM photomicrographs of CH:MK of 0.4 (a) and CH:MK of 0.4 with NaOH activation at various concentrations, 0.01 M (b), 0.1 M (c), 1 M (d), 3 M (e), 5 M (f) and 10 M (g).

dense microstructure. At 10 M NaOH, the compressive strength greatly decreased to 7.0 MPa due to the structure rearrangement and the formation of zeolitic products was hindered. NCSH compound and geopolymeric gel with a little amount of zeolitic phases was not as strong as CSH gel, CASH compound and zeolitic structures. In addition, the small particles were found in microstructure which implied that as the reason of decreasing of the strength in this product. The results also revealed that density tended to increase with an increase in NaOH concentration.

However, the curing of samples was done at low temperature of 25 °C. The strength of the samples especially at high NaOH concentration could be further improved with moderate temperature curing (45–70 °C) (Boonserm et al., 2012; Chindaprasirt et al., 2012; Hewlett, 1988).

Table 5
Compressive strength and density of alkaline activated CH–MK products with CH:MK of 0.4 at various NaOH concentrations.

Alkaline activation of CH:MK of 0.4	Properties of products	
	Compressive strength (MPa)/Std.	Density (g/cm^3)
Non-activation	17.0/0.52	1.06
0.01 M	19.0/0.60	1.06
0.1 M	18.0/0.23	1.08
1 M	12.0/0.43	1.03
3 M	13.0/0.18	1.11
5 M	17.0/0.89	1.16
10 M	7.0/0.65	1.35

Std. = standard deviation.

4. Conclusions

This study investigated the phase development due to pozzolanic reaction of MK and CH with alkaline activation. The conclusions were as follows;

1. The CH:MK ratios of 0.4 and 0.6 with CaO/SiO_2 (amorphous SiO_2) of 1.18 and 1.76 were the proper conditions to complete the pozzolanic reaction of MK as indicated by the higher pozzolanic reaction product contents of CSH gel and crystalline CASH compounds than those at the other ratios. This resulted in the high compressive strength of lime calcined clay materials.
2. The strength of CH:MK of 0.4 with alkaline activation at low NaOH concentration (0.01 and 0.1 M NaOH) was higher due to the formation of CSH (I) gel. At slightly higher NaOH concentration (1 M), the strength was significantly reduced due to the reduction of CSH (I) gel phase. At moderate NaOH concentrations (3 and 5 M), CSH (I) gel disappeared while zeolitic products, and NASH and NCSH compounds were formed and strength improved to be slightly less than those at the low NaOH concentration. A high NaOH concentration (10 M), the zeolitic products disappeared and alkali aluminosilicate hydrate was formed and adversely affected the strength.
3. The reaction of the mixture was dependent on the NaOH concentration. At low concentration of NaOH (<1 M), the pozzolanic reaction was dominant. The zeolitic reaction was dominant at medium NaOH concentration (1 M < NaOH <5 M) and geopolymerization became dominant at high NaOH concentration (>5 M).

Acknowledgment

This work was financially supported by Office of the Higher Education Commission (032/54), Chiang Mai Rajabhat University and by the Thailand Research Fund (TRF) under TRF Senior Research Scholar Contract No. RTA5480004. The Laboratories were supported by Physics and Materials department and by Industrial Chemistry department, Faculty of Science, Chiang Mai University, and Science Center, Chiang Mai Rajabhat University.

References

Alonso, S., Palomo, A., 2001a. Calorimetric study of alkaline activation of calcium hydroxide–metakaolin solid mixtures. Cem. Concr. Res. 31 (1), 25–30.
Alonso, S., Palomo, A., 2001b. Alkaline activation of metakaolin and calcium hydroxide mixtures: influence of temperature, activator concentration and solids ratio. Mater. Lett. 47 (1), 55–62.
ASTM C125-11a, 2011. Standard Terminology Relating to Concreate and Concrete Aggregate. Annual Book of ASTM Standard 4.02.
Bich, Ch., Ambroise, J., Péra, J., 2009. Influence of degree of dehydroxylation on the pozzolanic activity of metakaolin. Appl. Clay Sci. 44 (3–4), 194–200.
Bondar, D., Lynsdale, C.J., Milestone, N.B., Hassani, N., Ramezanianpour, A.A., 2011. Effect of adding mineral additives to alkali-activated natural pozzolan paste. Constr. Build. Mater. 25, 2906–2910.
Boonserm, K., Sata, V., Pimraksa, K., Chindaprasirt, P., 2012. Improved geopolymerization of bottom ash by incorporating fly ash and using waste gypsum as additive. Cem. Concr. Compos. 34 (7), 819–824.
Cabrera, J., Rojas, M.F., 2001. Mechanism of hydration of the metakaolin–lime–water system. Cem. Concr. Res. 31 (2), 177–182.
Carroll, D., Starkey, H.C., 1971. Reactivity of clay minerals with acids and alkalies. Clays Clay Minerals 19, 321–333.
Chen, J.J., Thomas, J.J., Taylor, H.F.W., Jennings, H.M., 2004. Solubility and structure of calcium silicate hydrate. Cem. Concr. Res. 34 (9), 1499–1519.
Chindaprasirt, P., Pimraksa, K., 2008. A study of fly ash–lime granule unfired bricks. Powder Technol. 182, 33–41.
Chindaprasirt, P., Jaturapitakkul, C., Chalee, W., Rattanasak, U., 2009. Comparative study on the characteristics of fly ash and bottom ash geopolymers. Waste Manag. 29 (2), 539–543.
Chindaprasirt, P., De Silva, P., Sagoe-Crentsil, K., Hanjitsuwan, S., 2012. Effect of SiO_2 and Al_2O_3 on the setting and hardening of high calcium fly ash based geopolymer systems. J. Mater. Sci. 47 (12), 4876–4883.
Davidovits, J., 1989. Geopolymers and geopolymeric materials. J. Therm. Anal. 35 (2), 429–441.
Davidovits, J., 1991. Geopolymers, inorganic polymeric new materials. J. Therm. Anal. 37 (8), 1633–1656.
Deschner, F., Winnefeld, F., Lothenbach, B., Seufert, S., Schwesig, P., Dittrich, S., Goetz-Neunhoeffer, F., Neubauer, J., 2012. Hydration of Portland cement with high replacement by siliceous fly ash. Cem. Concr. Res. 42, 1389–1400.
Fennis, S.A.A.M., Walraven, J.C., den Uijl, J.A., 2009. The use of particle packing models to design ecological concrete. HERON 54, 185–204.
Fernandez, R., Martirena, F., Scrivener, K.L., 2011. The origin of the pozzolanic activity of calcined clay minerals: a comparison between kaolinite, illite and montmorillonite. Cem. Concr. Res. 41, 113–122.
Frías, M., Sánchez de Rojas, M.I., Cabrera, J., 2000. The effect that the pozzolanic reaction of metakaolin has on the heat evolution in metakaolin-cement mortars. Cem. Concr. Res. 30 (2), 209–216.
García, L.I., Fernández-Jiménez, A., Teresa Blanco, M., Palomo, A., 2008. FTIR study of the sol–gel synthesis of cementitious gels: C-S-H and N-A-S-H. J. Sol–Gel Sci. Technol. 45 (1), 63–72.
García, L.I., Macphee, D.E., Palomo, A., Fernández-Jiménez, A., 2009a. Effect of alkalis on fresh C–S–H gels. FTIR analysis. Cem. Concr. Res. 39 (8), 147–153.
García, R., Vigil de la Villa, R., Rodríguez, O., Frías, M., 2009b. Mineral phases formation on the pozzolan/lime/water system. Appl. Clay Sci. 43 (3–4), 331–335.
García, L.I., Fernández-Jimenez, A., Palomo, A., Macphee, D.E., 2010. Effect on fresh C-S-H gels of the simultaneous addition of alkali and aluminium. Cem. Concr. Res. 40 (1), 27–32.
Granizo, M.L., Alonso, S., Blanco-Varela, M.T., Palomo, A., 2002. Alkaline activation of metakaolin: effect of calcium hydroxide in the products of reaction. J. Am. Ceram. Soc. 85 (1), 225–231.
Hewlett, P.C., 1988. Lea's Chemistry of Cement and Concrete, Special Cement, fourth ed. Linacre House Jordan Hill, Oxford, UK, pp. 783–840.
Hong, S.Y., Glasser, F.P., 2004. Phase relations in the CaO–SiO2–H2O system to 200 °C at saturated steam pressure. Cem. Concr. Res. 34 (9), 1529–1534.
Jaturapitakkul, C., Tangpagasit, J., Songmue, S., Kiattikomol, K., 2011. Filler effect of fine particle sand on the compressive strength of mortar. Int. J. Miner. Metal. Mater. 18 (2), 240–246.
Kakali, G., Perraki, T., Tsivilis, S., Badogiannis, E., 2001. Thermal treatment of kaolin: the effect of mineralogy on the pozzolanic activity. Appl. Clay Sci. 20 (1–2), 73–80.
Khale, D., Chaudhary, R., 2007. Mechanism of geopolymerization and factors influencing its development: a review. J. Mater. Sci. 42 (3), 729–746.
Mechti, W., Mnif, T., Samet, B., Rouis, M.J., 2012. Effects of the secondary minerals on the pozzolanic activity of calcined clay:case of quartz. IJRRAS 12 (1), 61–71.
Panagiotopoulou, Ch., Kontori, E., Perraki, Th., Kakali, G., 2007. Dissolution of aluminosilicate minerals and by-products in alkaline media. J. Mater. Sci. 42 (9), 2967–2973.
Poon, C.S., Lam, L., Kou, S.C., Wong, Y.L., Wong, R., 2001. Rate of pozzolanic reaction of metakaolin in high-performance cement pastes. Cem. Concr. Res. 31 (9), 1301–1306.
Richardson, I.G., 2004. Tobermorite/jennite- and tobermorite/calcium hydroxide-based models for the structure of C-S-H: applicability to hardened pastes of tricalcium silicate, β-dicalcium silicate, Portland cement, and blends of Portland cement with blast-furnace slag, metakaolin, or silica fume. Cem. Concr. Res. 34 (2), 1733–1777.
Sabir, B.B., Wild, S., Bai, J., 2001. Metakaolin and calcined clays as pozzolanic for concrete: a review. Cem. Concr. Compos. 23 (6), 441–454.
Shvarzman, A., Kovler, K., Grader, G.S., Shter, G.E., 2003. The effect of dehydroxylation/amorphization degree on pozzolanic activity of kaolinite. Cem. Concr. Res. 33 (3), 405–416.
Siddique, R., Klaus, J., 2009. Influence of metakaolin on the properties of mortar and concrete: a review. Appl. Clay Sci. 43 (3–4), 392–400.
Steveson, M., Sagoe-Crentsil, K., 2005. Relationships between composition, structure and strengthof inorganic polymers. J. Mater. Sci. 40 (16), 4247–4259.
Verdolotti, L., Iannace, S., Lavorgna, M., Lamanna, R., 2008. Geopolymerization reaction to consolidate incoherent pozzolanic soil. J. Mater. Sci. 43 (3), 865–873.
Vizcayno, C., Gutierrez, R.M., Castello, R., Rodriguez, E., Guerrero, C.E., 2010. Pozzolan obtained by mechanochemical and thermal treatments of kaolin, Appl. Clay Sci. 49 (4), 405–413.
Yip, C.K., Lukey, G.C., Van Deventer, J.S.J., 2005. The coexistence of geopolymeric gel and calcium silicate hydrate at the early stage of alkaline activation. Cem. Concr. Res. 35 (9), 1688–1697.
Yock, A., 2009. Geotermometry. Geothermal training programme. United Nation University, pp. 1–8.
Zhang, B., MacKenzie, K.J.D., Brown, I.W.M., 2009. Crystalline phase formation in metakaolinite geopolymers activated with NaOH and sodium silicate. J. Mater. Sci. 44 (17), 4668–4676.

KSCE Journal of Civil Engineering (2014) 18(5):1429-1435
DOI 10.1007/s12205-014-0637-5

Structural Engineering
pISSN 1226-7988, eISSN 1976-3808
www.springer.com/12205

Investigation of Properties of Lightweight Concrete with Calcined Diatomite Aggregate

Patcharapol Posi*, Surasit Lertnimoolchai, Vanchai Sata***, Tanakorn Phoo-ngernkham****, and Prinya Chindaprasirt*****

Received February 26, 2012/Accepted July 26, 2013/Published Online May 20, 2014

Abstract

This paper reports the investigation of the properties of Lightweight Concrete (LWC) made from Portland cement and diatomite aggregate. The chemical and physical properties of diatomite and the mechanical properties of LWC with regard to the effects of calcined temperature and gradation were studied. The uncalcined diatomite was crushed and calcined at 400, 600, and 800°C for 4 hours and used as lightweight aggregate. A constant Water to Cement ratio (W/C) of 2.0 and Aggregate to Cement ratio (A/C) of 1.6 were used for all mixes. The 28-day compressive strength of LWC of 6.4-11.9 MPa, porosity and water absorption of 34.0-49.4%, modulus of elasticity of 2.0-4.3 GPa, thermal conductivity of 0.166-0.192 W/mK, and unit weight of 1170-1300 kg/m^3 were obtained. The results indicated that the strength of concrete increased when the calcined temperature of diatomite and the amount of small-size aggregate were increased. The increase in temperature ridded the burnable elements and improved the properties of diatomite. The small-size aggregate produced good matrix-aggregate bonding and enhanced the strength of concrete. The calcined diatomite could, therefore, be used as good aggregate in making lightweight concrete.

Keywords: *lightweight aggregate, concrete, diatomite, compressive strength, unit weight, porosity, modulus of elasticity*

1. Introduction

Diatomite is a soft sedimentary rock and composed of fossil skeletons of phytoplankton, also known as diatom. It originated in fresh and salt water since the Eocene period and the main composition is amorphous silicon dioxide (SiO_2) (De Rojas *et al.*, 1999). Its beneficial characteristics includes lightweight due to high porosity and attractive dark-yellow shade due to high content of ferrous compound and semi-crystalline siliceous phase (Owen and Utha-aroom, 1999; Pimraksa and Chindaprasirt, 2009). The diatomite could, therefore, be used as lightweight aggregate for Lightweight Concrete (LWC).

LWC is a concrete with unit weight less than normal concrete and not exceeding 1840 kg/m^3 (ASTM C330-89, 1989). The purpose is to reduce the dead load of structure resulting in smaller and lighter structures and also with reduced cement content. The production of cement is an energy intensive operation and accounts for about 7% of the green house gas produced annually (Malhotra, 2002). Lightweight aggregate are popular for use in concrete because they offer some improved physical properties such as high insulating coefficient and superior sound-dampening quality (Jo *et al.*, 2007). The production of LWC is expanding and now includes all types of no-fines concrete of low density of 300-1200 kg/m^3 for block production (Chandra, 2002).

This research aims to use diatomite as lightweight aggregate in making LWC with improved physical properties. The knowledge of the use of diatomite in producing LWC would be beneficial to future applications of this material in the construction industry.

2. Experimental Program

2.1 Materials and Preparation

2.1.1 Materials

Materials consist of Ordinary Portland Cement (OPC) and Diatomite (DE) from Lampang province in northern Thailand.

*Ph.D. Student, Sustainable Infrastructure Research and Development Center, Dept. of Civil Engineering, Khon Kaen University, Khon Kaen 40002, Thailand (E-mail: patcharapolposi@gmail.com)
**Managing Director, Concrete Precision Unique, Udornthani 41000, Thailand (E-mail: cpuudon22@yahoo.com)
***Assistant Professor, Sustainable Infrastructure Research and Development Center, Dept. of Civil Engineering, Khon Kaen University, Khon Kaen 40002, Thailand (E-mail: vancsa@kku.ac.th)
****Ph.D. Student, Sustainable Infrastructure Research and Development Center, Dept. of Civil Engineering, Khon Kaen University, Khon Kaen 40002, Thailand (E-mail: tpcivil2526@gmail.com)
*****Professor, Sustainable Infrastructure Research and Development Center, Dept. of Civil Engineering, Khon Kaen University, Khon Kaen 40002, Thailand (Corresponding Author, E-mail: prinya@kku.ac.th)

Table 1. Chemical Composition of DE (by Weight)

Chemical compositions (%)	25DE	400DE	600DE	800DE
SiO_2	74.30	76.09	78.40	78.29
Al_2O_3	8.07	7.98	8.18	9.43
Fe_2O_3	5.35	5.46	5.19	7.08
CaO	0.48	0.43	0.47	0.54
K_2O	1.76	1.89	1.99	2.21
TiO_2	0.11	0.43	0.51	0.51
Na_2O	0.15	0.13	0.12	0.17
P_2O_5	0.11	0.08	0.09	0.11
BaO	0.04	0.04	0.04	0.04
MgO	0.47	0.43	0.47	0.56
LOI	9.10	7.00	4.50	1.00

Table 2. Physical Properties of DE

Materials	FA	MA	CA
Particle size (mm)	0.001-1.18	1.18-4.75	4.75-12.5
Fineness modulus	1.33	4.02	5.75
Unit weight (kg/m^3)	600	425	417
Water absorption (%)	61	102	112

The uncalcined DE was crushed and then classified as Fine Aggregate (FA), Medium Aggregate (MA), and Coarse Aggregate (CA). The DE aggregates were calcined and kept in the dry condition and used for the mix for ease of control and comparison. They were then calcined at 400, 600, and 800°C for 4 hours (Pimraksa and Chindaprasirt, 2009). The chemical compositions are shown in Table 1 and the physical properties are shown in Table 2. The DE consisted of a high content of SiO_2 with some Al_2O_3, Fe_2O_3, and SO_3. The other compounds viz., CaO, MgO, K_2O, and TiO_2 are also presence in a small quantity.

2.1.2 DE Aggregate Series

Three DE aggregate series were used for the preparation of LWC. As the effect of small aggregate portion is larger than that of large portion (Unal *et al.*, 2007), the CA portion was kept constant and the FA and MA portions were varied. A total of three aggregate series viz., series A, B, and C with FA:MA:CA ratios of 0:70:30, 30:40:30, and 70:0:30, respectively were used as shown in Table 3.

2.2 Mix Details

2.2.1 Mix Proportion

All mixtures were made with Water to Cement ratio (W/C) of 2.0 and Aggregate to Cement ratio (A/C) of 1.6. From trial mixes, the W/C of 2.0 was needed as the DE aggregates were porous. The A/C of 1.6 was selected as higher A/C produced very dry mixes and the casting was difficult. The details of the mixes are given in Table 3. The uncalcined DE (25°C), DE calcined at 400, 600, and 800°C are denoted by 25DE, 400DE, 600DE, and 800DE, respectively.

Table 3. Mix Proportions of Lightweight Concrete

DE	Series	Aggregate			W/C	A/C
		FA (%)	MA (%)	CA (%)		
25DE	A	0	70	30	2.0	1.6
	B	30	40	30		
	C	70	0	30		
400DE	A	0	70	30	2.0	1.6
	B	30	40	30		
	C	70	0	30		
600DE	A	0	70	30	2.0	1.6
	B	30	40	30		
	C	70	0	30		
800DE	A	0	70	30	2.0	1.6
	B	30	40	30		
	C	70	0	30		

2.2.2 Mixing

The OPC and DE were firstly mixed until the mixture was homogenous which took approximately 1½ minutes. Afterward, water was added and the mixing was done for another 1½ minutes. The fresh concretes were immediately cast in 50 × 50 × 50 mm cube molds in accordance with ASTM C109 (2002), and in 100 × 100 × 100 mm cube molds, and 150 × 300 mm cylindrical molds in accordance with ASTM C39 (2001). The specimens were covered with damp cloth and plastic sheet to prevent moisture loss and stored in a 25°C controlled room.

2.3 DTA and TGA, XRD, and SEM

The Differential Thermal Analysis (DTA) and Thermal Gravitation Analysis (TGA) were performed on DE to investigate its physical and chemical changes during heating (Kroehong *et al.*, 2011). Mineralogical compositions of as-received DE were determined using X-Ray Diffraction (XRD) and morphological composition using Scanning Electron Microscope (SEM) (Pimraksa and Chindaprasirt, 2009).

2.4 Compressive Strength

The 50 × 50 × 50 mm cube specimens were tested to determine the compressive strength at the age of 28 days in accordance with ASTM C109 (2002). The reported results were the average of three samples.

2.5 Porosity and Water Absorption

The 100 × 100 × 100 mm cube specimens were tested for the porosity and water absorption at the age of 28 days in accordance with ASTM C642 (2006). The porosity was calculated using Eq. (1) whereas, Eq. (2) was used for the calculation of water absorption. For porosity measurement, the specimens were boiled for 5 hr and then allowed to cool for not less than 14 hr to a final temperature of 20 to 25°C. The surface moisture of the specimen was then removed with a towel and the mass of specimen determined.

The methods for measuring porosity and absorption were used

successfully in a number of researches (Chindaprasirt and Rukzon, 2008; Rukzon and Chindaprasirt, 2008; Thokchom *et al.*, 2009). The reported results were the average of three samples.

$$\text{Porosity}(\%) = [(C-A)/(C-D)] \times 100 \quad (1)$$

$$\text{Absorption}(\%) = [(B-A)/A] \times 100 \quad (2)$$

Where, A = Mass of oven-dry sample in air (g)
B = Mass of surface-dry sample in air after immersion (g)
C = Mass of surface-dry sample in air after immersion and boiling (g)
D = Apparent mass of sample in water after immersion and boiling (g)

2.6 Unit Weight

The unit weight was determined as described in ASTM C138 (2009). The unit weight was measured at the ages of 28 days using the compressive strength specimens. The reported results were the average of three samples.

2.7 Modulus of Elasticity

The 150 × 300 mm cylinder specimens were tested for the chord modulus at the age of 28 days in accordance with ASTM C469 (2002). The reported results were the average of two samples.

2.8 Thermal Conductivity

The 50 × 50 × 50 mm cube specimens were tested to determine the thermal conductivity at the age of 28 days in accordance with ASTM D5930 (2009). The reported results were the average of three samples.

3. Result and Discussions

3.1 Scanning Electron Microscopy

The results of SEM of DE are shown in Fig. 1. The DE consisted of cylindrical shape particles approximately 10 μm in diameter and 30 μm in length with square cellular structure as shown in Fig. 1(a). The surface consisting of micro-pores made DE very porous and low in density (Pimraksa and Chindaprasirt, 2009; Pimraksa *et al.*, 2011). The calcination at temperatures of 400, 600, and 800ºC for 4 hours did not appear to drastically change the morphology of particles. The cylindrical shape particles with cellular surface were still easily detected as shown in Figs. 1(b)-1(d).

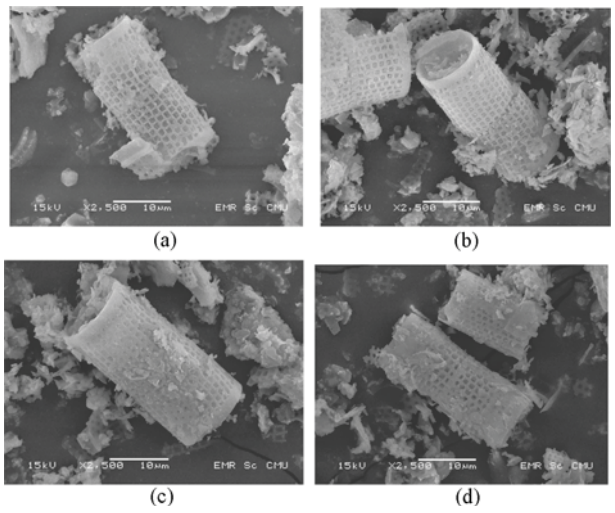

Fig. 1.SEM Photomicrographs of Diatomite: (a) Uncalcined DE (25DE), (b) 400DE, (c) 600DE, (d) 800DE

3.2 Differential Thermal Analysis (DTA) and Thermal Gravitation Analysis (TGA)

The results of DTA and TGA of diatomite are shown in Fig. 2. The endothermic peaks were observed at 71.6°C and 148.8ºC and were associated with loss of adsorbed water on particle surfaces of diatomite. The other peak at 482.2ºC ascribed to loss of dehydroxylation of clay minerals containing in DE (Pimraksa and Chindaprasirt, 2009). This, therefore, indicated that the optimum calcined temperature for reactive diatomite should not be less than 482ºC.

3.3 Mineralogical and Morphological Composition using XRD

The XRD results of DE are shown in Fig. 3. The DE contained

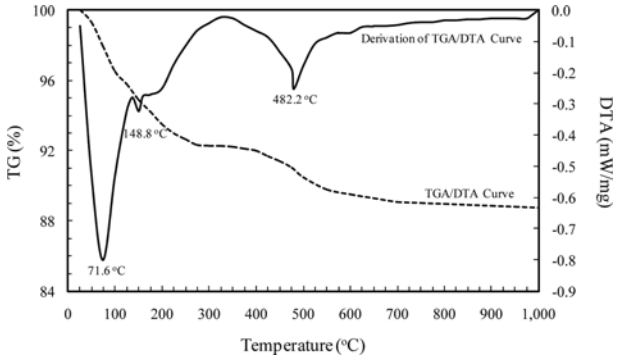

Fig. 2. DTA and TG Curves of Diatomite

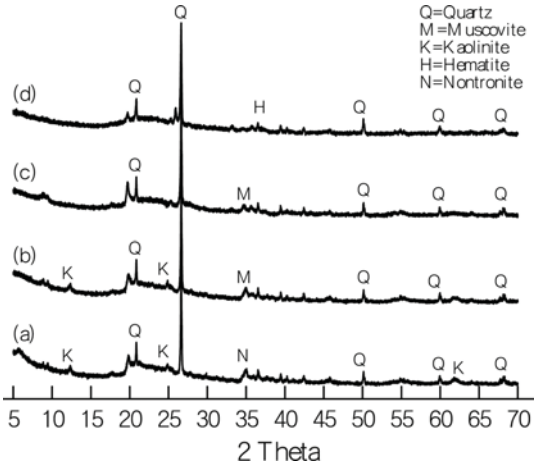

Fig. 3. XRD Patterns of Calcined DE: (a) Uncalcined DE, (b) 400ºC, (c) 600ºC, (d) 800ºC

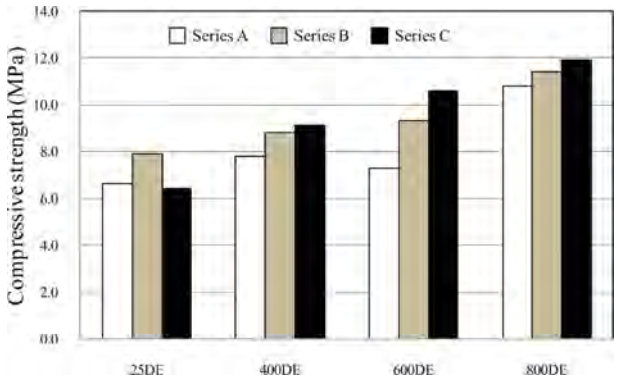

Fig. 4. Compressive Strength at 28 Days Lightweight Concrete

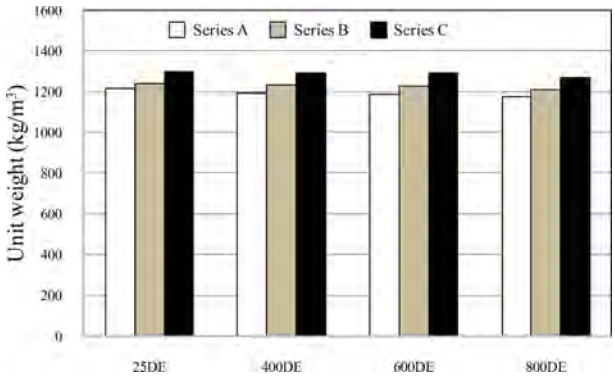

Fig. 5. Unit Weight at 28 Days of Lightweight Concrete

mainly quartz, kaolinite and some nontronite. Calcination at 400°C reduced the peaks of kaolinite and nontronite. At higher temperature of 600°C, the kaolinite and nontronite peak disappeared. This corresponded to the dehydroxylation of kaolinite when clay mineral (kaolinite) were calcined and thus became active (Baronio and Binda, 1997). This was confirmed by the disappearance of main peaks of kaolinite at 12.5, 24.8, and 61.8° 2θ. At 800°C, a small amount of hematite was observed. This mineral was stable and indicated that the calcinations temperature should be less than 800°C in order to obtain amorphous phase of DE and for the reduction of cost of calcination.

3.4 Compressive Strength

The results of compressive strength of lightweight concrete are shown in Fig. 4. The compressive strength slightly increased with the increasing calcined temperature of DE. For example, the 28-day compressive strengths of series B mixes for the 25DE, 400DE, 600DE, and 800DE were 7.9, 8.8, 9.3, and 11.4 MPa, respectively. The low compressive strength of the 25DE mix was due to the unstable and swelling of kaolinite (Charles *et al.*, 2007). The strength of 400DE mix was also low compared with those of 600DE and 800DE mixes. This conformed to the results of the DTA and TGA which indicated that the calcined temperature of DE should not be less than 482°C. A number of researches suggested the calcined temperature between 600-800°C as optimum temperature for DE (Pimraksa and Chindaprasirt, 2009; Pimraksa *et al*., 2011).

With regards to aggregate sizes, the mixes with a high amount of FA showed high compressive strength compared to those with the low amount of FA. For example, the 28-day compressive strengths of mixes with 600DE series A, B, and C were 7.3, 9.3, and 10.5 MPa, respectively. The small DE aggregate with high surface area resulted in the better bonding of matrix and aggregate than that of large DE leading to an increase in strength (Husem, 2003). Similar finding on the reduction of strength with the increase in coarse aggregate was reported (Unal *et al.*, 2007).

3.5 Unit Weight

The results of the unit weight of lightweight concretes are shown in Fig. 5. The unit weight slightly decreased with the increasing calcined temperature of DE and increased with the increasing amount of FA. For example, the unit weight of the concretes with 25DE, 400DE, 600DE, and 800DE of series A were 1216, 1193, 1185, and 1174 kg/m^3, respectively. The increased in calcined temperature resulted in a DE with a slightly reduced unit weight compared to the uncalcined DE, due to the calcination of burnable elements (Pimraksa and Chindaprasirt, 2009). The unit weight of series A, B, and C mixes with 800DE were 1174, 1211, and 1271 kg/m^3, respectively. The unit weights of FA, MA, and CA were 600, 425, and 417 k/m^3, respectively (Table 2). For series C mixes, the high amount of FA (small DE aggregate) filled the space in the matrices and made concrete more compact and stronger than those using low amount of FA.

3.6 Porosity and Water Absorption

The results of the porosity and water absorption are shown in Figs. 6 and 7. The porosities and water absorptions at the age of 28 days were obviously lowered with the increasing calcination temperature and amount of FA. The increase in calcined temperature reduced the burnable elements such as clay mineral kaolinite (Pimraksa and Chindaprasirt, 2009) as indicated by the result of mineralogical composition in Fig. 3. The burnable element was responsible for the high absorption of water. The increase in temperature thus slightly reduced the water absorption and porosity. For example, the porosities at 28 days of 25DE,

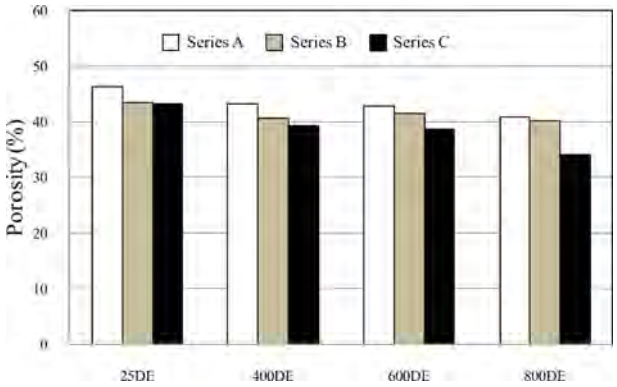

Fig. 6. Porosity at 28 Days of Lightweight Concrete

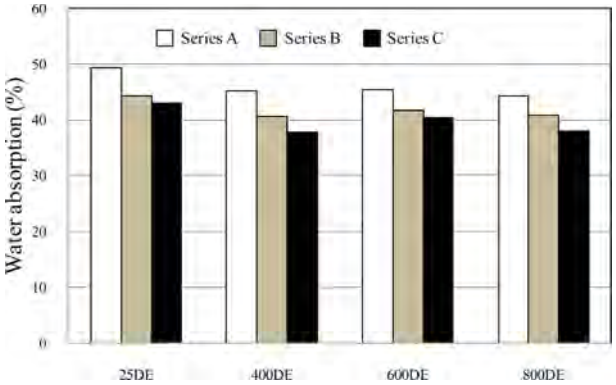

Fig. 7. Water Absorption at 28 Days of Lightweight Concrete

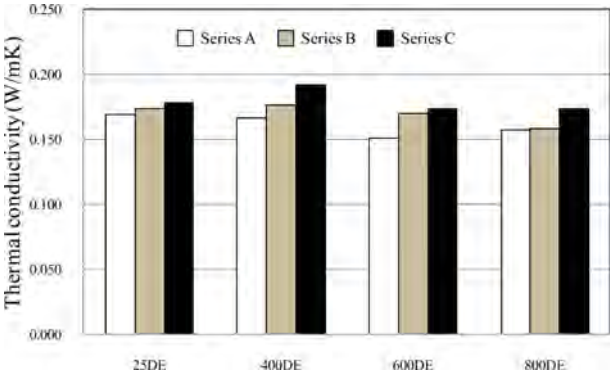

Fig. 9. Thermal Conductivity at 28 Days of Lightweight Concrete

400DE, 600DE, and 800DE of series C mixes were 43.2, 39.2, 38.7, and 34.0%, respectively and the porosities at 28 days of series A, B, and C of 800DE mixes were 40.9, 40.2, and 34.0%, respectively.

The water absorption slightly decreased with the increasing in calcination temperature and amount of FA in the same manner as the porosities. The water absorption at 28 days of 800DE mixes of series A, B, and C were 44.4, 40.9, and 37.9%, respectively. The water absorption increased with the increasing porosity as expected.

3.7 Modulus of Elasticity

The results of modulus of elasticity are shown in Fig. 8. The modulus of elasticity of LWC significantly increased with the increasing calcined temperature and amount of FA. The increase in calcined temperature to 600-800°C improved the properties of aggregate (Pimraksa and Chindaprasirt, 2009; Pimraksa *et al*., 2011; Yılmaz and Ediz, 2008; Zuhua *et al.*, 2009) and hence, its use resulted in the increased in modulus of elasticity. The increase in amount of FA also resulted in the increase in modulus of elasticity due to the small DE aggregates filled the space in matrices which made the concrete more compact and stronger than that with large DE. For example, the moduli of elasticity of 800DE mixes of series A, B, and C were 2.91, 3.56, and 4.33 GPa, respectively.

3.8 Thermal Conductivity

The results of the thermal conductivity of lightweight concretes are shown in Fig. 9. The thermal conductivity slightly decreased with the increasing calcined temperature of DE. For example, the thermal conductivity of the concretes with 25DE, 400DE, 600DE, and 800DE of series B were 0.174, 0.176, 0.170, and 0.158 W/mK, respectively. The reduction was due to the ridding of water molecule and other burnable minerals in aggregate with high calcination temperature (Pimraksa and Chindaprasirt, 2009). The reduction in the thermal conductivity is rather attractive thermal property of this LWC. The thermal conductivity increased with the increasing amount of FA.

The thermal conductivity values of series A, B, and C mixes with 600DE were 0.151, 0.170, and 0.174 W/mK, respectively. The thermal conductivity increased with the increasing of FA due to the increases in the filling of voids of small aggregate and the increase in the bonding of the small aggregate and the matrix and due to increased surface area and pozzolanic property of the aggregate.

3.9 Relationship of Compressive Strength, Modulus of Elasticity, Thermal Conductivity, Unit Weight, and Calcined Temperature

The relationship between modulus of elasticity and compressive strength of LWC is shown in Fig. 10. The modulus of elasticity tended to increase linearly to the square root of compressive

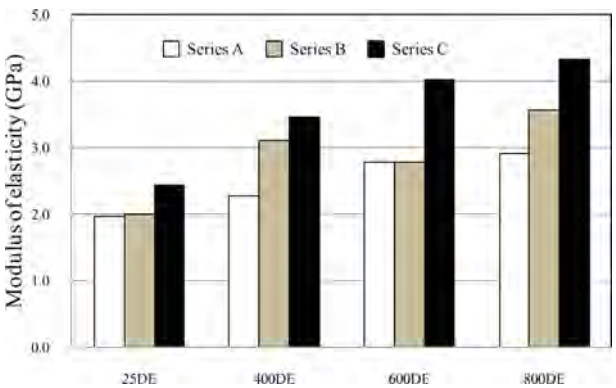

Fig. 8. Modulus of Elasticity at 28 Days of Light Weight Concrete

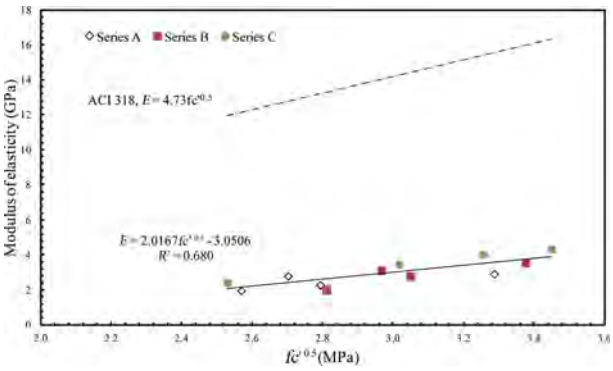

Fig. 10. Modulus of Elasticity of Lightweight Concrete

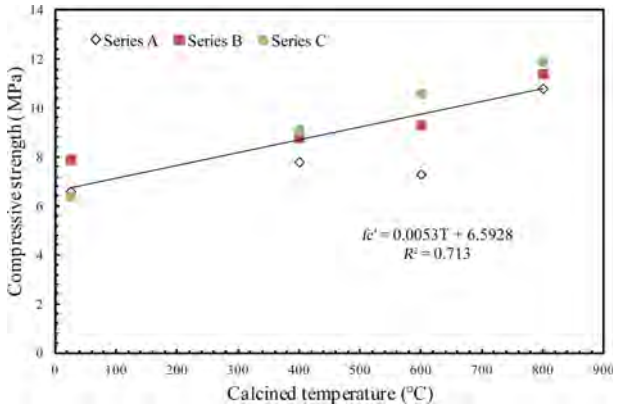

Fig. 11. Relationship between Compressive Strength and Calcined Temperature

strength. The relationship could be predicted in the form shown in Eq. (3). The resulted showed the same trend as that of other research (Chindaprasirt, 1980). The results indicated the modulus of elasticity between 2.0-4.3 GPa which is substantially lower than that of ACI 318 (2000) for normal concrete (Unal *et al.*, 2007). The trends of the relationship of the modulus of elasticity and the square root of compressive strength were similar.

$$E = 2.0167\sqrt{f_c'} - 3.0506 \quad (3)$$

Where E is modulus of elasticity (GPa) and f_c' is compressive strength (MPa).

Figure 11 shows the relationship of compressive strength and the calcined temperature of DE. The compressive strength increased with the increasing calcined temperature (Pimraksa *et al.*, 2011) and could be described by Eq. (4).

$$f_c' = 0.0053T + 6.5928 \quad (4)$$

Where f_c' is compressive strength (MPa) and T is temperature for calcined diatomite (C).

In addition, there appear to be a relationship between thermal conductivity and unit weight as shown in Fig. 12 and by Eq. (5). The unit weight increased with the increasing thermal conductivity

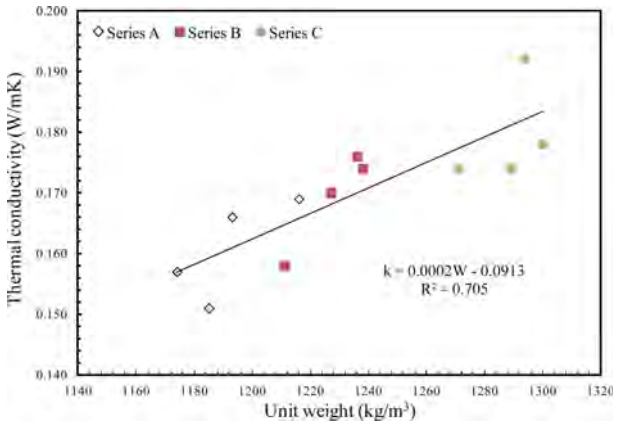

Fig. 12. Relationship between Thermal Conductivity and Unit Weight

(Uysal *et al.*, 2004). The thermal conductivity is, therefore, a function of density (Lu-Shu, 1980) as the unit weight increased, the void in the LWC reduced and the thermal conductivity increased.

$$k = 0.0002W - 0.0913 \quad (5)$$

Where k is thermal conductivity (W/mK) and W is unit weight (kg/m^3).

4. Conclusions

The calcined DE is a suitable material for making good lightweight concrete. The use of calcined DE aggregate increased compressive strength and modulus of elasticity, and reduced unit weight, porosity, water absorption, and thermal conductivity compared to those with uncalcined DE. The calcined temperatures of DE should be between 600-800°C. The aggregate sizes also had significant affect on the properties of LWC. The properties was improved with the increased amount of small aggregate due to the filling of space in the matrices which made concrete more compact and stronger than that with large aggregate. In addition, the lightweight concrete with compressive strength of 12.0 MPa and density of 1200 kg/m^3 could be classified as masonry concrete according to ASTM C331 (2010).

Acknowledgements

This work was supported by the Higher Education Research Promotion and National Research University Project of Thailand, Office of the Higher Education Commission, through the Advanced Functional Materials Cluster of Khon Kaen University No. AFM-2553-Ph.d-01, and the Thailand Research Fund (TRF) under the TRF Senior Research Scholar, Grant No. RTA5480004.

References

ACI 318M-95 (2000). *Building code requirements for structural concrete*, ACI Manual of Concrete Practice, Part 3.

ASTM C109 (2002). *Standard test method of compressive strength of hydraulic cement mortars (using 2-in. or [50 mm] cube speciments)*, Annual Book of ASTM Standard, Vol. 04.01.

ASTM C138 (2009). *Standard test of method for unit weight of mortar*, Annual Book of ASTM Standard, Vol. 04.01.

ASTM C330-89 (1989). *Specification for lightweight aggregates for structural concrete*, Annual Book of ASTM Standard, Vol. 04.02.

ASTM C331-10 (2010). *Standard specification for lightweight aggregates for concrete masonry units*, Annual Book of ASTM Standard, Vol. 04.02.

ASTM C39 (2001). *Standard test method for compressive strength of cylindrical concrete specimens*, Annual Book of ASTM Standard, Vol. 04.02.

ASTM C469 (2002). *Standard test method for static modulus of elasticity and poisson's ratio of concrete in compression*, Annual Book of ASTM Standard, Vol. 02.01.

ASTM C642 (2006). *Standard test method for density, absorption, and voids in hardened concrete*, Annual Book of ASTM Standard, Vol.

04.02.

ASTM D5930 (2009). *Standard test method for thermal conductivity of plastics by means of a transient line-source technique*, Annual Book of ASTM Standard, Vol. 04.01.

Baronio, G. and Binda, L. (1997). "Study of the pozzolanicity of some bricks and clays." *Construction and Building Materials*, Vol. 11, No. 1, pp. 41-46.

Chandra, S. B. L. (2002). *Lightweight aggregate concrete: Sciene, technology and application*, William Andrew Publishing, Norwich, New York, USA.

Charles, C., Diane, H., and McGeary, D. (2007). *Physical geology,* Eleventh Edition, McGraw-Hill Punlish, New York, USA.

Chindaprasirt, P. (1980). *Influence of load history on the properties of concrete*, PhD Thesis, The University of New South Wales, Australia.

Chindaprasirt, P. and Rukzon, S. (2008). "Strength, porosity and corrosion resistance of ternary blend Portland cement, rice husk ash and fly ash mortar." *Construction and Building Materials*, Vol. 22, No. 8, pp. 1601-1606.

De Rojas, M. I. S., Rivera, J., and Friìas, M. (1999). "Influence of the microsilica state on pozzolanic reaction rate." *Cement and Concrete Research*, Vol. 29, No. 6, pp. 945-949.

Husem, M. (2003). "The effects of bond strengths between lightweight and ordinary aggregate-mortar, aggregate-cement paste on the mechanical properties of concrete." *Materials Science and Engineering: A*, Vol. 363, Nos. 1-2, pp. 152-158.

Jo, B. W., Park, S. K., and Park, J. B. (2007). "Properties of concrete made with alkali-activated fly Ash Lightweight Aggregate (AFLA)." *Cement and Concrete Composites*, Vol. 29, No. 2, pp. 128-135.

Kroehong, W., Sinsiri, T., Jaturapitakkul, C., and Chindaprasirt, P. (2011). "Effect of palm oil fuel ash fineness on the microstructure of blended cement paste." *Construction and Building Materials*, Vol. 25, No. 11, pp. 4095-4104.

Kung, L.-S., Su, M.-Q., Shi, X.-S., and Li, Y.-X. (1980). "Research on several physico-mechanical properties of lightweight aggregate concrete." *International Journal of Lightweight Concrete*, Vol. 2, No. 4, pp. 185-191.

Malhotra, V. M. (2002). "Introduction: sustainable development and concrete technology." *Concrete International*, Vol. 24, No. 7, pp. 22.

Owen, R. B. and Utha-aroom, C. (1999). "Diatomaceous sedimentation in the Tertiary Lampang Basin, Northern Thailand." *Journal of Paleolimnology*, Vol. 22, No. 1, pp. 81-95.

Pimraksa, K. and Chindaprasirt, P. (2009). "Lightweight bricks made of diatomaceous earth, lime and gypsum." *Ceramics International*, Vol. 35, No. 1, pp. 471-478.

Pimraksa, K., Chindaprasirt, P., Rungchet, A., Sagoe-Crentsil, K., and Sato, T. (2011). "Lightweight geopolymer made of highly porous siliceous materials with various Na_2O/Al_2O_3 and SiO_2/Al_2O_3 ratios." *Materials Science and Engineering: A*, Vol. 528, No. 21, pp. 6616-6623.

Rukzon, S. and Chindaprasirt, P. (2008). "Mathematical model of strength and porosity of ternary blend Portland rice husk ash and fly ash cement mortar." *Computers and Concrete*, Vol. 5, No. 1, pp. 75-88.

Thokchom, S., Ghosh, P., and Ghosh, S. (2009). "Effect of water absorption, porosity and sorptivity on durability of geopolymer mortars." *ARPN Journal of Engineering and Applied Sciences*, Vol. 4, No. 7, pp. 28-32.

Unal, O., Uygunoğlu, T., and Yildiz, A. (2007). "Investigation of properties of low-strength lightweight concrete for thermal insulation." *Building and Environment*, Vol. 42, No. 2, pp. 584-590.

Uysal, H., Demirboğa, R., Şahin, R., and Gül, R. (2004). "The effects of different cement dosages, slumps, and pumice aggregate ratios on the thermal conductivity and density of concrete." *Cement and Concrete Research*, Vol. 34, No. 5, pp. 845-848.

Yılmaz, B. and Ediz, N. (2008). "The use of raw and calcined diatomite in cement production." *Cement and Concrete Composites*, Vol. 30, No. 3, pp. 202-211.

Zuhua, Z., Xiao, Y., Huajun, Z., and Yue, C. (2009). "Role of water in the synthesis of calcined kaolin-based geopolymer." *Applied Clay Science*, Vol. 43, No. 2, pp. 218-223.

Available online at www.sciencedirect.com

ScienceDirect

Ceramics International 40 (2014) 13025–13031

CERAMICS INTERNATIONAL

www.elsevier.com/locate/ceramint

Synthesis and characterization of $Ba_{0.85}Ca_{0.15}Ti_{0.9}Zr_{0.1}O_3$ ceramics by hydrothermal method

Sitchai Hunpratub[a], Santi Maensiri[b], Prinya Chindaprasirt[c,*]

[a]*Materials Science and Nanotechnology Programs, Faculty of Science, Khon Kaen University, Khon Kaen 40002, Thailand*
[b]*School of Physics, Institute of Science, Suranaree University of Technology, Nakhon Ratchasima 30000, Thailand*
[c]*Sustainable Infrastructure Research and Development Center, Department of Civil Engineering, Faculty of Engineer, Khon Kaen University, Khon Kaen 40002, Thailand*

Received 18 November 2013; received in revised form 4 April 2014; accepted 30 April 2014
Available online 9 May 2014

Abstract

$Ba_{0.85}Ca_{0.15}Ti_{0.9}Zr_{0.1}O_3$ (BCTZO) ceramics were prepared from nanopowders using a hydrothermal method. The phases and microstructures of samples were characterized by X-ray diffraction (XRD) and Scanning electron microscopy (SEM). The XRD results indicate that the ceramic samples have a pseudo-cubic phase structure with a small $CaTiO_3$ phase observed at 1100 and 1200 °C. The samples were dense and the average grain sizes increase with increasing sintering temperature and were 0.89, 3.53 and 12.09 μm for sintering temperatures at 1100, 1200 and 1300 °C, respectively. The dielectric constants, ferroelectric hysteresis loops and piezoelectric strain factors of BCZTO ceramics were also investigated. The results show that their values increase with the increase in average grain size of ceramic samples.

Keywords: $Ba_{0.85}Ca_{0.15}Ti_{0.9}Zr_{0.1}O_3$; Hydrothermal method; Dielectric constant; Ferroelectric hysteresis loop; Piezoelectric strain factor

1. Introduction

Ferroelectric materials with a perovskite structure have been extensively studied due to their wide applications in the fabrication of multilayer ceramic capacitors, actuators and electromechanical transducers [1]. Most of them belong to the family of lead-based perovskite oxides such as $PbTi_{1-x}Zr_xO_3$ (PZT) [2], $Pb(Zn_{1/3}Nb_{2/3})O_3$-$PbTiO_3$ (PZN-PT) [3] and $Pb(Mg_{1/3}Nb_{2/3})O_3$-$PbTiO_3$ (PMN-PT) [4] and have attracted a lot of attention due to their excellent ferroelectric, dielectric and piezoelectric properties. However, these compositions have the obvious disadvantage of volatility and toxicity of lead. Therefore, the scientific community has been searching for new materials with appropriate chemical and physical properties in order to replace the Pb-based compounds for environmentally friendly applications. There are many lead-free materials with perovskite structure such as $BaTiO_3$ (BT) [5,6], $Ba_{1-x}Ca_xTi_{1-y}Zr_yO_3$ (BCZTO) [7–9] $(Bi,Na)TiO_3$ (BNT) [10], and $(Na,K)NbO_3$ (NKN) [11]. These materials have been investigated in terms of their diffuse phase transition, dielectric, ferroelectric and piezoelectric properties.

Among these compounds, the BCTZO compounds have been widely investigated because it is shown to possess a large piezoelectric coefficient (d_{33}) of 620 pC/N for $0.5Ba_{0.7}Ca_{0.3}TiO_3$–$0.5BaTi_{0.8}Zr_{0.2}O_3$ (BZT–BCT) composites [12]. This spurs the researcher's interest on the effects of the doping proportion, poling and sintering process of polymorphic phase transition temperatures, dielectric constant and piezoelectric properties. In particular, the high-performance BZT–BCT ceramics with various compositions were obtained [13–16]. The structure is close to a morphotropic phase boundary (MPB) showing excellent dielectric constant and piezoelectric properties. The dielectric constant and piezoelectric properties of $(Ba_{0.9}Ca_{0.1})(Ti_{0.85}Zr_{0.15})O_3$ ceramics can be improved by an increase in grain size [17]. However, the high sintering temperatures over 1300 °C are required for large grain size and dense ceramics. Therefore, it is necessary to use nano size

*Corresponding author. Tel.: +66 4320 2355; fax: +66 4320 2355x12.
E-mail address: prinya@kku.ac.th (P. Chindaprasirt).

http://dx.doi.org/10.1016/j.ceramint.2014.04.166
0272-8842/

powders in the synthesis. The hydrothermal method which is effective for the synthesis of BZT–BCT nanopowders at low sintering temperature may lead to a dense structure and excellent electrical properties of samples.

In this study, the $Ba_{0.85}Ca_{0.15}Ti_{0.9}Zr_{0.1}O_3$ (BCTZO) ceramics prepared from nanopowders synthesized using a hydrothermal method with low sintering temperature were reported. The phase and microstructure of samples were investigated by X-ray diffraction (XRD) and Scanning electron microscopy (SEM). The dielectric constants, ferroelectric hysteresis loops and piezoelectric strain factors of the low sintering temperature BCZTO ceramics were also investigated.

2. Experimental

The BCZTO powders were prepared by hydrothermal method with $Ba(OH)_4$ (95%, Aldrich), $Ca(NO_3)_2.4H_2O$ (99.9%, Kanto chemical), $ZrCl_2O.8\ H_2O$ (99%, Kanto chemical), and TiO_2 (99%, Aldrich) as the starting materials. Initially, all materials were dissolved in de-ionized water under vigorous magnetic stirring for 10 h, and then NaOH solution with various concentrations (2 M, 6 M and 10 M) was added to the mixture. The solution was stirred using a magnetic stirrer at room temperature for another 10 h and transferred to the Teflon-lined stainless steel autoclave for hydrothermal treatment at 240 °C for 16 h. It was then left to cool down to room temperature. The product was washed with de-ionized water to remove sodium ions and dried in an oven at 80 °C for further characterization and fabrication of ceramic samples. The obtained powders were ground and mixed with 3wt% polyvinyl alcohol (PVA) binder. The mixed powders were pressed into discs with 13 mm in diameter and 1.5 mm in thickness. The disc samples were sintered at 1100, 1200, and 1300 °C for 3 h in air.

The obtained powders and sintered samples were characterized by XRD using PW3040 Philips X-ray diffractometer with CuK_α radiation ($\lambda = 0.15406$ nm), The Netherlands. For the structural analysis, the Rietveld refinement was performed on the XRD pattern to determine the phase contents using the X' Pert HighScore Plus software. The morphology and structure of these samples were characterized by a SEM (JEO VP1450, UK). The ceramic samples were polished to obtain the thickness of approximately 1 mm and were painted with silver paint and used as the electrode. The dielectric properties of the pasted ceramics were measured at different frequencies in the temperature range from −50 to 200 °C using Agilent 4294 A Precision impedance analyzer. The ferroelectric hysteresis loops of the pasted ceramics were measured using a modifier Sawyer-Tower circuit at room temperature with a frequency of 50 Hz. The piezoelectric properties of the pasted ceramics were polarized at room temperature in silicon oil for 20 min under an electric field of 1.5 kV/mm. After being held for 24 h at room temperature, the piezoelectric strain factor (d_{33}) of the pasted ceramics was measured using a d_{33} meter (Model 90-2030, APD International, Ltd.).

3. Results and discussion

The XRD patterns of the BCTZO powders synthesized at 240 °C for 16 h with 2 M, 6 M and 10 M solutions are shown in Fig. 1. All the BCTZO powders have a pseudo cubic-perovskite structure with $BaTiO_3$-like phase (JCPDS no. 31-0174). The impurity phases of $CaTiO_3$ (JCPDS no. 22-0153) and $BaZrO_3$ (JCPDS no. 06-0399) were also observed. The impurity phase of $BaZrO_3$ slightly increased when the NaOH concentration increased from 2 M to 6 M, and was not detected with 10 M NaOH sample. The $CaTiO_3$ phase slightly decreased with increasing NaOH concentration. This indicated that Zr^{4+} ions had entered the perovskite structure while only a small amount of Ca^{2+} ions had entered into $BaTiO_3$ lattices and formed $CaTiO_3$.

The peaks of $BaTiO_3$ were clearly observed and thus the particle size could be calculated with confidence. The average crystalline size (D) of BCTZO powders for 2 M, 6 M and 10 M NaOH were calculated from X-ray line broadening of the reflection planes (1 0 0), (1 1 0), (1 1 1), (2 0 0), (2 1 0) and (2 1 1) using Scherrer's equation with $D = k\lambda/(\beta \cos\theta)$, where λ is the wavelength of the X-ray radiation, k is a constant taken as 0.98, θ is the diffraction angle and β is the full width at half maximum [18]. The D values from this calculation are 31.4 ± 6.5, 27.8 ± 5.3 and 25.3 ± 5.3 nm for 2 M, 6 M and 10 M NaOH solutions, respectively. The lattice parameters were also calculated as shown in Table 1. The SEM micrograph of BCTZO powders are shown in Fig. 2. The nanoparticles are uniform in size with average particle sizes of 304.2, 262.5 and 227.9 nm for 2 M, 6 M and 10 M NaOH solutions, respectively and the particles are agglomerated. The XRD and SEM results confirmed that the particles were nano-particle and the size slightly reduced with increasing NaOH concentration.

XRD patterns of BCTZO ceramics as shown in Fig. 3 indicated the presence of the pseudo cubic-perovskite structure with $BaTiO_3$-like phase. The impurity phase of $CaTiO_3$ was observed in the samples sintered at 1100 and 1200 °C. This indicates that the Zr^{4+} ions substituted Ti^{4+} ions at the B sites

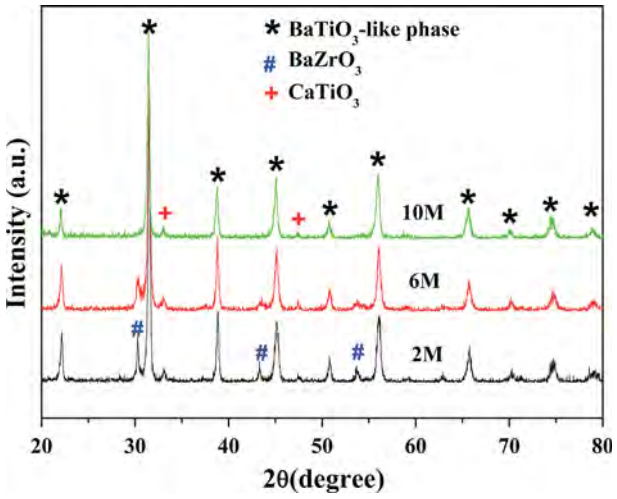

Fig. 1. XRD patterns of BCTZO nanopowders synthesized at 240 °C for 16 h with NaOH concentrations of 2 M, 6 M and 10 M.

Table 1
Various parameters of BCTZO powders synthesized at 240 °C for 16 h of NaOH content as 2, 6 and 10 M.

Various parameters	**Various NaOH content**		
	2 M	6 M	10 M
Phase (%Weight fraction)	(1) $BaTiO_3$-like phase (77.4%) (2) $BaZrO_3$ (9.6%) (3) $CaTiO_3$ (13.0%)	(1) $BaTiO_3$-like phase (76.3%) (2) $BaZrO_3$ (12.5%) (3) $CaTiO_3$ (11.2%)	(1) $BaTiO_3$-like phase (90.4%) (2) $BaZrO_3$ (0%) (3) $CaTiO_3$ (9.2%)
Good fit	1.152	1.050	1.121
Average crystalline size (nm) by XRD	31.4 ± 6.5	27.8 ± 5.3	25.3 ± 5.3
Lattice parameter (Å)	4.0207	4.0192	4.0235
Average particle size (nm) by SEM	304.2	262.5	227.9

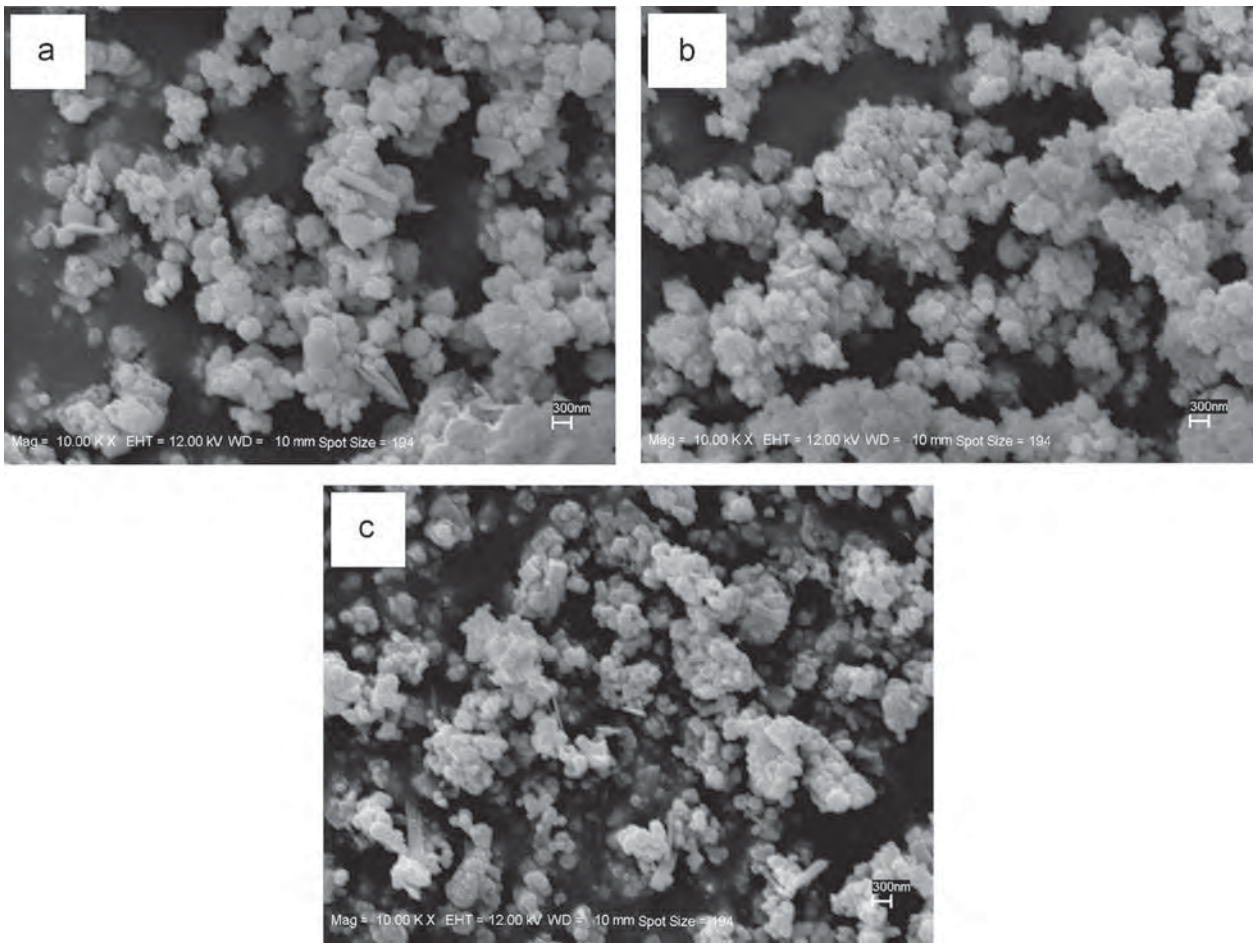

Fig. 2. SEM images of BCTZO nanopowders with NaOH concentrations of (a) 2 M, (b) 6 M and (c) 10 M.

of BTZO lattice because the ionic radius of Zr^{4+} (0.072 nm) is larger than that of Ti^{4+} (0.0608 nm). The samples sintered at 1300 °C have a pure phase and systematic shift of the XRD peaks at high angle (2θ). This indicates that the solubility of $CaTiO_3$ in BZT lattice increases with sintering temperature.

The SEM micrographs of BCTZO ceramics are shown in Fig. 4. All ceramic samples are dense and homogeneous at high sintering temperature. The average grain sizes of BCTZO ceramics are 0.85, 3.53 and 12.09 μm as temperature increases from 1100 to 1300 °C. This result confirmed that the BCTZO ceramics were prepared from nanopowders using a hydrothermal method. It can improve the homogeneity of grains and dense structure of the obtained BCTZO ceramics at low sintering temperature (1300 °C) when compare with those obtained from the conventional solid state reaction technique which require high temperature to form the dense ceramics [19].

The temperature dependence of dielectric constant (ε') and dissipation factor ($\tan\delta$) for the BCTZO samples at 100 Hz, 1 kHz, 10 kHz, 100 kHz and 1 MHz are shown in Fig. 5(a–c). A single broad dielectric peak is observed for the sintered

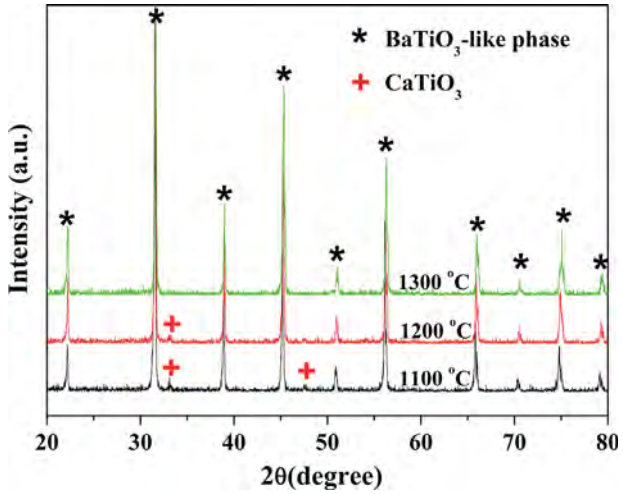

Fig. 3. XRD patterns of BCTZO ceramics sintered at 1100, 1200 and 1300 °C for 3 h.

ceramics at 1100 and 1200 °C. However, with high sintering temperature of 1300 °C, two dielectric peaks were observed. They corresponded to the phase transition temperatures of rhombohedral–tetragonal (~20 °C) and tetragonal–cubic (~70 °C) [12]. This indicates the coexistence of the two phase structures in this sintered sample which may lead to good electrical properties. The sintered samples at 1100 and 1200 °C exhibited the broadening diffuse phase transition behavior. This behavior could be induced by many reasons such as the microscopic composition fluctuation, the merging of micro-domains into macro-domains, the local disorder mode through local strain, and the relaxor behaviors of fine-grain size, grain boundary and paraelectric phase [7,20]. Therefore in this case, the effect of the paraelectric $CaTiO_3$ phase at low sintering temperature can be attributed to the lowering and broadening of dielectric constant arising from the inhibition of the grain growth in these samples [21]. In the previously published research, the modified Curie–Weiss law was successfully used to describe the diffuser ferroelectric behavior [22]. It is known that the classical ferroelectrics follow the Curie–Weiss law above Curie temperature and is expressed by the following relationship:

$$\frac{1}{\varepsilon'} = \frac{(T - T_0)}{C} \tag{1}$$

where T_0 is the Curie–Weiss temperature and C is the Curie–Weiss constant. The inverse dielectric constant as a function of temperature at constant frequency of 10 kHz is shown in Fig. 6. It is observed that T_0 changes from 78.3 °C to 85.8 and 97.9 °C as a result of the increase in sintering temperatures from 1100 °C to 1200 and 1300 °C. To explain the diffuser behavior, the parameter ΔT_m is used to show the degree of deviation. The dielectric constant of BCTZO ceramics follows the Curie–Weiss law at temperature higher than ΔT_m which is defined as

$$\Delta T_m = T_{dev} - T_m \tag{2}$$

here, T_{dev} is the temperature at which dielectric permittivity starts to deviate from Curie–Weiss law and T_m is the temperature at maximum dielectric permittivity. It can be found that ΔT_m values are 60, 70 and 60 °C for sintering temperatures of 1100, 1200 and 1300 °C, respectively. The differences in the ΔT_m values relatively small in this case and this method, therefore, cannot be used to explain the diffuser behavior. The modified Curie–Weiss law for the diffuseness phase transition is, therefore, used to explain

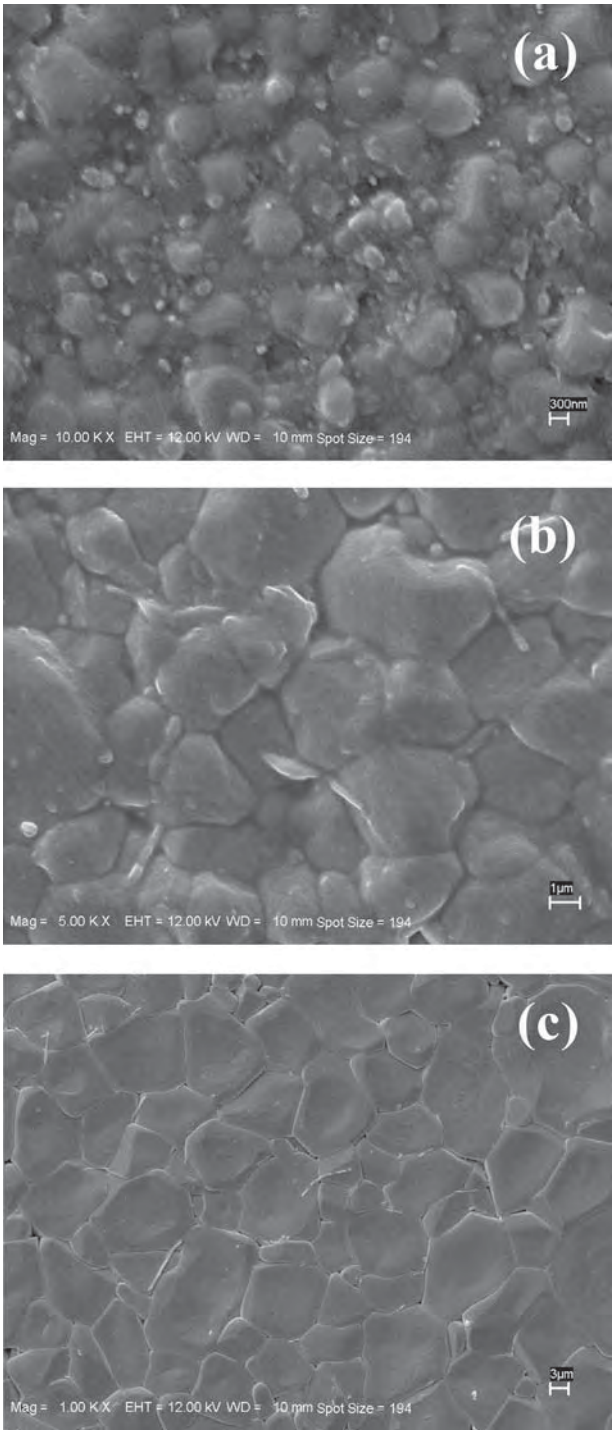

Fig. 4. SEM images of BCTZO ceramics sintered at (a) 1100, (b) 1200, and (c) 1300 °C.

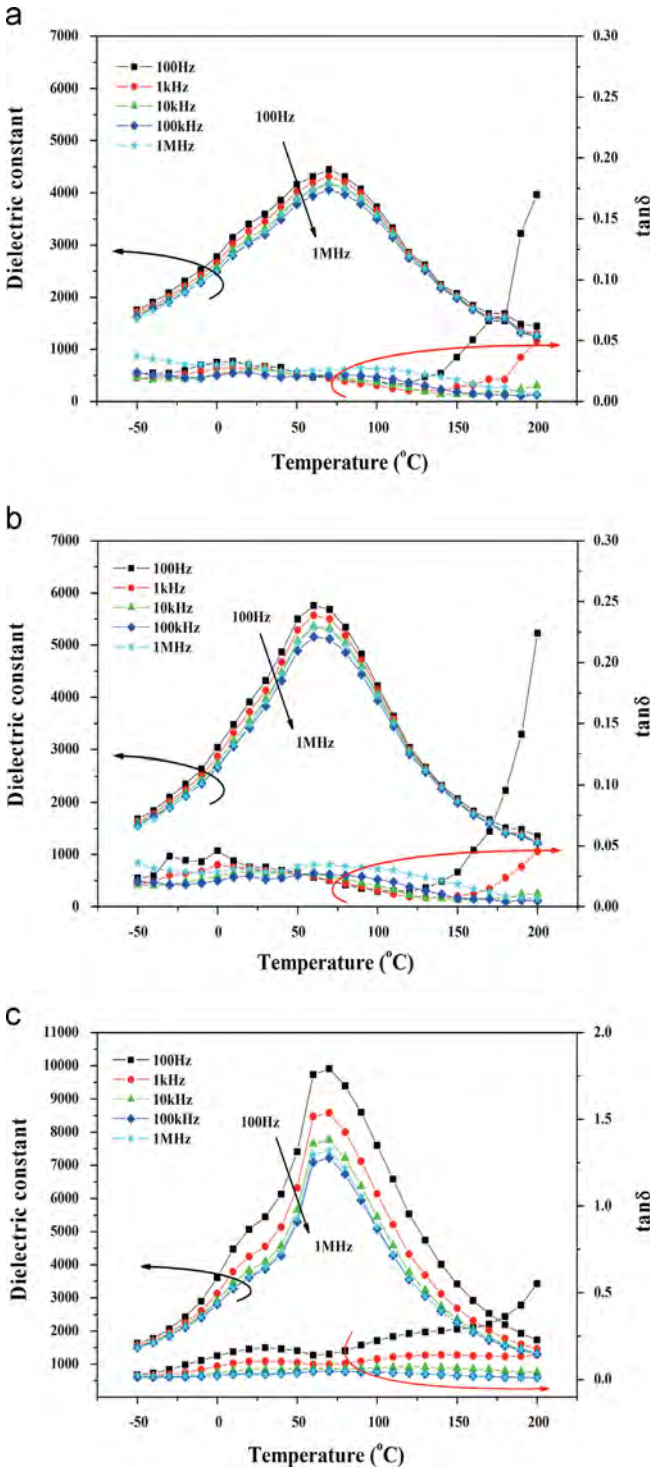

Fig. 5. The frequency and temperature dependence of dielectric constant and tan δ of BCTZO ceramics sintered at (a) 1100, (b) 1200, and (c) 1300 °C.

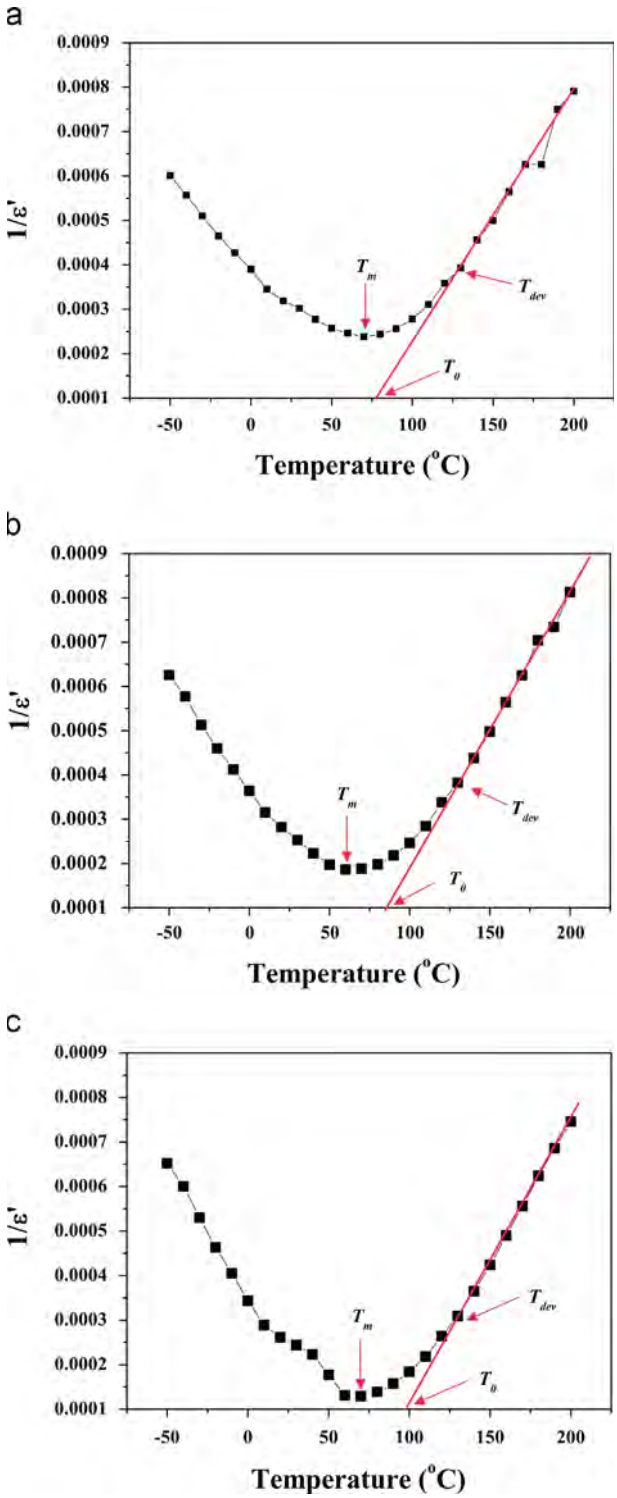

Fig. 6. The temperature dependence of the inverse dielectric constant of BCTZO ceramics sintered at (a) 1100, (b) 1200, and (c) 1300 °C.

this phenomenon as

$$\frac{1}{\varepsilon'} - \frac{1}{\varepsilon'_m} = \frac{(T - T_m)^\gamma}{C'} \tag{3}$$

where γ is modified constant with $1 < \gamma < 2$. The value of γ gives information about the character of phase transition. Its limiting values are $\gamma = 1$ and $\gamma = 2$. The value of γ is 1 for the case of a normal ferroelectric and $\gamma < 2$ (quadratic) is valid for an ideal ferroelectric relaxer or diffuser. A plot of ln $(1/\varepsilon' - 1/\varepsilon'_m)$ as a function of ln $(T–T_m)$ is shown in Fig. 7 for BCTZO samples. By curve fitting of Eq. (3), the γ values, determining the degree of diffuseness of phase transition, is obtained from the slope of ln $(1/\varepsilon' - 1/\varepsilon'_m)$ vs. ln $(T–T_m)$ plot which is shown

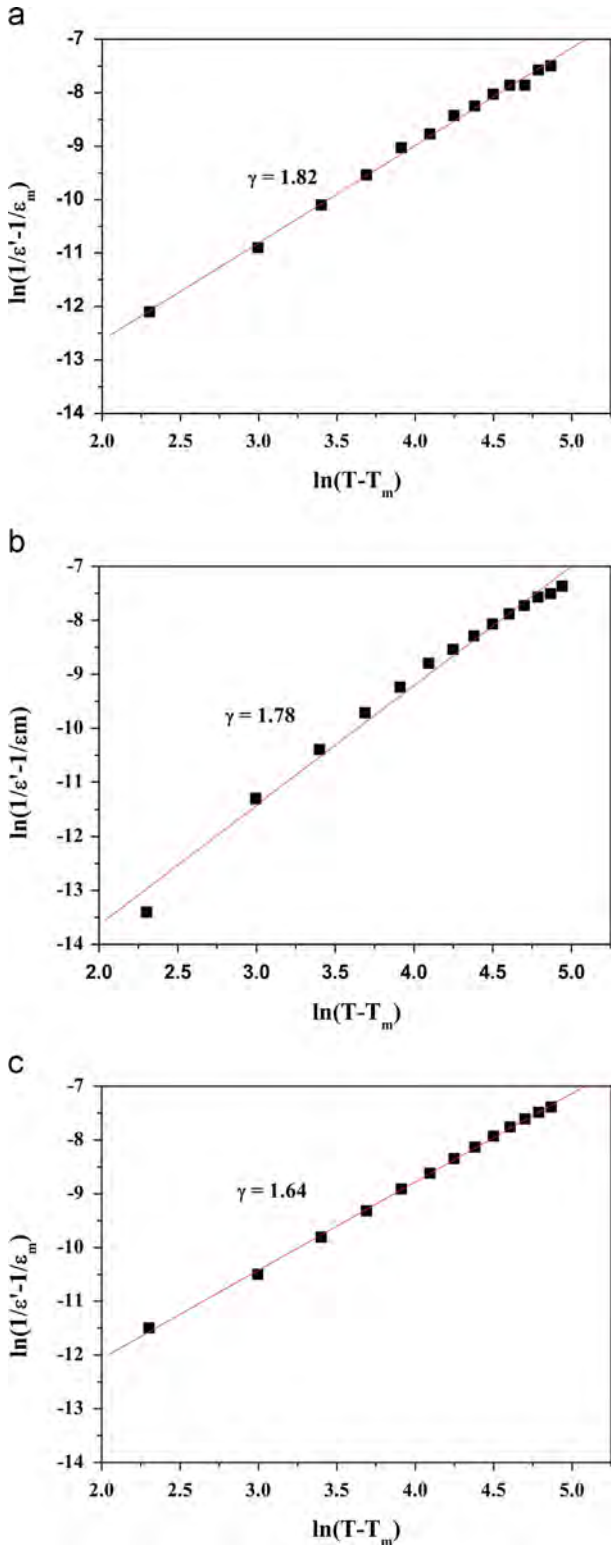

Fig. 7. Plot of $\ln(1/\varepsilon' - 1/\varepsilon'_m)$ as a function of $\ln(T-T_m)$ of BCTZO ceramics sintered at (a) 1100, (b) 1200, and (c) 1300 °C.

in Table 2. The γ values are 1.82, 1.78 and 1.64 for 1100, 1200 and 1300 °C. The high γ values of the sintered samples at 1200 and 1300 °C indicate the diffused phase transition which is supported by the small grain size and the mixing of para-electric $CaTiO_3$ at low sintering temperature [21].

Table 2
Various parameters of BCTZO ceramics sintered at 1100, 1200 and 1300 °C for 3 h for NaOH content of 10 M.

Various parameters	Sintering temperature		
	1100 °C	1200 °C	1300 °C
Phase	(1) $BaTiO_3$-like phase (2) $CaTiO_3$	(1) $BaTiO_3$-like phase (2) $CaTiO_3$	(1) $BaTiO_3$-like phase
Lattice parameter (Å)	4.0121	4.0066	4.0007
Average grain size (μm)	0.89	3.53	12.09
ε'_m	4,190	5,360	7,760
T_0 (°C)	78.3	85.8	97.9
T_m (°C)	70	60	70
ΔT_m (°C)	60	70	60
γ	1.82	1.78	1.64
$2P_r$ (μC/cm^2)	3.33	7.27	21.67
$2E_c$ (kV/cm)	2.52	3.04	4.53
d_{33} (pC/N)	52	123	164

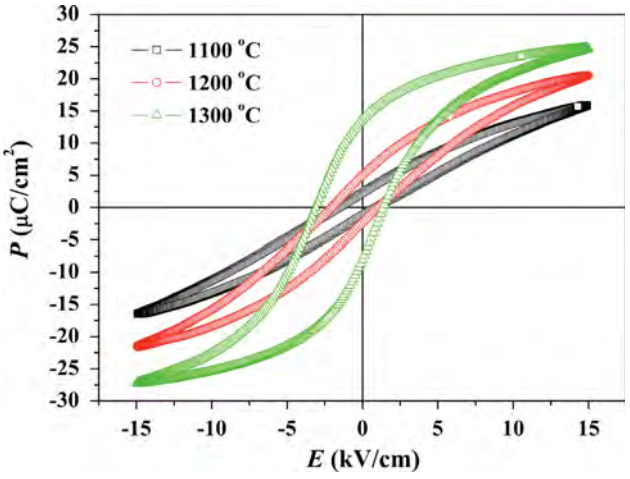

Fig. 8. The ferroelectric hysteresis loop of BCTZO ceramics sintered at different temperature measuring at frequency of 50 Hz.

Fig. 8 shows the ferroelectric hysteresis loops of BCTZO ceramics with different sintering temperature measured at 50 Hz at room temperature. The ceramic samples show the ferroelectric character. The remanent polarization ($2P_r$) and coercive electric field ($2E_C$) as a function of the sintered samples are shown in Table 2. The $2P_r$ values increase with increasing sintering temperature and are 3.33, 7.27 and 21.67 μC/cm^2 for 1100, 1200 and 1300 °C, respectively. The previous works indicated that the P_r value depends on the grain size, crystalline structure and Curie temperature of sample [23–26]. Tian et al. [23] reported that the decreasing P_r values of $(Ba_{1-x}Ca_x)(Zr_{0.1}Ti_{0.9})O_3$ ceramics depend on the change of crystalline structure. Li et al. [24] showed that the P_r values of $Ba_{0.7}Ca_{0.3}Ti_{0.9}O_3$ diphasic piezoelectric ceramics also reduce with the decrease of grain size of sample and the

variation of E_C values is not large. Therefore in this work, the P_r and E_C values increased because of the decrease of cubic paraelectric phase of $CaTiO_3$ and the increase in grain size with increasing sintering temperature. The piezoelectric strain factors (d_{33}) of BCZTO ceramics are shown in Table 2. The observed d_{33} values increase with increasing sintering temperature with maximum d_{33} value of 164 pC/N at 1300 °C. This is lower than that of ceramics prepared by conventional solid state method because of the smaller grain size.

The above result indicates that dense BCZTO ceramics with a high dielectric constant and a good remanent polarization can be fabricated at low sintering temperature of 1300 °C comparing with those prepared by the conventional solid state method. However, this method gives low d_{33} values similar to those by the sol–gel method [27].

4. Conclusion

The $Ba_{0.85}Ca_{0.15}Ti_{0.9}Zr_{0.1}O_3$ (BCTZO) ceramics were prepared from nanopowders using a hydrothermal method. The XRD results indicate that the ceramic samples have a pseudo-cubic phase structure with a small amount of $CaTiO_3$ at low sintering temperature. The average grain sizes increase with increasing sintering temperature and were 0.89, 3.53 and 12.09 μm for sintering temperatures at 1100, 1200 and 1300 °C, respectively. The optimum values of dielectric constants (ε'_m), remanent polarization ($2P_r$), coercive electric field ($2E_c$) and piezoelectric strain factors (d_{33}) of BCZTO ceramics for samples sintered at 1300 °C were 7,760, 21.67 μC/cm^2, 4.53 kV/cm and 164 pC/N, respectively.

Acknowledgments

This work was supported by the Higher Education Research Promotion and National Research University Project of Thailand, Office of the Higher Education Commission, through the Advanced Functional Materials Cluster of Khon Kaen University; the Thailand Research Fund (TRF) under the TRF Senior Research Scholar, Grant no. RTA5480004; and TRF and Khon Kaen University under the TRF-Royal Golden Jubilee Ph.D. program Grant no. PHD/0352/2551.

References

[1] J.F. Tressler, S. Alkroy, R.E. Newnham, Piezoelectric sensors and sensor materials, J. Electroceram. 2 (1998) 257–272.
[2] E. Sawaguchi, Ferroelectricity versus antiferroelectricity in the solid solutions of $PbZrO_3$ and $PbTiO_3$, J. Phys. Soc. Jpn. 8 (1953) 615–629.
[3] J. Kuwata, K. Uchino, S. Nomura, Phase transitions on the $Pb(Zn_{1/3}Nb_{2/3})O_3$ – $PbTiO_3$ system, Ferroelectrics 37 (1) (1981) 579–582.
[4] S.W. Choi, T.R. Shruot, S.J. Jang, A.S. Bhalla, Morphotropic phase boundary in $Pb(Mg_{1/3}Nb_{2/3})O_3$–$PbTiO_3$ system, Mater. Lett. 8 (1989) 253–255.
[5] H. Takahashi, Y. Numamoto, J. Tani, S. Tsurekawa, Piezoelectric properties of $BaTiO_3$ ceramics with high performance fabricated by microwave sintering, Jpn. J. Appl. Phys. 45 (2006) 7405.
[6] K. Tomoaki, Y. Kang, A. Masatoshi, Barium titanate piezoelectric ceramics manufactured by two-step sintering, Jpn. J. Appl. Phys. 46 (2007) 7035.
[7] X.-G. Tang, Effect of grain size on the electrical properties of (Ba,Ca)(Zr, Ti)O_3 relaxor ferroelectric ceramics, J. Appl. Phys. 97 (2005) 034109.
[8] S.K. Rout, E. Sinha, S. Panigrahi, J. Bera, T.P. Sinha, Phase formation and dielectric phase transition in $Ba_{1-x}Ca_xTi_{0.6}Zr_{0.4}O_3$ solid solution, J. Phys. Chem. Solid 67 (2006) 2257–2262.
[9] M.-S. Yoon, S.-C. Ur, Effect of A-site Ca and B-site Zr substitution on dielectric properties and microstructure in tin-doped $BaTiO_3$–$CaTiO_3$ composites, Ceram. Int. 34 (2008) 1941–1948.
[10] E. Aksel, J.L. Jones, Advances in lead-free piezoelectric materials for sensors and actuators, Sensors 10 (2010) 1935–1954.
[11] G. Shirane, R. Newnham, R. Penisky, Dielectric and phase transitions of $NaNbO_3$ and $Na,KNbO_3$, Phys. Rev. Lett. 96 (1954) 581–588.
[12] W. Liu, X. Ren, Large piezoelectric effect in Pb-free ceramics, Phys. Rev. Lett. 103 (2009) 257602.
[13] W. Li, Z.J. Xu, R.Q. Chu, P. Fu, G.Z. Zang, Piezoelectric and dielectric properties of $(Ba_{1-x}Ca_x)(Ti_{0.95}Zr_{0.05})O_3$ lead-free ceramics, J. Am. Ceram. Soc. 93 (10) (2010) 2942–2944.
[14] H.X. Bao, C. Zhou, D.Z. Xue, J.H. Gao, X.B. Ren, A modified lead-free piezoelectric BZT-xBCT system with higher T_C, J. Phys. D : Appl. Phys. 43 (2010) 465401.
[15] S. Su, R.Z. Zuo, S.B. Lu, Z.K. Xu, X.H. Wang, L.T. Li, Poling dependence and stability of piezoelectric properties of $Ba(Zr_{0.2}Ti_{0.8})O_3$-$(Ba_{0.7}Ca_{0.3})TiO_3$ ceramics with huge piezoelectric coefficients, Curr. Appl. Phys. 11 (2011) S120–S123.
[16] P. Wang, Y.X. Li, Y.Q. Lu, Enhanced piezoelectric properties of $(Ba_{0.85}Ca_{0.15})(Ti_{0.9}Zr_{0.1})O_3$ lead-free ceramics by optimizing calcination and sintering temperature, J. Eur. Ceram. Soc. 31 (2011) 2005–2012.
[17] J. Wu, D. Xiao, B. Wu, W. Wu, J. Zhu, Z. Yang, J. Wang, Sintering temperature-induced electrical properties of $(Ba_{0.9}Ca_{0.1})(Ti_{0.85}Zr_{0.15})O_3$ lead-free ceramics, Mater. Res. Bull. 47 (2012) 1281–1284.
[18] B.D. Cullity, S.R. Stock, Elements of X-Ray Diffraction, third ed., Prentice Hall, New Jersey, 2001.
[19] M. Jiang, Q. Lin, D. Lin, Q. Zheng, X. Fan, X. Wu, H. Sun, Y. Wan, L. Wu, Effect of MnO_2 and sintering temperature on microstructure, ferroelectric, and piezoelectric properties of $Ba_{0.85}Ca_{0.15}Ti_{0.9}Zr_{0.1}O_3$ lead-free ceramics, J. Mater. Sci. 48 (2013) 1035–1041.
[20] X.G. Tang, J. Wang, X.X. Wang, H.L.W. Chan, Effect of grian size on the dielectric properties and tunabilities of sol-gel derived Sintering temperature-induced electrical properties of $Ba(Zr_{0.2}Ti_{0.8})O_3$ ceramics, Solid State Commun. 131 (2004) 163–168.
[21] W. Li, Z. Xu, R. Chu, P. Fu, G. Zang, Structural and dielectric properties in the $(Ba_{1-x}Ca_x)(Ti_{0.95}Zr_{0.05})O_3$ ceramics, Curr. Appl. Phys. 12 (2012) 748–751.
[22] K. Uchino, S. Mathur, Critical exponents of the dielectric constants in diffused-phase-transition crystals, Ferroelectrics 44 (1) (1982) 55–61.
[23] Y. Tian, X. Chao, L. Wei, P. Liang, Z. Yang, Phase transition behavior and electrical properties of lead-free $(Ba_{1-x}Ca_x)(Zr_{0.1}Ti_{0.9})O_3$ piezoelectric ceramics, J. Appl. Phys. 113 (2013) 184107.
[24] C.-X. Li, B. Yang, S.-T. Zhang, R. Zhang, W.-W. Cao, Effects of sintering temperature and poling conditions on the electrical properties of $Ba_{0.70}Ca_{0.30}TiO_3$ diphasic piezoelectric ceramics, Ceram. Int. 39 (2013) 2967–2973.
[25] W. Cai, C. Fu, J. Gao, H. Chen, Effects of grain size on domain structure and ferroelectric properties of barium zirconate titanate ceramics, J. Alloys Compnd. 480 (2009) 870–873.
[26] C.C. Leu, C.Y. Chen, C.H. Chien, M.N. Chang, Domain structure study of $SrBi_2Ta_2O_9$ ferroelectric thin films by scanning capacitance microscopy, Appl. Phys. Lett. 82 (2003) 3493.
[27] J. Li, X. Sun, X.S. Zhang, Q. Chen, Z.H. Peng, P. Yu, Synthesis and characterization of sol−gel derived $(Ba_{0.9}Ca_{0.1})(Ti_{0.85}Zr_{0.15})O_3$–$x$CuO ceramics, Phys. Status Solidi A 210 (2013) 533–537.

Arab J Sci Eng (2014) 39:6001–6007
DOI 10.1007/s13369-014-1217-1

RESEARCH ARTICLE - CIVIL ENGINEERING

Effect of High-Speed Mixing on Properties of High Calcium Fly Ash Geopolymer Paste

Prinya Chindaprasirt · Pre De Silva · Sakonwan Hanjitsuwan

Received: 6 March 2013 / Accepted: 15 June 2013 / Published online: 5 June 2014

Abstract Geopolymers are produced by mixing aluminosilicate materials with alkaline activators, and the mixing process has a considerable impact on the dissolution of raw materials. This research studies the effects of mixing time, with a high-speed centrifuge mixer (1,000 rpm), on the setting and hardening properties of high calcium fly ash-based geopolymer paste. Setting time, strength, phase development, microstructure and porosity of the pastes were investigated. The results indicated that the increase in mixing time retarded the setting time which provided time for dissolution of starting materials. The optimum mixing time at high speed should be 1 min in order to obtain high strength and dense matrix in contrast to 10 min for the normal mixing. The mixing time also had an effect on the pore structure hence the total porosity of the paste.

Keywords Geopolymer · High calcium fly ash · Mixing parameter · Setting time · Compressive strength · Porosity

الخلاصة

يتم إنتاج المبلمرات الجيولوجية عن طريق خلط مواد ألومينا السيليكات بمنشطات قلوية، وعملية الخلط لديها تأثير كبير في حل المواد الخام. يدرس هذا البحث آثار وقت الخلط، مع خلاط جهاز للطرد المركزي بسرعة عالية (1000 دورة في الدقيقة)، على خصائص الإعداد والتصلب من رماد متطاير ذي كالسيوم مرتفع وأساسه معجون المبلمر الجيولوجي. وقد تم التحقيق في وقت الإعداد، والقوة، ونمو الحالة، والبنية المجهرية والمسامية للمعاجين. وأشارت النتائج إلى أن الزيادة في وقت الخلط تؤخر وقت الإعداد مما يوفر وقتا للبدء بحل المواد. إن زمن الخلط الأمثل عند سرعة عالية يجب أن تكون دقيقة واحدة من أجل الحصول على قوة عالية ومصفوفة كثيفة وعلى النقيض من عشر دقائق للخلط العادي. وأظهر وقت الخلط أيضا تأثيرا في هيكل المسام وبالتالي المسامية الكلية للمعجون.

1 Introduction

Fly ash is one of the important source materials for making geopolymer due to its high percentage of amorphous silica and alumina content [1,2]. The alkali activation of fly ash is a chemical process that transforms glassy phases (partially or totally amorphous and/or metastable) into compact well-cemented composites known as geopolymers [3]. When fly ash comes into contact with alkali solution, dissolution of silicate and aluminate species from the source materials starts [4]. Then, polymerization between dissolved silicate and aluminate species occurs leading to well-developed 3D structure of geopolymer. The extent of dissolution becomes an important step in the synthesis as the properties of the final product depend on the Si/Al ratio of the polymer. In addition, the presence of calcium in the system especially when high calcium fly ash is used as source material also plays an important role on the setting and strength development of geopolymer [5]. Phoo-ngernkham et al. [6] explained that the high calcium content leads to the formation of calcium silicate hydrate which coexisted with aluminosilicate geopolymer products.

P. Chindaprasirt
Sustainable Infrastructure Research and Development Center, Department of Civil Engineering, Faculty of Engineering, Khon Kaen University, Khon Kaen 40002, Thailand

P. De Silva
School of Arts & Sciences (NSW), Australian Catholic University, North Sydney, NSW 2059, Australia

S. Hanjitsuwan (✉)
Program of Civil Technology, Faculty of Industrial Technology, Lampang Rajabhat University, Lampang 52100, Thailand
e-mail: yim_kachan@yahoo.com

Thus, high calcium fly ash is suitable as source materials for making good geopolymer.

Proper mixing of initial raw materials is a very important step in any chemical synthesis process. It has been shown with Portland cement-based systems that mixing step plays a major role in initial dissolution of raw materials [7]. The movement of particles during mixing occurs by convective and dispersive transport mechanisms. The convective transport is a forced, directed movement of larger portions of the mix (coarse dispersion). Dispersive transport is the random movement of individual particles due to collisions between the particles which leads to a mixing in small area (fine dispersion), as well as a disintegration of agglomerates. Mixing parameters has to be chosen in a way that it provides adequate energy to achieve a homogeneous mixture via proper mixing of raw materials. It has been shown that for Portland cement-based systems, mixing time and speed/velocity of mixing can be optimized to achieve best outcomes [7].

Mixing time is one of the important parameters of mixing procedures, and it can be varied by the type of cement, mix proportion, amount of water or plasticizer added [8]. A study based on glass-ionomer cements [9] has shown that mixing time has an effect on the setting time and the strength of the product. The setting time of glass-ionomer cements was decreased as mixing time increased, with an increase in compressive strength to a maximum at 12 s of mixing time. The material essentially pre-gelled after few seconds of mixing and increasing mixing time resulted in breaking of the gel matrix and poor final properties. Moreover, most of published data discuss mainly the effect of dissolution of ions from starting materials. However, other parameters such as the type of starting material, speed and time of mixing, temperature, the media of dissolution or solvent and solid to liquid ratio [10–13] also play an important role on the efficiency of synthesis.

Normally, the mechanical mixing of hydraulic cement is prescribed by ASTM C305 [14]. The mixer shall be an electrically driven mechanical mixer of the epicyclic type, which imparts both a planetary and a revolving motion to the mixer paddle. Moreover, a few researches used the high-speed centrifuge mixer (Thinky mixer) to synthesis geopolymer [15–17]. In the thinky mixer, the principle is based on the simultaneous rotation and revolution (planetary) motions, where the mixer equipment rotates the container holding the material and at the same time revolves the container. Thinky mixer allows uniform and simultaneous mixing, degassing and dispersion of the materials. The previous research [18] study on setting time of fly ash geopolymer indicated that the mixing speed of Thinky mixer did not have significant effect on setting time, whereas the increased time of mixing tended to increase both initial and final sets.

This research studied the effect of mixing when used a high-speed mixer (1,000 rpm) at various mixing time on the setting time, compressive strength, mineral composition, microstructure and porosity of high calcium fly ash geopolymer pastes, and the results are compared with those prepared using a normal mixer (140 rpm).

2 Materials and Experimental Procedures

2.1 Materials

Lignite high calcium fly ash (FA) from Mae Moh power station in northern Thailand was used as a starting material. The chemical compositions were 35.21 % SiO_2, 16.57 % Al_2O_3, 13.66 % Fe_2O_3, 25.52 % CaO, 2.73 % Na_2O, 1.99 % K_2O, 3.28 % MgO and 1.04 % other by weight. The mineral compositions of fly ash are shown in Fig. 1. The FA consisted of a glassy matrix as shown by the hump at 25°–35° 2theta and crystalline phases of quartz (SiO_2), magnesioferrite ($MgFe_2O_4$), hematite (Fe_2O_3), anhydrite ($CaSO_4$) and lime (CaO). The sodium silicate solution with 28.70 % SiO_2, 8.90 % Na_2O, and 62.50 % H_2O by weight and ten molar NaOH solutions were used as alkali activated solutions.

2.2 Geopolymer Synthesis

The mix formulation of fly ash geopolymer used in this study is $Na_2O.1.17Al_2O_3.4.80SiO_2.11.45H_2O$ with the initial molar ratios of SiO_2/Al_2O_3, Na_2O/SiO_2, Na_2O/Al_2O_3, CaO/SiO_2 of 4.10, 0.21, 0.85 and 0.69, respectively. The constant ratio of liquid alkaline to fly ash (L/A) and the ratio of sodium silicate to sodium hydroxide solution were 0.40 and 0.67, respectively. The mixing procedure started with first mixing of FA and NaOH solution. Sodium silicate solution was then added to the mixture and mixed until a homogeneous paste was obtained.

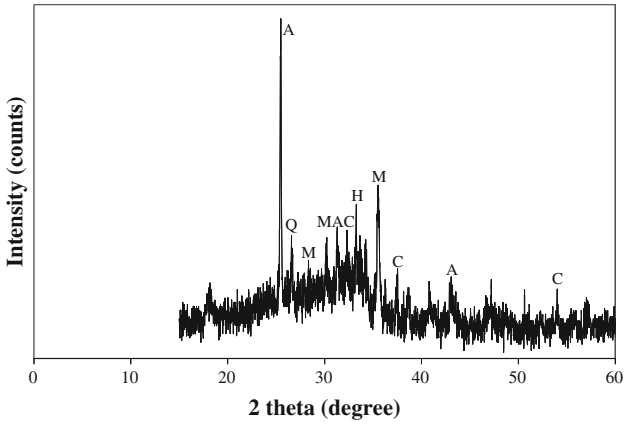

Fig. 1 XRD of fly ash (A = anhydrite, Q = quartz, M = magnesioferrite, C = lime, H = hematite)

For the study of the effect of high-speed planetary centrifugal mixer (Thinky), the periods of mixing time of 1, 3 and 6 min were used at a constant speed (1,000 rpm). For the low-speed normal mixer (140 rpm) as described in ASTM C 305 [14], the mixing time of 10 min was used as suggested by pervious published researches [5,19].

After mixing, the setting time of fresh fly ash geopolymer pastes was tested at room temperature (22 °C) as described in ASTM C191 [20] using Vicat needle apparatus. The pastes were cast in 25×25×25 mm cubes mold. The molds were vibrated for 30 s to obtain good compaction and three layer wrapped with cling film to avoid moisture loss before curing at 60 °C for 24 h. They were then demolded and kept in a controlled room at 22 °C and 50 % RH. The compressive strengths were tested as described in ASTM C109 [21] at the age of 7 days. The reported compressive strength of geopolymer pastes was tested from five samples, and average compressive strength of all samples was considered within ±10 % of mean resulted. The phase development by X-ray diffraction (XRD), microstructure by scanning electron microscope (SEM) and porosity by mercury intrusion porosimetry (MIP) were studied on the hardened geopolymer pastes at age of 7 days.

3 Results

3.1 Setting Time

The initial and final setting times of geopolymer pastes with 1, 3 and 6 min high-speed mixing times and with 10 min mixing time using normal mixer are shown in Fig. 2. The results indicated that the setting time of high calcium fly ash geopolymer paste increased with mixing time. For high-speed mixer, the initial setting time of 1, 3 and 6 min pastes was 19, 33 and 33 min, respectively, while the final setting times were 47, 65 and 80 min, respectively. For normal mixer, the initial and final setting times of 10 min paste were 60 and 100 min, respectively, and were in line with the previously published data [6,22].

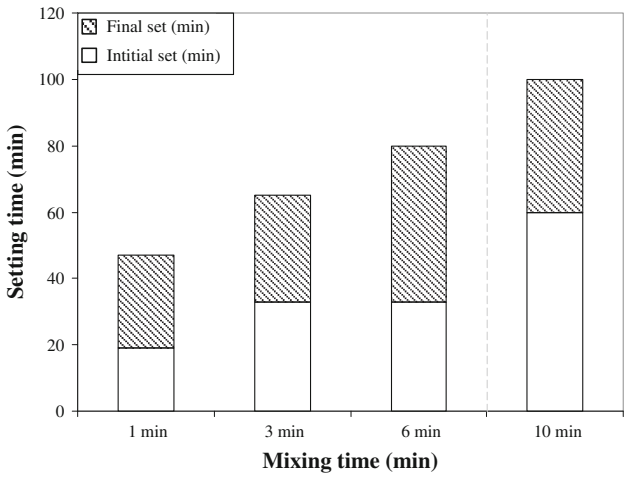

Fig. 2 Initial and final setting time of geopolymer pastes

Generally, the setting time of the normal geopolymer systems is mainly controlled by the dissolved silica and alumina ions content [23,24]. Pimraksa et al. [25] reported that the amorphous phase of Mae Moh high calcium fly ash was found to be approximately 52 %. Chindaprasirt et al. [26] explained that the amorphous phase of high calcium fly ash had high reaction degree and thus influenced the setting behavior. The increase in the time of mixing increased the time of dissolution of silica and alumina ions from raw materials to the geopolymer matrix [11,27]. Previous results indicated that the leaching of Si and Al ions in NaOH solution was dependent on mixing time [11]. Those results suggested that the initial and final set were related to many parameters such as liquid to ash ratio, sodium silicate to sodium hydroxide ratio, sodium hydroxide concentration and temperature of setting time testing [11,19,23,24]. The speed of mixing would also affect the leaching and the reaction of the silica, alumina and other ions. Accordingly, the initial molar ratio of SiO_2/Al_2O_3 (4.10) would change during leaching and geopolymerization. In a previous study, it was explained that the SiO_2/Al_2O_3 ratio, liquid to ash ratio, NaOH concentration and temperature also affected the rheology properties and setting behavior of fresh geopolymer pastes [28,30]. In addition, the results of this study showed that the mixing time (Thinky mixer - 1,000 rpm) also had an effect on the dissolution of silica and alumina ions from raw materials to the solution. Longer mixing times delayed the setting time of pastes.

3.2 Compressive Strength

The results of compressive strength of harden geopolymer pastes are shown in Table 1. For high-speed mixing, the strengths of pastes with 1, 3 and 6 min mixing were 75.1, 74.3 and 59.7 MPa, respectively, which were 120, 119 and 95 % of that of control paste (the paste made using the conventional mixer) of 62.6 MPa. The results indicated that high strength pastes could be obtained with high-speed mixing time of 1–3 min. The increase in mixing time to 6 min resulted in a

Table 1 Compressive strength result of geopolymer pastes

Mixing time	Compressive strength (MPa)
High-speed mixing	
1 min	75.1
3 min	74.3
6 min	59.7
Normal mixing 10 min (control)	62.6

drop of the strength of paste. It generally that increased mixing time would facilitate the dissolution of Si^{4+} and Al^{3+} from the raw materials and hence product formation [27]. However, for the fly ash system investigated in this study, there seems to be an optimum mixing time of Thinky mixer favors maximum strength. This implies that rate of dissolution is not the only factor controlling strength. The rate of precipitation and other parameters play a role in controlling the strength development of these mixtures. The different mixing may also have played important role on the leaching of silica and alumina ions, porosity and denseness of the pastes.

3.3 Mineralogy of Geopolymer Paste

The XRD patterns of geopolymer pastes with high-speed mixing and normal mixing are shown in Fig. 3a–d. The XRD patterns of the geopolymer pastes (Fig. 3a–d) are similar with that of FA (Fig. 1). The amorphous phases were easily detected as broad hump around 25°–38° 2theta representing a small shift of this hump compared with that of fly ash [5,11]. For high-speed mixing for 1 min, quartz, calcium carbonate, calcium silicate hydrate (CSH) and magnesioferrite were detected as shown in Fig. 3a. The presence of CSH phase can be confirmed by the presence of peaks at 29.5 degree and 32.05 degree [31]. Quartz and magnesioferrite were the remnant of the phases found in fly ash. Calcium carbonate possibly came from the reaction between calcium oxide and carbon dioxide. For 1 min high-speed mixing, the peak of CSH was very prominent indicating a substantial amount of hydration reaction occurred and CSH formed. The CSH coexisted with the geopolymer products and enhanced the strength of the geopolymer [32].

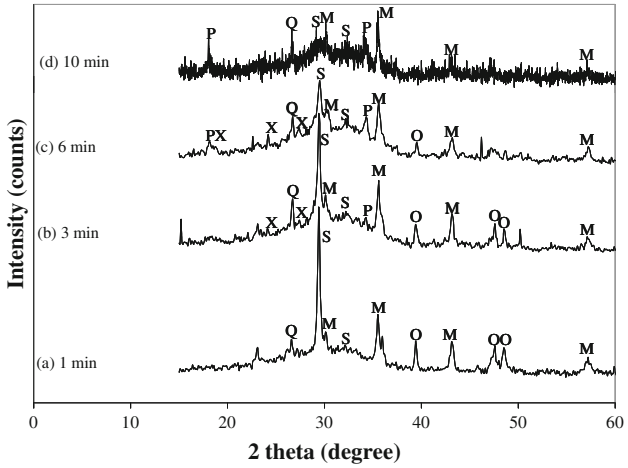

Fig. 3 Mineral compositions of geopolymer pastes with various mixing times at 1,000 rpm and normal mixing at 10 min (Q = quartz, M = magnesioferrite, O = calcium carbonate, X = phase x, S = calcium silicate hydrate, P = calcium hydroxide)

For 3 min paste, the peak of CSH reduced compared with that of 1 min paste. In addition, phase X ($Na_{14}Al_{12}Si_{13}O_{51}.6H_2O$) and calcium hydroxide were detected. The reduction in CSH resulted in an excess in calcium and this reflected in the appearance of calcium hydroxide. For 6 min paste, the peak of CSH reduced further compared with those of 1 and 3 min pastes. From the XRD results, the increase in mixing time (1, 3 and 6 min) resulted in increased phase X and calcium hydroxide with reduction in CSH and the decrease in compressive strength.

The setting time of paste was related to formation of CSH. At 1 min high-speed mixing, the setting time was relatively short and associated with the formation of large amount of CSH. The mixing at high speed for 3 and 6 min reduced the amount of CSH formed, and the setting time of pastes were increased. The amount of sodium-aluminosilicate hydrate (NASH) also increased with the increase in the high-speed mixing time as indicated by the large hump at 25°–38° 2theta [5,11,31]. The increase in the amount of NASH gel compensated the reduction in the formation of CSH.

For 10 min normal mixing (Fig. 3d), the CSH and calcium hydroxide were found and phase X and calcium carbonate disappeared. The amount of CSH was, however, less than those of high-speed mixing pastes. This resulted in the longer setting time than those of the high-speed mixing and also resulted in the normal strength level of paste.

3.4 Morphology of Geopolymer Paste

The morphology of hardened geopolymer pastes with high-speed mixing times of 1 and 6 min and normal mixing for 10 min (control) are shown in Fig. 4a–c, respectively. The SEM showed that the structure of paste was dense with unreacted fly ash particles embedded in a continuous matrix. The 1 min high-speed mixing paste (Fig. 4a) was slightly denser than the 6 min paste (Fig. 4b) and normal mixing paste (Fig. 4c). The SEM of pastes confirmed to strength and XRD results. It also contained white globules of CSH or CASH in the matrix. The CSH was easily detected in the 1 min high-speed mixing paste, and this is conformed to the result of X-ray diffraction. However, for the 6 min high-speed mixing paste, the matrix contained less CSH and increased number of cracks which led to low strengths observed with this sample. For 10 min normal mixing paste (Fig. 4c), the structure looked very similar to the 6 min high-speed mixing paste and this reflected in similar compressive strengths of the two mixes.

The EDXA analyses on the dense matrix area of control, 1 and 6 min pastes show composition oxides of SiO_2, Al_2O_3 and CaO as shown in Fig. 4a–c. In all three mix compositions investigated, the percentage of CaO was rather high at around 20 % in the matrix. Therefore, this percentage of CaO confirmed the presence of Ca^{2+} as CSH or CASH phase.

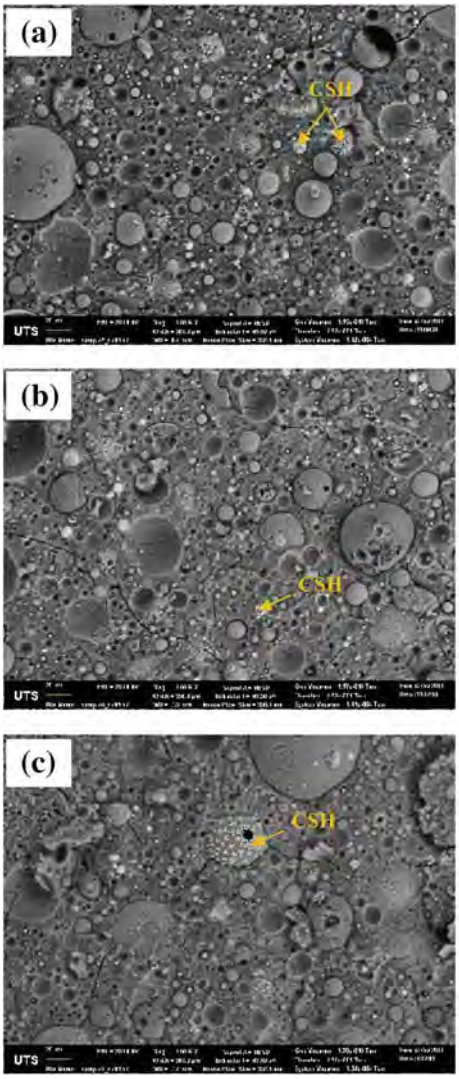

Formulas	Intensity (%)
SiO_2	27.02
Al_2O_3	9.55
CaO	26.19

Formulas	Intensity (%)
SiO_2	28.50
Al_2O_3	10.54
CaO	21.62

Formulas	Intensity (%)
SiO_2	22.71
Al_2O_3	9.17
CaO	26.04

Fig. 4 SEM of geopolymer pastes **a** high-speed mixing for 1 min **b** high-speed mixing for 6 min **c** normal mixing for 10 min

Moreover, for the 1 min high-speed mixing paste, the SiO_2/ Al_2O_3 ratio was 2.82 and confirmed to previous study [5] which reported the SiO_2/ Al_2O_3 ratio range between 2.80-3.50 with significant influence on strength development. On the other hand, the SiO_2/ Al_2O_3 ratio of 1 and 3 min high-speed mixing pastes were 2.70 and 2.47, respectively.

3.5 Porosity and Average Pore Diameter of Geopolymer Paste

The results for percentage of pore volume of geopolymer pastes are shown in Fig. 5. The total porosities of 1, 3 and 6 min of pastes were 20.19, 22.20 and 23.28 %, respectively. The total porosity increased slightly with increased mixing time. The increase in mixing time increased air void and large capillary pores and thus adversely affected the compressive strength. For the high-speed mixing, the time of mixing of 1 min was sufficient to produce dense paste with low pore volume. Prolong mixing resulted in the increase in porosity mainly in the air void and large capillary pore. In particular, the large capillary pores increased from 1.68 % for 1 min paste to 6.8 and 8.6 % for 3 and 6 min pastes, respectively. For 6 min mixing time, the pastes were coherent and deterred the formation of CSH with increase in pore volume due to the condensation of water and formation of additional large capillary pores. For the 10 min paste, the total porosity was 21.89 % and was in the same order as those of 3 and 6 min pastes. However, the pore consisted mainly of air void and large capillary pore of 6.5 and 14.8 %, respectively. This indicated that the short duration high-speed mixing could be used to produce homogeneous and degassed geopolymer pastes.

The graphs of pore diameter and incremental pore volumes of geopolymer pastes are shown in Fig. 6. The high-speed mixing and the normal mixing produced different patterns of pore distributions. The high-speed mixing produced pastes with three main categories of pore. A small portion of air void, a large portion of medium and large capillary pores and a sizable portion of gel pores. The normal mixing

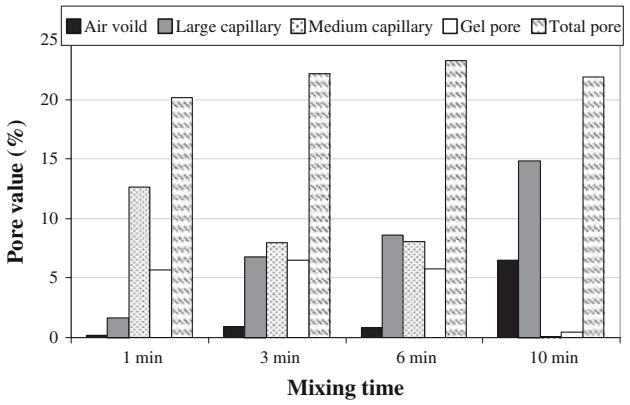

Fig. 5 Percentage of pore volume of geopolymer pastes

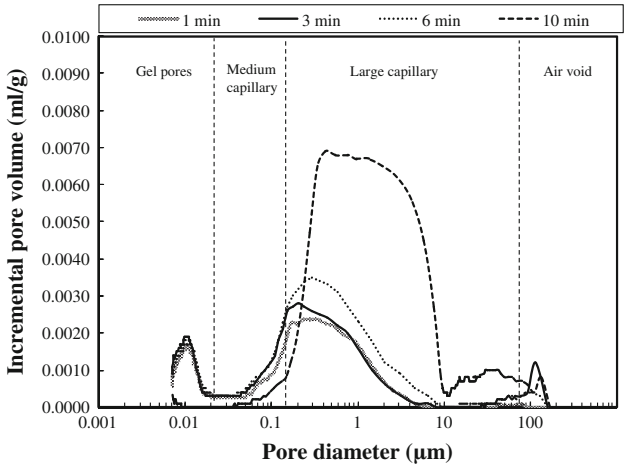

Fig. 6 The relationships between the differential pore volume and pore diameter of geopolymer pastes

produce pastes with predominantly large capillary and air voids. The amount of gel pores in the high-speed mixing pastes seemed to be associated with the formation of CSH and/or CASH. Although not large amount, the air voids of the 3 and 6 min pastes indicated the possible trapping of some air in homogenous paste during high-speed mixing. As demonstrated here also, the high-speed mixing of only 1 min was sufficient to produce geopolymer paste with high strength and low porosity.

4 Conclusions

From this study, it can be concluded that the properties of the high calcium fly ash geopolymer pastes are dependent on the mixing speed and time. High-speed mixing for 1 min was sufficient to produce homogenous and dense paste with high compressive strength of 75.1 MPa due to the formation of CSH and/or CASH. Additional mixing time delayed the setting time and produced pastes with slightly lower strength due to the reduced formation of CSH. The normal mixing required more mixing time in the order of 10 min to have good strength and this further delayed the setting time with less formation of CSH. High-speed mixing produced geopolymer paste with high strength and low porosity compared to normal mixing which produced a lower strength paste with substantial amount of large capillary and air voids.

Acknowledgments The financial supports from the TRF Senior Research Scholar (Grant No. RTA 5480004), Program of Civil Technology, Faculty of Industrial Technology, Lampang Rajabhat University and Australian Catholic University are gratefully acknowledged. We are also indebted to Dr. R. Wuhrer of the Microstructure Analysis Unit, University of Technology Sydney for the help in SEM and to the Material Science and Engineering, CSIRO for the help in compressive strength test.

References

1. Guo, X.; Shi, H.; Chen, L.; Dick, W.A.: Alkali-activated complex binders from class C fly ash and Ca-containing admixtures. J. Hazard. Mater. **173**(1–3), 480–486 (2010)
2. Thokchom, S.; Mandal, K.K.; Ghosh, S.: Effect of Si/Al ratio on performance of fly ash geopolymers at elevated temperature. Arabian J. Sci. Eng. **37**, 977–989 (2012)
3. Palomo, A.; Grutzeck, M.W.; Blanco, M.T.: Alkali-activated fly ashes: a cement for the future. Cem. Concr. Res. **29**(8), 1323–1329 (1999)
4. Komnitsas, K.; Zaharaki, D.: Geopolymerisation: a review and prospects for the minerals industry. Miner. Eng. **20**(14), 1261–1277 (2007)
5. Chindaprasirt, P.; De Silva, P.; Sagoe-Crenstil, K.; Hanjitsuwan, S.: Effect of SiO_2 and Al_2O_3 on the setting and hardening of high calcium fly ash-based geopolymer systems. J. Mater. Sci. **47**(12), 4876–4883 (2012)
6. Phoo-ngernkham, T.; Chindaprasirt, P.; Sata, V.; Pangdaeng, S.; Sinsiri, T.: Properties of high calcium fly ash geopolymer pastes containing Portland cement as additive. Int. J. Miner. Metall. Mater. **20**(2), 214–220 (2013)
7. Lowke, D.; Schiessl, P.: Effect of mixing energy on fresh properties of SCC. In: Proceedings of the Fourth International RILEM Symposium on Self-Compacting Concrete and Second North American Conference on the Design and Use of Self-Consolidating Concrete, Chicago, USA (2005)
8. Davisaon, J.I.: The effect of mixing time on the compressive strength of masonry mortars. Div. Build. Res. Natl. Res. Counc. Can. **114**, 1–12 (1976)
9. Prentice, L.H.; Tyas, M.J.; Burrow, M.F.: The effect of mixing time on the handling and compressive strength of an encapsulated glass-ionomer cement. Dental Materials **21**(8), 704–708 (2005)
10. Guo, X.; Shi, H.; Dick, W.A.: Compressive strength and microstructural characteristics of class C fly ash geopolymer. Cem. Concr. Compos. **32**(2), 142–147 (2010)
11. Rattanasak, U.; Chindaprasirt, P.: Influence of NaOH solution on the synthesis of fly ash geopolymer. Miner. Eng. **22**(12), 1073–1078 (2009)
12. Van Jaarsveld, J.G.S.; Van Deventer, J.S.J.; Lukey, G.C.: The characterisation of source materials in fly ash-based geopolymers. Mater. Lett. **57**(7), 1272–1280 (2003)
13. Yip, C.K.; Lukey, G.C.; Provis, J.L.; van Deventer, J.S.J.: Effect of calcium silicate sources on geopolymerisation. Cem. Concr. Res. **38**(4), 554–564 (2008)

14. ASTM C305: Standard practice for mechanical mixing of hydraulic cement pastes and mortars of plastic consistency. Annual Book of ASTM Standard, Vol. 04.01 (2005)
15. Rickard, W.D.A.; Van Riessen, A.; Walls, P.: Thermal character of geopolymers synthesized from class F FA containing high concentrations of iron and alpha quartz. Int. J. Appl. Ceram. Technol. **7**(1), 81–88 (2010)
16. Temuujin, J.; van Riessen, A.: Effect of fly ash preliminary calcination on the properties of geopolymer. J. Hazard. Mater. **164**(2–3), 634–639 (2009)
17. Temuujin, J.; van Riessen, A.; MacKenzie, K.J.D.: Preparation and characterisation of fly ash based geopolymer mortars. Constr. Build. Mater. **24**(10), 1906–1910 (2010)
18. Hanjitsuwan, S.; Silva, D.P.; Chindaprasirt, P.: Effect of speed and time of mixing in setting time and strength of high calcium fly ash geopolymer. In: Paper Presented at the 4th KKU International Conference 2012 (KKU-IENC 2012), Khon Kaen, Thailand (2012)
19. Chindaprasirt, P.; Chareerat, T.; Sirivivatnanon, V.: Workability and strength of coarse high calcium fly ash geopolymer. Cem. Concr. Compos. **29**(3), 224–229 (2007)
20. ASTM C191: Standard test method for time of setting of hydraulic cement by vicat needle. Annual Book of ASTM Standard, Vol. 04.01 (2008)
21. ASTM C109: Standard test method of compressive strength of hydraulic cement mortars (using 2-in. or [50 mm] cube specimens). Annual Book of ASTM Standard, Vol. 04.01 (2002)
22. Rattanasak, U.; Pankhet, K.; Chindaprasirt, P.: Effect of chemical admixtures on properties of high-calcium fly ash geopolymer. Int. J. Miner. Metall. Mater. **18**(3), 364–369 (2011)
23. Silva, P.D.; Sagoe-Crenstil, K.: Medium-term phase stability of Na_2O–Al_2O_3–SiO_2–H_2O geopolymer systems. Cem. Concr. Res. **38**(6), 870–876 (2008)
24. Silva, P.D.; Sagoe-Crenstil, K.; Sirivivatnanon, V.: Kinetics of geopolymerization: role of Al_2O_3 and SiO_2. Cem. Concr. Res. **37**(4), 512–518 (2007)
25. Pimraksa, K.; Hanjitsuwan, S.; Chindaprasirt, P.: Synthesis of belite cement from lignite fly ash. Ceram. Int. **35**(6), 2415–2425 (2009)
26. Chindaprasirt, P.; Chareerat, T.; Hatanaka, S.; Cao, T.: High strength geopolymer using fine high calcium fly ash. J. Mater. Civ. Eng. **23**(3), 264–270 (2011)
27. Na Wittayanan, R.: The effect of pre-dissolution time to geopolymer properties. Master Thesis, Kasetsart University (2009)
28. Favier, A.; Habert, G.; d'Espinose de Lacaillerie, J.B., Roussel, N.: Mechanical properties and compositional heterogeneities of fresh geopolymer pastes. Cem. Concr. Res. **48**(0), 9–16 (2013)
29. Poulesquen, A.; Frizon, F.; Lambertin, D.: Rheological behavior of alkali-activated metakaolin during geopolymerization. J. Non-Cryst. Solids **357**(21), 3565–3571 (2011)
30. Romagnoli, M.; Leonelli, C.; Kamse, E.; Gualtieri, M.L.: Rheology of geopolymer by DOE approach. Constr. Build. Mater. **36**(0), 251–258 (2012)
31. Lecomte, I.; Henrist, C.; Liegeois, M.; Maseri, F.; Rulmont, A.; Cloots, R.: (Micro)-structural comparison between geopolymers, alkali-activated slag cement and Portland cement. J. Eur. Ceram. Soc. **26**, 3789–3797 (2006)
32. Somna, K.; Jaturapitakkul, C.; Kajitvichyanukul, P. Chindaprasirt, P.: NaOH-activated ground fly ash geopolymer cured at ambient temperature. Fuel **90**(6), 2118–2124 (2011)

Properties of Wood Flour/Expanded Polystyrene Waste Composites Modified With Diammonium Phosphate Flame Retardant

Prinya Chindaprasirt,[1] Salim Hiziroglu,[2] Chattichai Waisurasingha,[1] Pornnapa Kasemsiri[3]
[1]*Sustainable Infrastructure Research and Development Center, Department of Civil Engineering, Faculty of Engineering, Khon Kaen University, Khon Kaen 40002, Thailand*

[2]*Department of Natural Resource Ecology and Management, Oklahoma State University, 303-G Agricultural Hall, Stillwater, Oklahoma 74078*

[3]*Department of Chemical Engineering, Faculty of Engineering, Khon Kaen University, Khon Kaen 40002, Thailand*

The objective of the study was to evaluate properties of waste plastic composite samples manufactured from expanded polystyrene waste (EPS) and sawdust containing diammonium phosphate (DAP) as flame retardant. Thermal degradation along with dimension stability and mechanical characteristics of the specimens as a function of DAP content were determined. The wood fiber/EPS composite modified with DAP content up to 20 wt% resulted in the best linear burning rate. The rate of thermal degradation of samples also substantially decreased while limiting oxygen index and char residual increased. Overall dimension stability in the form of water absorption and thickness swelling along with flexural characteristics of the samples were found comparable to those of commercial wood plastic composites. The wood fiber/EPS containing DAP showed high potential for use as wood composite products with adequate fire resistance. POLYM. COMPOS., 00:000–000, 2014. © 2014 Society of Plastics Engineers

INTRODUCTION

Wood plastic composite (WPC) is material that consists of wood and thermoplastics or thermosets [1]. WPCs are relatively new products as compared to the long history of natural lumber or traditional wood composites such as particleboard or fiberboard. Nowadays, the industrial scope of WPCs has expanded rapidly into various applications such a building, interior decoration, door, window, flooring and automotive interior sectors [2, 3]. WPC products have been produced from different types of natural fiber resources and virgin thermoplastics including polyethylene (HDPE) [4], polypropylene (PP) [5], polyvinyl chloride (PVC) [6], polystyrene (PS) [7], poly(lactic acid) (PLA) [8]. However, effort on investigation of recycled thermoplastic matrix with natural fiber composite is still very limited. Generally, polyolefins-based plastics are widely used for many applications, including packaging, which can potentially be recovered for recycling. Plastic is significant source as raw material for the development of thermoplastic composites with natural fibers, due to its large volume and low cost [9, 10]. These composites provide several advantages, including low cost, low density, low manufacturing energy, low CO_2 emission, and renewability [11]. Recently, the physical and mechanical properties of wood composite based on plastic waste and palm leaves were investigated and indicated that the obtained properties of wood composites proved an acceptable final and promising WPC product. It can be efficiently used in outdoor structure and construction industry [12]. In addition, Poletto et al. [13] observed that using of recycle expanded PS as matrix for WPC had a potential in manufacturing of low density composites with high mechanical properties. However, the application of WPCs is still limitation due to the problem of fire performance. The main components of WPC such a wood and plastic are thermally degradable and combustible materials [14]. Therefore, improvement

Correspondence to: P. Kasemsiri; e-mail: pornkas@kku.ac.th
Contract grant sponsor: National Research Council of Thailand; contract grant sponsor: Thailand Research Fund (TRF); contract grant number: RTA5480004 (TRF Senior Research Scholar); contract grant sponsor: Office of the Higher Education Commission (Higher Education Research Promotion and National Research University Project of Thailand, through the Advanced Functional Materials Cluster of Khon Kaen University).
DOI 10.1002/pc.22977
Published online in Wiley Online Library (wileyonlinelibrary.com).

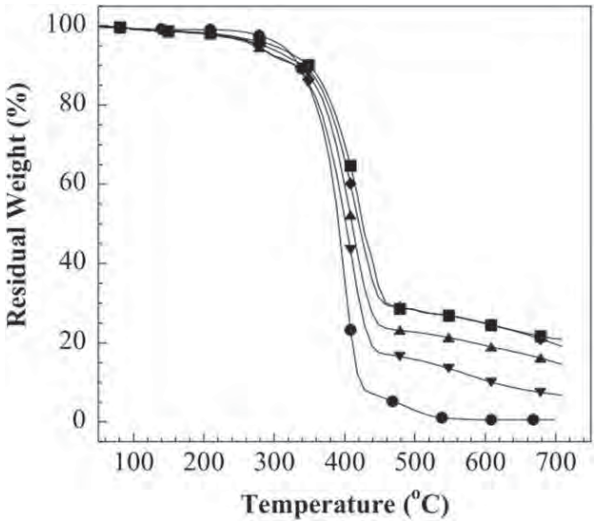

FIG. 1. TGA thermograms of wood flour/EPS composites modified with DAP: (●) 0 wt% DAP, (▼) 10 wt% DAP, (▲) 20 wt% DAP, (◆) 30 wt% DAP, and (■) 40 wt% DAP.

of flame retardancy of the composite materials plays a very important role to comply with the safety requirements of the wood composite products.

A number of flame retardants for polymers and composites have been developed, and many of these are suitable for use in fiber-based composites [15]. Especially, nonhalogenated-based flame retardant, phosphorus containing compounds are frequently used as flame retardants owing to their low generation of smoke and toxic gases. They work very effectively in condensed phase by formation of char which is difficult to ignite. Char inhibits gaseous products from diffusing to the pyrolysis zone and protects the polymer surface from heat and air [16]. From previous works, Chen [17] and Gaan and Sun [18] investigated using diammonium phosphate (DAP) as fire retardant in natural fiber. It was found that such product was safe, inexpensive, and more efficient at improving the limiting oxygen index (LOI) of natural fiber than other phosphorus compounds such as tributyl phosphate, tri-allyl phosphate, or triallyl phosphoric triamide. Suardana et al. [15] also observed that jute and coconut fiber treated with 5% DAP provide the best linear burning rate, i.e., the burning time of wood composite increased up to 69% for jute reinforced PP and 36% for coconut reinforced PP. Furthermore, the effect of boron and phosphate compounds on fire properties of wood–PP composites was studied by Ayrilmis et al. [19]. The heat release rates from the cone calorimeter tests indicated that the phosphate treatments provided better improvements in the fire performance than the boron treatments. Consequently, it appears that DAP was a good candidate for improvement of fire resistance of WPCs.

Currently, there is no information about flammability, thermal degradation, as well as physical and mechanical properties of the wood fiber/EPS composites modified with flame retardant. Therefore, the objectives of this work are to produce the wood composites from expanded PS waste and sawdust including evaluate the effects of flame retardant (DAP) content in the composites on properties of the wood flour/EPS composites.

EXPERIMENTAL

Materials

The EPS was acquired from the packaging of food, electronic goods and home appliances. Wood sawdust particles obtained from carpentry and wood-working processes and supplied by a wood manufacture from Khon Kaen in the northeast of Thailand was used as wood flour. The average size of wood flour used in this work was in the range of 100–300 μm. DAP (≥98% purity) was purchased from Ajax Finerchem. The specimens were produced by a conical co-rotating twin screw extruder (Labtech LTE 20-40) and injection molded (Manumold).

Preparation of Wood Flour/EPS Composites Modified with DAP

The EPS was preheated in oven at temperature of 110°C for 15 min. In the next step, EPS samples were ground in a rotary knife mill into flakes, with a particle size range from 5 to 15 mm. Wood flour was dried at a temperature of 105°C for 24 h in a laboratory oven until they reached a constant weight. Samples were prepared with EPS flakes and 0, 10, 20, 30, and 40 wt% of DAP with addition of 20 wt% wood flour. The mixtures were then processed in a co-rotating twin-screw extruder at 200 rpm at 170°C. The specimens were produced by employing injection molder at a barrel temperature in range of 160 and 190°C and mold temperature of 40 ± 2°C.

Characterization of the Composite Samples

The thermal degradation of the wood flour/EPS composites was studied using a TGA-50, Shimadzu. The testing temperature program was ramped at a heating rate of 20°C/min from room temperature to 700°C under nitrogen atmosphere. The purge nitrogen gas flow rate was maintained at 20 ml/min. The sample mass used was 10–20 mg. Degradation temperature of each specimen was determined from the temperature at 5% weight loss whereas char yield was obtained the weight residue at 600°C.

LOI values of samples were measured using an instrument from Stanton Redcroft on bar ($70 \times 7 \times 3$ mm^3) in accordance with the standard oxygen index test as per ASTM D2863-10. The test was based on the determination of the lowest volume concentration of oxygen in a gas mixture of nitrogen and oxygen (O_2 and N_2) required

 DOI 10.1002/pc

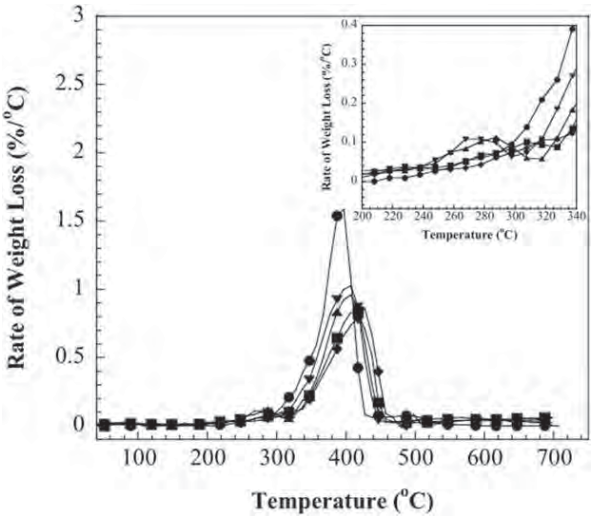

FIG. 2. TGA derivative curves of wood flour/EPS composites modified with DAP: (●) 0 wt% DAP, (▼) 10 wt% DAP, (▲) 20 wt% DAP, (◆) 30 wt% DAP, and (■) 40 wt% DAP.

for ignition and the onset of burning. LOI values were calculated according to the following equation:

$$\text{LOI}\,(\%) = \frac{O_2}{O_2 + N_2} \times 100. \quad (1)$$

The flame retardant properties of the wood flour/EPS composites were measured in accordance with ASTM D 635-10. Specimens with dimensions of 125 × 13 × 3 mm^3 were held horizontally in the burning test. They were ignited by fuel gas at one of the ends of the sample. The flame time from the first mark (25 mm from the ignition end) until the second mark (100 mm from the ignition end) was measured to determine the linear burning rate (V) of the sample.

Attenuated total reflection infrared (FTIR-ATR) spectra of all samples after LOI testing were acquired by Bruker Tensor 27 spectrometer. All spectra were taken as a function of time with 64 scans at a resolution of 4 cm^{-1} and a spectral range of 4000–650 cm^{-1}.

Water absorption and thickness swelling characteristics of the samples were conducted following ASTM D 570-98. Before testing, the thickness and weight of each sample were measured. All samples were submerged in distilled water and the weight measurements were performed at 2, 6, 24 h up, and 1 week. The samples were removed, wiped, weighed, and immediately returned to water bath at each test period. The amount of water adsorbed was calculated based on the initial conditioned mass of each sample. The samples were removed, wiped, weighed and immediately returned to water bath at each test period. The amount of water adsorbed was calculated based on the initial conditioned mass of each sample.

Flexural modulus and flexural strength of the wood polymer composite specimens were determined according to ASTM D 790-10 employing a Universal Testing Machine, Instron, Model 5567 equipped with a 10 kN load cell. The measurement was performed in a 3-point bending mode with a support span of 48 mm at the crosshead speed of 1.2 mm/min. The dimension of the each specimen was 12.7 × 60 × 3.2 mm^3.

RESULTS AND DISCUSSION

Thermal Degradation

Thermal degradation of wood flour-EPS composites was investigated by thermogravimetric analysis (TGA) as illustrated in Figs. 1 and 2. The degradation temperature (T_d) of the wood flour/EPS composites was 328°C

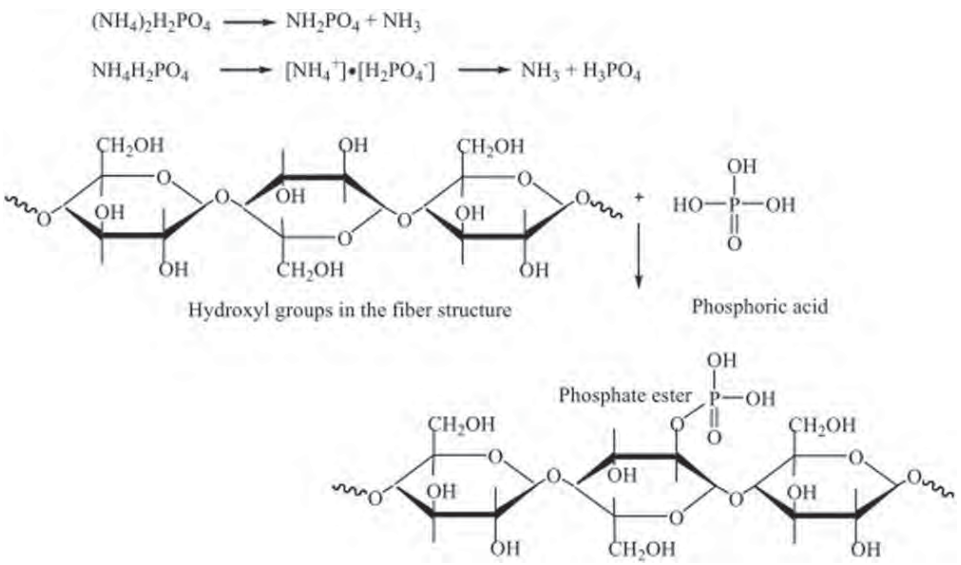

SCH. 1. The possible reaction between phosphoric acid (H_3PO_4) and primary hydroxyl groups during thermal decomposition.

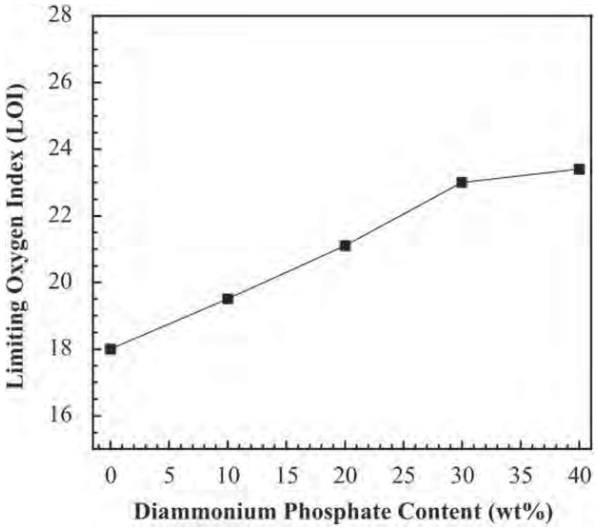

FIG. 3. Limiting oxygen index (LOI) of wood flour-EPS composites at various DAP contents.

whereas wood flour/EPS composites modified with DAP at 10–40 wt% showed the T_d values within range of 267–269°C. As shown in Fig. 1, the T_d's of wood flour/EPS composites modified DAP were found to be slightly lower than that of the unmodified wood flour/EPS composites. Due to flame retardant decomposition under temperature scan, DAP tended to be released from the specimens before degradation of EPS matrix and wood flour. Meanwhile, the char yields of wood flour/EPS composites in the presence of DAP were observed to be higher than that of the unmodified wood flour/EPS composites as illustrated in Fig. 1. The char yields of wood flour/EPS composites modified with DAP tended to increase with increasing DAP contents, i.e., 0.54 (0 wt% DAP), 10.61 (10 wt% DAP), 19.40 (20 wt% DAP), 24.80 (30 wt% DAP), and 25.01 (40 wt% DAP). The improved char yield was probably caused by the esterification of phosphoric acid (H_3PO_4) and primary hydroxyl groups in the fiber during thermal decomposition of DAP. This interaction leads to the thick and compact char [20, 21]. It has been observed that DAP was easily converted to H_3PO_4 because the ammonia cations (NH_4^+) were driven off at low temperature [22]. The possible reaction between phosphoric acid (H_3PO_4) and primary hydroxyl groups during thermal decomposition was depicted in Scheme 1. Similar results were also observed in the wood composites manufactured using natural fiber treated with DAP and PP/PLA as matrix [15]. Char yield of material has been correlated with its flame retardancy. Increasing char yield implied greater fire resistance of the sample as it was proposed that char formation would limit production of combustion gases, inhibit combustion gases from diffusing to the pyrolysis zone and protect the polymer surface from heat and air [16]. Therefore, the fire-resistant property of wood flour/EPS composites improved with the DAP addition.

Furthermore, the thermal decomposition of wood flour/EPS composites was also examined by the derivatives of TGA thermograms. Generally, pyrolysis of hemicellulose, cellulose and lignin occurred at temperatures around 220–315, 315–400, and 160–500°C, respectively [23–25]. Figure 2 depicts two main decomposition steps of all samples. The temperatures for the maximum mass loss at first

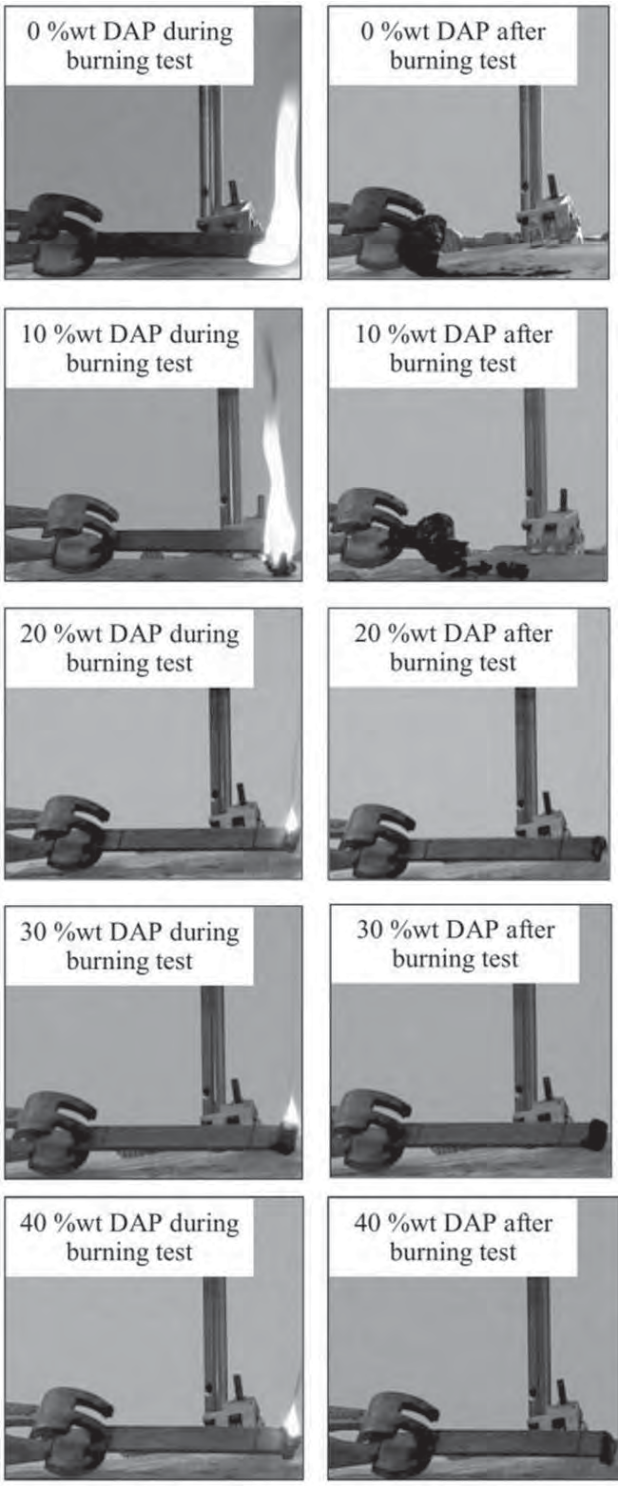

FIG. 4. Pictures of horizontal burning test.

DOI 10.1002/pc

TABLE 1. The horizontal burning test of the wood flour/EPS composites.

Wood flour-EPS composites at various DAP contents (wt%)	Linear burning rate (mm/min)
0	44.6 ± 3.1
10	26.1 ± 0.9
20	Flame front did not pass 25-mm reference mark
30	Flame front did not pass 25-mm reference mark
40	Flame front did not pass 25-mm reference mark

step were observed around 282 and 298°C for the unmodified and DAP-modified wood flour/EPS composites, respectively. The presence of DAP in wood flour/EPS composites reduced the first decomposition temperature. This behavior could be attributed to the first decomposition step corresponded to the decomposition of hemicellulose, lignin, and release of DAP's component such as NH_3 and H_2O [26]. The char residual from this step might act as heat insulator to protect and improve thermal stability for other components at the second step. Figure 2, the second decomposition temperature of wood flour/EPS composite was determined as 393°C whereas those of DAP-modified wood flour/EPS composites at 10–40 wt% were observed within the range of 404–426°C. The second decomposition temperature substantially increased with increasing DAP contents. Moreover, the rate of weight loss also revealed that wood flour/EPS composites modified with DAP reduced the degradation rate from 1.57 to 0.86%/°C when they were modified with DAP having a range of 0–40 wt%. The results confirmed the observed

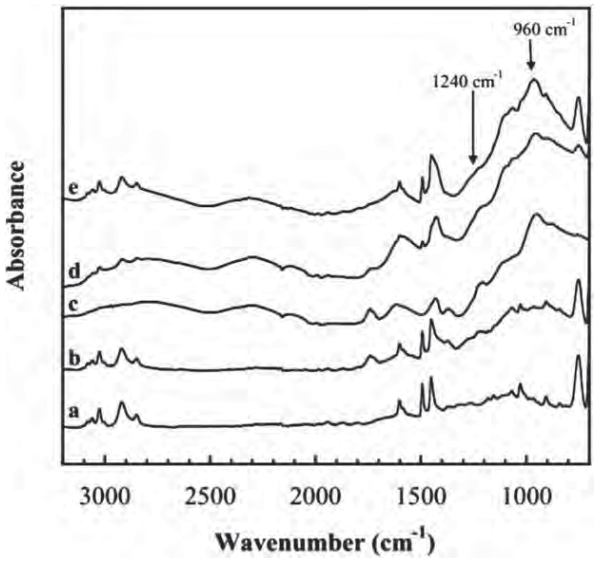

FIG. 5. ATR spectra of char residues of wood flour/EPS composites modified with DAP: 0 wt% DAP (a), 10 wt% DAP (b), 20 wt% DAP (c), 30 wt% DAP (d), and 40 wt% DAP (e).

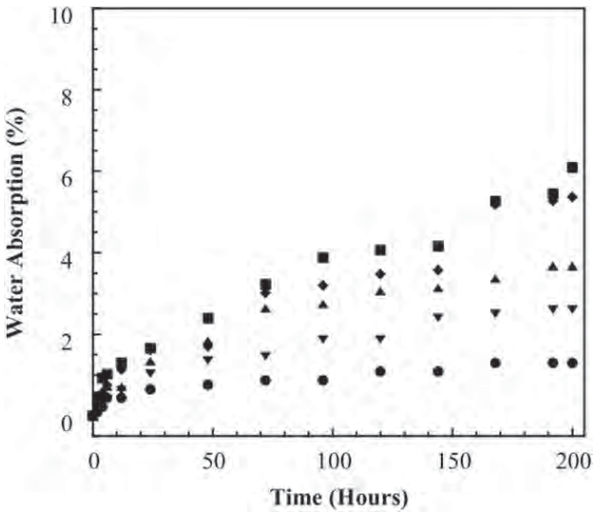

FIG. 6. Percentage water absorption of wood flour/EPS composites modified with DAP: (●) 0 wt% DAP, (▼) 10 wt% DAP, (▲) 20 wt% DAP, (◆) 30 wt% DAP content, and (■) 40 wt% DAP content.

enhancement in thermal stability of these wood composites at second step.

Flame Retardancy

LOI is widely used as a simple and precise method for evaluation of fire self-extinguishment and to determine the flame retardant properties of polymeric material [26]. The lager the LOI value of the material, the less susceptible it is to burn. In general, air is composed of approximately 21 vol% oxygen, any material with an LOI of less than 21 will easily burn in air. Materials with LOI between 21 and 27.9 vol% are well known as slow burning. Above this range, materials are considered to be self-extinguishing [27]. Figure 3 shows LOI data of all wood flour/EPS composites modified with DAP at various

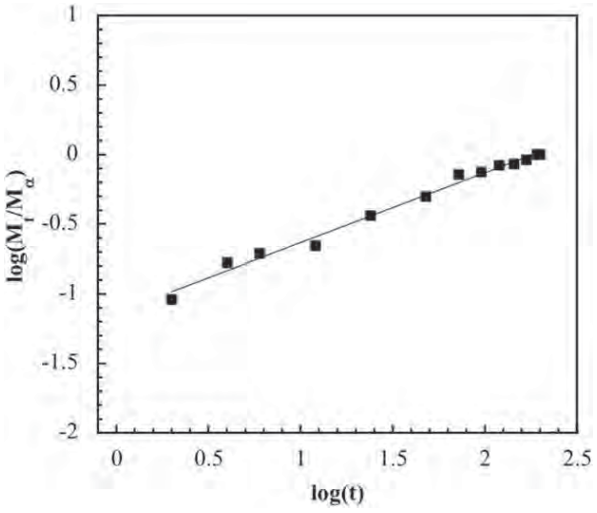

FIG. 7. Diffusion curve fitting plots of wood flour/EPS composite modified with 20 %wt DAP to determine *n* parameter.

TABLE 2. Diffusion case selection parameters and diffusion coefficients of the wood flour/EPS composites.

Wood flour-EPS composites at various DAP contents (% wt)	N	Diffusion coefficient $\times$ 10^{-9} (m^2/s)
0	0.46	1.18
10	0.48	1.60
20	0.52	4.26
30	0.56	4.39
40	0.50	4.96

contents. The unmodified-DAP wood flour/EPS composites was founded to be easy flammable and its LOI was only 18 because both EPS and wood flour were easily flammable materials. The LOI of wood flour/EPS composites tended to increase from 19.5 to 24.3 when these specimens were modified with DAP within a range of 10–40 wt%. The higher LOI values confirmed that DAP was an effective flame retardant for wood flour/EPS composites. These results were also consistent with those char yield values found from the TGA characteristics of samples. The char yields also increased with increasing DAP content, as shown in Fig. 1. The char of samples formed during combustion and acted as a protective layer so that oxygen diffusion to the surface of the specimen was prevented resulting in more oxygen needed for combustion process. Such results are in good agreement with the findings of the PP- and PE-based wood composite modified with ammonium phosphate [15].

Burning rates of wood flour/EPS composites containing different DAP contents are depicted in Fig. 4 and displayed in Table 1. The unmodified-DAP wood flour/EPS composites showed the highest linear burning rate at 44.6 $\pm$ 3.1 mm/min whereas the addition of 10 wt% DAP reduced the burning rate to 26.1 $\pm$ 0.9 mm/min. In case of modification with 20–40 wt% DAP, the flame front did not pass 25-mm reference mark as illustrated in Fig. 4. These results implied that the additions of 20 wt% DAP in wood flour/EPS composites was a sufficient and its burning rate was significantly lower than that of commercial WPCs of about 7.1–18.1 mm/min [28]. Based on the flame retardancy results, it is clearly seen that during fire disaster with high temperature, building decoration materials made of flame retardant modified WPCs would show better performance in gaining time for rescuing.

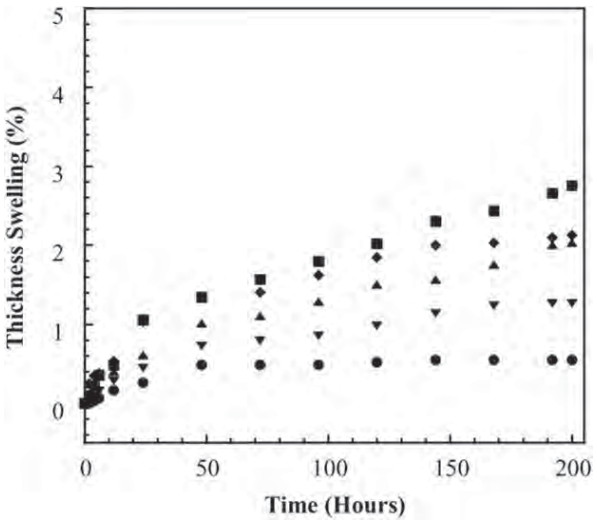

FIG. 9. Percentage thickness swelling of wood flour/EPS composites modified with DAP: (●) 0 wt% DAP, (▼) 10 wt% DAP, (▲) 20 wt% DAP, (◆) 30 wt% DAP, and (■) 40 wt% DAP.

Attenuated Total Reflection Infrared Analysis of Char Residues

To better understand the action of the flame retardant, further study of the structures of char residues after the LOI test were observed by FTIR-ATR. Figure 5 shows

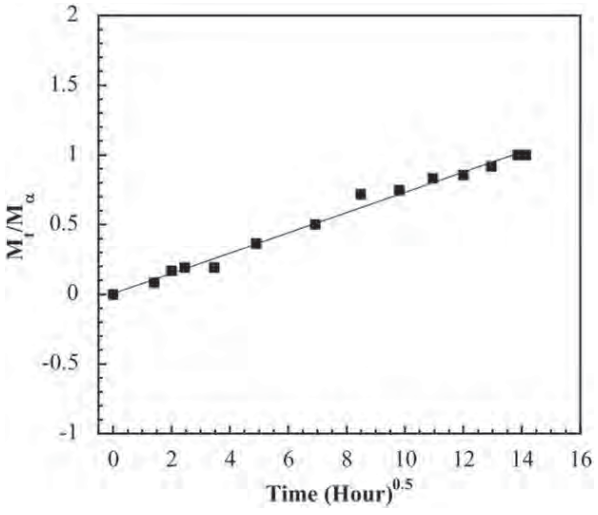

FIG. 8. Diffusion curve fitting plots of wood flour/EPS composite modified with 20 %wt DAP to determine diffusion coefficient.

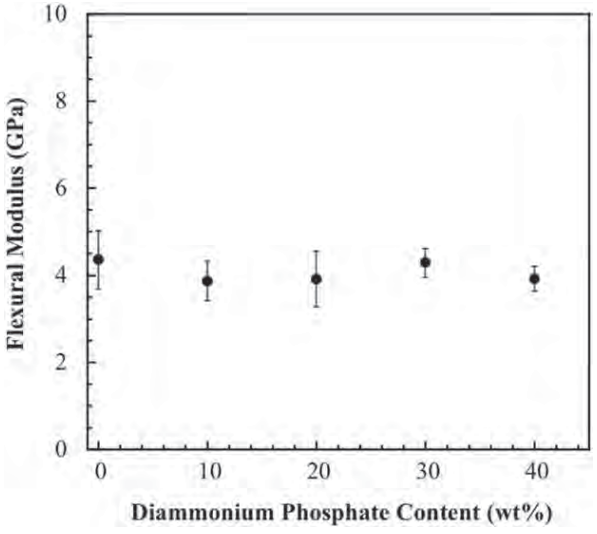

FIG. 10. Flexural modulus of wood flour/EPS composites modified with DAP.

DOI 10.1002/pc

TABLE 3. Flexural modulus and flexural strength of various wood plastic composites.

Composite type	Mass fraction of fiber (wt%)	Mass fraction of flame retardant (wt%)	Flexural modulus (GPa)	Flexural strength (MPa)
Commercial wood flake reinforced HDPE [33]	50–70	–	2.7–3.1	18–31
Recycled-HDPE bio-composite from rice husk and sawdust as filler and flame retardants (sodium meta-silicate and zinc borate) [34]	41.6	0–40	2.0–2.5	16–18
Wood flour–PE composite modified with various types of flame retardants [35]	50	2.5–10	3.6–5.2	30–36
Wood flour–PP composite modified with various types of flame retardants [36]	25	5–25	2.9–3.3	53–56

the strong absorption of phosphorus ester at 960 cm^{-1} (P-O-C, aromatic streching) and 1240 cm^{-1} (P=O) for the char residues of wood flour/EPS composites modified with DAP [15, 29]. It implied that the interaction between phosphoric acid and the primary hydroxyl group provided phosphate ester as mentioned in Scheme 1. These results were also consistent with the increasing of char yield from the TGA results.

Water Absorption of the Wood Flour/EPS Composites

The values of water absorption and thickness swelling for the wood flour/EPS composites at varied DAP loadings are shown in Fig. 6. The percentage of water absorbed plotted against time for all samples showed a similar behavior, i.e., the samples absorbed water more rapidly during first stages (0–24 h). The water adsorption values of samples were in range of 0.64–1.66% after 24 h and 1.26–6.05% after 200 h of immersion. The water absorption values were significantly lower than the reported commercial WPC of 4.59% after 24 h of immersion [28]. Moreover, the water absorption of all samples increased with increasing DAP content. This is likely caused by the hydrogen bonding of the water molecules to free OH groups presented in the DAP structure, and possible diffusion of water molecules into the composite. The similar tends of water absorption were also observed in the wood–PP composites modified with phosphate compounds as flame retardant [19].

Kinetic of Water Sorption

It is necessary to study the kinetic water sorption to have better understanding of the water sorption mechanism and to minimize water uptake of materials. Generally, the analysis of diffusion mechanism and kinetics was performed based on Fick's theory. The generalized equation can be expressed as:

$$\frac{M_t}{M_\alpha} = kt^n \tag{2}$$

where M_t is the moisture content at time t; and M_α is the moisture content at equilibrium; k and n are constants.

The diffusion behaviors can be classified as: super case II ($n > 1$), case II ($n = 1$), anomalous ($1/2 < n < 1$), classical/Fickian ($n = 1/2$), or pseudo-Fickian ($n < 1/2$). From the plots of log M_t/M_α versus log t, a good linear correlation was observed and slope value of wood flour/EPS composite modified with 20 %wt DAP was also calculated from the fitted curve, as illustrated in Fig. 7. The obtained slope values of all samples were summarized in Table 2. The absorption of water in the wood flour/EPS composites approached toward the Fickian diffusion case, as the value of n were determined to be in the range of 0.46–0.56. Generally, the water adsorption in natural fiber reinforced plastics usually follows Fickian behavior [30].

Transport Coefficients

The diffusion coefficient (D) is the most important parameter of the Fick's model. This parameter presents the ability of solvent molecules to penetrate inside the composite structure and can be calculated using the following equation:

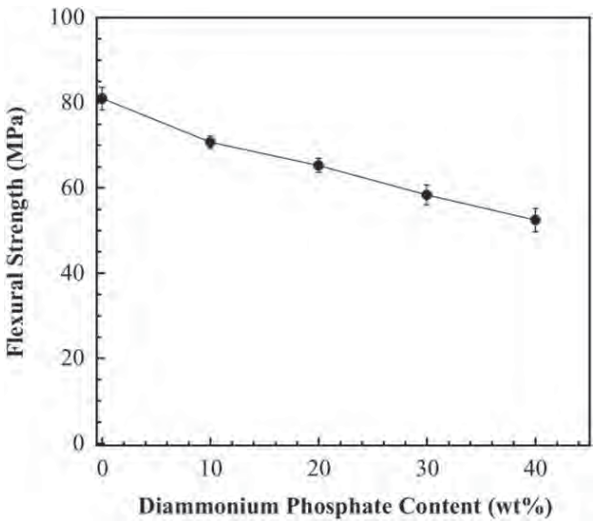

FIG. 11. Flexural strength of wood flour/EPS composites modified with DAP.

$$\frac{M_t}{M_\alpha} = \frac{4}{L}\left(\frac{D}{\pi}\right)^{0.5} t^{0.5} \quad (3)$$

where L is the thickness of sample.

From *Eq. 3*, the diffusion coefficient was obtained from the slope of the plot of M_t/M_α versus $(\text{time})^{0.5}$, as depicted in Fig. 8. The obtained values from curves fitting were shown in Table 2. The diffusion coefficient values of wood flour/EPS composites expectedly showed an increasing trend with increasing DAP contents. This was due to the hydrophilic characteristics of DAP incorporated.

Thickness Swelling of the Samples

The thickness swelling (TS) of sawdust filled EPS is illustrated in Fig. 9. The thickness swelling of specimens increased with increasing DAP content similar to water absorption results. The TS values of 0–40 wt% DAP samples after 24 h and 7 days water immersion varied from 0.26 to 1.06%. Overall TS values of the samples were within the same range of that of commercial wood-based composite products such as fiberboards (1.6–5.45%) [31]. As shown in Fig. 8, the thickness swelling increased only in the initial stage and thereafter remained almost constant. After 7 days, the thickness swelling leveled off and the percentages of the TS values were observed to be within the range of 0.55–2.43% which was lower than the low-density polyethylene wood composite modified with carbon nanotube (4–7.8%) [32].

Flexural Properties of Wood Flour/EPS Composites

Flexural properties of wood flour/EPS composites modified with DAP at different contents are illustrated in Fig. 10. The average flexural modulus of our wood composites ranged from 3.9 to 4.4 GPa. From Table 3, the flexural modulus of wood flour/EPS composites was significantly higher than those of reported wood plastic composites, e.g., commercial wood particles reinforced HDPE (2.7–3.1 GPa) [33], recycled-HDPE biocomposite from rice husk and saw dust as filler and flame retardants (sodium metasilicate and zinc borate: 2.0–2.5 GPa) [34] as well as wood flour–PE composite and –PP composite modified with various types of flame retardants (3.6–5.2 and 2.9–3.3 GPa, respectively) [35, 36]. Figure 11 exhibits the flexural strength of wood flour/EPS composites ranging from 52 to 81 MPa. The flexural strength of composites slightly decreased when the amount of DAP increased. Similar trend of result was also observed in the wood flour–PP composite modified with DAP due possibly to, the poor compatibility between DAP on the fiber surface and polymer matrix [15]. However, all wood flour/EPS composites still showed higher flexural strength than the major wood plastic composite products listed in Table 3.

CONCLUSIONS

The effect of DAP on thermal degradation, flammability, dimension stability, and mechanical properties of wood flour/EPS composites was investigated. The fire resistant properties of the wood flour/EPS composites tended to increase with the increasing DAP contents. The rate of thermal degradation substantially reduced from 1.57 to 0.86%/°C. Especially, wood fiber/EPS composite modified with DAP up to 20 wt% provided the best linear burning rate. Both water absorption and thickness swelling values were within same range of commercial wood plastic composite. Flexural modulus and flexural strength characteristics were higher than those of commercial wood plastic composite and other wood composite modified with flame retardant. Based on results, wood flour/EPS modified with DAP has a potential to use in furniture, floor, and decoration panels which can increase security of interior building with increasing time for rescuing during fire disaster.

REFERENCES

1. A. Ashori, H.M. Behzad, and A. Tarmian, *Compos. B*, **47**, 308 (2013).
2. L. Zhu, J. Cao, Y. Wang, R. Liu, and G. Zhao, *Polym. Compos.*, (2013).
3. J. Cai, M. Jia, P. Xue, Y. Ding, and X. Zhou, *Polym. Compos.*, **34**, 1567 (2013).
4. N. Lu and S. Oza, *Compos. B*, **45**, 1651 (2013).
5. A. Chavooshi and M. Madhoushi, *Constr. Build. Mater.*, **44**, 214 (2013).
6. S. Rimdusit, D. Atthakorn, S. Damrongsakkul, D. Saramas, and S. Tiptipakorn, *J. Appl. Polym. Sci.*, **124**, 943 (2012).
7. A.S. Singha and R.K. Rana, *Mater. Design.*, **41**, 289 (2013).
8. N. Petchwattana, S. Covavisaruch, and N. Euapanthasate, *Mat. Sci. Eng. A Struct.*, **523**, 64 (2013).
9. S.E. Selke and I. Wichman, *Compos. A*, **35**, 321 (2004).
10. K.B. Adhikary, S.S. Pang, and M.P. Staiger, *Compos. B*, **39**, 807 (2008).
11. H.S. Kim, B.H. Lee, S.W. Choi, S. Kim, and H.J. Kim, *Compos. A*, **38**, 1473 (2007).
12. M.A. Binhussain and M.M. El-Tonsy, *Constr. Build. Mater.*, **47**, 1431, (2013).
13. M. Poletto, J. Dettenborn, M. Zeni, and A.J. Zattera, *Waste. Manage.*, **31**, 779 (2013).
14. B.H. Lee, H.S. Kim, S. Kim, H.J. Kim, B. Lee, Y. Deng, Q. Feng, and J. Luo, *Constr. Build. Mater.*, **25**, 3044 (2011).
15. N.P.G. Suardana, M.S. Ku, and J.K. Lim, *Mater. Design.*, **32**, 1990 (2013).
16. M. Sponton, L.A. Mercado, J.C. Ronda, M. Galia, and V. Cadiz, *Polym. Degrad. Stab.*, **93**, 2025 (2008).
17. G. Chen, *Wood Fiber. Sci.*, **41**, 105 (2009).
18. S. Gaan and G. Sun, *Polym. Degrad. Stab.*, **92**, 968 (2007).
19. N. Ayrilmis, T. Akbulut, and T. Dundar, *Constr. Build. Mater.*, **33**, 63 (2012).

 DOI 10.1002/pc

20. H. Seefeldt, U. Braun, and M.H. Wagner, *Macromol. Chem. Phys.*, **213**, 22 (2012).
21. H. Seefeldt and U. Braun, *Macromol. Mater. Eng.*, **297**, 814 (2012).
22. S. Liodakis, I.K. Fetsis, and I.P. Agiovlasitis, *J. Therm. Anal. Calorim.*, **98**, 285 (2009).
23. V. Alvarez, E. Rodriguez, and A. Vazquez, *J. Therm. Anal. Calorim.*, **85**, 383 (2006).
24. L.B. Manfredi, E.S. Rodriguez, M. Wladyka-Przybylak, and A. Vazquez, *Polym. Degrad. Stab.*, **91**, 255 (2006).
25. F. Yao, Q. Wu, Y. Lei, W.H. Guo, and Y.J. Xu. *Polym. Degrad. Stab.*, **93**, 90 (2008).
26. Z.X. Zhang, J. Zhang, B.X. Lu, Z.X. Xin, C.K. Kang, and J.K. Kim. *Compos. B*, **43**, 150 (2013).
27. P. Bajaj, Handbook of Technical Textiles, Woodhead Pub, Cambridge (2000).
28. A.A. Klyosov, Wood Plastic-Composites, Wiley, New Jersey (2007).
29. G. N. Mathur, L. D. Kandpal, and A.K. Sen, Recent Advances in Polymers and Composites. Allied Publishers. LTD, New Delhi (2000).
30. A. Espert, F. Vilaplana, and S. Karlsson, *Compos. A*, **35**, 1267 (2004).
31. M.R. Roger, Handbook of Wood Chemistry and Wood Composites, Taylor & Francis Group, Boca Raton, FL (2005).
32. H.Y. Kordkheili, M. Farsi, and Z. Rezazadeh, *Compos. B*, **44**, 750 (2013).
33. P.W. Balasuriya, L. Ye, and Y.W. Mai, *Compos. A*, **32**, 619 (2001).
34. M.R.Y. Hamid, M.H. Ab Ghani, and S. Ahmad, *Ind. Crops. Prod.*, **40**, 96 (2013).
35. N.M. Stark, R.H. White, S.A. Mueller, and T.A. Osswald, *Polym. Degrad. Stab.*, **95**, 1903 (2013).
36. M. Sain, S.H. Park, F. Suhara, and S. Law, *Polym. Degrad. Stab.*, **83**, 363 (2004).

Role of Filler Effect and Pozzolanic Reaction of Biomass Ashes on Hydrated Phase and Pore Size Distribution of Blended Cement Paste

Prinya Chindaprasirt[1]; Theerawat Sinsiri[2]; Wunchock Kroehong[3]; and Chai Jaturapitakkul, A.M.ASCE[4]

Abstract: The role of filler effect and pozzolanic reaction of biomass ash on hydrated phase and pore size distribution of blended cement paste was studied. Rice husk ash (RHA), palm oil fuel ash (POFA), and river sand (RS) were ground to two fineness values, and used to replace Type I portland cement (OPC) at 0, 20, and 40% by weight of binder. A water to binder ratio of 0.35 was used. The compressive strength, pore size distribution, and thermogravimetric analyses of the blended cement pastes were investigated. Partial replacement of OPC with fine RHA and POFA at a dosage of 20% by weight of binder resulted in pastes with higher compressive strengths than that of OPC paste. The compressive strengths of RHA paste were slightly higher than those of POFA pastes at the same age. The differences between mass losses (at 30–450°C) of RS and RHA (or POFA) blended pastes at the same fineness, curing time, and replacement rate were due to the pozzolanic reaction, which increased in accordance with particle fineness and cement replacement rate. In addition, the weight losses (at 30–450°C) due to the pozzolanic reaction were higher than those due to the filler effect. The use of fine RHA and POFA enhanced the pozzolanic reaction, and reduced the average pore diameters of pastes. **DOI: 10.1061/(ASCE)MT.1943-5533.0000921.** *© 2013 American Society of Civil Engineers.*

Author keywords: Biomass ash; Filler effect; Pozzolanic reaction; Thermogravimetric analysis; Porosity; Hydrated phase.

Introduction

Currently, there are many types of pozzolans such as fly ash and silica fume used as supplementary cementations materials in the concrete industry. In Thailand, rice husk ash (RHA) is a byproduct of electricity generation biomass power plants. It has been estimated that more than 1.6 million tons of RHA are produced every year (Wansom et al. 2010). Palm oil fuel ash (POFA) is a byproduct of the burning of palm shells, empty fruit bunches, and palm fiber in palm oil factories. The annual production of POFA is greater than 100,000 tons. Ground RHA and POFA are good pozzolanic materials, and can be used to replace portland cement up to 30% by binder weight (Ganesan et al. 2008; Rukzon et al. 2009; Sata et al. 2004). Use of ground RHA and POFA to partially replace Type I ordinary portland cement (OPC) improves its resistance to chloride penetration (Chindaprasirt et al. 2008; Ganesan et al. 2008) and sulfate resistance (Chatveera and Lertwattanaruk 2011; Tangchirapat et al. 2009).

The compressive strength of OPC mortar or concrete with pozzolanic material is contributed by three major causes, as follows: (1) a hydration reaction between cement and water, (2) the filler effect of small particles that leads to a more homogeneous paste, and (3) a pozzolanic reaction occurs when silicon dioxide (SiO_2) and aluminum trioxide (Al_2O_3) in a pozzolanic material react with calcium hydroxide [$Ca(OH)_2$]. Thermal analysis has been used successfully to analyze the hydration products (Chaipanich and Nochaiya 2010; Chaipanich et al. 2010; Wongkeo and Chaipanich 2010). These studies show that there are three main temperature intervals associated with dehydration of hydration products, decomposition of $Ca(OH)_2$, and mass loss of calcium carbonate ($CaCO_3$).

The pozzolanic reaction has two effects, as follows: (1) there is a decrease in the amount of $Ca(OH)_2$ in accordance with the increases in curing time, replacement level, and fineness of pozzolan [the $Ca(OH)_2$ has an adverse effect on strength and durability of concrete]; and (2) calcium-silicon-hydrogen (C-S-H), calcium-aluminum-hydrogen (C-A-H), and calcium-aluminum-silicon-hydrogen (C-A-S-H) phases increase in accordance with increasing curing time. C-S-H possesses greater mechanical strength than C-A-H and C-A-S-H, whereas $Ca(OH)_2$ has low strength because it has a lamellar structure (Askarinejad et al. 2012; El-Bouny 1994).

Use of pozzolanic materials to partially replace cement in concrete gives the filler effect and pozzolanic reaction. However, it could delay the early strength development due mainly to the insufficient fineness of pozzolan. A number of studies have reported the results of both the filler effect and pozzolanic reaction. Goldman and Bentur (1993) found that the microfiller effect (from carbon black) led to a greater strength than the pozzolanic reaction of silica fume. Tangpagasit et al. (2005) studied the packing effect and the pozzolanic reaction of fly ash on the compressive strength of mortar. They reported that the strength due to the pozzolanic reaction of 20% fly ash at 3 days was 3% of the control, and at 28 and 90 days increased to 20 and 27%, respectively. Jaturapitakkul et al.

[1]Professor, Sustainable Infrastructure Research and Development Center, Dept. of Civil Engineering, Faculty of Engineering, Khon Kaen Univ., Khon Kaen 40002, Thailand. E-mail: prinya@kku.ac.th

[2]Assistant Professor, School of Civil Engineering, Institute of Engineering, Suranaree Univ. of Technology, Nakorn Ratchasima 30000, Thailand (corresponding author). E-mail: sinsiri@g.sut.ac.th

[3]Lecturer, Dept. of Civil Engineering, Faculty of Engineering and Architecture, Uthenthawai Campus, Rajamangala Univ. of Technology Tawan-ok, Bangkok 10330, Thailand. E-mail: wunchock_k@hotmail.com

[4]Professor, Dept. of Civil Engineering, Faculty of Engineering, King Mongkut's Univ. of Technology Thonburi, Bangkok 10140, Thailand. E-mail: chai.jat@kmutt.ac.th

Note. This manuscript was submitted on January 11, 2013; approved on August 13, 2013; published online on August 15, 2013. Discussion period open until January 15, 2014; separate discussions must be submitted for individual papers. This paper is part of the ***Journal of Materials in Civil Engineering***, © ASCE, ISSN 0899-1561/(0)/$25.00.

(2011) reported that the pozzolanic reaction of ground palm oil fuel ash increased in accordance with increasing particle fineness, cement replacement rate, and age of mortar. In addition, the compressive strength due to the pozzolanic reaction had a greater effect than the filler effect.

Researchers have reported use of river sand (RS) as an inert material to replace Type I portland cement to evaluate influences the hydration reaction, filler effect, and pozzolanic reaction on the compressive strength, sulfate resistance, and chloride resistance (Jaturapitakkul et al. 2007; Chindaprasirt et al. 2008; Sinsiri et al. 2012). However, the separation of the hydration reaction, filler effect, and pozzolanic reaction on the hydrated phase and total porosity of blended cement pastes has not been well established. Thus, the objective of the research reported in this paper is to study the role of filler and pozzolanic reaction of biomass ash on the hydrated phase and pore size distribution of blended cement paste. The results should help lay the foundation for the use of biomass ash in concrete and help reduce the volume of waste disposed in landfills.

Experimental Details

Materials

The materials used in the research reported in this paper are portland cement Type I (i.e., OPC) in accordance with ASTM C150-09 (ASTM 2009). Rice husk ash and palm oil fuel ash from a thermal power plant in Thailand were used as a pozzolan, and the inert material used was ground river sand (RS). The RHA, POFA, and RS were ground to two fineness values, i.e., a coarse material with similar median particle size to OPC, with a grinding machine. The fine rice husk ash (FRHA), fine palm oil fuel ash (FPOFA), and fine river sand (FRS) were obtained from the sieving and milling. They were first sieved through a sieve No. 200. After sieving, they were intense ground using attrition milling for 60 min. Attrition milling was selected based on the work of Kumar et al. (2008) and Kumar and Kumar (2011), who reported efficient milling of slag to median particle sizes of 3.9 μm after 60 min of milling. The finenesses of the milled materials were measured after milling to ensure the required fineness. Table 1 shows the physical properties and chemical compositions of materials. The sums of SiO_2, Al_2O_3, and Fe_2O_3 in course rice husk ash (CRHA) and FRHA were 91.1 and 89.2%, respectively, which are higher than 70% for Class N pozzolan specified in ASTM C618-01 (ASTM 2001). For coarse palm oil fuel ash (CPOFA) and FPOFA, the sums were 56.9 and 58.6%, respectively. The results are similar to those obtained by Awal and Hussin (1997), who reported that POFA might be grouped between Class C and F pozzolan in accordance with ASTM C618-01 (2001), and the sum of SiO_2, Al_2O_3, and Fe_2O_3 content of palm oil fuel ash used in their study was 59.7%, which was close to the findings in the research reported in this paper. The major chemical compositions of coarse river sand (CRS) and FRS were 92.0 and 91.2% SiO_2, respectively. For quantitative X-ray diffraction (XRD), an analysis based on the Rietveld method was performed and calculated using Bruker's TOPAS. The percentages of amorphous CRHA, FRHA, CPOFA, and FPOFA were 70.1, 69.6, 70.2, and 67.2% (by mass), respectively. The CRS and FRS, however, contains 100% (by mass) crystalline phase. Thus, ground RS is inert material. The results agree with those of Idir et al. (2011) and Kiattikomol et al. (2000). The median particle sizes of OPC, CRHA, CPOFA, and CRS were 14.6, 14.8, 15.6, and 15.9 μm in accordance with a laser particle size analyzer and Blaine fineness values of 3,600, 7,600, 6,700, and 3,900 cm^2/g, respectively (Rukzon et al. 2009; Jaturapitakkul et al. 2011). For the fine particle size group, the median particle sizes and Blaine finenesses of FRHA, FPOFA, and FRS were 1.9, 2.1, and 2.2 μm, and 18,000, 14,900, and 6,300 cm^2/g, respectively. Fig. 1 shows a comparison of the particle size distributions of Type I portland cement RS, RHA, and POFA. The two group of materials particle size are similar to the particle size of the cement and smaller, respectively.

Mix Proportion of Cement Paste

The OPC was replaced with ground RHA, POFA, and RS at 0, 20, and 40% by weight of binder. A water to binder (WB) ratio of 0.35 was used for all blended cement pastes to separate the hydration reaction, filler effect, and pozzolanic reaction. Keeping the same water to cement ratio for comparison is convenient especially for the strength at same WB ratio, but this method gives different workability of mixes. After mixing, the cement pastes were immediately cast into cube specimens of $50 \times 50 \times 50$ mm. The cast specimens were covered with plastic to prevent water loss. After casting for 24 h, the specimens were removed from the molds and cured in saturated lime water at a temperature of 23 ± 2°C. The compressive strength was tested using $50 \times 50 \times 50$-mm cube specimens in accordance with ASTM C109-02 (ASTM 2002) at ages of 7, 28, and 90 days. Five samples were tested for each age group.

Table 1. Chemical and Physical Compositions of Materials

Chemical composition (%)	OPC	CRHA	CPOFA	CRS	FRHA	FPOFA	FRS
Silicon dioxide (SiO_2)	20.8	88.8	54.0	92.0	87.8	55.7	91.2
Aluminum oxide (Al_2O_3)	4.7	0.6	0.9	1.6	0.5	0.9	1.8
Iron oxide (Fe_2O_3)	3.4	1.7	2.0	0.6	0.9	2.0	0.2
Calcium oxide (CaO)	65.3	1.1	12.9	0.9	1.2	12.5	0.7
Magnesium oxide (MgO)	—	0.6	4.9	0.1	0.6	5.1	0.1
Sodium oxide (Na_2O)	0.1	0.2	1.0	0.1	0.2	1.0	0.1
Potassium oxide (K_2O)	0.4	2.0	13.5	2.2	2.2	11.9	2.3
Sulfur trioxide (SO_3)	2.7	0.1	4.0	—	0.1	2.9	—
Loss on ignition (LOI)	0.9	3.6	3.7	2.1	5.2	4.7	1.8
Quantitative X-ray diffraction, Rietveld method							
Amorphous (%)	—	70.1	70.2	—	69.6	67.2	—
Crystalline (%)	—	29.9	29.8	100.0	30.4	32.8	100.0
Physical properties of materials							
Specific gravity	3.14	2.29	2.36	2.59	2.31	2.48	2.61
Median particle size, d_{50} (μm)	14.6	14.8	15.6	15.9	1.9	2.1	2.2
Blaine fineness (cm^2/g)	3,600	7,600	6,700	3,900	18,100	14,900	6,300

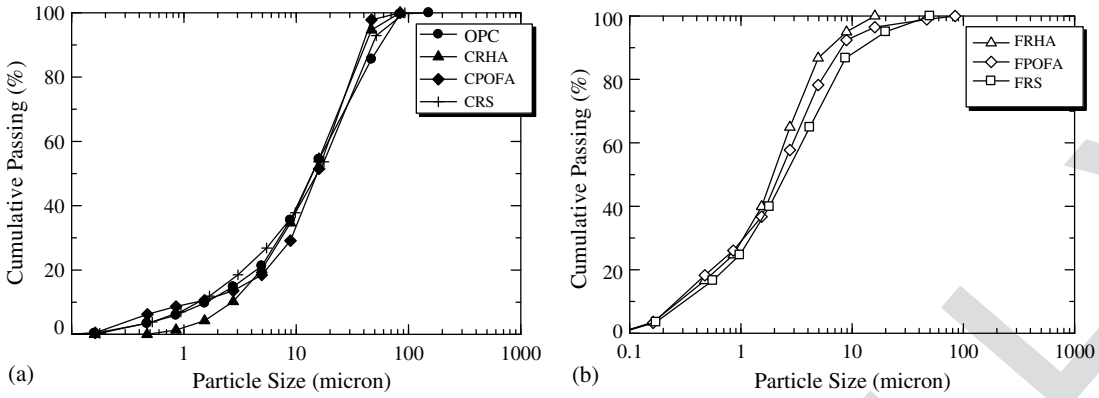

F1:1 **Fig. 1.** Particle size distributions of the materials: (a) coarse material; (b) fine material

Thermal Analysis

The samples were submerged directly into liquid nitrogen for 5 min and were then evacuated at a pressure of 0.5 Pa at 40°C for 48 h. This method has been used previously to stop the hydration reaction of cement paste (Galle 2001; Konecny and Naqvi 1993). The samples were subjected to thermogravimetric analysis using Netzsch STA 409 C/CD equipment. The samples were heated from room temperature to 1,000°C at a heating rate of 10°C/ min under a nitrogen atmosphere. The weight loss of sample in the range of 30–450°C was determined to semiquantitatively calculate the gel products of the blended cement pastes. The amount of $Ca(OH)_2$ was calculated from the weight loss between 450 and 580°C (El-Jazairi and Illston 1977).

Determination of the Porosity of the Pastes

The pore size distribution in hardened cement pastes was determined using a mercury intrusion porosimeter (MIP) with a pressure range from 0–228 MPa (0–33,000 lb · in^{-2}). The samples were obtained by carefully breaking the cube specimens with a chisel. Representative samples thickness of 3–6 mm weighing between 1 and 1.5 g were taken from the middle part of specimen. Before testing, the hydration reaction was stopped with liquid nitrogen (Galle 2001; Konecny and Naqvi 1993). The pressure was expressed with the Washburn (1921) equation. A constant contact angle of 140° and a constant surface tension of mercury 480 dynes/ cm were used for the pore size calculation.

Results and Discussion

Compressive Strength

Table 2 shows the compressive and normalized compressive strength of pastes. The compressive strengths of ground RS blended paste especially at the high replacement were significantly less than that of OPC paste at the same age. This effect is due to the inert material and the reduced amount of OPC, which causes low hydration reaction (Tangpagasit et al. 2005). The compressive strength of paste with FRS was higher than that of CRS because the small particles of FRS filled the voids and increased the compressive strength of the paste. These results confirmed that the small particles exerted a filler effect and contributed to the compressive strength of the pastes (Goldman and Bentur 1993; Tangpagasit et al. 2005).

The compressive strengths at 28 days of all pastes containing coarse ashes were less than that of OPC paste. After 90 days, the compressive strengths of 20CRHA and 20CPOFA pastes were higher than that of OPC paste, whereas those of 40CRHA and 40CPOFA were still lower. For the 20% replacement of fine ashes, the compressive strengths at 28 days of 20FRHA and 20FPOFA pastes were higher than that of OPC paste. The higher strengths indicated that the FRHA and FPOFA were better dispersed in the blended cement paste and gave a faster pozzolanic reaction, leading to an increased C-S-H compared with the coarser pastes.

The increased compressive strengths of blended cement paste were due to filler effect and pozzolanic reaction. The small particles

Table 2. Compressive Strengths of Pastes

Symbol	Compressive strength (MPa)				Normalized compressive strength (%)			
	7 days	28 days	60 days	90 days	7 days	28 days	60 days	90 days
OPC	53.0	75.0	84.6	99.1	100.0	100.0	100.0	100.0
20CRS	42.9	60.8	67.9	78.6	80.9	81.1	80.3	79.3
40CRS	31.5	45.6	51.5	59.6	59.4	60.8	60.9	60.1
20FRS	45.0	63.4	70.8	82.1	84.9	84.5	83.7	82.8
40FRS	34.2	49.2	55.4	63.9	64.5	65.6	65.5	64.5
20CRHA	49.8	74.2	88.3	106.0	94.0	98.9	104.4	107.0
40CRHA	42.4	64.7	77.4	92.1	80.0	86.3	91.5	92.9
20FRHA	52.9	78.7	93.1	113.2	99.8	104.9	110.0	114.2
40FRHA	44.5	66.9	79.5	96.1	84.0	89.2	94.0	97.0
20CPOFA	48.3	72.0	84.6	102.0	91.1	96.0	99.6	102.9
40CPOFA	41.0	61.5	72.8	88.1	77.4	82.0	85.7	88.9
20FPOFA	51.9	77.3	92.2	109.6	97.9	103.1	108.6	110.6
40FPOFA	44.0	66.5	78.6	94.1	83.0	88.7	92.6	95.0

filled the voids of paste, allowing for denser packing within the matrix phase. The pozzolanic reaction also increased as the fine pozzolanic materials was able to react better with $Ca(OH)_2$ to form extra hydration products than that of coarser pozzolans. Incorporation of ashes refined the porosity of paste and resulted in high compressive strength (Chindaprasirt et al. 2005, 2007). These results suggested that both RHA and POFA with high fineness are good pozzolanic materials and can be used to replace portland cement. The use of 20% replacement produced pastes with higher compressive strength. However, 40% replacement led to a slight reduction in compressive strengths of 40FRHA and 40FPOFA pastes to 96.1 and 94.1 MPa, or 97.0 and 95.0% of that of the OPC paste at 90 days, respectively. The reduction was due to the large reduction in OPC and the associated reduced hydration.

Thermal Analysis of the Blended Cement Pastes: Influence of Ground River Sand on Hydrated Phase

Fig. 2 shows the thermogravimetric analysis (TGA) curves of OPC paste and RS blended pastes. The mass loss transitions occurred in three steps, as follows: (1) mass loss from dehydration of ettringite, C-S-H, C_2ASH_8 , and C_4AH_{13} at 30–450°C (Bai et al. 2003); (2) mass loss of $Ca(OH)_2$ occurred at 450–580°C (El-Jazairi and Illston 1977); and (3) 580–1000°C represented the mass loss of calcium carbonate ($CaCO_3$; El-Jazairi and Illston 1977). The mass loss at 30–450°C of RS blended pastes increased in accordance with fineness and decreased in accordance with replacement level. It was likely that the addition of fine RS, the particles of which were finer than those of portland cement, caused segmentation of large pores and increased nucleation sites for precipitation of hydration products in cement paste similarly to the addition of fine fly ash (Mehta 1987). This mass loss increased in accordance with curing time as a result of the increase in hydration reaction, which caused an increase in compressive strength (Kroehong et al. 2011).

Fig. 3 shows the $Ca(OH)_2$ content of OPC paste and RS blended pastes. The $Ca(OH)_2$ content of all pastes increased in accordance with curing time as a result of hydration of cement. The $Ca(OH)_2$ content of RS blended pastes was less than that of OPC paste especially at high replacement level due to the reduced reaction from the reduced OPC content and the nonreactive RS. The $Ca(OH)_2$ content of FRS blended pastes was less than those of pastes with the CRS due to the higher nucleation effect of fine particles (Askarinejad et al. 2012; El-Bouny 1994; Metha 2007).

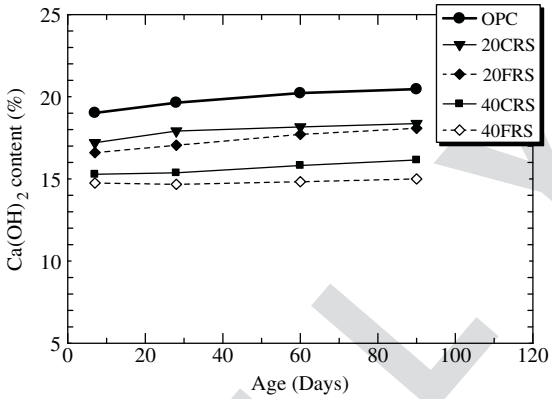

Fig. 3. $Ca(OH)_2$ content of OPC and RS blended cement pastes

Table 3. $Ca(OH)_2$ Content of Pastes

Symbol	$Ca(OH)_2$ (%)			
	7 days	28 days	60 days	90 days
OPC	19.02	19.64	20.22	20.46
20CRS	17.20	17.91	18.16	18.37
20CRHA	15.57	15.45	15.37	14.34
20CPOFA	15.82	15.74	15.44	15.10
40CRS	15.28	15.37	15.82	16.15
40CRHA	12.12	11.01	9.45	8.83
40CPOFA	12.28	11.30	9.65	9.24
20FRS	16.60	17.05	17.71	18.08
20FRHA	14.80	14.13	13.64	13.33
20FPOFA	15.24	14.87	14.42	13.93
40FRS	14.75	14.67	14.83	15.00
40FRHA	11.46	9.09	7.68	6.43
40FPOFA	11.75	10.06	7.85	7.19

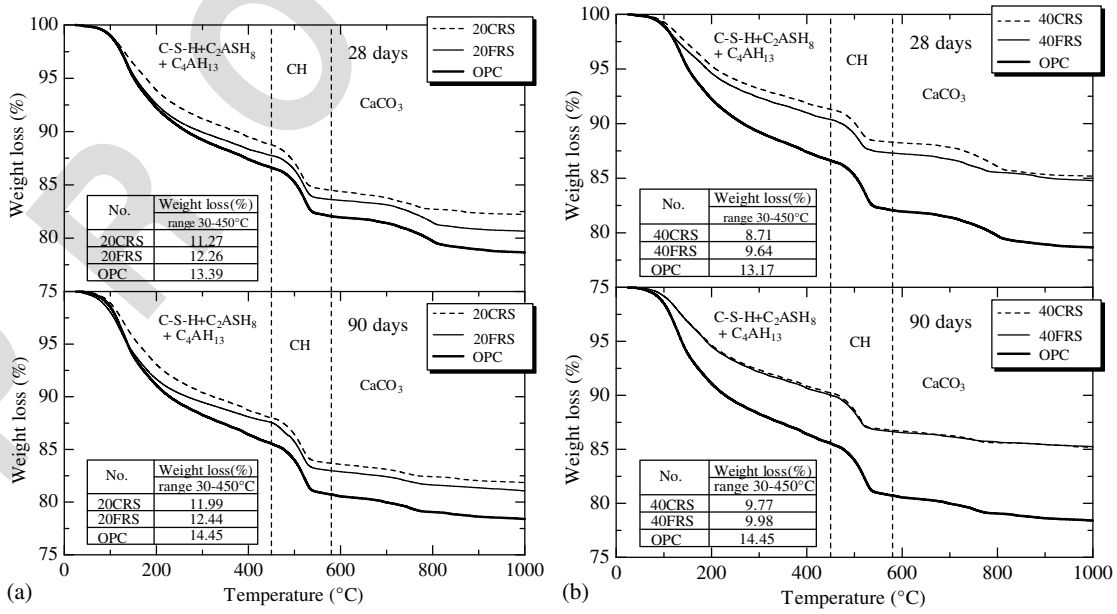

Fig. 2. Thermogravimetric analysis curves of OPC and RS blended cement pastes: (a) 20% replacement; (b) 40% replacement

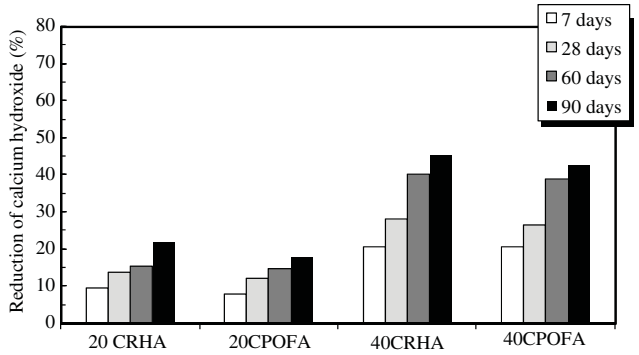

F4:1 **Fig. 4.** Reduction of $Ca(OH)_2$ content of CRHA and CPOFA pastes

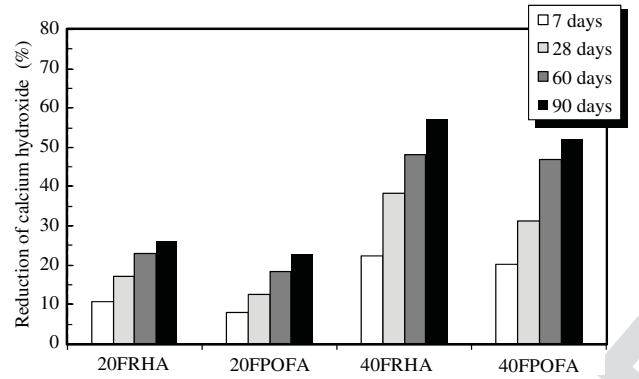

F5:1 **Fig. 5.** Reduction of $Ca(OH)_2$ content of FRHA and FPOFA pastes

Thermal Analysis of the Blended Cement Pastes: Influence of Pozzolanic Reaction on Hydrated Phase

Table 3 shows the results of $Ca(OH)_2$ contents of pastes at 7, 28, 60, and 90 days. Figs. 4 and 5 show the reductions of $Ca(OH)_2$ content of RHA and POFA pastes, which were determined from the difference in $Ca(OH)_2$ content between RS blended pastes and RHA (or POFA) pastes with the same particle size, replacement level, and age. The $Ca(OH)_2$ contents of RS blended pastes were higher than those of RHA and POFA pastes because the SiO_2 in RS was nonreactive. For the coarse pozzolans, the $Ca(OH)_2$ content of 20CRHA, 20CPOFA, 40CRHA, and 40CPOFA pastes were reduced from the ages of 28 to 90 days from 15.57 to 14.34%, 15.82 to 15.10%, 12.12 to 8.83%, and 12.28 to 9.24% (or approximately 22, 18, 45, and 43%) compared with RS blended pastes, respectively. The reductions of $Ca(OH)_2$ content in the RHA and POFA pastes indicated its consumption by the pozzolanic reaction. In addition, the reduction of $Ca(OH)_2$ content for high replacement level was higher than that of low replacement level. For fine pozzolans, the $Ca(OH)_2$ contents of 20FRHA, 20FPOFA, 40FRHA, and 40FPOFA pastes were also reduced from the ages of 28 to 90 days from 14.80 to 13.33%, 15.24 to 13.93%, 11.46 to 6.43%, and 11.75 to 7.19% (or approximately 26, 23, 57, and 52%) compared with RS blended pastes, respectively. The $Ca(OH)_2$ contents of RHA and POFA pastes decreased in accordance with the increases in curing time, fineness, and replacement level (Barbhuiya et al. 2009; Chindaprasirt et al. 2007; Poon et al. 2001).

Figs. 6 and 7 show the TGA results for RS, RHA, and POFA blended pastes. The first mass losses (at 30–450°C) of RHA and POFA pastes were higher than those of RS blended pastes. For example, the mass losses of 20CRHA, 20CPOFA, 40CRHA, and 40CPOFA pastes at 28 days were 12.27, 11.41, 11.95, and 11.87%, respectively, whereas those of 20CRS and 40CRS blended pastes at 28 days were less at 11.27 and 8.71%, respectively. At 90 days, they increased to 13.71, 13.39, 13.36, and 12.74%, whereas those of 20CRS and 40CRS blended pastes were still less at 11.99 and 9.77%, respectively. The first mass losses of CRHA and CPOFA pastes were higher than those of RS blended pastes, especially at a higher replacement level, due to the pozzolanic reaction of RHA and POFA compared with no pozzolanic reaction of RS. For pastes with fine ashes, the first mass loss of FRHA and FPOFA pastes were similar to those of CRHA and CPOFA pastes, but the first mass losses for the FRHA and FPOFA pastes were higher than those of the CRHA and CPOFA pastes because FRHA and FPOFA had large surface areas, which produced increased

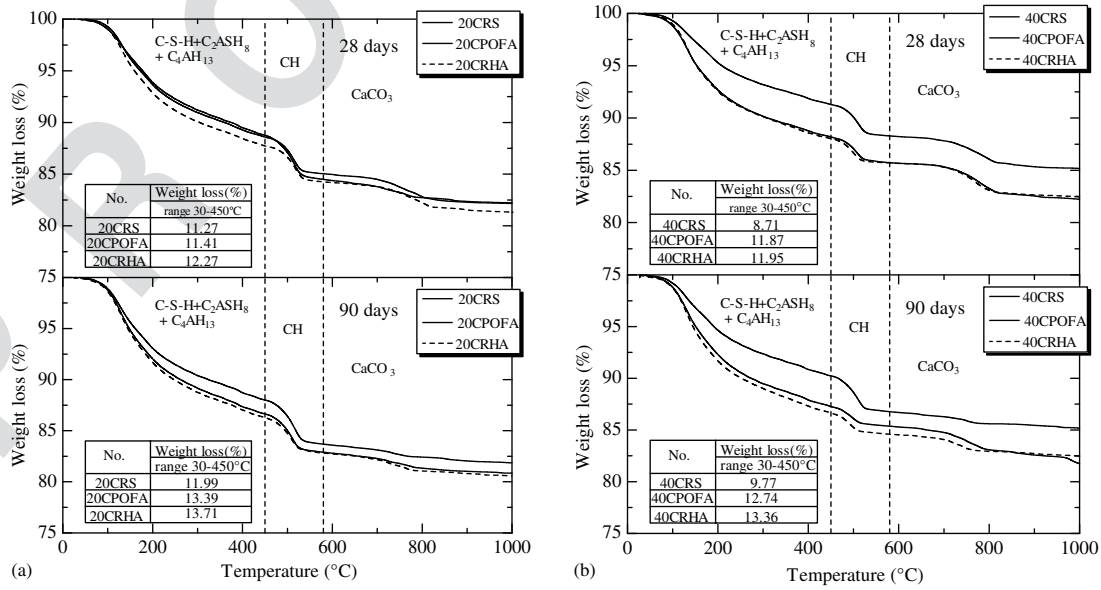

F6:1 **Fig. 6.** Thermogravimetric analysis curves of CRS, CRHA, and CPOFA pastes: (a) 20% replacement; (b) 40% replacement

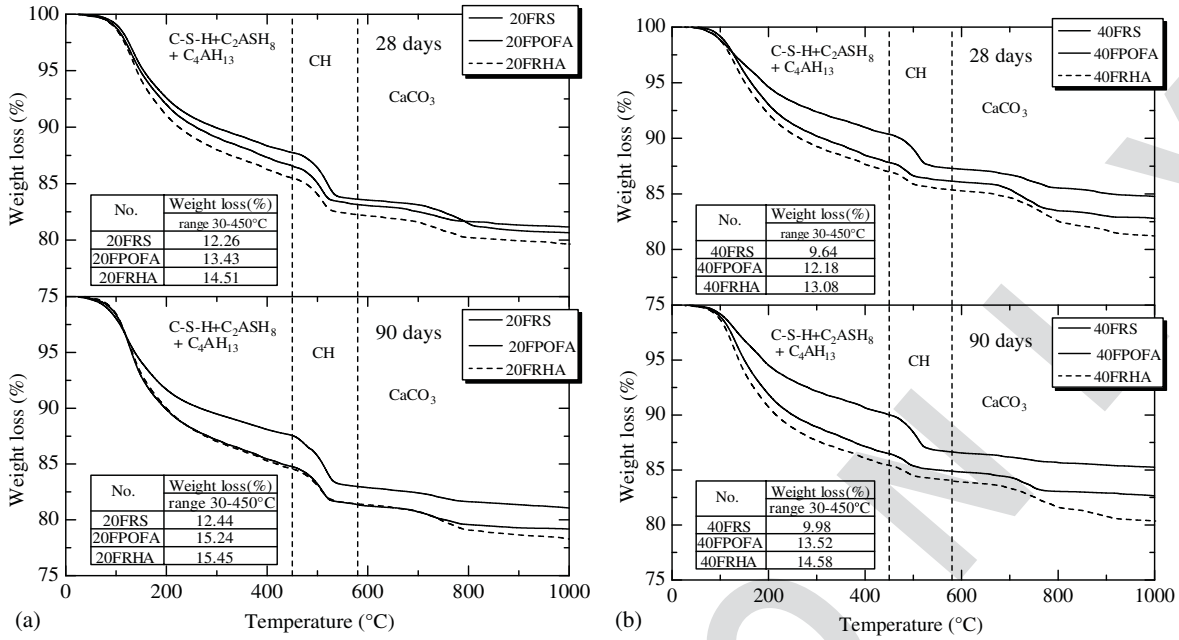

F7:1 **Fig. 7.** Thermogravimetric analysis curves of FRS, FRHA, and FPOFA pastes: (a) 20% replacement; (b) 40% replacement

C-S-H, C_2A-S-H_8, and C_4A-H_{13}. These first mass loss (at 30–450° C) increased in accordance with curing time, particle fineness, and cement replacement rate.

Thermal Analysis of the Blended Cement Pastes: Relationships between Mass Losses of C-S-H $+C_2ASH_8 + C_4AH_{13}$ and Compressive Strength

Fig. 8 shows the relationships between mass losses of C-S-H + C_2-A-S-H_8 + C_4-A-H_{13}, and compressive strengths of FRHA and FPOFA pastes, at 90 days. The mass losses of C-S-H + C_2-A-S-H_8 + C_4-A-H_{13} were divided into three portions, as follows: (1) cement hydration, (2) filler effect, and (3) pozzolanic reaction. The mass losses of C-S-H, C_2-A-S-H_8, and C_4-A-H_{13} of CRS blended cement paste is cement hydration. The difference in the mass losses of C-S-H, C_2-A-S-H_8, and C_4-A-H_{13} between the blended cement paste with inert material with high fineness and the blended cement paste with inert material with the same particle size as the cement is the filler effect. The mass losses of C-S-H, C_2-A-S-H_8, and C_4-A-H_{13} due to the pozzolanic reaction is the difference in the C-S-H, C_2-A-S-H_8, and C_4-A-H_{13} between the RHA or POFA paste, and the inert material paste. The use of 20% RHA and POFA increased the mass losses of C-S-H + C_2-A-S-H_8 + C_4-A-H_{13} and increased the compressive strength compared with those of OPC paste at 90 days due to the filler effect, and the pozzolanic reaction of both RHA and POFA. However, the mass losses of C-S-H + C_2-A-S-H_8 + C_4-A-H_{13} of 40% RHA and POFA were slightly less than that of OPC paste. The mass losses of C-S-H + C_2-A-S-H_8 + C_4-A-H_{13} due to the pozzolanic reaction increased in accordance with increasing replacement of RHA and POFA, but the losses from cement hydration were reduced. The weight losses of C-S-H + C_2-A-S-H_8 + C_4-A-H_{13} due to the pozzolanic reaction were higher than those due to the filler effect, which were similar to the findings of Jaturapitakkul et al. (2011). At this range of displacement level of 0–40%, the cement hydration was the major contributor to strength development of the blended cement and to a lesser extent the pozzolanic reaction. The filler effect also contributed but to a much lesser extent.

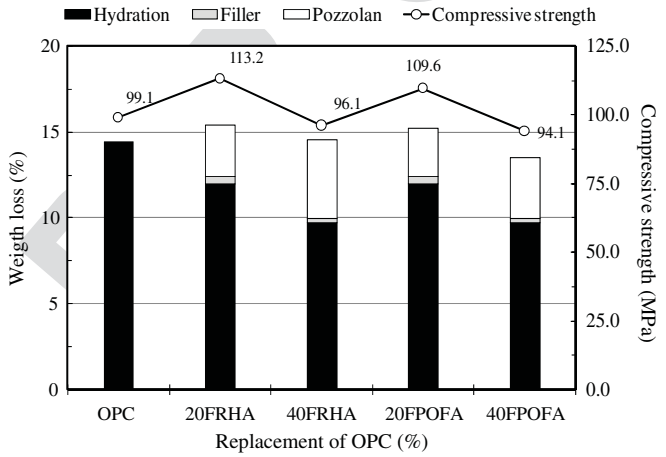

F8:1 F8:2 **Fig. 8.** Mass losses of C-S-H + C_2-A-S-H_8 + C_4-A-H_{13} and compressive strength of pastes at 90 days

Pore Size Distribution of Blended Cement Paste: Influence of Filler Effect on Total Porosity

Fig. 9 shows the results of total porosity of OPC and RS blended pastes. The total porosities of pastes reduced in accordance with curing. For example, the total porosities of OPC pastes were 22.8, 20.1, 17.4, and 16.6% at ages of 3, 7, 28, and 90 days, respectively. Total porosities of RS blended pastes were higher than that of OPC paste. The total porosities increased in accordance with the incorporation of RS and increased in accordance with the replacement level. For example, the total porosity of 20CRS blended pastes at 28 days was 24.0%, whereas that of 40CRS blended paste was higher at 28.5% because of the reduction in cement content and the associated reduced C-S-H. The differences between total porosities of fine RS and coarse RS blended pastes at the same replacement level and age was the filler effect, designated as ΔF_P. The total porosity of paste containing fine RS was less than that of paste containing coarse RS because the small particle size led to good dispersion and filler effect, and reduced the

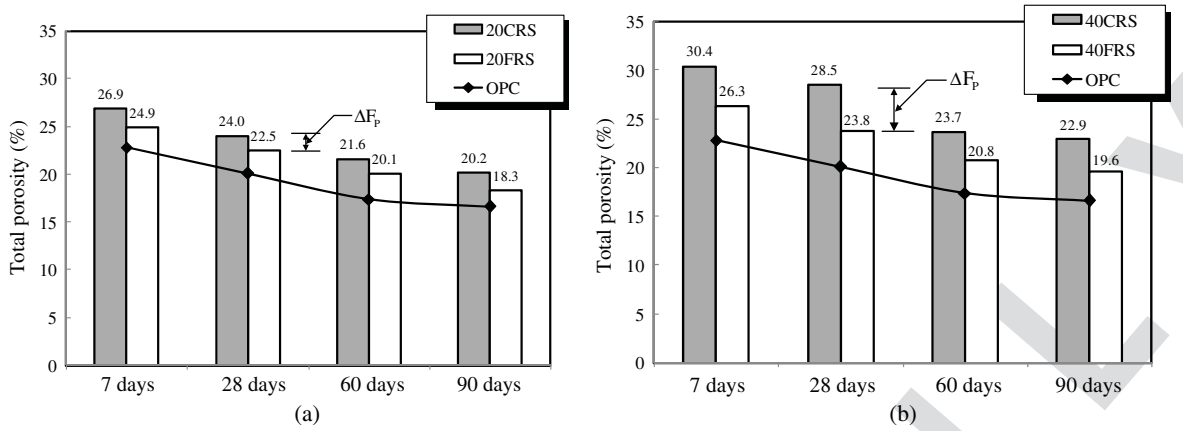

F9:1 **Fig. 9.** Total porosity of OPC and RS blended cement pastes: (a) 20% replacement; (b) 40% replacement

voids (Goldman and Bentur 1993; Isaia et al. 2003; Tangpagasit et al. 2005). The total porosity of the paste due to the filler effect increased in accordance with an increase in the replacement of inert material.

Pore Size Distribution of Blended Cement Paste: Influence of Pozzolanic Reaction on Total Porosity

Figs. 10 and 11 show the results of total porosity of pastes. For pastes with CRHA and CPOFA with the same particle as that indicated in Fig. 10, the total porosities of CRHA and CPOFA pastes were higher than those of OPC paste at all ages, but less than those of RS pastes at the same replacement and curing time. However, at 90 days, the total porosities of 20CRHA, 20CPOFA, and 40CRHA pastes were 16.8, 17.3, and 17.4, which were slightly more than 16.6% of OPC paste because of the pozzolanic reaction of RHA and POFA. The results are in agreement with Li and Ding (2003). For the case of pastes with a small particle as that indicated in Fig. 11, the total porosities of 20% FRHA and 20FPOFA pastes were less than those of OPC paste and RS pastes at all ages. Total porosities of 40FRHA and 40FPOFA paste at 90 days were less than that OPC paste, because the high fineness RHA and POFA had a faster pozzolanic reaction. The differences between total

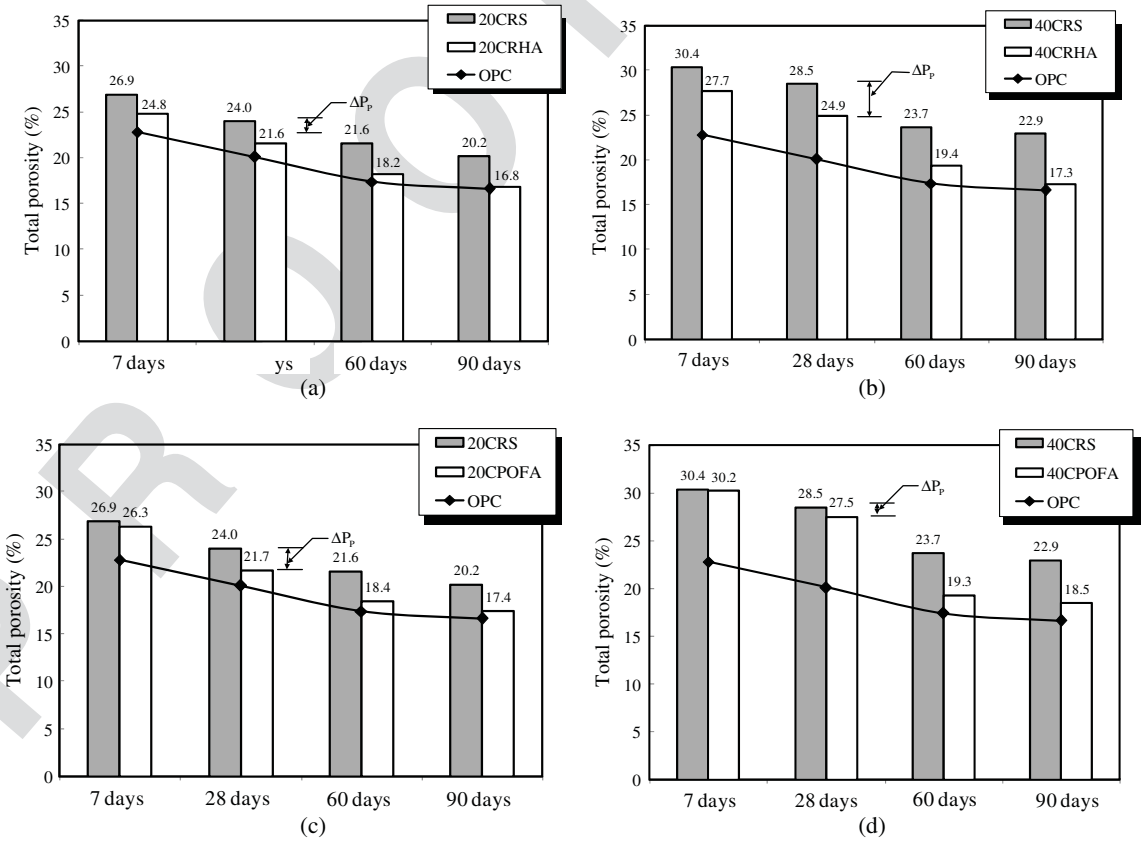

F10:1 **Fig. 10.** Total porosity of the OPC, CRS, CRHA, and CPOFA blended cement pastes: (a) 20% replacement of OPC, CRS, and CRHA; (b) 40%
F10:2 replacement of OPC, CRS, and CRHA; (c) 20% replacement of OPC, CRS, and CPOFA; (d) 40% replacement of OPC, CRS, and CPOFA

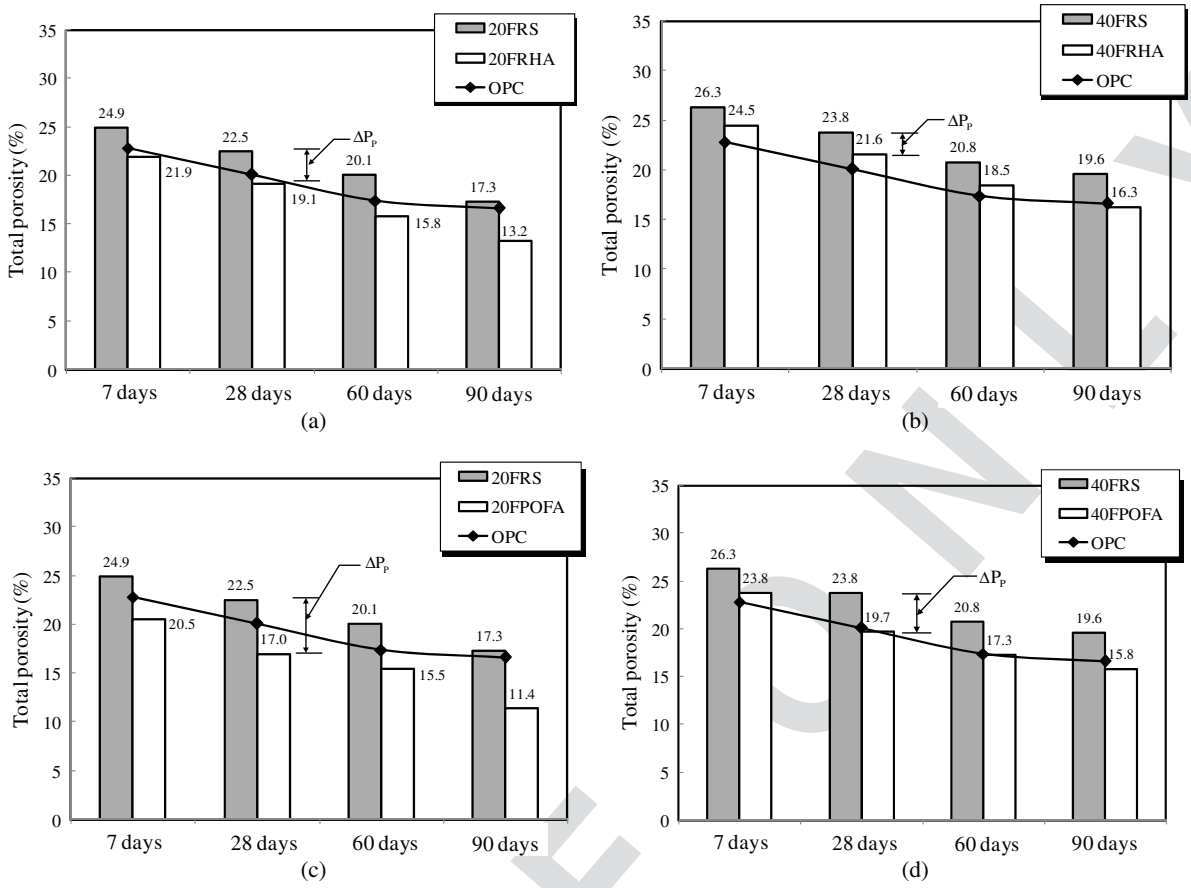

F11:1 F11:2 **Fig. 11.** Total porosity of the OPC, FRS, FRHA, and FPOFA blended cement pastes: (a) 20% replacement of OPC, FRS, and FRHA; (b) 40% replacement of OPC, FRS, and FRHA; (c) 20% replacement of OPC, FRS, and FPOFA; (d) 40% replacement of OPC, FRS, and FPOFA

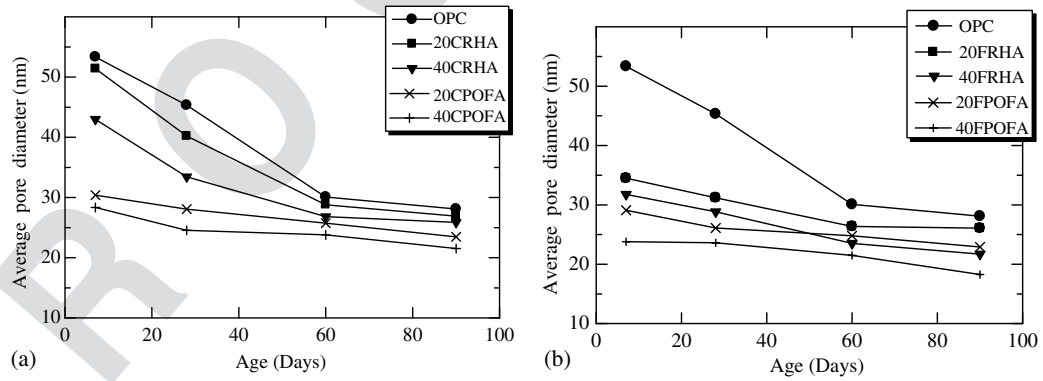

F12:1 **Fig. 12.** Average pore diameters in accordance with curing time: (a) CRHA and CPOFA pastes; (b) FRHA and FPOFA pastes

porosities of RS blended pastes and RHA (or POFA) pastes at the same replacement level and age were the pozzolanic reaction, designated as ΔP_P. The small particles showed a good filler effect in reducing the voids of cement paste. This again confirmed that the pozzolanic reaction of fine ashes was higher than that of the coarse ashes, with also increased filler effect of fine ashes. The results confirmed that partial replacement of OPC with fine RHA and POFA at rate of 20% by weight of binder had lower total porosity than that of OPC paste at all ages.

Pore Size Distribution of Blended Cement Paste: Effect of the Pozzolanic Reaction on the Pore Size Distribution

Fig. 12 shows the average pore diameters of all pastes. The average pore diameters of the OPC paste at 7, 28, 60, and 90 days were 53.4, 45.3, 30.1, and 28.1 nm, respectively. For pastes with CRHA and CPOFA with the same particle sizes as the cement, the 20 and 40% CRHA (or CPOFA) pastes had average pore diameters that were less than those of OPC paste at all ages, whereas the total porosity was higher than that of the OPC paste. For pastes

containing high fineness RHA and POFA, the average pore diameters of the 20 and 40% of FRHA (or FPOFA) pastes were less than that of the OPC paste, and the total porosity of 20FRHA and 20FPOFA paste was less than that of the OPC paste at all ages. The average pore diameter decreased in accordance with the use of RHA and POFA, and in accordance with an increase in the replacement level. In addition, the fine particles of RHA and POFA were more effective in reducing the average pore diameter due to dispersion, the filler effect, and increased pozzolanic reactions (Chindaprasirt et al. 2005; Frías and Cabrera 2000).

Conclusions

Based on the results of the research reported in this paper, the following conclusions can be drawn:

- Use of ground RHA and POFA with particle sizes smaller than that of OPC to replace portland cement Type I at 20% by weight of binder lead to a high compressive strength. In addition, the compressive strengths of the RHA pastes were slightly higher than those of the POFA pastes.
- The mass loss (at 30–450°C) of RS blended pastes increased in accordance with curing time, particle fineness, and cement replacement rate. The increase in compressive strength was due to the filler effect. In contrast, the $Ca(OH)_2$ content in the fine RS pastes was less than that in the coarse RS blended pastes.
- The differences between mass loss (at 30–450°C) of RS and RHA (or POFA) blended pastes at the same fineness, curing time, and replacement rate was due to the pozzolanic reaction, which increased in accordance with particle fineness and cement replacement rate. In addition, the weight losses (at 30–450°C) due to the pozzolanic reaction were higher than those due to the filler effect. Reduction of the $Ca(OH)_2$ content in the RHA and POFA pastes decreased in accordance with increases in the curing time and cement replacement rate of the blended cement.
- Use of both RHA and POFA with high fineness reduced the total porosity of the RHA and POFA pastes. The average pore diameters of the RHA and POFA pastes were smaller than those of the OPC paste. The effect due to the pozzolanic reaction was greater than that due to the filler effect.

Acknowledgments

The financial support of the Commission on Higher Education of Thailand for a grant under the Strategic Scholarships for Frontier Research Network for the Joint Ph.D. Program, Thai doctoral degree, Thailand Research Fund (TRF) under the TRF Senior Research Scholar contract No. RTA5480004, and the TRF New Researcher Scholarship, grant No. MRG5280178, is acknowledged.

References

Askarinejad, A., Pourkhorshidi, A. R., and Parhizkar, T. (2012). "Evaluation the pozzolanic reactivity of sonochemically fabricated nano natural pozzolan." *Ultrason. Sonochem.*, 19(1), 119–124.

ASTM. (2001). "Standard specification for coal fly ash and raw or calcined natural pozzolan for use as a mineral admixture in concrete." *C618-01*, West Conshohocken, PA.

ASTM. (2002). "Standard test method of compressive strength of hydraulic cement mortars (using 2-in. or [50 mm] cube speciments)." *C109-02*, West Conshohocken, PA.

ASTM. (2009). "Standard specification for portland cement." *C150-09*, West Conshohocken, PA.

Awal, A. S. M. A., and Hussin, M. W. (1997). "The effectiveness of palm oil fuel ash in preventing expansion due to alkali-silica reaction." *Cement Concr.Compos.*, 19(4), 367–372.

Bai, J., et al. (2003). "Compressive strength and hydration of wastepaper sludge ash-ground granulated blast furnace slag blended pastes." *Cement Concr.Compos.*, 33(8), 1189–1202.

Barbhuiya, S. A., Gbagbo, J. K., Russell, M. I., and Basheer, P. A. M. (2009). "Properties of fly ash concrete modified with hydrated lime and silica fume." *Constr. Build. Mater.*, 23(10), 3233–3239.

Chaipanich, A., and Nochaiya, T. (2010). "Thermal analysis and microstructure of portland cement-fly ash-silica fume pastes." *J. Thermal Anal. Calorim.*, 99(2), 487–493.

Chaipanich, A., Nochaiya, T., Wongkeo, W., and Torkittikul, P. (2010). "Compressive strength and microstructure of carbon nanotubes-fly ash cement composites." *Mater. Sci. Eng.*, 527(4–5), 1063–1067.

Chatveera, B., and Lertwattanaruk, P. (2011). "Durability of conventional concretes containing black rice husk ash." *J. Environ. Manage.*, 92(1), 59–66.

Chindaprasirt, P., Jaturapitakkul, C., and Sinsiri, T. (2005). "Effect of fly ash fineness on compressive strength and pore size of blended cement paste." *Cement Concr.Compos.*, 27(4), 425–428.

Chindaprasirt, P., Jaturapitakkul, C., and Sinsiri, T. (2007). "Effect of fly ash fineness on microstructure of blended cement paste." *Constr. Build. Mater.*, 21(7), 1534–1541.

Chindaprasirt, P., Rukzon, S., and Sirivivatnanon, V. (2008). "Resistance to chloride penetration of blended portland cement mortar containing palm oil fuel ash, rice husk ash and fly ash." *Constr. Build. Mater.*, 22(5), 932–938.

El-Bouny, V. B. (1994). "Caractérisation des pâtes de ciment et des bétons–Méthodes, analyses, interprétations." *Technical Rep.*, Laboratorie Central des Ponts et Chaussées, Paris (in French).

El-Jazairi, B., and Illston, J. M. (1977). "A simultaneous semi-isothermal method of thermogravimetry and derivative thermogravimetry, and its application to cement pastes." *Cement Concr.Compos.*, 7(3), 247–257.

Frías, M., and Cabrera, J. (2000). "Pore size distribution and degree of hydration of metakaolin-cement pastes." *Cement Concr.Compos.*, 30(4), 561–569.

Galle, C. (2001). "Effect of drying on cement-based materials pore structure as identified by mercury intrusion porosimetry: A comparative study between oven-, vacuum-, and freeze-drying." *Cement Concr.Compos.*, 31(10), 1467–1477.

Ganesan, K., Rajagopal, K., and Thangavel, K. (2008). "Rice husk ash blended cement: Assessment of optimal level of replacement for strength and permeability properties of concrete." *Constr. Build. Mater.*, 22(8), 1675–1683.

Goldman, A., and Bentur, A. (1993). "The influence of microfillers on enhancement of concrete strength." *Cement Concr.Compos.*, 23(4), 962–972.

Hubler, M. H., Thomas, J. J., and Jennings, H. M. (2011). "Influence of nucleation seeding on the hydration kinetics and compressive strength of alkali activated slag paste." *Cement Concr.Compos.*, 41(8), 842–846.

Idir, R., Cyr, M., and Tagnit-Hamou, A. (2011). "Pozzolanic properties of fine and coarse color-mixed glass cullet." *Cement Concr.Compos.*, 33(1), 19–29.

Isaia, G. C., Gastaldini, A. L. G., and Moraes, R. (2003). "Physical and pozzolanic action of mineral additions on the mechanical strength of high-performance concrete." *Cement Concr.Compos.*, 25(1), 69–76.

Jaturapitakkul, C., Kiattikomol, K., Tangchirapat, W., and Saeting, T. (2007). "Evaluation of the sulfate resistance of concrete containing palm oil fuel ash." *Constr. Build. Mater.*, 21(7), 1399–1405.

Jaturapitakkul, C., Tangpagasit, J., Songmue, S., and Kiattikomol, K. (2011). "Filler effect and pozzolanic reaction of ground palm oil fuel ash." *Constr. Build. Mater.*, 25(11), 4287–4293.

Kiattikomol, K., Jaturapitakkul, C., and Tangpagasit, J. (2000). "Effect of insoluble residue on properties of portland cement." *Cement Concr.Compos.*, 30(8), 1209–1214.

Konecny, L., and Naqvi, S. J. (1993). "The effect of different drying techniques on the pore size distribution of blended cement mortars." *Cement Concr.Compos.*, 23(5), 1223–1228.

Kroehong, W., Sinsiri, T., Jaturapitakkul, C., and Chindaprasirt, P. (2011). "Effect of palm oil fuel ash fineness on the microstructure of blended cement paste." *Constr. Build. Mater.*, 25(11), 4095–4104.

Kumar, S., et al. (2008). "Mechanical activation of granulated blast furnace slag and its effect on the properties and structure of portland slag cement." *Cement Concr.Compos.*, 30(8), 679–685.

Kumar, S., and Kumar, R. (2011). "Mechanical activation of fly ash: Effect on reaction, structure and properties of resulting geopolymer." *Ceram. Int.*, 37(2), 533–541.

Li, Z., and Ding, Z. (2003). "Property improvement of portland cement by incorporating with metakaolin and slag." *Cement Concr.Compos.*, 33 (4), 579–584.

Mehta, P. K. (1987). "Studies on the mechanisms by which condensed silica fume improves the properties of concrete: Durability aspects." *Proc., Int. Workshop on Condensed Silica Fume in Concrete*, 1–17.

Poon, C. S., Lam, L., Kou, S. C., Wong, Y. L., and Wong, R. (2001). "Rate of pozzolanic reaction of metakaolin in high-performance cement pastes." *Cement Concr.Compos.*, 31(9), 1301–1306.

Rashad, A. M., Zeedan, S. R., and Hassan, H. A. (2012). "A preliminary study of autoclaved alkali-activated slag blended with quartz powder." *Constr. Build. Mater.*, 33(1), 70–77.

Rukzon, S., Chindaprasirt, P., and Mahachai, R. (2009). "Effect of grinding on chemical and physical properties of rice husk ash." *Int. J. Miner. Metall. Mater.*, 16(2), 242–247.

Sata, V., Jaturapitakkul, C., and Kiattikomol, K. (2004). "Utilization of palm oil fuel ash in high-strength concrete." *J. Mater. Civ. Eng*.

Sinsiri, T., Kroehong, W., Jaturapitakkul, C., and Chindaprasirt, P. (2012). "Assessing the effect of biomass ashes with different finenesses on the compressive strength of blended cement paste." *Mater. Des.*, 42(1), 424–433.

Tangchirapat, W., Jaturapitakkul, C., and Kiattikomol, K. (2009). "Compressive strength and expansion of blended cement mortar containing palm oil fuel ash." *J. Mater. Civ. Eng*.

Tangpagasit, J., Cheerarot, R., Jaturapitakkul, C., and Kiattikomol, K. (2005). "Packing effect and pozzolanic reaction of fly ash in mortar." *Cement Concr.Compos.*, 35(6), 1145–1151.

Wansom, S., Janjaturaphan, S., and Sinthupinyo, S. (2010). "Characterizing pozzolanic activity of rice husk ash by impedance spectroscopy." *Cement Concr.Compos.*, 40(12), 1714–1722.

Washburn, E. W. (1921). "Note on a method of determining the distribution of pore size in a porous materials." *Proc. Natl. Acad. Sci. USA*, 7(4), 115–116.

Wongkeo, W., and Chaipanich, A. (2010). "Compressive strength, microstructure and thermal analysis of autoclaved and air cured structural lightweight concrete made with coal bottom ash and silica fume." *Mater. Sci. Eng.*, 527(16–17), 3676–3684.

Queries

1. Please specify the ASCE Membership Grades for all of the authors who are members.

2. NEW! ASCE Open Access: Authors may choose to publish their papers through ASCE Open Access, making the paper freely available to all readers via the ASCE Library website. ASCE Open Access papers will be published under the Creative Commons-Attribution Only (CC-BY) License. The fee for this service is $1750, and must be paid prior to publication. If you indicate Yes, you will receive a follow-up message with payment instructions. If you indicate No, your paper will be published in the typical subscribed-access section of the Journal.

3. Do the heading levels in the paper reflect your original intent?

4. Please convert the "tons" units, mentioned twice in the first paragraph of the Introduction, to SI units, or indicate that you intended "metric tons."

5. Are the definitions provided for "C-S-H," "C-A-H," and "C-A-S-H," mentioned in the third paragraph of the Introduction, correct?

6. Is "TOPAS," mentioned in the first paragraph of the "Materials" section, an acronym that has a definition? If so, please spell it out.

7. Do the edits we made to Table 1 retain your original meaning?

8. Are "STA" and "C/CD," mentioned in the first paragraph of the "Thermal Analysis" section, acronyms that have a definition? If so, please spell them out.

9. Please convert the "dynes" units, mentioned in the first paragraph of the "Determination . . . " section, to SI units.

10. Although ASCE style permits third- and higher-level headings, readers often find them difficult to follow at a glance. Therefore, all of the third- and higher-level headings were changed to second-level headings. Do you approve of this style change?

11. The citation "Metha 2007," mentioned in the last paragraph of the "Thermal Analysis of the Blended Cement Pastes: Influence of Ground . . . " section, is not present in the References list. Please provide the full details for "Metha 2007," and we will insert it in the References list and link it to this citation.

12. The reference "Hubler et al. 2011" is not mentioned anywhere in the text. ASCE style requires that all entries in the References list be mentioned at least once in the paper. Please indicate a place in the text, tables, or figure captions where we may insert a citation to "Hubler et al. 2011," or indicate that the entry can be deleted from the References list.

13. Please specify the name and location (city/country) of the publisher (or sponsor), not the location of the conference, of the conference proceedings reference "Mehta 1987."

14. The reference "Rashad et al. 2012" is not mentioned anywhere in the text. ASCE style requires that all entries in the References list be mentioned at least once in the paper. Please indicate a place in the text, tables, or figure captions where we may insert a citation to "Rashad et al. 2012," or indicate that the entry can be deleted from the References list.

15. This query was generated by an automatic reference checking system. This reference (Sata et al. 2004) could not be located in the databases used by the system. While the reference may be correct, we ask that you check it so we can provide as many links to the referenced articles as possible.

16. Please provide the updated information for Sata et al. 2004 reference.

17. This query was generated by an automatic reference checking system. This reference (Tangchirapat et al. 2009) could not be located in the databases used by the system. While the reference may be correct, we ask that you check it so we can provide as many links to the referenced articles as possible.

18. Please provide the updated information for Tangchirapat et al. 2009 reference.

19. This query was generated by an automatic reference checking system. This reference (Washburn 1921) could not be located in the databases used by the system. While the reference may be correct, we ask that you check it so we can provide as many links to the referenced articles as possible.